AN INVESTIGATION OF THE KINETICS FOR THE FAST PYROLYSIS OF LOBLOLLY PINE WOODY BIOMASS

A Thesis
Presented to
The Academic Faculty

by

Alexander W. Williams

In Partial Fulfillment
of the Requirements for the Degree
Doctor of Philosophy in the
G. W. Woodruff School of Mechanical Engineering

Georgia Institute of Technology
August 2011

AN INVESTIGATION OF THE KINETICS FOR THE FAST PYROLYSIS OF LOBLOLLY PINE WOODY BIOMASS

Professor J. Rhett Mayor, Advisor
G. W. Woodruff School of Mechanical Engineering
Georgia Institute of Technology

Professor John Muzzy
Department of Chemical Engineering
Georgia Institute of Technology

Professor Matthew Realff
Department of Chemical Engineering
Georgia Institute of Technology

Professor Srinivas Garimella
G. W. Woodruff School of Mechanical Engineering
Georgia Institute of Technology

Professor Shreyes Melkote
G. W. Woodruff School of Mechanical Engineering
Georgia Institute of Technology

Date Approved: 16 May 2011

ACKNOWLEDGEMENTS

I would like to thank the Chevron Corporation for providing the financial backing for this investigation, Dr. Kasi David for providing biomass samples and the thermogravimetric analysis data for *Pinus taeda* used in Section 6.6 and Dr. Mary Lynn Realff for providing the biomass particle size evaluations used in Section 7.7.1.

I am grateful to my committee members: Dr. Matthew Realff, Dr. John Muzzy, Dr. Srinivas Garimella and Dr. Shreyes Melkote, whose analysis, evaluation and recommendations provided much improvement to this work.

In particular I owe a great debt to my advisor Dr. Rhett Mayor, who has continually challenged and pushed me to become both a great researcher and a great engineer. Without his encouragement, I would not have even considered the pursuit of my doctorate.

Most of all I would like to express my appreciation and love for my wife Suzie, without whom graduate school would have been a much less enjoyable period of my life.

TABLE OF CONTENTS

LIST OF TABLES

LIST OF FIGURES

SUMMARY

In the search for fossil fuel alternatives the production of bio-oil through the pyrolysis of biomass is one method which has shown evidence of scalability, meaning that the technology could be scaled up for the processing of biomass on the order of tons per day. Pyrolysis is the thermal degradation of compounds in the absence of oxygen. Of particular interest is the pyrolysis of sustainable energy crops such as Loblolly pine (*Pinus taeda*). The goal of this study is to develop a new method of characterizing the fast pyrolysis of biomass for the advancement of reactor design. The objectives are to determine bulk kinetic coefficients for the isothermal fast pyrolysis of biomass, evaluate the interchangeability of fast and slow pyrolysis kinetic parameters and compare generally accepted pyrolysis mechanisms derived from a common data set. A technical objective is to apply the most suitable derived kinetic parameters to model pyrolysis within a moving bed reactor.

A novel fast pyrolysis micro-reactor is presented along with its design and development process. The micro-reactor allows for the control over both temperature and residence time of the reacting biomass. This system provides the experimental data for the characterization of biomass pyrolysis kinetic parameters. Thermal validation tests are presented and experimental yield results are given for raw Loblolly Pine, Avicel cellulose and Beechwood xylan for the derivation of kinetic descriptors. Cellulose and xylan results show good agreement with literature when the proper experimental conditions are met and whole wood pyrolysis results clearly demonstrate the dissimilarity between fast and slow pyrolysis apparent kinetic rates.

The experimental results are then used to evaluate five different pyrolysis kinetic model configurations: single component global pyrolysis, two component global pyrolysis, product based pyrolysis, pseudo-component based pyrolysis and pseudo-component pyrolysis with an intermediate solid compound. Pseudo-component models are of particular interest because they may provide a generalized model, parameterized by the fractional composition of cellulose, hemicellulose and lignin in biomass species. Lignin pyrolysis yields are calculated to evaluate the suitability of a pseudo-component parallel non-competing superposition pyrolysis model. Lignin yields are estimated by taking the difference between whole wood pyrolysis and predicted cellulose and hemicellulose pyrolysis behaviors. The five models are then evaluated by comparison of predicted yields to the results for the pyrolysis of Scots pine (*Pinus sylvestris*) and Norway spruce (*Picea abies*). Model evaluations show that pseudo-component superposition is not suitable as a generic pyrolysis model for the fast pyrolysis of biomass observed using the micro-reactor. Further analytical evaluations indicate that the assumption of parallel non-competing reactions between pseudo-components is not valid. Among the other models investigated the intermediate solid compound model showed the best fit to the verification experimentation results followed closely by the two component global model.

Finally, the derived kinetic parameters are applied to the design of moving bed vacuum pyrolysis reactors which provide for the separation of heat and mass transfer pathways, resulting in the reduction of char entrainment and secondary reactions within collected bio-oils. Reaction kinetics and porous bed heat and mass transfer are accounted for within the bed model. Model development and predictive results are presented and sensitivity to activation energy variations investigated.

CHAPTER 1

INTRODUCTION

1.1 Introduction

The search for scalable and sustainable alternative fuel sources has been a research topic for decades and has been of greater interest than ever in recent years. The primary driver for bio-fuels development is legislation forcing cost parity with drilled oil. For example, the United States Energy Independence and Security Act of 2007 mandates that 36 billion gallons of renewables be blended into the transportation fuel supply by 2022 [1] and the European Union Renewable Energy Directive 2009/28/EC set a transportation energy supply target of 10% from renewable energy sources by 2020. [2] Policies such as these and the potential for a mandatory carbon cap and trade market within the United States are the most significant driving forces behind renewable fuel development. The utilization of biomass as an energy source has been identified as a necessary component to reach these national goals and conform to future policy mandates with regard to fuel sourcing.

Biomass feedstocks are a significant source of energy and their conversion into more useful forms of energy is the center of much investigation. On a national basis, forest lands in the contiguous United States are estimated to produce 368 million dry tons annually on a sustainable basis. [3] This includes fuel wood harvesting, wood processing mill and pulp and paper mill residues, urban wood residues including construction and demolition debris, logging and site clearing residues, and fuel treatment operations to reduce fire hazards. This does not include areas currently inaccessible by roads or environmentally sensitive areas. In particular, the use of Loblolly pine (*Pinus taeda*) as an energy feedstock has been identified as a potentially significant

source of fuel. Loblolly pine is currently the most common plantation-grown species in the southern part of the United States due to its rapid growth and ease of establishment. As of 2002, the southeastern United States pine forests covered more than 36 million ha and accounted for nearly 60% of US industrial wood production and 16% of the world's total wood production. [4] Within these plantings, there is more than 360GJ/ha of potential bio-energy remaining after primary harvesting [5, 6] with a 25-35 year harvest interval for a given tree stand. [7] These estimates result in a projected 432PJ of bio-energy obtainable from southeastern United States pine forests on an annual basis.

The extraction of useful compounds from biomass generally falls into two process categories: processes that involve anaerobic digestion and fermentation; processes that involve the addition of heat. [8] Within the latter set of processes, pyrolysis is of interest due to its feedstock flexibility and potential for scale-up. The fast pyrolysis of biomass is considered a viable thermochemical pathway to renewable liquid products with a diverse array of possible product compositions. [9, 10] The process has been studied for both liquid fuels production and targeted chemical feedstocks and is typically characterized by a carefully controlled pyrolysis reaction temperature, short vapor residence times followed by rapid cooling of pyrolysis vapors and high heating rates. [9]

Biomass pyrolysis has attracted substantial attention from research scientists with efforts extending both to detailed modeling of pyrolysis reactions and to experimental investigation of the process from a variety of directions. However, biomass feedstocks are complex organic molecules that are difficult to completely characterize. Typically, there are large variations in chemical composition and molecular structure between species and also within species to a lesser degree. Physical models fail to predict product outcomes either qualitatively or quantitatively, due to these complexities. As such, the coupling of physical models with empirical data is pursued for the purpose

of directing the design of pyrolysis reactors. [11, 12]

This work will be addressing the derivation of fast pyrolysis kinetic parameters for the advancement of reactor design. Several definitions of fast pyrolysis have been given [13, 14, 15] with operating temperatures ranging from 575°C to 1000°C and heating rates ranging from 10°C/s to 300°C/s. For the purpose of this study, fast pyrolysis will be constrained to heating rates greater than 50°C/s. Cited advantages of fast pyrolysis over other methods include low production costs, low energy input, and CO_2 neutrality. [10, 9] Liquid intermediates are also a desirable outcome offering the potential for a versatile biomass byproduct for both fuel and diverse chemical applications. [10, 9]

Further characterization of biomass kinetic parameters is necessary for two reasons: 1. The wide range of activation energies and pre-exponential factors that have been reported for describing biomass pyrolysis; [16] 2. The disconnect between typical pyrolysis characterization methodologies and scalable technologies for bulk fuel production. Biomass pyrolsyis kinetics are typically characterized using thermogravimetric (TGA) ovens or custom pyrolysis apparati.

1.2 Research Objectives

The goal of the proposed research is to develop a new method of characterizing the fast pyrolysis of Loblolly pine and apply the derived kinetics to a multi-physics pyrolysis model for the advancement of reactor design. In support of this goal, the following research objectives will be pursued:

1. To measure the mass conversion efficiency of biomass undergoing isothermal fast pyrolysis as a function of time.

2. To test the hypothesis that slow pyrolysis derived Arrhenius coefficients do not accurately describe the isothermal fast pyrolysis of biomass.

3. To test the hypothesis that conversion rates of biomass undergoing isothermal fast pyrolysis can be predicted by feedstock composition based upon known conversion rates of cellulose, hemicellulose and lignin.

4. To evaluate the predictive power of generally accepted pyrolysis bulk kinetic mechanisms.

5. To demonstrate the application of fast pyrolysis kinetics to the design of moving bed vacuum pyrolysis reactors.

1.3 Thesis Organization

This study presents a new methodology for the derivation of fast pyrolysis kinetic parameters as process descriptors for the purpose of advancing pyrolysis reactor design and furthering the understanding of process fundamentals. A novel micro-reactor for the fast pyrolysis of biomass is presented in Chapter 2. The micro-reactor enables the rapid heating of biomass samples and collection of reaction products, while controlling reactor temperature and particle residence times. Reactor design requirements are presented along with the design process followed to achieve the set requirements. The isothermal performance of the system is verified through infrared imaging techniques. Heating rates of biomass samples are measured for solid wood wafers and projected estimates made for the thin particle beds used during actual pyrolysis testing.

Chapter 3 presents a detailed treatment of the experimental protocols and methodologies developed for the study of kinetics in pyrolysis reactions using the micro-reactor system. In addition, a detailed treatment of the characterization of experimental error in micro-reactor yield-results using classical Kline-McKlintock uncertainty analysis is presented at the end of Chapter 3.

Bulk reactant based reaction mechanisms are investigated in Chapter 4. The literary basis for the mechanisms is presented followed by the mathematical derivations of

each model utilizing isothermal fast pyrolysis experimental yields. Best-fit determination methods are presented including the use of χ^2 goodness of fit parameters and particle swarm optimization methods for the determination of globally best fit kinetic parameters. Finally, the experimental whole wood pyrolysis results are presented for Loblolly pine and kinetic parameters are derived for the models presented.

Pseudo-component based reaction mechanisms are investigated in Chapter 5. Model structures are presented for both a pure pseudo-component model and one with an intermediary compound. These models are evaluated based upon both isolated pseudo-component pyrolysis kinetic parameters and using a global best fit for all kinetic parameters constrained only by the fractional composition of the biomass by pseudo-components. Isolated pseudo-component kinetics are experimentally determined for the first method and the interactions of pseudo-components is investigated. Global best fit kinetic parameters are then determined using on the pseudo-component fractional constraint.

Chapter 6 presents the evaluation and comparison of the pyrolysis models presented in Chapters 4 and 5. The model predictions are evaluated against a set of validation data and percentage error in predictions compared. Slow pyrolysis results are then presented and slow and fast pyrolysis derived kinetic parameters are then compared using an Arrhenius plot. Finally, the extensibility of the models is evaluated against a set of alternate species.

The derived single component kinetic parameters are applied to a multi-physics moving bed vacuum pyrolysis model in Chapter 7. The analytical development of the model is presented as well as the implementation of the system of equations into a finite difference solution scheme. Simulation results are then presented for several pyrolysis bed parameter cases. The results from one set of boundary conditions are applied to the sizing of a pilot scale moving bed reactor and the impact of activation energy variation evaluated.

A summary of the individual section results, the study conclusions and contributions are presented in Chapter 8. Recommendations for future work are made including extensions to the present study and additional questions raised by the results presented in this work.

CHAPTER 2

DEVELOPMENT OF A NOVEL MICRO-REACTOR SYSTEM FOR THE MEASUREMENT OF ISOTHERMAL FAST PYROLYSIS YIELDS

2.1 Introduction

This chapter presents a novel micro-reactor for the isothermal fast pyrolysis of biomass. A review of common experimental pyrolysis apparati is provided discussing both slow (low heating rate) and fast (high heating rate) pyrolysis systems. The design requirements for the isothermal micro-reactor are presented as well as the functional decomposition design process followed. An overview of the micro-reactor is conducted, breaking the system down into key subsystems. The influence of introduced vibratory energy is evaluated for the improvement of particle flow within the reactor using analysis of variance (ANOVA). Verification tests are presented for both the system isothermality and projected heating rates. Finally, initial commissioning tests are presented and the system's ability to produce isothermal pyrolysis product yield results evaluated.

2.1.1 Salient Literature

In 1963 Roberts and Clough [17] investigated the pyrolysis of Beechwood cylinders embedded with thermocouples for *in situ* temperature measurement. The study showed that pyrolysis activation energy and heat of reaction vary with experimental conditions. Samples were pyrolyzed in a tubular furnace with the mass loss being tracked through a lever arm type balance. Pyrolysis activation energies for a single component global model were calculated based upon a best fit to the mass loss data assuming a

single component global reaction scheme. The results showed two different activation energies and heats of reaction distinguished by wood temperatures either above or below 280°C.

Experimental investigations into better understanding biomass pyrolysis have been successful at examining specific configurations of reactions utilizing a variety of apparati and analysis equipment. The thermogravimetric analysis (TGA) oven is the most common tool for pyrolysis kinetic studies at low heating rates ($\lesssim 1$°C/s). TGA ovens are frequently the system of choice for reaction coefficient derivations due to the large volume of data obtained for relatively small samples sizes and minimal operator effort. The systems function by simultaneously recording the sample mass and oven temperature while heating the oven chamber at a specified rate or maintaining a set temperature.

Grønli [18] used a differential TGA oven for the derivation of kinetic parameters for individual biomass components and several whole wood species. Samples from a birch, a spruce, a pine and extracted cellulose, hemicellulose and lignin were pyrolyzed at a heating rate of 0.08°C/s (5°C/min). Single component global models were fit to each of the sample results and a pseudo-component model was fitted to the whole wood pyrolysis results. Tested cellulose samples showed variability in the DTG curves in both shape and magnitude which was attributed to differences as a result of the source of the cellulose. It was concluded, however, that cellulose pyrolysis is well represented by a single first order reaction and that complicated sequential step models are not necessary. Lignin results showed volatilization spread out across a wide temperature range and hemicellulose results were deemed inconclusive due to inorganic impurities (*i.e.* minerals). From the whole wood pyrolysis results it was determined that a three component model fit the pine and spruce DTG curves well but a fourth component was required for the birch DTG curve fits to obtain good agreement with the data. Furthermore, Grønli concluded that the volatilized fractions

associated with each pseudo-component were not tractable back to the actual wood compositions, a conclusion in direct opposition to that drawn by Ward and Braslaw [19]. This type of direct disagreement over the suitability of pseudo-component mechanisms as whole wood pyrolysis descriptors is repeated throughout the literature and subsequently merited further investigation.

Milosavljevic and Suuberg [20] studied the pyrolysis of cellulose specifically with respect to the impact of heating rate and final reactor temperature. Experiments were performed using a standard TGA oven with testing at both constant heating rate and ramp and hold conditions. Constant heating rate tests were performed at rates between 0.0015 and 0.016°C/s ($0.092 - 0.93$°C/min). Ramp and hold tests were performed in two sets with target temperatures between 265 and 375°C with heating rates between 0.017 and 1°C/s ($1 - 60$°C/min).

2.1.2 Challenges Associated with TGA Ovens

The challenges associated with TGA as an experimental instrument for pyrolysis investigations have been studied by several researchers. In 1980 Chornet and Roy [21] drew attention to the fact that large discrepancies exist within literature concerning cellullosic biomass pyrolysis kinetics. In 1998 Antal *et al.* [22] demonstrated that systematic temperature measurement errors were to blame for discrepancies in kinetic parameter values as a result of heating rates and that sample variabilities (particularly in cellulose studies) were to blame for many reported variations in activation energy values. Additionally, Antal *et al.* challenged the community to conduct a thorough study of systematic thermal errors within TGA systems based upon a common pyrolysis test sample. In 1999 Grønli *et al.* [23] answered that call to evaluate the variability between TGA oven results by testing the same sample of cellulose at multiple laboratories. Avicel PH-105 cellulose was tested in five different TGA oven models among eight laboratories at heating rates of 0.08 and 0.67°C/s (5 and 40°C/min).

The activation energy and pre-exponential values showed good agreement, amongst the measurements at the same heating rate. However, both the pre-exponential factor and activation energy best fit values were lower for the higher heating rate results than for the lower heating rate results. Grønli attributed this to thermal lag within the systems. Additionally, the final residual sample mass was lower, on average, for the higher heating rate tests but also showed a larger standard deviation than those measured the for the lower heating rate. This too was attributed to thermal lag. The study concluded that significant care must be taken in the evaluation of pyrolysis kinetics (specifically from TGA data) to account for uncertainties in temperature measurements.

2.1.3 High Heating Rate Reactor Configurations

Commercially available devices do not exist for high heating rate kinetic characterization studies but a wide variety of purpose built reactors have been developed for studying high heating rate pyrolysis reactions. Within these studies, however, little agreement exists with respect to the interchangeability of fast and slow pyrolysis kinetic parameters.

Di Blasi and Lanzetta [24] tested oat spelt xylan using a radiantly heated quartz tube thermobalance. Heating rates varied from 27 to 36°C/s with the target temperature range of $200 - 340$°C. Kinetic parameters were derived assuming a two stage sequential mechanism. Kinetic parameters were derived using a two stage mechanism that required an intermediate compound. Within the model, this intermediate could not pyrolyze until a specified duration into the reaction regardless of the quantity of intermediate component that may be present. In a similar study by the same authors [25] cellulose fibers were pyrolyzed using the same radiantly heated quartz tube furnace. Two types of tests were performed, constant radiant flux and controlled temperature. The two controlled temperature cases were evaluated at 300 and 350°C

with heating rates ranging from $19 - 56°C/s$. Particle layers were restricted to below $60\mu m$ to ensure thermally thin characteristics were present. It was stated, however, that temperature measurements were approximate because the thermocouple was not in direct contact with the samples. Constant heat flux experimental results showed that the cellulose entered into a heat transfer limited regime above $\sim 325°C$. The kinetic parameters derived were in modest agreement with literature.

A later study was conducted by Di Blasi and Branca [26] using two different experimental reactors for the pyrolysis of Beechwood. A fluidized bed reactor was used to measure product quantities (char, gas and oil) while a similar radiantly heated tubular quartz furnace with integrated thermobalance and *in situ* thermocouple was used to measure volatilization rates. Reactor temperates from $\sim 315 - 450°C$ were tested and both single component global and product based models were derived from Beechwood pyrolysis experimental results. Heating rates of $16.7°C/s$ were reported for the radiant tube reactor. The derived models were shown to qualitatively fit the experimental results in the kinetically controlled regime, stated to be for temperatures $\leq 435°C$, for the tested reactors. In comparison to slow pyrolysis models, the authors concluded that disagreement in final predicted char yields indicated a lack of interchangeability between fast and slow pyrolysis kinetics. Additionally, disagreement with other fast pyrolysis studies was attributed to variations in reactor heating configurations.

Thurner and Mann [27] derived kinetic descriptors for the pyrolysis of oak sawdust following the Shafizadeh product based model. Experimentation was carried out in a custom tube furnace apparatus enabling the collection of reaction products for individual identification and *in situ* sample temperature measurement. A TGA oven was not used because of the need to measure actual sample temperature and the collect pyrolysis products. Kinetic parameters derived from the experimental results showed poor agreement with experimental data reported in the literature. The large

discrepancies observed between the study results and literature were attributed to variations in heating conditions between experimental systems.

Jensen *et al.* [28] utilized a tube batch reactor for the pyrolysis of straw at reported heating rates of up to 50°C/s. The reactor consisted of a vertical quartz tube containing a suspended basket of straw particles radiantly heated from a surrounding tube furnace. The temperature of the oven was monitored via a thermocouple suspended within the quartz tube below the sample. Pyrolysis products were carried out of the reactor by a nitrogen purge for further analysis.

A thorough cataloging of reaction products was performed by Zhang *et al.* [29] with the pyrolysis reactions taking place in a horizontal quartz tube furnace. Oven temperatures reached up to 1400 °C and heating rates were reported to be above 1.7 °C/s. Gas and liquid products were collected during separate tests for GC/MS characterization.

Nunn *et al.* [30] pyrolyzed powdered sweet gum hardwood using an electric screen heater reactor for the derivation of single component global kinetics. Batches of 100mg were reacted in a helium environment with heating rates of up to 100°C/s reported with target temperatures between 330 and 1130°C. Once peak temperatures were reached the system was quenched with an average cooling rate of 200°C/s. Conversion estimates were based upon the residual char within the mesh screen. A comparison of kinetic rates to other studies, however, showed poor agreement.

Fluidized bed and entrained flow reactors are frequently employed for high throughput pyrolysis studies. Westerhof *et al.* [31] investigated the impact of residence time and and reactor temperature on pine pyrolysis using a 1kg/h fluidized bed reactor. Temperatures between 330 and 580°C were investigated with oils collected for stability analysis.

Scott *et al.* [32, 33] utilized two different pyrolysis reactors to investigate the impact of temperature on the fast pyrolysis of both Avicel cellulose and red maple

sawdust. The first was a reactor termed the *ultrapyrolysis* entrained flow reactor which used preheated nitrogen before mixing with virgin biomass in a highly turbulent *thermovortactor* and passing it into a liquid nitrogen cooled *cryovortactor*. This unit was operated at temperatures from $650 - 1000°C$ with gas residence times of 50-900ms. The second reactor was a fluidized bed reactor which operated in the temperature range of $400 - 750°C$ with gas residence times of 300-1500ms. Product yield quantities and gas compositions showed good agreement between the reactors using a gas chromatograph.

Samolada and Vasalos [34] utilized a fluidized bed with preheated sand particles to pyrolyze fir wood. Heating rates of 1000°C/s were estimated for temperatures between 400 and 500°C with particle sizes between 300 and 425μm. Conversion rates were estimated based upon the volatilized matter as the char samples were inseparable from the sand. Results showed good agreement when compared to studies with very similar heating conditions.

DeSisto *et al.* [35] pyrolyzed *Pinus strobus* (Eastern White pine) at 400, 500 and 600°C in a bubbling fluidized bed reactor for the production and characterization of pyrolysis oils. The oils were analyzed using GC/MS, C NMR, a viscometer, pH meter and a bomb calorimeter. Char yields were highest at 400°C and gas yields were highest at 600°C. The higher char fraction at 400°C was attributed to a possibly incomplete reaction of the biomass.

Boukis et al. [36, 37] configured a circulating fluidized bed reactor operating with a maximum capacity of 150kg per batch utilizing particles of less than 2mm in size. The tested reactor temperature was approximately 500°C utilizing char and sand recirculated through a combustor to provide the process heat.

An entrained flow pyrolysis reactor unit was developed in the 1980's at the Georgia Institute of Technology Engineering Experiment Station (now called the Georgia

Tech Research Institute). The entrained flow unit utilized a propane burner to provide heating gas which was mixed with nitrogen in order to carry biomass particles vertically through a stainless steel pipe. The biomass particles underwent rapid heating and pyrolysis during the the passage through the pipe prior to entering a cyclone to remove the solids. The heavier pyrolysis volatiles were then condensed in an air cooled condenser and a demister. Oil yields were reported to be 36.4% by mass with modeling predicting 70% yields in an optimized configuration. [38, 39, 40, 41]

In addition to radiant heat sources and fluidized beds, several less conventional systems have been implemented for the study of pyrolysis.

Lin *et al.* [42] utilized a pyroprobe reactor in conjunction with a TGA oven to study the kinetics and products of cellulose pyrolysis. A pyroprobe operates by heating a small sample directly in contact with a resistive heating filament. Within the work of Lin *et al.* sample sizes of 4-5mg of cellulose were reacted with reported heating rates of 2.5°C/s. Liquid products were collected for HPLC analysis while gaseous products were carried out for GC/MS analysis. Kinetic parameters were derived for a single component global first order model based upon TGA results.

A pyroprobe was also used by Boateng [43] to pyrolyze switchgrass charcoal for gas chromatograph analysis of the products. Using a platinum filament, nominal heating rates of $20,000$°C/s were reported with estimated actual sample heating rates of 300°C/s, though this was never experimentally or analytically verified. Samples of 1mg were reacted at target temperatures between 500 and 1000°C.

Rotating cone reactors enable direct contact heating of biomass particles through conduction interactions with the reactor walls and heated sand. Centrifugal forces carry the sand and biomass from the base of a rotating cone up to the exit at the top. Heating rates as high as 100°C/s have been reported. These systems offer the option of recirculating the biomass but do provide for the separation of solid products and sand. [44, 45]

Peacock and Bridgwater [46] presented an ablative pyrolysis reactor based around four rotating axisymmetric blades to apply pressure for the decrease of contact resistance between biomass particles and the electrically heated reaction plate. Reaction temperatures of 450, 550 and 600°C were tested and throughputs of up to $2.5kg/h$ were achieved. In another paper Peacocke *et al.* [47] compared the yields and analyzed the oils produced from the ablative plate pyrolysis reactor to those from a wire-mesh pyrolysis reactor. The wire-mesh reactor heated biomass samples trapped between two resistively heated mesh walls with reported heating rates between 0.1 and 5000°C/s. The pyrolysis products from both reactors were analyzed using a GC and a FTIR analyzer. The results showed that the two reactor configurations, despite both providing high heating rates, produced significantly different liquid products. The authors attributed the difference to thermal gradients within particles reacting inside the ablative plate reactor.

An operational bench scale auger reactor at Mississippi State University is currently being utilized for pyrolysis oil production, analysis and characterization. The system was used to investigate pine wood, pine bark, oak wood and oak bark. Residence times of ~ 50 seconds are reported for particles ranging in size from $2 - 4mm$ and reacting at 450°C. A GC/MS analysis was performed on the liquid products identifying and quantifying 30 different bio-oil components. [48, 49, 50]

Thangalazhy-Gopakumar *et al.* [51] also utilized an auger reactor to evaluate the impact of processing temperature on the bio-oils produced using this reactor configuration. Four reactor temperatures from 425 to 500°C were tested and oils collected for density, pH and water content measurements as well as GC/MS characterization. Results showed a maximum oil yield was obtained for a reactor temperature of 450°C. Chemical compositions were determined with 33 compounds identified using GC/MS.

Despite the multitude of reaction configurations which have been utilized to better understand pyrolysis, none have yet to achieve fine temperature control, fast heating

rates, and product separation for mass balance. TGA ovens and similar apparati provide fine temperature control but are limited by low heating rates. Radiantly heated systems can achieve higher heating rates than TGA but do not offer fine control over the reaction temperature. Heated carrier sand systems such as rotating cone reactors and circulating fluidized beds do effectively control reaction temperature and provide for rapid heating rates but require the separation of carrier sand and residual pyrolysis solids for the analysis of solid products. Additionally, the separation would have to occur nearly instantaneously to prevent the pyrolysis from continuing past the point of ejection from the reactor. Bubbling fluidized beds and entrained flow reactors can achieve high heating rates as well as modestly accurate temperature control, but require very large volumes of process gases. Consequently, a new reactor design is needed to provide high heating rates, fine reactor temperature control and product separation for further analysis. This reactor can then be used to evaluate and compare multiple pyrolysis kinetic schemes using the same core data. Additionally, the derived kinetic parameters under fast pyrolysis conditions can be directly compared to slow pyrolysis kinetic results utilizing the same biomass feedstock for direct evaluation of kinetic parameter interchangeability.

2.2 Reactor Design Requirements

The design of an isothermal reactor using conduction as the primary means of heat transfer was pursued. This decision was made based upon the need to separate heat and mass transfer pathways for facilitating product collection as well as reactor parameter controls. A set of system requirements was developed to guide the micro-reactor design process. The first requirement was that the system must be able to handle a sample of 50mg of finely ground biomass. Additionally, the sample should reach reaction temperature in less than 1 second. This was an aggressive target but

was considered necessary in driving towards the idealized case of instantaneous heating of the sample for pyrolysis kinetic investigations. The third requirement was that isothermal conditions had to be held over the reaction surface at temperatures up to 450°C. An inert environment must be maintained within the reactor and the dwell time of reaction products must be minimized for the minimization of secondary reactions. The system must also be capable of individually collecting liquid products and residual chars. Finally, it was required that the reactor be able to handle the individual constituents of wood (cellulose, hemicellulose and lignin) as well as catalytically treated biomass. A summary of the specifications is given in Table 2.1.

A traditional function decomposition design approach was adopted, as summarized by the function tree in Figure 2.1. All of the functions were addressed through the three main subsystems of solids transport, the reaction chamber and volatile product collection/removal.

2.3 Micro-Reactor Overview

A key feature of the micro-reactor is the unique glass containment lid that is used to contain the reaction surface and heating system. A solid model of the reactor chamber cross-section is shown in Figure 2.2 with key components highlighted. The core of the reactor is the stainless steel reaction plate that is fastened rigidly to the upper surface of a copper hot plate. The thermal contact resistance at the interface is reduced using thermal compound applied during the reactor assembly. Three 150W

Table 2.1: Micro-reactor design specifications summary

Specification	Target
Target Sample Size	50mg
Max Temperature	450°C
Heating Time	1s
Product Dwell Time	$\leq$ 2s
Sample Types	Cellulose, Hemicellulose, Lignin, Catalytically Treated Biomass

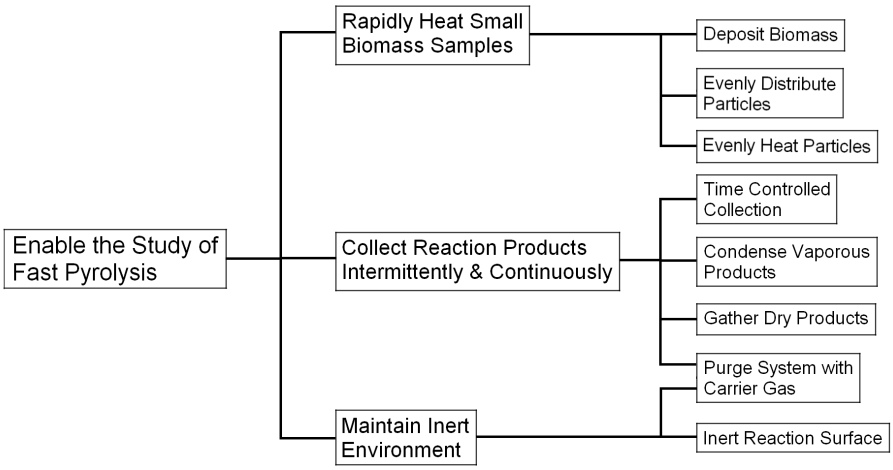

Figure 2.1: Fast pyrolysis reactor function tree

cartridge heaters embedded within the copper plate provide the heating power for the reactor. The heaters are regulated by a PID temperature controller with feedback from a thermocouple at the hot plate and reaction plate interface. Biomass deposits are spread around and removed from the reaction surface using the scraper/spreader arms shown. The copper hot plate is mounted on thin-walled stainless steel posts in order to improve the thermal standoff and isolation from the foundation structure of the reactor. The chamber is enclosed by the glass reactor cover which provides thermal insulation from the atmosphere and low potential for product condensation due to the smooth surfaces. Additionally, the glass reactor cover directs the flow of incoming helium and outgoing vaporous products so as to minimize premature product condensation through laminar flow.

Operation of the system is semi-continuous with samples of biomass being added in individual deposits of approximately 50mg. All reaction and collection surfaces were cleaned thoroughly with acetone and dried prior to all pyrolysis tests to minimize or eliminate contamination of the products (*e.g.* via residual oils from a previous test). The system components are massed and the reactor is then reassembled and preheated to the set reaction temperature and purged with helium. Prior to deposit each sample is premassed, inserted into the reaction chamber through the sealed

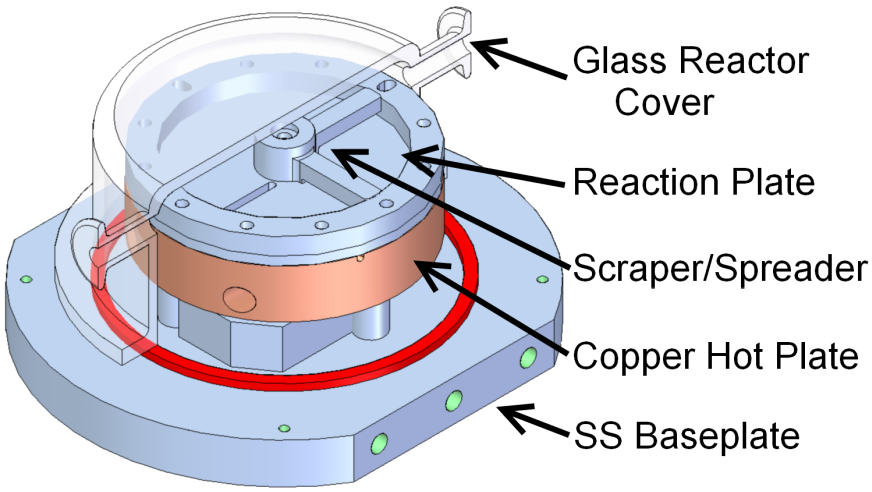

Figure 2.2: Micro-reactor chamber section view highlighting particle distribution componentry

stopcock chip drop, and rapidly spread over the reaction plate surface through a 270° sweep of the spreader arm. Each sample is allowed to react for the set residence time, after which the residual solids are scraped off of the reaction plate and into the chip catch. A helium purge gas is continuously pushed through the system to carry all vaporous reaction products out to the liquid nitrogen cooled condenser for collection. This cycle is repeated until the targeted number of drops is reached. The condenser is removed and sealed approximately 60 seconds after the removal of the residual solids for the last drop within a run. The chip catch is removed as well, with care being taken to remove all residuals from the surfaces and crevices of the reaction chamber. The condenser, stopcock chip drop and chip catch are massed again to determine the quantity of reaction products by mass. The flow of mass within the reactor is shown in Figure 2.3 illustrating the reactant, product and carrier gas flows in the system. A photograph of the complete system is contained in Figure 2.4.

The handling of samples within the micro-reactor starts with the stopcock chip drop. This was designed with an all-glass construction to provide thermal isolation from the the reaction surface. Samples deposited using the stopcock chip-drop

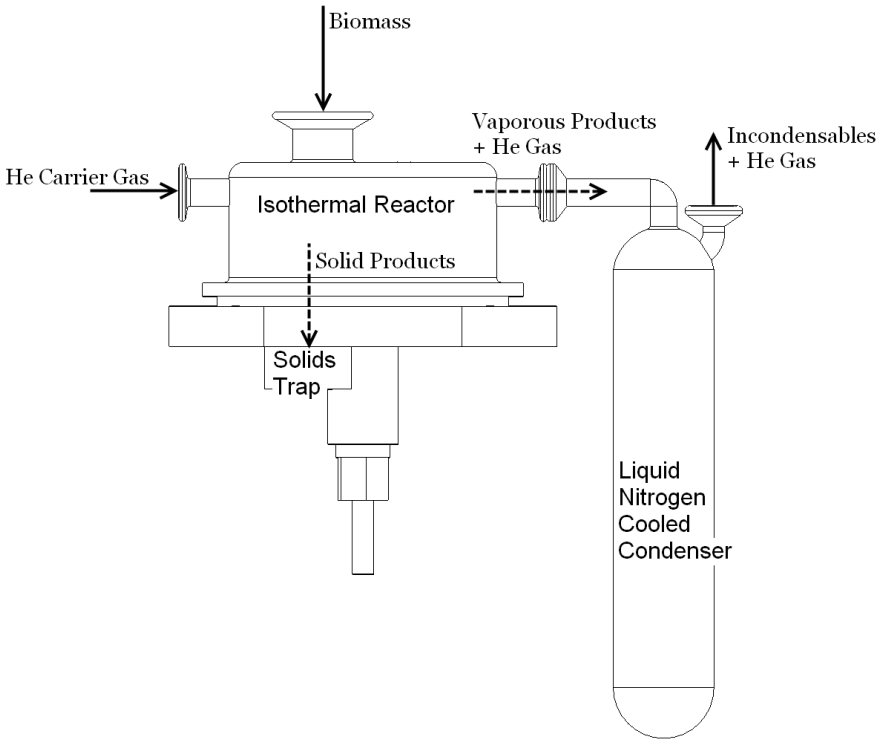

Figure 2.3: Reactor mass flow diagram accounting for influx and efflux of masses

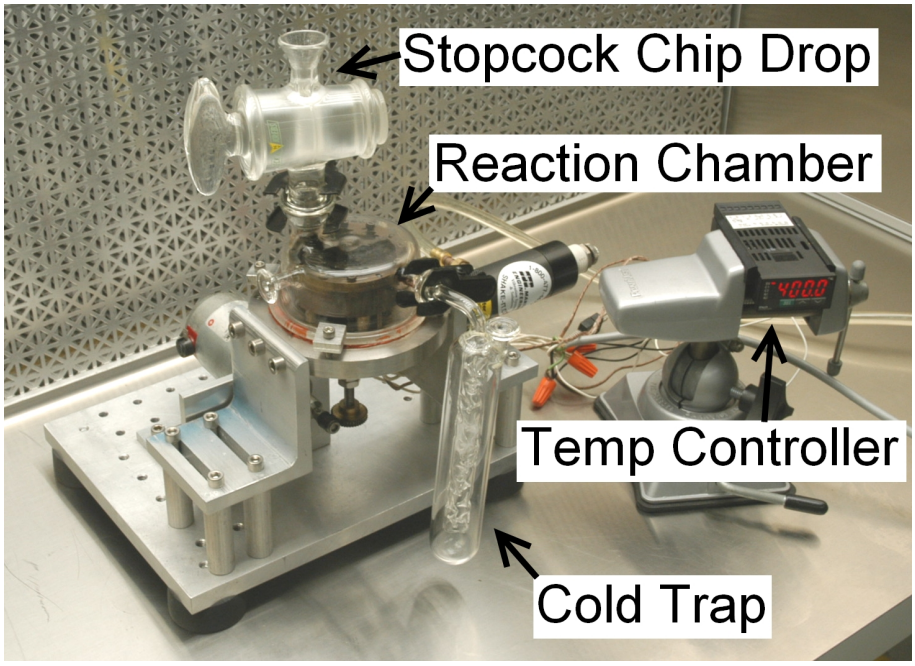

Figure 2.4: Photograph of complete micro-reactor system

were spread around the reaction plate surface using the scraper/spreader arm system and vibratory assistance, which will be further discussed in Section 2.3.1. Sample residence times were controlled using a Basic Stamp computer controller which manipulated the scraper/spreader arm position via a DC motor and timer. The digitally controlled timing of spreading, scraping and vibratory transducer activation provided for repeatability between tests.

Isothermal conditions were accomplished using the copper hot plate to spread/diffuse the heat provided by the cartridge heaters. This was verified using an infrared imaging system as presented in Section 2.4. The heating rate target of 1 second was approached using the direct contact heating of biomass particles spread atop the reaction plate surface. Analytical and experimental validation of the heating rates is presented in Section 2.4.

Secondary reactions were minimized through the use of the glass reactor lid, room temperature helium purge gas and favorable flow pathways. The glass surface prevented the condensation of vaporous products prior to reaching the condenser. The helium purge gas was directed across the reaction plate surface with an average flow velocity of approximately 1m/s resulting in laminar flow. Additionally, the incoming temperature of the helium was $\sim 22^{\circ}$C which provided for quench cooling of the pyrolysis product, thus reducing the potential for secondary reactions.

Product collection was provided for using the sweeper arm and chip catch for the solids and a custom cold trap condenser for the liquid products. Previous iterations had utilized Liebig, Graham and traditional cold finger condensers but none provided both the effective collection of condensible products and a low initial mass. The low initial mass was necessary for the accuracy of collected oil measurements.

The isolated individual constituents of biomass as well as catalytically treated biomass samples are processable within this system with the exception of organosolv

lignin. Organosolv lignin, as it is a polymer, melted following contact with the pre-heated reaction plate surface and could not be removed by the scraper arm as it was in liquid form. Consequently, the testing of organosolv lignin was ineffective within the micro-reactor system.

2.3.1 Vibratory Assisted Particle Distribution

Vibratory energy was added to the reactor system using a Martin Vibration Systems NTS 180HF pneumatic transducer to fluidize the particle flow and assist in particle spreading. Vibration assisted spreading assessment was conducted on the micro-reactor system at room temperature with the glass reactor lid removed. Vibration amplitude and frequency were measured using a PCB 353B33 accelerometer mounted to the reactor support structure by a post holding it at the same level as the reaction plate. Four frequency levels were tested along with two levels of transducer amplitude. The tested frequencies were 85Hz, 94Hz, 103Hz and 110Hz, identified as levels 1-4 respectively. Tested amplitudes were set based upon a damper screw setting with 8.1mm of protrusion for the low amplitude setting and 9.1mm of protrusion for the high amplitude setting. Additionally the tests were performed in two sets, the former denoted by -1 and the latter denoted by 1. The reason for this was that some settings were improperly tuned for the initial test set resulting in incompletely testing the 4 frequencies. Subsequent testing was performed to complete the full factorial arrangement. Because a second set of tests was added to the original random set, a blocking factor (identified as *Set*) was designated to investigate the effect of the separation.

Table 2.2 contains the experimental testing matrix that was used containing factor levels and actual measured pressure, damper length, mass deposit and measured shaker frequency. Dominant frequencies were determined utilizing a FFT analysis of the accelerometer data. An example of a captured waveform and its corresponding

Table 2.2: Experimental testing matrix containing run order, set levels and measured values

Run	Freq	Amp	Set	P_{set} [psi]	L_{damper} [mm]	Freq [Hz]	Mass [g]
1	2	-1	-1	28	8.14	93.8	0.0499
2	4	-1	-1	49	8.14	108.4	0.054
3	4	-1	-1	49	8.14	108.4	0.0541
4	1	1	-1	19	9.03	85.0	0.0529
5	3	1	-1	42	9.03	103.5	0.0459
6	3	1	-1	42	9.03	103.5	0.0563
7	4	-1	-1	49	8.11	109.4	0.0521
8	3	1	-1	42	9.08	103.5	0.0456
9	2	1	-1	29	9.18	93.8	0.0468
10	2	1	-1	29	9.18	93.8	0.0452
11	2	-1	-1	28	8.07	93.8	0.0524
12	3	-1	-1	40	8.07	102.5	0.0494
13	2	1	-1	29	9.15	93.8	0.054
14	3	-1	-1	40	8.04	103.5	0.0541
15	2	-1	-1	28	8.04	93.8	0.0533
16	3	-1	-1	40	8.04	104.5	0.0545
17	1	1	-1	19	9.06	85.9	0.0473
18	1	1	-1	19	9.06	85.0	0.0453
19	4	1	1	51	9.13	110.4	0.0509
20	1	-1	1	18	8.12	85.0	0.0576
21	1	-1	1	18	8.12	85.0	0.5010
22	4	1	1	51	9.08	109.4	0.5760
23	4	1	1	51	9.08	110.4	0.5870
24	1	-1	1	18	8.13	85.0	0.0584

FFT are given in Figure 2.5.

Images of the reaction plate surface, following the completion of spreading and vibration, were extracted from video recordings of the spreading tests. The images of the fully distributed chips were manually cropped to include only the inner portion of the reactor plate (*i.e.* that not covered by the plate rim). Image contrast was maximized to isolate the chip locations as white and the remainder of the image as black using the image processing software Paint.NET. [52] Comparison to the original images was also made and glare elements manually removed from the high contrast image. A photograph of the system without vibratory assistance and an

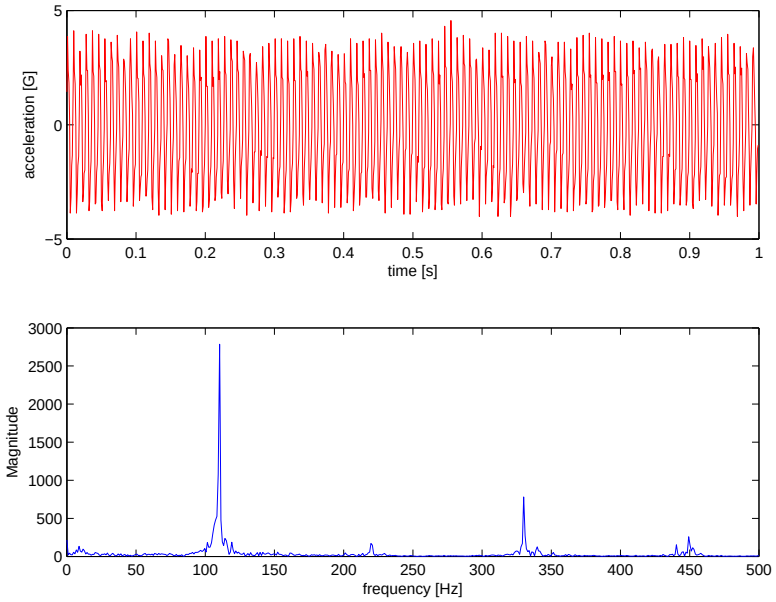

Figure 2.5: Accelerometer results and corresponding FFT for Run 1 of vibratory assisted spreading tests

example image showing the effect of vibratory assistance along with its high contrast manipulation are shown in Figure 2.6. The complete set of raw and manipulated image pairs are contained in Appendix A.

Average and standard deviation results for the area over mass image analysis outcomes are contained in Table 2.3. According to the mean values, the best performing

(a) (b) (c)

Figure 2.6: (a) Particle spreading with no vibration (b) Particle spreading with vibratory assistance (c) Contrast modified image utilized in image processing

Table 2.3: Statistical analysis results of mass over area table data, values in g/mm^2

	Amplitude			
	-1		1	
Freq	mean	s.d.	mean	s.d.
1	9.68E-05	1.07E-05	8.76E-05	9.492E-06
2	7.68E-05	1.47E-06	8.35E-05	1.101E-05
3	9.52E-05	8.27E-06	9.24E-05	8.180E-06
4	8.82E-05	9.62E-06	8.45E-05	7.861E-06

treatment (factor level combination) is found at frequency 2 and amplitude -1 followed by frequency 2 and amplitude 1. The third best performing treatment was frequency 4 at amplitude 1.

ANOVA performed on the spreading experimental mass over area results is contained in Table 2.4. Within the table *SS* is the sum of squares for each *source*, *d.o.f.* is the degrees of freedom allocated to each *source*, *MS* is the mean square (which is equal to the variance of the *source*) and *F* is the observed F statistic value. Numerically, the *p-value* is the probability that the observed F statistic is less than the critical F value for the degrees of freedom of the *source* and system. Functionally, the p-value is the probability that the null hypothesis is correct. The null hypothesis is by default that the effect (*Source*) is insignificant. [53] Based upon the probability results given in the last column of Table 2.4, it is suggested that the frequency at which the system is driven is the most significant factor as it's null hypothesis has only a 6.4% probability of being correct. The *amplitude* factor, amplitude-frequency *interaction* factor and the *set* factor all are indicated as having low significance given the high p-values calculated.

Despite the superior numerical performance of frequency 2, qualitative analysis of spreading images indicated a disqualifying factor. For frequency 2 at both high and low amplitude settings, the spreading effectiveness was such that particulate was moved to the chip drop slot during spreading. Consequently frequency 2 could not be used as this would result in removing unreacted biomass from the reactor system and

Table 2.4: Three way ANOVA results from spreading experiments

Source	SS	d.o.f.	MS	F	p-value
Amp	3.04E-11	1	3.04E-11	0.394	0.540
Freq	6.93E-10	3	2.31E-10	2.99	0.064
Interaction	1.98E-10	3	6.62E-11	0.857	0.485
Set	5.78E-11	1	5.78E-11	0.749	0.400
Error	8.39E-09	15	7.72E-11		
Total	9.37E-09	23			

adversely affecting the experimental mass balance. Frequency 4 at a high amplitude setting was the next best performing treatment and analysis of its spreading images indicated that no spill over occurred. This treatment corresponded to a frequency of $\sim$ 110Hz and a damper setting of $\sim$ 9.1mm, resulting in 2.4g's (RMS) of acceleration at the plate level.

2.4 Verification of Thermal Performance Metrics

2.4.1 Spatial Variation of Reactor Plate Temperatures

System thermal performance was validated to ensure fast pyrolysis reaction conditions were facilitated. Surface temperature distributions were evaluated by spreading a layer of talc atop the reaction plate surface and capturing infrared thermal images at multiple temperatures. Isothermal conditions were validated through IR thermal imaging techniques. Analytical thermal predictions were made for the heating of a wooden wafer to allow for estimations of heating rates and heater power requirements. The predicted heating rates were validated through the heating of a wooden wafer with surface temperatures also measured using an infrared camera. The comparison of analytical predictions and experimental outcomes for a given wafer thickness allowed for the validation of heating rates for other wafer thicknesses.

For the evaluation of temperature distribution on the reactor plate an approximately 1mm thick layer of talc powder was packed atop the plate using a steel slug as

a tamp. The talc was necessary because of the high reflectivity of the polished stainless steel plate. The images were acquired with the IR camera positioned orthogonal to the reactor plate and the glass reactor cover removed. Four reactor temperatures were tested to cover the range of anticipated reactor testing conditions: 300, 350, 400 and 450°C. Three replicate images were obtained for each temperature setting.

A FLIR A20 thermal imaging system was used to capture the calibrated IR images. An emissivity of 0.68 was set within the image processor for temperature evaluation. This value was determined based upon tuning to match the reactor set temperature. Consequently, the relative relationships between datum are accurate but the temperatures themselves do not account for the heat loss due to natural convection. Three analysis rings were applied to each image to capture the average and standard deviations of temperatures within the defined regions and evaluate the temperature fluctuations over the face of the plate. The rings are numbered AR01-AR03 from left to right. One thermal image from each temperature is contained in Figures 2.7a-e.

The statistical results by temperature and region are contained in Table 2.5. While the statistical results do indicate standard deviations from $5 - 10$°C, the imaging results in Figures 2.7a-e show unexpectedly inconsistent thermal gradients over the plate surface. Considering the large copper thermal reservoir and that the thin stainless steel plate does not have a directionally dependent thermal conductivity and the symmetry of the system, it would be anticipated that if thermal gradients did exist they would appear to be of a more continuous nature than is observed. Consequently, it is expected that non-uniformity in the talc pack is the root cause of the large standard deviations. The average values between regions, however, show good agreement particularly within the 400°C results which is the temperature about which the majority of tests will center.

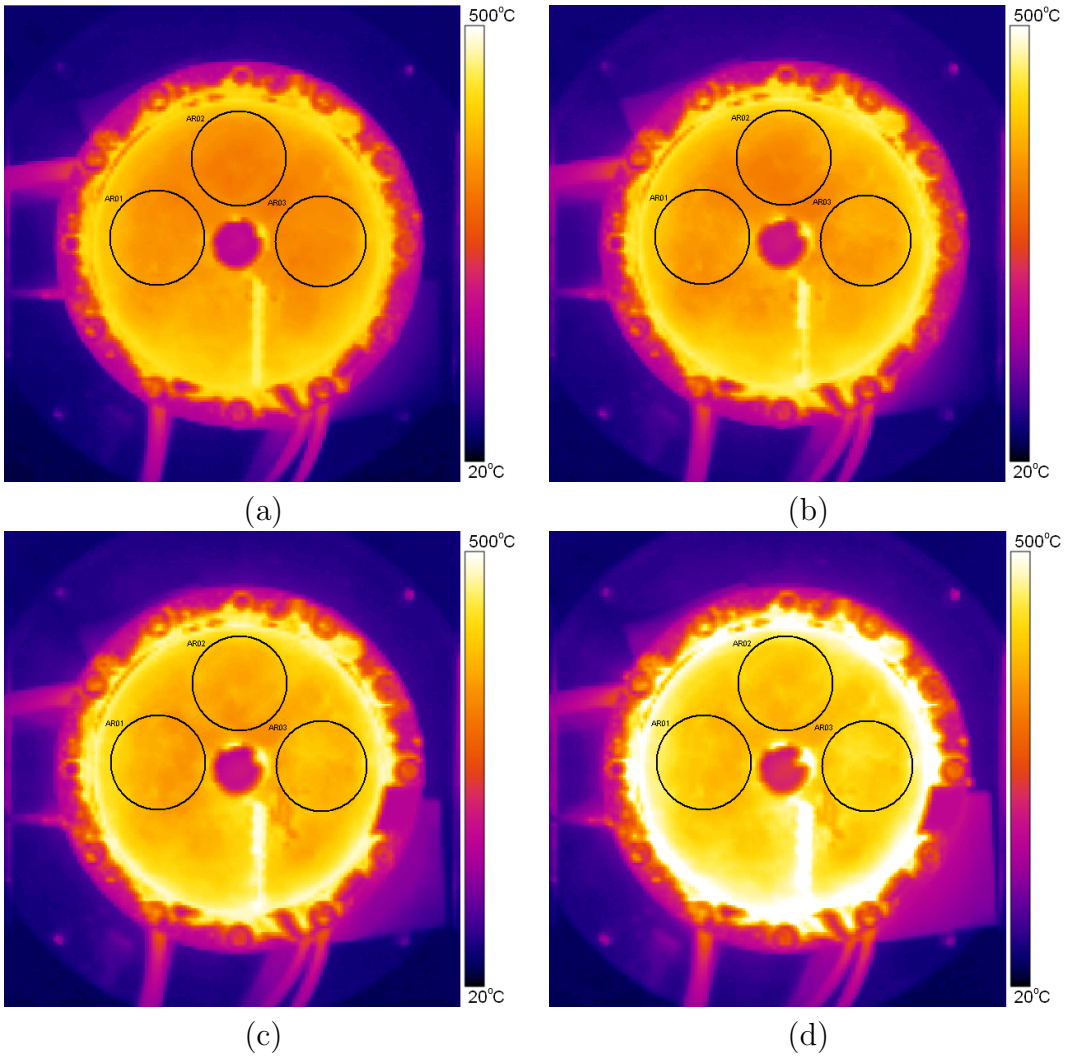

Figure 2.7: Thermal images of talc covered reactor plate for isothermality evaluations for set temperatures of (a) 300°C, (b) 350°C, (c) 400°C, (d) 450°C

Table 2.5: Infrared imaging analysis ring results for isothermality tests

Temp [°C]	$\bar{T}_{AR01}$[°C]	σ_{AR01}[°C]	$\bar{T}_{AR02}$[°C]	σ_{AR02}[°C]	$\bar{T}_{AR03}$[°C]	σ_{AR03}[°C]
300	305	7	296	7	302	5
300	305	7	296	7	302	5
300	305	6	296	7	300	6
350	350	7	345	10	352	6
350	348	8	345	9	352	5
350	349	7	342	10	351	6
400	396	9	397	7	402	5
400	397	9	397	7	402	5
400	396	9	397	7	401	5
450	443	10	442	7	449	6
450	443	10	442	7	449	6
450	443	10	442	7	449	6

2.4.2 Verification of Heating Rates

Wooden wafer heating tests were performed and a transient heating model was formulated to provide for the approximation of initial biomass heating rates within the micro-reactor. Wafer surface temperature measurements were taken again using a FLIR A20 thermal camera mounted above the reactor plate.

Six 1.3mm thick pine wafers cut from lumber stock were tested at two differing temperatures, one below the expected onset of pyrolysis (250°C) and one in the middle of the intended reaction temperature range for pyrolysis studies (400°C). A 1-D heat transfer model was developed for the wooden wafer by analytically solving the heat equation for a constant temperature lower boundary and a convective upper boundary. The intent of this model was only to approximate the heating rates at the anticipated biomass layer thickness of 400μm. Consequently, the vaporization of water and the endothermicity of the pyrolysis reactions were not considered.

The system will be represented by the 1-D heat equation for the transfer of heat through the wooden wafer from the hot reaction plate surface to the naturally convected air above. Equation 2.1 gives the heat equation simplified for 1-D transient heat transfer with no generation assuming constant physical properties,

$$-\kappa\frac{\partial^2 T}{\partial z^2} = \rho c_p \frac{\partial T}{\partial t} \tag{2.1}$$

where T is the temperature, z is the direction of heat transfer, κ is the thermal conductivity of the wood wafer, ρ is the wood density, c_p is the specific heat of the wood and t is time. The initial condition and boundary conditions for the wood layer are given in Equations 2.2-2.4,

$$T(0,t) = T_s \tag{2.2}$$

$$-\kappa\frac{\partial T}{\partial z}(w,t) = h\left(T(w,t) - T_{air}\right) \tag{2.3}$$

$$T(z,0) = T_0 \tag{2.4}$$

where T_s is the reaction plate surface temperature, k is the thermal conductivity of the wood, w is the thickness of the wood, T_{air} is the ambient temperature, T_0 is the initial temperature of the wood and h is the convection coefficient. The initial temperature of the wood (T_0) was different from the ambient temperature because the wafer was inadvertently preheated when in close proximity to the reaction plate surface just prior to being forced into contact with the plate. The value T_0 was taken from infrared imaging results of the wafer.

Solving for the steady state solution yields Equation 2.5.

$$T_{ss}(z) = T_s + \frac{zh(T_{air} - T_s)}{\kappa + hw} \tag{2.5}$$

The transient solution is then given by Equation 2.6,

$$T(z,t) = T_{ss} + \sum_{n=1}^{\infty} b_n sin(\lambda_n z)\mathrm{e}^{-\lambda_n^2 \alpha t} \tag{2.6}$$

where λ_n is the n^{th} solution to Equation 2.7 and b_n is the n^{th} solution to Equation 2.8,

$$tan(\lambda_n w) = -\frac{\kappa}{h}\lambda_n \tag{2.7}$$

$$b_n = \frac{\int_0^w g(z) sin(\lambda_n z)\, dz}{\int_0^w sin^2(\lambda_n z)\, dz} \tag{2.8}$$

where g(z) is given by Equation 2.9.

$$g(z) = T(z,0) - T_{ss}(z) = T_0 - T_s + \frac{zh(T_{air} - T_s)}{\kappa + hw} \tag{2.9}$$

Equations 2.7, 2.8 and 2.9 can then be used to solve for $T(z,t)$ by substitution into Equation 2.6. The series was expanded out to twenty terms to minimize instability at very small simulation times (< 1) which was necessary for the evaluation of initial heating rates.

Wood properties were taken from published correlations and tables from the USDA Forest Products Laboratory [54] for Loblolly pine. Both the thermal conductivity and specific heat account for the moisture content of lumber, nominally 12%. The thermal conductivity value used here is for heat transfer transverse to the grains. The wood properties used are contained in Table 2.6. The convection coefficient was initially approximated at $h_{nat} = 13.3\text{W/m}^2\text{K}$ for the 250°C plate temperature and at $h_{nat} = 15\text{W/m}^2\text{K}$ for the 400°C plate temperature using standard horizontal isothermal hot plate natural convection correlations between the wafer and the ambient air. [55] Radiation effects were also considered using an effective convection coefficient considering both radiative and natural convection heat losses as per Equation 2.10,

$$h_{eff} = \epsilon\sigma(T_s + T_\infty)(T_s^2 + T_\infty^2) + h_{nat} \tag{2.10}$$

where ϵ is the emissivity of wood (taken to be 0.95 as per reference [56]) and σ is the Stephan-Boltzmann constant. Equation 2.10 was substituted into Equation 2.6 and solved for using the variation in the wooden wafer surface temperature throughout

Table 2.6: Properties and constants used for analytical predictions at 225°C and 400°C

T_s [°C]	225	400
c_p [kJ/kgK]	2.28	2.83
κ [W/mK]	0.15	0.15
ρ [kg/m^3]	510	510

the simulation. The radiative contribution to the effective convection coefficient is 11W/m^{2}K for the 250°C plate at the end of the simulation. The resulting final effective convection coefficient is $h_{eff} = 24.3$W/m^{2}K for the 250°C plate simulation.

The height of the wood layer within simulations was varied from 0.4 to 1.3mm. The maximum thickness of 1.3 mm was set based upon the minimum wafer thickness which could be repeatably manufactured. Simulations were carried out down to a thickness of 0.4mm because that represented the anticipated approximate biomass layer thickness after vibratory assisted spreading completes. The spacing between simulations was then set at 0.3mm to evenly distribute results between 0.4mm and 1.3mm wafer thicknesses.

Wafer heating experiments were performed using the micro-reactor core mounted on a dedicated test stand. This enabled the observation of the exposed wafer surface using the IR camera calibrated for a common emissivity of wood ($\epsilon = 0.9$). [56] Measurements of room temperature wafers were used to verify this emissivity value. Wafers were held against the reaction plate surface using two cross bars weighted by a through shaft attached to a steel mass below. The applied pressure was to prevent separation between the wafer and the reaction surface due to thermally induced warping of the wafer during heating as well as to minimize the contact resistance at the wafer-plate interface. The applied load was approximately 5N to the surface of the wafer. As previously mentioned, an impinging flow of compressed air was applied to the camera lens to keep it at a constant 22°C (room temperature) and prevent the condensation of pyrolysis vapors on the lens. Additionally, a vacuum pump was used

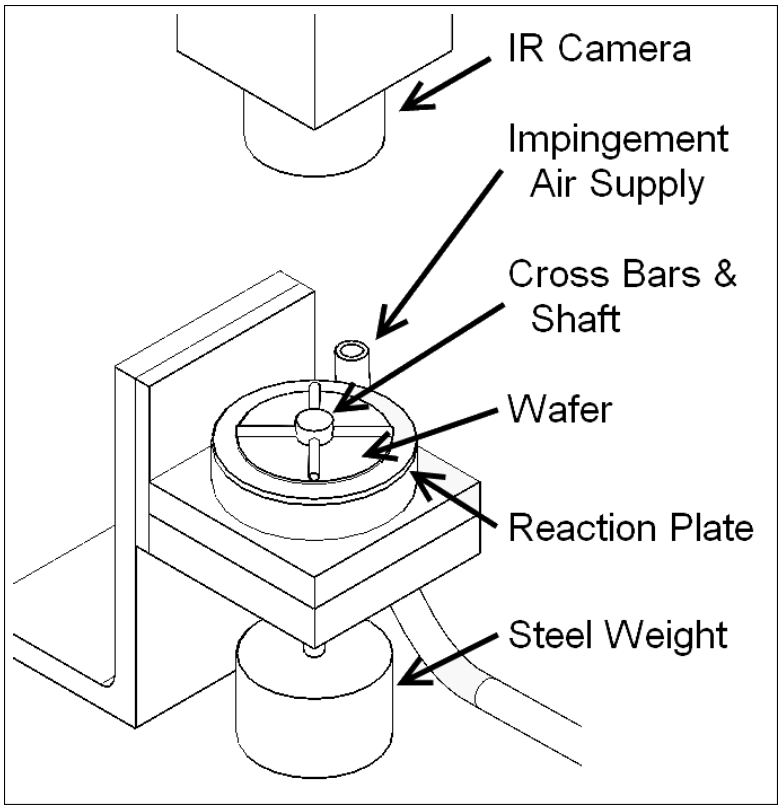

Figure 2.8: Wafer heating rate test stand assembly diagram

to remove pyrolysis vapors from the optical pathway during 400°C testing to prevent the obscuring of the infrared image by vaporous pyrolysis products. A diagram of the test bed assembly can be seen in Figure 2.8.

Six wafers were tested, of which the mean thickness was measured to be 1.28mm with a standard deviation of 0.027mm. The first three wafers were tested at 225°C to evaluate the model without the presence of pyrolysis. Wafers four through six were tested at 400°C to demonstrate the initial heating rates at the wafer surface. Wafer surface temperatures were only measurable up to 250°C due to camera range limitations. Values measured above 250°C are out of the calibrated range but are reported for completeness.

Following the preheating of the reactor core the wafer was loaded onto the through shaft and placed above the reaction plate with a layer of foil below, shielding it from the thermal radiation of the plate. After attaching the weight the foil was removed

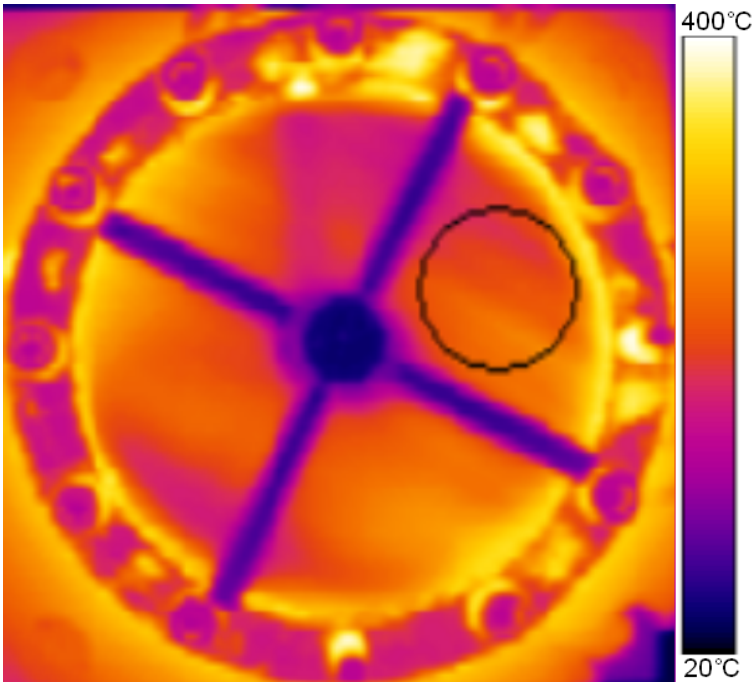

Figure 2.9: Infrared image of the wafer during a 400°C heating rate test with the analysis region shown by the black border

and the wafer and clamping mechanism were dropped to the reaction plate surface.

Wafer temperatures were taken from an analysis ring allowing for the averaging of the temperatures within the defined boundaries shown in Figure 2.9. The ring size corresponds to an approximately 18mm diameter circle on the surface of the wafer within which temperature standard deviations were on the order of 5°C throughout the experimentation.

Measured surface temperatures and calculated heating rates are plotted in Figures 2.10 a-d along with the corresponding model predictions. A single representative experimental curve was selected for each plate temperature.

The effective convection coefficient proved to over-predict the final wafer surface temperature by $\sim$ 5°C for the 225°C plate temperature and a subsequent best fit convection coefficient value was then determined for an improved final temperature fit using $h_{fit} = 25.5 W/m^2K$. The small departure using the effective convection coefficient of Equation 2.10 is attributed to the additional natural convective effects

from the exposed plate rim and forced convective effects from an air stream which impinged upon the IR camera lens increasing the rate of mixing of the hot and cool air above the plate. The impinging stream was $\sim$ 15cm from the reaction plate and was necessary to hold a constant temperature within the optics and prevent pyrolysis products from condensing on the lens. The same best-fit convection coefficient was also applied to the 400°C model because the presence of pyrolysis does not allow for a convection coefficient estimation.

The average of each run's maximum heating rate across the three tested wafers for the 225°C tests was 18.7°C/s with a standard deviation of 2.2°C/s. The average of each run's maximum heating rate across the three tested wafers for the 400°C tests was 29.2°C/s with a standard deviation of 5.9°C/s. The predicted maximum heating rates were 24.5°C/s for the 225°C plate temperature and 34.8°C/s for the 400°C plate temperature. The calculated difference between the theoretical and experimental values was 31% and 19% for the 225°C and 400°C tests respectively.

The heating rates of thin biomass layers in the range of 0.4-1.3mm were predicted using the previously presented wood heat transfer model. Figures 2.11 a and b present the projected results for temperature and heating rate, respectively, for a plate temperature of 400°C.

2.4.3 Discussion of Heating Verification Results

For both the 225°C and 400°C plate temperatures the wood heating model over predicts the temperature for the great majority of the test and predicts heating rates that are on average higher than experimentally measured. In the pure heat transfer case of 225°C (*i.e.* no pyrolysis occurred) the slower heating rate is most likely attributable to the vaporization of water contained within the wafer and imperfect correlations for the specific heat and thermal conductivity. An increase in the value

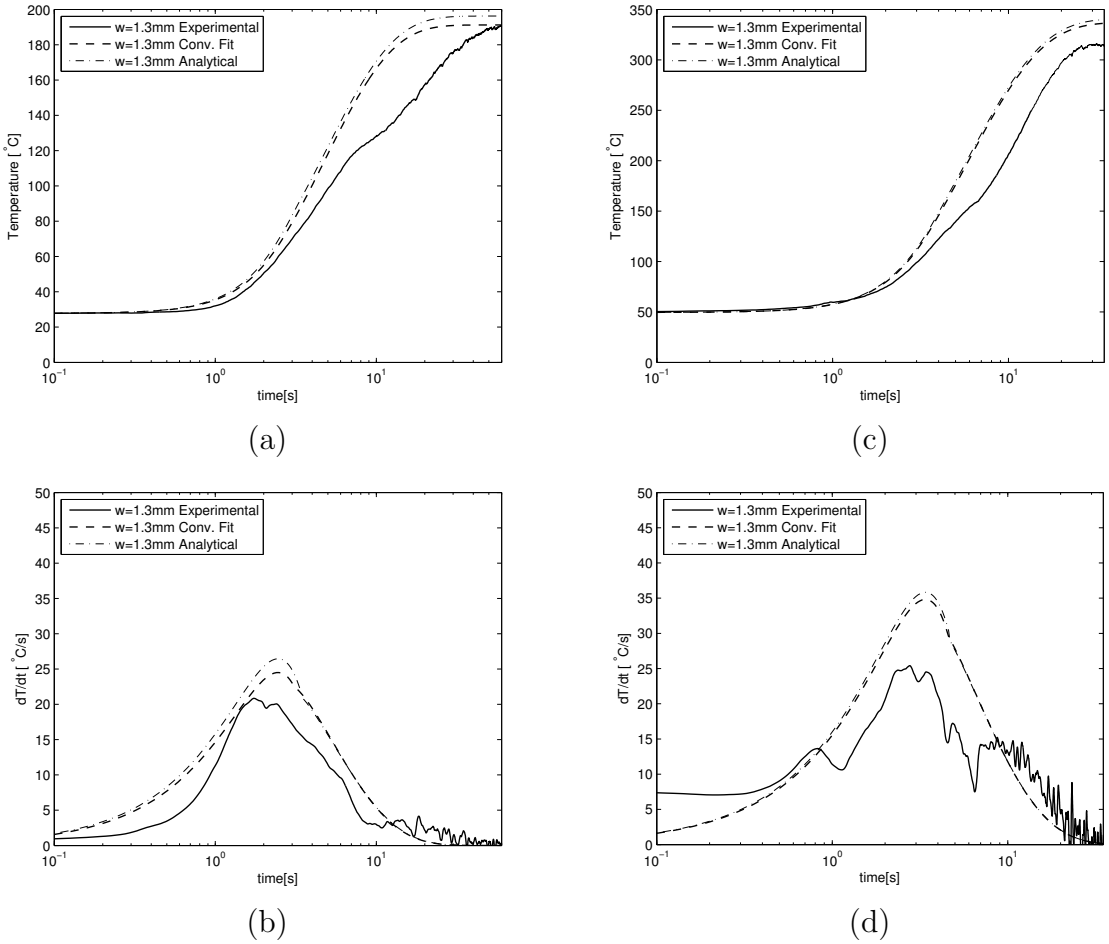

Figure 2.10: Wafer surface temperature experimental and theoretical results:(a) 225°C temperature plot (b) 225°C heating rate plot (c) 400°C temperature plot (d) 400°C heating rate plot

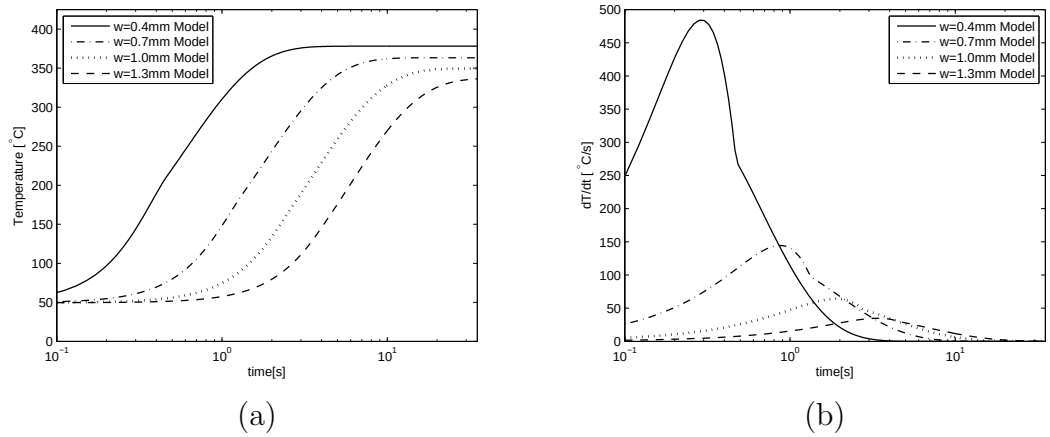

Figure 2.11: Predicted surface temperatures (a) and heating rates (b) in wafers of different thicknesses for 400°C plate temperature

of the thermal conductivity by 10% results in a maximum predicted heating rate increase of 16%. An increase in the value of the specific heat by 10%, however, results in a decrease in the predicted maximum heating rate of 13%. An increase in the convection coefficient by 10% results in a predicted maximum heating rate decrease of only 5%. These coarse sensitivity evaluations indicate that at the operating point, the model is most sensitive to thermal conductivity and specific heat values both of which are difficult to accurately characterize. [54] This most likely explains the bulk of the deviation from experimental values. For the 400°C tests the deviation from the curve is attributable to both the effects mentioned for the 225°C case as well as the endothermicity of pyrolysis occurring at the bottom of the wafer in contact with or close to the plate.

The model for a wood layer thickness of 0.4mm predicts a maximum heating rate of of 484°C/s. Within the 400°C wafer predictions, if the previously calculated 19% error in the heating rate measurement is assumed to hold true for other wafer thicknesses, then the adjusted heating rate for a 0.4mm wafer would be 392°C/s. Even if a very conservative estimate were taken assuming 50% error the heating rate is well above the required 50°C/s and is significantly higher than heating rates reported for other experimental fast pyrolysis reactors: $19-56$°C/s for a radiantly heated furnace [25]; ~ 100°C/s for rotating cone reactors [44, 45].

It is acknowledged that the convective loading conditions under which the infrared imaging tests occurred are different than those within the enclosed micro-reactor during actual pyrolysis testing. It is expected, however, that the internal flow conditions will facilitate convective coefficients on the same order as those observed here.

2.5 Commissioning and Response Mapping Tests

Initial results obtained from testing Loblolly pine at 400°C are presented here to demonstrate the type of results obtained using the micro-reactor. Loblolly pine experimental time and temperature bounding methods are presented in Chapter 3.

The first set of micro-reactor tests was performed for the evaluation of Loblolly pine yields and oil quality at 400°C. Residence times within this first set were progressively added between the determined bounds of 120 and 10 seconds as was needed to better describe the curve and all tests were performed in triplicate. A fourth test was added at the 10 second residence time to provide sufficient oil for LHV analysis. This initial set provided the residence time structure to be utilized at other reactor temperatures for mapping the product yields and its experimental structure is given in Table 2.7.

A summary of the initial Loblolly pine 400°C reactor temperature experimental results is given in Table 2.8 and plotted in Figure 2.12. The results showed the expected trends and demonstrated good repeatability of the micro-reactor.

Table 2.7: Preliminary response mapping of pyrolysis tests at 400°C using the micro-reactor system

Test	Residence Time [s]	Reactor Temp [°C]
1	120	400
2	120	400
3	120	400
4	50	400
5	50	400
6	50	400
7	20	400
8	20	400
9	20	400
10	30	400
11	30	400
12	30	400
13	10	400
14	10	400
15	10	400
16	10	400
17	90	400
18	90	400
19	90	400

Lower heating values, based upon the higher heating value (HHV) minus the latent heat of vaporization of water in the combustion products, were measured and are tabulated in Table 2.9 and graphically depicted in Figure 2.13 for the raw unreacted pine and captured products at each dwell time. The lower heating values for the bio-oil increased from 9.56MJ/kg to 11.16MJ/kg from 10 to 30 seconds followed by a leveling out from 30 to 50 seconds. Between 30 and 90 seconds the bio-oil LHV increased by 13% from 11.16MJ/kg to 12.45MJ/kg. Solids LHV results steadily increased from 20.33MJ/kg to 26.03MJ/kg from 10 to 90 seconds with the LHV plateauing between 90 and 120 seconds. Compared to the raw wood the bio-oil had 49% and 34% lower LHV at 10 and 90 seconds respectively. The solids, however, had about 8% to 40% higher LHV at 10 and 120 seconds respectively.

2.5.1 Procedural Modification Based Upon Initial Results

Further testing at a later date indicated an unanticipated variation in the oil yields for a 400°C and 120s dwell test. The new set of tests had a mean oil yield of 0.679g/g and a standard deviation of 0.211g/g. This is a 25% departure from the initial results reported in Table 2.8. Upon further investigation it was determined that a procedural oversight was to blame. Within the initial 400°C Loblolly pine tests the liquid nitrogen dewar was filled and the condenser then added to the coolant and connected to the micro-reactor. This process required several minutes to allow the condenser to cool

Table 2.8: Loblolly pine pyrolysis average product yields and standard deviations calculated for the original 400°C tests using the old condenser procedure with gas yields calculated by difference

Residence Time [s]	$\bar{\eta}_o$ [g/g]	σ_o [g/g]	$\bar{\eta}_s$ [g/g]	σ_s [g/g]	$\bar{\eta}_g$ [g/g]	σ_g [g/g]
10	0.263	4.41E-2	0.605	4.02E-2	0.132	5.36E-3
20	0.376	1.56E-2	0.463	1.32E-2	0.162	2.57E-3
30	0.393	2.50E-2	0.417	1.77E-3	0.190	2.33E-2
50	0.450	1.84E-2	0.323	5.77E-3	0.227	2.10E-2
90	0.545	1.11E-2	0.231	3.21E-3	0.224	1.40E-2
120	0.546	1.35E-2	0.212	3.22E-3	0.242	1.66E-2

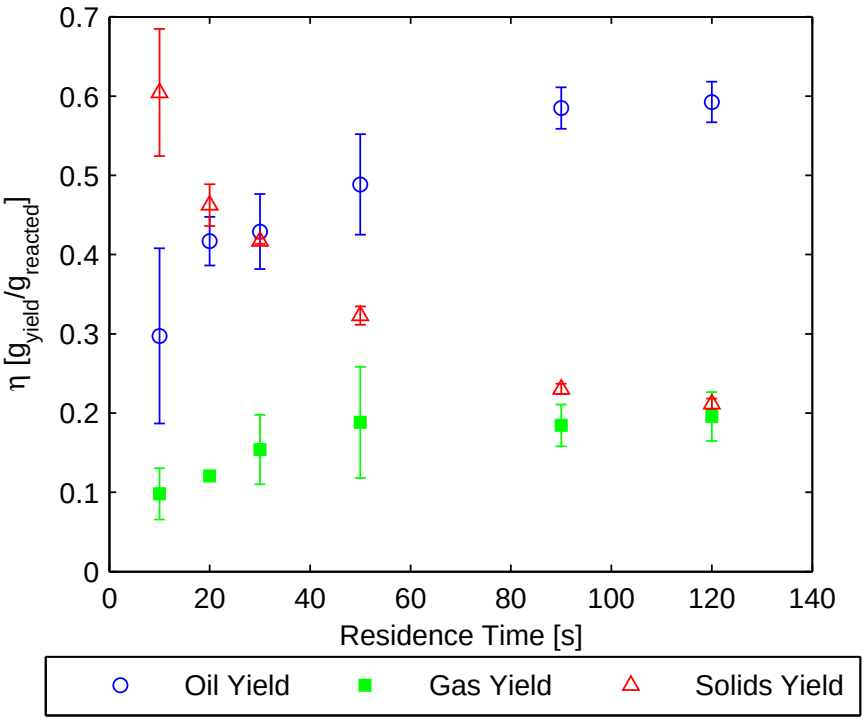

Figure 2.12: Original Loblolly pine 400°C results mean values with two standard deviation error bars

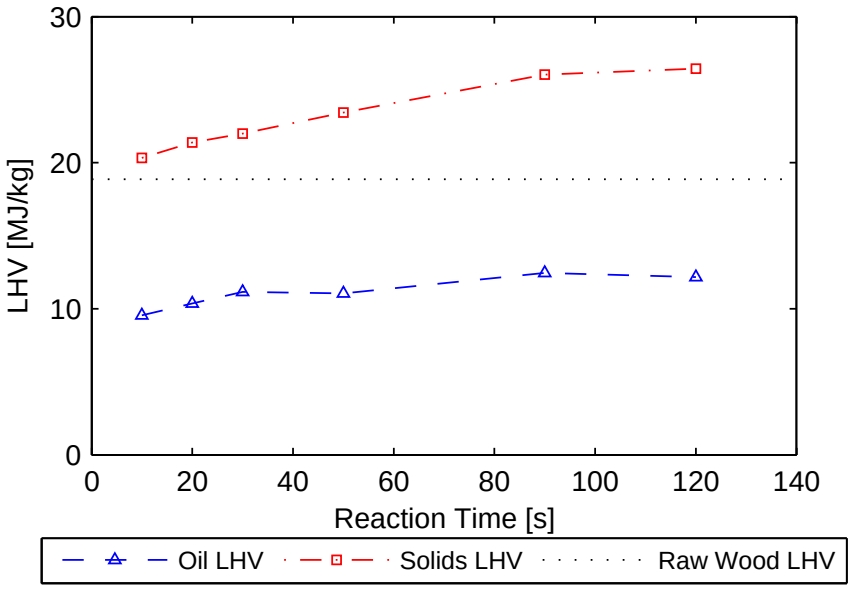

Figure 2.13: Lower heating value results for bio-oils and solids compared to the unreacted pine feedstock

Table 2.9: Lower heating values of raw unreacted Loblolly pine, collected bio-oil products, and collected solid products

Residence Time $[s]$	$LHV_{solid}[MJ/kg]$	$LHV_{oil}[MJ/kg]$
10	20.33	9.56
20	21.37	10.36
30	21.98	11.16
50	23.44	11.05
90	26.03	12.45
120	26.44	12.18
Raw Pine	18.87	–

as it was lowered to prevent violent boiling of the liquid nitrogen. During this time, ambient air was sucked into the condenser and its water vapor and CO_2 condensed within the cold trap. The testing facility ambient conditions were very close to those of the outside atmosphere and consequently were subject to large humidity variations thus explaining the large departure from one testing set to another.

A modification was made to the experimental procedure to evaluate the impact of sucking ambient air into the cold trap. The cold trap was first attached to the micro-reactor chamber and the entire system heated and purged with helium prior to adding liquid nitrogen to the dewar. This resulted in both lower oil yields (which were to be expected if the hypothesis regarding ambient air component condensation was correct) and good agreement between oil yields over the remainder of tests performed on the micro-reactor at varying temperatures.

2.6 Summary

A new experimental fast pyrolysis micro-reactor design was presented along with its development process and transient thermal analyses used in validating the reactor's biomass heating rate performance. The reactor provides for the control of feedstock residence time within the reactor, allowing for the derivation of conversion rates as a function of residence time. The use of conduction as the primary mode of heat

transfer allowed for the separation of heat transfer and product removal pathways. This in turn facilitated the use of a low temperature carrier gas resulting in product quenching and the minimization of secondary reactions within pyrolysis products. The separation of heat transfer and pyrolysis product removal mechanisms also allowed for the collection of separate solid and liquid pyrolysis products without the need for additional separation equipment.

Vibratory energy was introduced into the system and the settings operating envelope investigated to find the frequency and amplitude setting combination which minimized dispersed chip surface density. Through a full factorial experimental investigation, the best settings combination was determined to be at a driving frequency of $\sim$110Hz and a high amplitude setting corresponding to $\sim$2.4g's of acceleration (RMS). ANOVA results showed that frequency was the dominant factor in chip dispersion with a null hypothesis p-value of 6.4%.

The reactor was shown to facilitate low temperature isothermal fast pyrolysis by achieving maximum heating rates of 29.2°C/s for a reactor temperature of 400°C on a 1.3mm thick wooden wafer. Heating rates for a biomass layer thickness of 0.4mm are projected to be on the order of 400°C/s based upon analytical and experimental results comparison.

Design requirements for sample size, operating temperature, product dwell time, and processable sample types were met with the exception of the processing of lignin. The sample heating performance is projected to achieve the 1 second heating time design requirement.

Results obtained from fast pyrolysis experiments on Loblolly pine were presented. These demonstrated the micro-reactor's capabilities in obtaining pyrolysis products as well as mass conversion rate data. This mass conversion rate data allows for the derivation of reaction descriptors of an Arrhenius form. Utilization of the derived reaction descriptors will provide for improved fast pyrolysis models when coupled

with accurate heat and mass transfer models. These models in turn provide better design tools for reactor design and evaluation.

CHAPTER 3

METHODOLOGY FOR EXPERIMENTALLY DERIVING FAST PYROLYSIS YIELDS

3.1 Introduction

This chapter presents the experimental protocols for the measurement of fast pyrolysis product yields using the micro-reactor presented in Chapter 2. Test species selection and sample preparation methods are presented followed by the experimental procedure for the testing of samples. The calculation of product yields using experimental results is covered in detail and applied to an example data set. The evaluation of instrumentally induced uncertainty within product yield measurements is also presented and applied to the example data set.

3.2 Test Species Selection and Sample Preparation

The core species for the basis of this study is Loblolly pine. It is an abundant feedstock with demonstrated regenerative harvesting within the pulp and paper industry and has been identified as a key sustainable energy crop. [5, 57] Pyrolysis experiments on this species will provide the core data for the single component global model, two component global model, product based model and intermediate product model. The Loblolly pine samples were gathered from a complete debarked tree trunk ground and mixed to form a homogeneous mixture.

All wood samples were processed using a Wiley mill with a #40 mesh screen to filter the particulate. According to ASTM standards [58] a #40 mesh corresponds to a nominal sieve opening of 425μm. A Wiley mill is a griding machine which utilizes a set of rotating blades to shear the fed material against stationary blades on the

housing. The filter size sets the maximum particle size which can be ejected from the mill. Following grinding the samples are then dried at 75 °C until the mass stabilizes, which typically requires about 4 hours. This resulted in a final moisture content of 3.57% by mass within the Loblolly pine. All samples were stored within a desiccator until pyrolyzed.

3.3 Experimental Procedure

Each experiment starts with a known quantity of biomass which is deposited into the preheated reaction chamber through a stopcock chip drop mechanism. Throughout the duration of the pyrolysis the volatiles are swept out of the reaction chamber by the helium purge gas into the liquid nitrogen cooled condenser. The uncondensed volatiles and the helium carrier gas leave the system and are exhausted through a fume hood. Solid products are swept into a solids trap below the reaction chamber. For consistency, residence time control was automated through a custom programmable integrated circuit controller. The cycle is repeated until the designated quantity of mass is reacted. The samples from each test were collected by removing and massing the solids trap and removing and sealing the condenser. Once condensation ceased to form on the exterior of the condenser the condensed bio-oil was collected by pouring the liquid into sampling viles. The explicit step by step test procedure is given in Table 3.1 and the test documentation sheet used is contained in Appendix B.

Table 3.1: Micro-reactor step by step testing protocol

Step	Description	Outputs
	Reactor Preparation	-
1	Wipe down inside and outside of stopcock components with glass-wipes whetted with high purity acetone	-

Continued on next page...

Table 3.1: Micro-reactor testing protocol (continued)

Step	Description	Outputs
2	Rinse with high purity acetone and wipe down inside and outside of reactor lid using cotton tipped applicators to clean within crevices	-
3	Rinse with high purity acetone and clean chip catch with cotton tipped applicators	-
4	Wipe down chip catch plugs with cotton tipped applicators	-
5	Dry all parts using compressed air	-
6	Rinse inside and outside of condenser with high purity acetone making sure to thoroughly coat inside surfaces with acetone	-
7	Add a quantity of acetone to the bottom of the condenser and shake vigorously so as to clean out the condenser crevices	-
8	Dry outside of condenser with compressed air	-
9	Flush condenser interior with compressed air via the inlet port for 1 minute	-
10	Flush condenser interior with compressed air via the outlet port (*i.e.* reversed flow) for 3 minutes	-
11	Check for any residual acetone apparent within the condenser crevices, if any is found, continue flushing with compressed air until removed	-
12	Apply high vacuum grease to stopcock interfacial surface and seat the mating components	-
13	Separate and mass the stopcock core	$m_{core,f}$
14	Mass the stopcock shell	$m_{shell,f}$
15	Mass the chip catch	$m_{catch,i}$
16	Mass the reactor lid	$m_{lid,i}$
17	Add condenser stand to balance and tare the balance	-
18	Mass the condenser with attached end caps, o-rings and spring clamps	$m_{cond,i}$

Continued on next page...

Table 3.1: Micro-reactor testing protocol (continued)

Step	Description	Outputs
19	Blow off the reaction plate with compressed air to remove any debris	-
20	Clean the reaction plate surface with high purity acetone and cotton tipped applicators	-
21	Clean the stainless steel baseplate with high purity acetone and cotton tipped applicators	-
22	Dry the reaction plate and stainless steel base plate with compressed air	-
23	Align the reactor lid 30° counter-clockwise (ccw) from the chip drop (in line with the first screw ccw	-
24	Attach reactor lid clamps and tighten $\sim 1/2$ turn at a time in a ccw pattern until the silicon gasket shows no separation from the reactor lid lip	-
25	Attach the chip catch underneath while checking to ensure quark gasket integrity	-
26	Assemble the stopcock and attach to the top of the reaction chamber and tighten the clamp	-
27	Using the condenser clamps attach the helium inlet to the reactor	-
28	Align and fasten the motor underneath the reactor	-
29	Turn on helium flow and reactor temperature controller and record the time of day	$time_{on}$
30	Record activation time	-
31	Set reactor temperature on temperature controller	-
32	Define variables dwell1, dwell2, dwell3,and dwell4 within BASIC stamp program	-
33	Load updated program onto the controller box	-

Continued on next page...

Table 3.1: Micro-reactor testing protocol (continued)

Step	Description	Outputs
34	Add liquid nitrogen to Dewar	-
35	After the reactor has reached the set temperature and a minimum of 5 minutes following the initiation of helium flow, slowly lower the cold trap into the dewar and connect to the reactor lid	-
36	Wait a minimum of 2 min for the condenser to cool	-
	Sample Preparation and Reactor Operation Sequence	-
37	Mass weighing dish, record reading and tare balance	$m_{dish,i}$
38	Add $\sim$ 0.05g of sample to the weighing dish and record the reading	m_{sample}
39	Deposit the sample into the stopcock chip drop	-
40	Tare balance with empty pan	-
41	Mass the empty weighing dish and record the reading	$m_{dish,f}$
42	Start the reaction timer by pushing the start switch	-
43	Immediately rotate the stopcock to deposit the sample	-
44	The reactor will automatically distribute and remove the biomass according to timing parameters stipulated within the program loaded onto the BASIC stamp controller	-
45	Return the stopcock chip drop to the upright position	-
46	Repeat steps 35-43 until the pre-determined number of drops has been completed	-
	Reactor Disassembly	
47	Seal off the condenser outlet using an end cap and the helium inlet clamp	-
47	Remove the condenser from the Dewar and seal the inlet using an end cap and the reactor outlet clamp	-
48	Set the condenser aside to allow for warming to room temperature	-

Continued on next page...

Table 3.1: Micro-reactor testing protocol (continued)

Step	Description	Outputs
49	Turn off helium flow and temperature controller and record the time of day	$time_{off}$
50	Remove stopcock chip drop and reactor lid and set aside to cool to room temperature	-
51	Using a razor blade, gently scrape any residual particulate on the reaction plate surface into the chip drop slot	-
52	Brush through the chip drop slot using a slip of card-stock paper to clean out lingering particles	-
53	Remove the chip catch and set aside to cool to room temperature	-
54	Once at room temperature mass the separate stopcock core	$m_{core,f}$
55	Mass the stopcock shell	$m_{shell,f}$
56	Once at room temperature mass the chip catch	$m_{catch,f}$
57	Once at room temperature mass the reactor lid	$m_{lid,f}$
58	Transfer residual solids to a labeled storage vile	-
59	Once the condenser has reached room temperature, dry the exterior using compressed air to remove any condensed water	-
60	Using the condenser stand, tare the balance and remass the condenser	$m_{cond,f}$
61	If collecting oils for further analysis, uncap the condenser and pour the collected oils into labeled storage viles (this only applied to 400°C tests)	-
	Post-Experiment Reactor Cleaning	
62	Remove high vacuum grease from stopcock chip drop components using paper towels	-
63	Blow any residual chips from the stopcock chip drop, reactor lid and chip catch using compressed air	-

Continued on next page...

Table 3.1: Micro-reactor testing protocol (continued)

Step	Description	Outputs
64	Clean the reactor lid using a low grade acetone to remove any condensed oils	-
	Note: If testing cellulose it is necessary to precede acetone rinsing with purified water [a]	-
65	Rinse the condenser inside and out using low grade acetone to remove all condensed pyrolysis products	-
	Note: In the case of cellulose testing, the water rinse should be performed before the acetone rinse	-
66	After rinsing, add a quantity of acetone to the bottom of the condenser and shake vigorously so as to clean out the condenser crevices	-
67	Flush the condenser with compressed air until the major surfaces are clear of liquid, more thorough drying is not necessary as the system will be cleaned with high purity acetone before use	-

[a]The variation in rinsing protocol for cellulose is because cellulose liquid products are not acetone soluble but are water soluble. All other tested pyrolysis feedstock liquid products are not water soluble but are acetone soluble.

3.3.1 Product Yield Calculation Method

The product yields are calculated using the measured outputs following an experiment. Calculation of the mass deposited into the stopcock chip drop was performed according to Equation 3.1,

$$m_{deposit,n} = m_{sample,n} - (m_{dish,f} - m_{dish,i}) \tag{3.1}$$

The actual reacted mass was calculated by then subtracting the residual mass within the stopcock chip drop from the sum of the individual deposited masses according to Equation 3.2,

$$m_{react} = \sum_{n} m_{deposit,n} - (m_{shell,f} + m_{core,f} - m_{shell,i} - m_{core,i}) \tag{3.2}$$

Collected masses of oil and residual solids were calculated using Equations 3.3 and 3.4,

$$m_{oil} = m_{cond,f} - m_{cond,i} \tag{3.3}$$

$$m_{solid} = m_{catch,f} - m_{catch,i} \tag{3.4}$$

The respective yields were calculated using Equations 3.5 and 3.6,

$$\eta_{oil} = \frac{m_{oil}}{m_{react}} = \frac{m_{cond,f} - m_{cond,i}}{m_{react}} \tag{3.5}$$

$$\eta_{solid} = \frac{m_{solid}}{m_{react}} = \frac{m_{catch,f} - m_{catch,i}}{m_{react}} \tag{3.6}$$

Finally, the gaseous product mass and yield were estimable by difference according to Equations 3.7 and 3.8,

$$m_{gas} = m_{react} - m_{solid} - m_{oil} \tag{3.7}$$

$$\eta_{gas} = \frac{m_{gas}}{m_{react}} \tag{3.8}$$

The gas mass and yield are referred to as *estimable* because the gas mass closes the mass balance and consequently absorbs any experimental error.

3.4 Representative Data Set

A representative data set will be used to demonstrate the application of the mathematic methods for the remainder of this chapter. The raw results from a 400°C 120 second dwell test on Loblolly pine are shown in Table 3.2. Increases in the stopcock

Table 3.2: Example raw test results from Loblolly pine at 400°C and a 120 second dwell time

Object	Before [g]	After [g]
Stopcock Shell	100.867	100.874
Stopcock Core	195.141	195.245
Chip Catch	39.7333	39.7915
Cold Trap and Plugs	120.114	120.257

Sample	Dish Start [g]	Sample [g]	Dish End [g]
1	0.2897	0.0478	0.2918
2	0.2918	0.0546	0.2925
3	0.2925	0.0554	0.2913
4	0.2927	0.0533	0.2936
5	0.2936	0.0472	0.2944
6	0.2944	0.0517	0.2955
7	0.2915	0.0571	0.2938
8	0.2938	0.0467	0.2932

Table 3.3: Calcualted results from Loblolly pine at 400°C and a 120 second dwell time

Collected Solids Mass [g]	0.0582
Reacted Mass [g]	0.297
Collected Oil Mass [g]	0.143
Solids Yield [g/g]	0.196
Oil Yield [g/g]	0.482
Gas Yield [g/g]	0.322

shell and core masses indicated the quantity of raw biomass that is trapped within the parts and is not deposited. This mass is subtracted from the sum of deposited mass as shown in Equation 3.2. The change in the chip catch mass reflects the quantity of residual solids as per Equation 3.4 and the change in the cold trap and plug mass reflects the quantity of collected oil as per Equation 3.3. Through the application of Equations 3.1-3.8 the test yield results are calculated as shown in Table 3.3.

3.5 Instrumental Error Analysis of Calculated Yields

A Kline-McClintock uncertainty analysis was performed to quantify the instrumental error present within the calculated yields. [59] Mass measurements were performed on

a Scientech ZSA 210D micro balance. Masses greater than 100g are given at 0.001g resolution with a standard deviation of 0.0015g while masses less than 100mg are given at 0.0001g resolution with a standard deviation of 0.00015g. [60]

The basic equation for single measurement uncertainty as a result of instrumentation is given by Equation 3.9, [59]

$$\Delta f = \left[\sum_{p} \left(\frac{\partial f}{\partial v_p} \Delta v_p \right)^2 \right]^{\frac{1}{2}} \tag{3.9}$$

where Δ denotes the uncertainty of the subsequent term and f is a function of p variables denoted by v.

Consider for a moment only the yield of oil from a set of runs, the instrumental uncertainty in the oil yield for a single run can be calculated using Equations 3.1-3.5 applied to Equation 3.9. The resultant equation to calculate the uncertainty present in the oil yield is shown in Equation 3.10,

$$\Delta\eta_{oil} = \left[\left(\frac{\partial \eta_{oil}}{\partial m_{cond,i}} \Delta m_{cond,i} \right)^2 + \left(\frac{\partial \eta_{oil}}{\partial m_{cond,f}} \Delta m_{cond,f} \right)^2 + \left(\frac{\partial \eta_{oil}}{\partial m_{react}} \Delta m_{react} \right)^2 \right]^{\frac{1}{2}} \tag{3.10}$$

Solving for the partials results in Equation 3.11,

$$\Delta\eta_{\text{oil}} = \left[\left(\frac{1}{m_{react}} \Delta m_{cond,i} \right)^2 + \left(\frac{1}{m_{react}} \Delta m_{cond,f} \right)^2 + \left(-\frac{m_{cond,f} - m_{cond,i}}{m_{react}^2} \Delta m_{react} \right)^2 \right]^{\frac{1}{2}} \tag{3.11}$$

Uncertainties such as $\Delta m_{cond,i}$ are equal to the standard deviation given by the balance manufacturer because they are direct measurements. The uncertainty of the reacted biomass (Δm_{react}) is calculated by applying Equation 3.9 to Equation 3.2 to get Equation 3.12,

$$\Delta m_{react} = \left[\sum_{i=1}^{n} \left(\frac{\partial m_{react}}{\partial m_{dep,n}} \Delta m_{deposit} \right)^2 + \left(\frac{\partial m_{react}}{\partial m_{shell,f}} \Delta m_{shell,f} \right)^2 + \left(\frac{\partial m_{react}}{\partial m_{core,f}} \Delta m_{core,f} \right)^2 + \left(\frac{\partial m_{react}}{\partial m_{shell,i}} \Delta m_{shell,i} \right)^2 + \left(\frac{\partial m_{react}}{\partial m_{core,i}} \Delta m_{core,i} \right)^2 \right]^{\frac{1}{2}} \quad (3.12)$$

where n is the number of individual biomass deposits made within a run. The shell and core uncertainties are based upon direct measurement uncertainty. All of the partial terms are equal to 1 because the equation for m_{react} (Equation 3.2) is just a direct summation of components. The uncertainty associated with the deposited mass is then given by Equation 3.13,

$$\Delta m_{deposit,n} = \left[\left(\frac{\partial m_{deposit}}{\partial m_{sample}} \Delta m_{sample} \right)^2 + \left(\frac{\partial m_{deposit}}{\partial m_{dish,f}} \Delta m_{dish,f} \right)^2 + \left(\frac{\partial m_{deposit}}{\partial m_{dish,i}} \Delta m_{dish,i} \right)^2 \right]^{\frac{1}{2}} \quad (3.13)$$

for which the partial terms are again all equal to 1 because $m_{deposit,n}$ is only a summation. Equations 3.10-3.13 then provide the uncertainty of a single experimental oil yield. The uncertainty of an average oil yield over three runs is given by Equation 3.14,

$$\begin{aligned} \Delta \bar{\eta}_{oil} &= \left[\left(\frac{\partial \bar{\eta}}{\partial \eta_1} \Delta \eta_1 \right)^2 + \left(\frac{\partial \bar{\eta}}{\partial \eta_2} \Delta \eta_2 \right)^2 + \left(\frac{\partial \bar{\eta}}{\partial \eta_3} \Delta \eta_3 \right)^2 \right]^{\frac{1}{2}} \\ &= \left[\left(\frac{1}{3} \Delta \eta_1 \right)^2 + \left(\frac{1}{3} \Delta \eta_2 \right)^2 + \left(\frac{1}{3} \Delta \eta_3 \right)^2 \right]^{\frac{1}{2}} \end{aligned} \quad (3.14)$$

Instrumental uncertainties for the solid and gas yields were calculated using the same method.

The instrumental uncertainty associated with the experimental oil yield for the 120 second dwell results given in Section 3.4 is calculated according to Equations 3.15 - 3.18,

$$\begin{aligned}
\Delta m_{deposit,n} &= \left[(0.0001\text{g})^2 + (0.001\text{g})^2 + (0.001\text{g})^2\right]^{\frac{1}{2}} \\
&= 0.0014\text{g} \qquad (3.15) \\
\Delta m_{react} &= \left[8(0.0014\text{g})^2 + (0.001\text{g})^2 + (0.001\text{g})^2 + (0.001\text{g})^2 + (0.001\text{g})^2\right]^{\frac{1}{2}} \\
&= 0.0044\text{g} \qquad (3.16) \\
\Delta \eta_{oil} &= \left[\left(\frac{0.001\text{g}}{0.2967\text{g}}\right)^2 + \left(\frac{0.001\text{g}}{0.2967\text{g}}\right)^2 + \left(-\frac{120.257\text{g} - 120.114\text{g}}{(0.2967\text{g})^2}0.0044\text{g}\right)^2\right]^{\frac{1}{2}} \\
&= 0.0089\text{g} \qquad (3.17)
\end{aligned}$$

Note that Equation 3.15 given the uncertainty of a single deposit and this value applies to all eight of the sample deposits within the experiment.

Following the same procedure for the other two 120 second residence time tests for Loblolly pine at 400°C allows for the calculation of the instrumental uncertainty associated with the average oil yield as given by Equation 3.18,

$$\begin{aligned}
\Delta \bar{\eta}_{oil} &= \left[\left(\frac{0.0069\text{g}}{3}\right)^2 + \left(\frac{0.0089\text{g}}{3}\right)^2 + \left(\frac{0.0089\text{g}}{3}\right)^2\right]^{\frac{1}{2}} \\
&= 0.0083\text{g} \qquad (3.18)
\end{aligned}$$

This calculated uncertainty amounts to 5.1% of the average oil yield obtained at 400°C and 120 seconds for Loblolly pine pyrolysis. The same procedure was used for the solid and gas yield instrumental uncertainty calculations and applied to the other tested temperatures and residence times.

3.6 Summary

The selection of Loblolly pine and its preparation as the primary feedstock for this study were presented. Loblolly pine was selected primarily because of its abundance within the Southeastern region of the United States and its proven sustainable harvesting by the lumber and paper industries. The step by step experimental procedure

is given for the generation of isothermal pyrolysis yield data using the micro-reactor. The subsequent computational methods for extracting pyrolysis yields from the micro-reactor result were presented providing a pathway to high fidelity isothermal pyrolysis data. Finally, the propagation of instrumental error was evaluated using a Kline-McClintock uncertainty analysis approach and was applied to an example set of data from the pyrolysis of Loblolly pine at 400°C. In the demonstrated case the instrumental error was calculated to be approximately 5%. These methods will be applied in the following chapters for the derivation of fast pyrolysis kinetic parameters and the evaluation of experimentally introduced error.

CHAPTER 4

INVESTIGATION OF THE KINETICS OF BULK REACTANT BASED REACTION MECHANISMS

4.1 Introduction

In this chapter bulk kinetic mechanisms of wood pyrolysis are evaluated. These include pyrolysis models with whole raw wood going to char and volatiles (oils + gases) as well as whole raw wood going to the three separate pyrolysis products of char, oil and gas. Within the first group of models a single component global model will be evaluated as well as a two component global model. Each of the three models will be developed mathematically. The best fit determination method including the development of the statistical treatment and the numerical solution method are presented. The experimental yields from the pyrolysis of Loblolly pine are then presented and utilized to obtain kinetic parameters. The results are plotted against the single variable statistic results from the data and residuals plots analyzed.

4.2 Salient Literature

Biomass pyrolysis kinetic modeling is historically rooted in the modeling of coal pyrolysis. In 1946 Bamford *et al.* [61] studied pyrolysis as a step in the combustion of wood. The pyrolysis was treated as a single component devolatilization mechanism following a first order Arrhenius reaction mechanism based upon previous coal pyrolysis models. Since this first application, single component models of an Arrhenius form have frequently been implemented for the modeling of biomass pyrolysis.

The Arrhenius reaction rate model was formulated as a descriptor for chemical reactions between gaseous components but has also shown applicability to other types

of reactions such as those with aqueous ionic solutions. The Arrhenius equation is commonly understood and accepted within the pyrolysis community as an imposed form for describing the solid state kinetics, due to lacking a physically tractable pathway for the molecular level interactions. As an example of the molecular complexity of the bio-oils, Azeez *et al.* [62] identified 80 separate molecules within pyrolysis bio-oils utilizing GC/MS and noted that this accounted for less than 45% of the mass of the bio-oil. Other studies [63, 48, 64] have presented similar findings showing dozens of identified molecules while still only accounting for a fraction of the bio-oil mass. Therefore, in this study, and in keeping with the general understanding of the community, an imposed Arrhenius form will be pursued.

In 1963 Roberts and Clough [17] investigated the pyrolysis of Beechwood cylinders embedded with thermocouples for *in situ* temperature measurement. The intent of the study was to show that pyrolysis activation energy and heat of reaction vary with experimental conditions. Samples were pyrolyzed in a tubular furnace with the mass loss being tracked through a lever arm type balance. Pyrolysis activation energies for a single component global model were calculated based upon a best fit to the mass loss data assuming a single component global reaction scheme. The results showed two different activation energies and heats of reaction distinguished by wood temperatures either above or below 280°C.

Product based pyrolysis models have been considered since introduced by Shafizadeh and Chin [65] in 1977. The authors claimed three independent parallel reactions in converting wood to *combustible volatiles* (gas), *tar* (liquids), and *char* (solids) followed by a secondary reaction scheme converting *tar* products into combustible *volatiles* and *char*.

Milosavljevic and Suuberg [20] studied the pyrolysis of cellulose specifically with respect to the impact of heating rate and final reactor temperature. Single component global models were fit to the experimental results. The authors concluded that

higher heating rate experiments which reached reactor temperatures above $\sim 325°C$ gave lower activation energies (140-155kJ/mol) while experiments at lower reactor temperatures gave a much higher activation energy of approximately 218kJ/mol.

Branca *et al.* [66] evaluated pseudo-component based as well as single and two component global models using a TGA oven at heating rates of $0.05 - 1.8°C/s$ ($3 - 108°C/min$). The pseudo-component based model used TGA derived kinetics from the previously mentioned study by Grønli *et al.* [67] as well as best fit components to the experimental results as a comparison. The single component global model used two sets of kinetic parameters taken from literature, one with a high activation energy and one with a low activation energy. The two component model simply added an additional component to the single component model and separated the two according to cellulose+lignin and hemicellulose. Results showed that the pseudo-component model from literature only fit the heating rate conditions for which the kinetic parameters were derived and deviated significantly at higher heating rates. The best fit coefficients based upon the experimental results showed good agreement amongst all tested temperatures. Overall, the pseudo-component and two component models provided nearly equivalent fits with much poorer fits obtained using the single component model.

4.3 Model Structures and Derivations

Five model forms will be fitted to the fast pyrolysis experimental results. The purpose of this is to evaluate the actual quality of each model's fit, compare it to to other common pyrolysis models, and then evaluate the inter-species predictive capability. Micro-reactor tests produce results in the form of yield versus time at set temperatures. A best fit half-life model is then fit to the yield results using a Chi-squared minimization procedure. This model follows the form of Equation 4.1,

$$\eta_i(t) = c_i \left(1 - \frac{1}{2}^{t/\tau_i}\right) \tag{4.1}$$

where c_i is the maximum convertible quantity of product i (in g/g), t is time and τ_i is the half-life of the formation of component i. When considering the total production of volatiles, the half-life is equated with the total progress of the pyrolysis reaction. The half-life value is related to the rate of reaction by Equation 4.2,

$$k_i = \frac{\ln 2}{\tau_i} \tag{4.2}$$

where k_i is the rate of formation of product i. After calculating rates of formation for multiple temperatures, the Arrhenius equation parameters of Equation 4.3 can be estimated,

$$k_i = A_i \mathrm{e}^{-E_{a,i}/\mathrm{R}T} \tag{4.3}$$

where A_i is the pre-exponential factor, $E_{a,i}$ is the activation energy, R is the universal gas constant, and T is the reactor temperature for the tests from which k_i was derived.

This process, of deriving k values from raw experimental data and subsequent E_a and A values, will be utilized to calculate the rates of formation of pyrolysis products in the comparison of fast and slow pyrolysis models discussed in Chapter 6.6. Within the model comparison presented in Chapter 6, however, the coefficients E_a, A and c will be solved for globally using the best fit methodology discussed in Section 4.4. This method utilizes equations 4.1-4.3 but in reverse by evaluating the rate coefficients for a given set of kinetic parameters (E_a and A) and then solving for the predicted conversions. These conversions are then evaluated against the data to determine the goodness of fit of the input kinetic parameters within the model.

In many pyrolysis models the application of these coefficients for pyrolysis predictions would require an iterative process because of highly transient thermal conditions. The predictive work presented here for model comparisons, however, is for the

evaluation of predicted conversions within the micro-reactor and assumes isothermal conditions which provide for some simplification in their application.

4.3.1 Single Component Global Model

The single component global pyrolysis model is the simplest to be considered. It consists of a single pyrolysis reaction transforming raw virgin wood into char and volatile products. The mechanism was first proposed by Bamford *et al.* [61] as a step in the combustion of wood. This mechanism is depicted in Figure 4.1a. Gas and oil products are lumped together and treated as one product referred to as volatiles. The assumption is made that the char and volatiles always form in a fixed ratio equal to that of the final char and volatiles ratio. Thus the reaction can be characterized by a single set of kinetic parameters. The rate of pyrolysis is described by the Arrhenius equation shown in Equation 4.4,

$$k_p = A_p \mathrm{e}^{-E_{a,p}/\mathrm{R}T} \tag{4.4}$$

where the subscript p refers to the global pyrolysis reaction. The yields of char and volatiles are then predicted using Equations 4.5 and 4.6,

$$\eta_v(t) = c_v \left(1 - \frac{1}{2}^{tk_p(T)/\ln 2}\right) \tag{4.5}$$

$$\eta_c(t) = c_c \left(1 - \frac{1}{2}^{tk_p(T)/\ln 2}\right) \tag{4.6}$$

where c_v is the maximum quantity of volatiles to be formed and c_c is the maximum quantity of char to be formed as predicted by the model. Because volatiles and char represent the only products to be formed, the models are interdependent on the relationship: $c_c = 1 - c_v$.

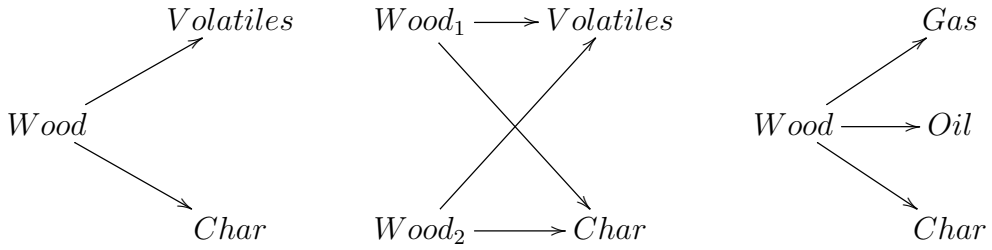

Figure 4.1: Pyrolysis model diagrams: (a) Single component global (b) Two component global (c) Product based

4.3.2 Two Component Global Model

The two component global pyrolysis model is simply an extension of the single component model. It consists of a two simultaneous pyrolysis reactions transforming raw virgin wood into char and volatile products. This mechanism is depicted in Figure 4.1b. The yields of char and volatiles are predicted using Equations 4.7 and 4.8,

$$\eta_v(t) = c_{v1}\left(1 - \frac{1}{2}^{tk_{p1}(T)/\ln 2}\right) + c_{v2}\left(1 - \frac{1}{2}^{tk_{p2}(T)/\ln 2}\right) \tag{4.7}$$

$$\eta_c(t) = c_{c1}\left(1 - \frac{1}{2}^{tk_{p1}(T)/\ln 2}\right) + c_{c2}\left(1 - \frac{1}{2}^{tk_{p2}(T)/\ln 2}\right) \tag{4.8}$$

The values for c_{v1} and c_{v2} are determined by best fit while c_{c1} and c_{c2} are calculated based upon the volatiles best fit and assumed constant proportionality of formation between the volatile and char fractions. This relationship is described by Equations 4.9 and 4.10,

$$1 = c_{v1} + c_{v2} + c_{c1} + c_{c2} \tag{4.9}$$

$$\frac{c_{c1}}{c_{c2}} = \frac{c_{v1}}{c_{v2}} \tag{4.10}$$

The initial starting components Wood_1 and Wood_2 (from Figure 4.1b) are equal to the sum of their respective c_v and c_c terms. They are assumed based upon the best fits and do not necessarily correlate to a wood component fraction.

4.3.3 Product Based Model

The product based model, like the pseudo-component model, also requires three times as many Arrhenius kinetic terms as the single component global model with the intent of providing a better prediction of the overall proportionality of products produced. The underlying assumption is that all three pyrolysis products form independently in parallel competing reactions. For the sake of this work it will be assumed that all of the reactions involved are first order. The mechanism is depicted in Figure 4.1c.

Recall that the experimental results obtained using the micro-reactor give the oil and residual solids yield at each residence time and reactor temperature tested. The gas quantity is calculated by difference with respect to the reacted virgin biomass.

Equation 4.1 is fit to each component at each reactor temperature to give reaction half-lives based on oil and gas yield results. The residual solids mass, however, by itself does not indicate the quantity of char formed except when convergence over time is observed. At all other residence times the residual solids contain both char and unreacted biomass. Consequently, the formation of the char is assumed to occur at the same rate as the total volatiles (thus using the kinetic parameters derived for the global single component pyrolysis model in Equation 4.4).

For reactions occurring under isothermal conditions the rate coefficients calculated using the derived kinetic parameters are constant. In this case the individual product yields as a function of time can be solved for analytically. The individual product yields as a function of time are given by Equations 4.11-4.13,

$$\eta_c(t) = c_c \left(1 - \frac{1}{2}^{tk_c(T)/\ln 2}\right) \tag{4.11}$$

$$\eta_g(t) = c_g \left(1 - \frac{1}{2}^{tk_g(T)/\ln 2}\right) \tag{4.12}$$

$$\eta_o(t) = c_o \left(1 - \frac{1}{2}^{tk_o(T)/\ln 2}\right) \tag{4.13}$$

where the subscripts c, o and g refer to char, oil and gas respectively. The maximum convertible quantities of each component (c) are solved for by ratio of the rate parameters. This is only applicable when isothermal pyrolysis is assumed to take place because the kinetically predicted rate of pyrolysis (k) does not change over time. The c values are then calculated using Equation 4.14,

$$c_i = \frac{k_i}{k_c + k_o + k_g} \tag{4.14}$$

4.4 Best-fit Determination

A best fit determination method was applied to evaluate each of the selected pyrolysis models while considering the individual data points as well as the data variance. The most common best fit method found within pyrolysis literature is the application of least squared errors. This method does not, however, provide any dependency upon the spread of the data itself but equally weights every data point. The χ^2 parameter for goodness of fit is obtained by weighting the least squared errors with the standard deviation estimated for each residence time and reactor temperature combination. Using this method, smaller confidence interval data points will then receive a greater weight within the determination of the best fit.

This method allows for the comparison of kinetic models and the subsequent determination of the best fit among them. It is not expected that an ideal fit will be obtained because the model forms are imposed and are not derived from the actual chemical phenomena occurring during pyrolysis. [68] The models are, however,

commonly accepted forms for representing the pyrolysis of biomass and have received much attention and application.

Best-fit coefficients were found through minimizing the χ^2 goodness of fit parameter calculated as per Equation 4.15, [69]

$$\chi^2 = \sum_{i=1}^{n} \left(\frac{\eta_i(t,T) - \eta_{model}(t,T)}{\sigma(t,T)} \right)^2 \tag{4.15}$$

where n is the number of runs, η_i is the mass conversion measured for run i, σ is the standard deviation and η_{model} is calculated from Equation 4.1 at time t and reactor temperature T. The best fit activation energy (E_a), pre-exponential factor (A) and convertible fraction (c) were solved for all temperature results simultaneously to produce global best fits.

The reduced (normalized) χ^2 value is used to compare models and account for the impact of an increasing number of model parameters and independent data points. The reduced χ^2 parameter is calculated using Equation 4.16,

$$\chi^2_\nu = \frac{\chi^2}{\nu} \tag{4.16}$$

where ν is the degrees of freedom for estimating the error. Confidence regions were also calculated for the best fit parameters using an F-test as shown in Equation 4.17, [70]

$$F_{(p,\nu-p,1-\alpha)} = \frac{\left(\chi^2_{max} - \hat{\chi}^2\right)/p}{\hat{\chi}^2/(\nu - p)} \tag{4.17}$$

where p is the number of parameters solved for in the model equation, $\hat{\chi}^2$ is the minimum value determined for the best fit and χ^2_{max} is the maximum value which falls on the border of the $100(1-\alpha)\%$ confidence interval. Recall that an F statistic is equal to the unexplained variation (that which is a result of experimental error and model form selection) and explained variation (that which is a result of controlled

changes). Therefore the difference between the best fit χ^2 value and the altered χ^2 value as a result of manipulating a given parameter allows for the calculation of an explained variation. The unexplained variation is that which defines the $\hat{\chi}^2$ value. The confidence region borders are then defined by the parameter pairs which result in χ^2 values equal to χ^2_{max}. Individual parameter confidence intervals are determined by holding all other terms constant and increasing or decreasing the targeted term until χ^2_{max} is reached.

The normalized χ^2 values provide both an absolute evaluation of the quality of the fit and a means of comparing the fits of each model. An ideal fit would correspond to a reduced χ^2 value equal to 1. This is unlikely to be obtained, however, due to the imposition of the model form as previously discussed.

Simultaneous solution of the global best fit parameters was accomplished using a particle swarm optimization algorithm to minimize the objective function outlined in Equation 4.15. The algorithm works by distributing particles (seed points) throughout the parameter space which then search to find minima based upon local gradients, random motion, and the previously best global minimum. Particles are given velocities which are affected by both their individual best position according to history and the global best position. The random motion aspect of the particles in particular makes it superior to a simple gradient descent method due to the possibilities of multiple local minima. Additionally, by sharing information between particles about the current best global minima, particles are much less inclined to get trapped within local minima and remain useful as they continue to investigate the path between current and global best locations.

The algorithm flow chart is depicted in Figure 4.2. A more thorough treatment of particle swarm optimization can be found in references [71, 72, 73].

The initial particle distributions were based upon pseudo-random seeding. Using this method a matrix of evenly distributed particle positions was generated and the

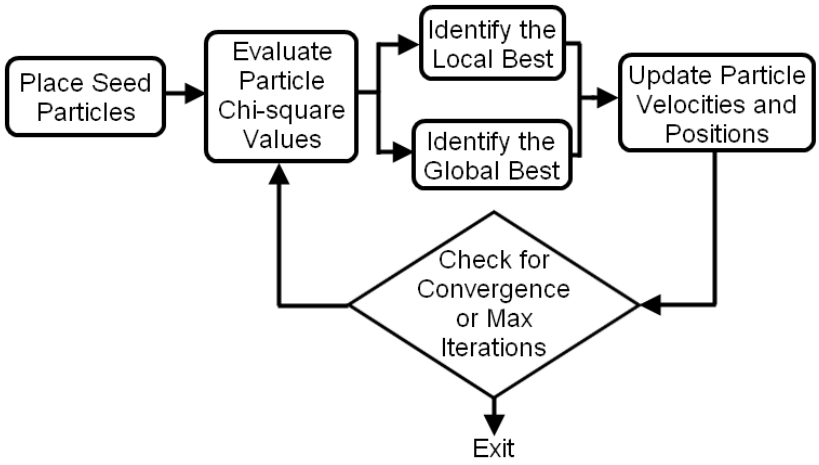

Figure 4.2: Particle swarm optimization algorithm block diagram

seed points assigned initial positions within the domain such that no two points share the same value for any given coefficient. Thus the initial evaluations of the objective function are orthogonal to each other. [53] This method allows for the parameter space to be seeded throughout without overloading the number of initial particles or requiring complicated seed distribution algorithms. An example of two-dimensional pseudo-random seeding is shown in Figure 4.3. This method is particularly useful when investigating multi-dimensional parameter spaces within which more structured seeding approaches can become cumbersome, such as for the twelve component intermediate product model of Section 5.3.2. A full domain search approach could be applied for the determination of simpler model coefficients. The particle swarm optimization approach methods had to be applied for more complicated models, however, and so were then applied to all models for consistency.

The convergence criteria required the standard deviation of the particles' χ^2 values to be less than 0.2 at which point the particles were determined to have reached a common minima. Multiple simulations are run to decrease the chance that global minima are missed.

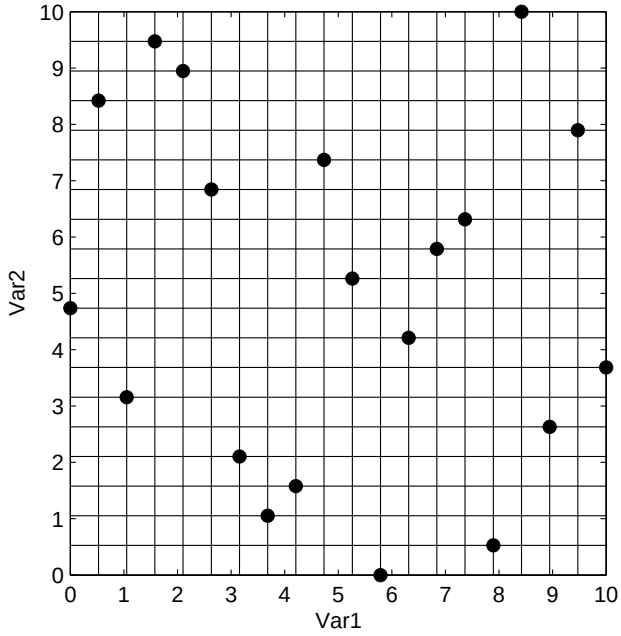

Figure 4.3: Example pseudo-random seeding plot for a simplified 2-D seeded parameter space

4.5 Experimental Bounding

Reactor temperatures for Loblolly pine were selected based upon previously published TGA results for the species as well as arguments from literature which make the case for low temperature pyrolysis. Published TGA curves by Fu *et al.* [74] on Loblolly pine indicate that by 400°C the loss of mass has nearly halted. According to Reed and Guar [75] the pyrolysis temperature of 400°C is just past the observed onset of fast pyrolysis in large particles of wood during charcoal manufacture, thus it represents a coarse lower temperature bound. This fast pyrolysis transition point indicates the temperature at which liquids become the dominant product over char formation. Scott *et al.* [76] concluded from an investigation on bubbling fluidized bed reactors that operation in the range of $400-450$°C produces better oil yields as higher temperatures tend toward gaseous product production and lower temperatures tend toward char production. Additionally, Scott *et al.* concluded that product vapors

should be kept below the range of $400-420°C$ for the purpose of minimizing secondary reactions within pyrolysis products resulting in tar formation.

Arrhenius coefficients derived from TGA data were used to estimate the kinetic limitations of the reaction to find the upper time bound for experimentation. Rate equation coefficients were taken from literature values [18] from experiments run on *Pinus sylvestris* (also known as Scots pine or Norway pine) which is of the same taxonomical genus as Loblolly pine. The kinetic approximation was based upon a system of three individual non-competing reactions representing each individual biomass component (cellulose, hemicellulose and lignin) and was fit to a Scots pine TGA derivative curve.

Using the TGA derived values and a set reactor temperature of 400°C, the rate constant k was determined from the Arrhenius rate equation shown in Equation 4.3. The half lives for the individual reactions were then calculated from Equation 4.2 and applied to Equation 4.18,

$$\eta_{Sylvestris} = c_{hemi}\left(1-\frac{1}{2}^{t/\tau_{hemi}}\right)+c_{cell}\left(1-\frac{1}{2}^{t/\tau_{cell}}\right)+c_{lignin}\left(1-\frac{1}{2}^{t/\tau_{lignin}}\right) \quad (4.18)$$

The upper time bound was set at 120 seconds as it represented a point at just above 75% predicted completion of pyrolysis. To reach 95% completion of the reaction at 400 °C it would take ∼1100 seconds, which is not a practical residence time for this experimental system. Kinetic parameter values taken from literature are contained in Table 4.1 along with the calculated values for k_i and τ_i.

Up to 1 second of deviation can exist from the set residence time within each sample drop as a result of the sample deposit mechanism used. Setting a maximum of 10% error in the residence time limited the lower time bound to 10 seconds.

Ultimately five temperatures and six residence times were selected for testing based on the determined time and temperature operating spaces. The time spread was chosen to capture the anticipated conversion trends at low residence times as

Table 4.1: Results from a pseudo-component independent reaction Arrhenius model for Scots pine [18] (top) and calculated rate constants and half-lives at 400°C (bottom)

	Hemicellulose	Cellulose	Lignin
E_a [kJ/kmol]	122.7	267.8	32.8
A [1/s]	2.63E8	1.26E20	4.79E-1
c [g/g$_{\text{reacted}}$]	0.296	0.323	0.183
k [1/s]	7.88E-2	2.06E-1	1.36E-3
$\tau_{\frac{1}{2}}$ [s]	8.80	3.36	508.95

Table 4.2: Selected operating temperatures and residence times for Loblolly pine fast pyrolysis experimentation

Species	Residence Time [s]	Reactor Temperature [°C]
Pinus taeda	10, 20, 30, 50, 90, 120, 300	380, 390
Pinus taeda	10, 20, 30, 50, 90, 120	400, 410, 420

well as the maximum convertible quantity at slightly longer residence times. The selected time spread for temperatures below 400°C was modified to add the 300 second residence time because of the slower rate of pyrolysis at decreasing temperatures. A summary of the selected operating temperatures and times for Loblolly pine is contained in Table 4.2.

4.6 Experimental Structure and Results

Experiments were conducted in two sets for bulk kinetic model data generation. The first experimental set encompassed the reactor temperatures of 380, 390, 410 and 420°C. The second set constituted a completely randomized retest of the 400°C reactor temperature. The test matrices for the two sets are given in Tables 4.3 and 4.4. Single variable statistic results for all five temperatures are given in Table 4.5.

Table 4.3: Testing matrix for Loblolly pine pyrolysis tests at 380, 390, 410 and 420°C

Test	Residence Time [s]	Reactor Temp [°C]	Test	Residence Time [s]	Reactor Temp [°C]	Test	Residence Time [s]	Reactor Temp [°C]
1	50	420	27	20	390	53	90	390
2	20	420	28	90	380	54	50	380
3	50	410	29	90	380	55	300	380
4	50	420	30	30	380	56	300	380
5	20	410	31	30	390	57	300	390
6	30	410	32	120	380	58	300	380
7	30	420	33	50	390	59	300	390
8	30	420	34	50	380	60	300	390
9	90	420	35	120	380	61	10	390
10	20	420	36	20	390	62	10	420
11	90	410	37	20	390	63	10	390
12	20	410	38	20	380	64	10	420
13	90	420	39	20	380	65	120	410
14	90	420	40	50	390	66	120	420
15	30	410	41	30	380	67	10	410
16	50	410	42	90	380	68	10	420
17	90	410	43	20	380	69	10	380
18	90	410	44	30	390	70	120	410
19	30	420	45	120	390	71	120	420
20	30	410	46	120	380	72	10	380
21	50	410	47	90	390	73	10	410
22	20	410	48	30	390	74	120	410
23	20	420	49	30	380	75	10	390
24	50	420	50	120	390	76	10	380
25	120	390	51	50	380	77	120	420
26	90	390	52	50	390	78	10	410

Table 4.4: Randomized testing matrix for Loblolly pine pyrolysis tests at 400°C

Test	Residence Time [s]	Reactor Temp [°C]	Test	Residence Time [s]	Reactor Temp [°C]
1	120	400	10	120	400
2	10	400	11	30	400
3	30	400	12	90	400
4	10	400	13	20	400
5	120	400	14	90	400
6	10	400	15	20	400
7	90	400	16	30	400
8	20	400	17	50	400
9	50	400	18	50	400

Table 4.5: Loblolly pine pyrolysis average product yields and standard deviations for 380, 390, 400, 410 and 420°C reactor temperatures with gas yields calculated by difference

380°C						
Residence Time [s]	$\bar{\eta}_o$ [g/g]	σ_o [g/g]	$\bar{\eta}_s$ [g/g]	σ_s [g/g]	$\bar{\eta}_g$ [g/g]	σ_g [g/g]
10	0.180	7.34E-2	0.644	5.93E-3	0.176	7.49E-2
20	0.172	1.27E-2	0.594	1.97E-2	0.234	3.17E-2
30	0.205	2.93E-2	0.532	1.74E-2	0.263	2.13E-2
50	0.222	4.78E-3	0.474	4.90E-3	0.303	9.54E-3
90	0.342	4.71E-2	0.383	1.92E-2	0.275	3.02E-2
120	0.339	2.06E-2	0.339	5.25E-3	0.323	2.10E-2
300	0.422	2.10E-2	0.253	1.82E-2	0.325	2.72E-2
390°C						
Residence Time [s]	$\bar{\eta}_o$ [g/g]	σ_o [g/g]	$\bar{\eta}_s$ [g/g]	σ_s [g/g]	$\bar{\eta}_g$ [g/g]	σ_g [g/g]
10	0.174	1.89E-2	0.597	1.14E-2	0.229	2.75E-2
20	0.247	6.54E-2	0.510	2.67E-3	0.243	6.34E-2
30	0.259	6.06E-2	0.472	1.41E-2	0.270	7.15E-2
50	0.320	8.29E-2	0.401	1.03E-2	0.279	8.03E-2
90	0.397	5.68E-2	0.302	1.73E-2	0.301	4.56E-2
120	0.392	6.54E-2	0.263	2.36E-2	0.344	4.19E-2
300	0.475	5.53E-2	0.228	1.68E-2	0.297	7.20E-2
400°C						
Residence Time [s]	$\bar{\eta}_o$ [g/g]	σ_o [g/g]	$\bar{\eta}_s$ [g/g]	σ_s [g/g]	$\bar{\eta}_g$ [g/g]	σ_g [g/g]
10	0.136	2.62E-2	0.527	2.43E-2	0.337	2.87E-2
20	0.292	2.02E-2	0.420	2.65E-2	0.289	1.84E-2
30	0.393	9.14E-3	0.364	4.39E-3	0.243	1.26E-2
50	0.431	3.15E-2	0.269	3.29E-3	0.300	3.48E-2
90	0.487	2.53E-2	0.227	4.22E-3	0.286	2.71E-2
120	0.494	2.49E-2	0.206	8.65E-3	0.300	3.08E-2
410°C						
Residence Time [s]	$\bar{\eta}_o$ [g/g]	σ_o [g/g]	$\bar{\eta}_s$ [g/g]	σ_s [g/g]	$\bar{\eta}_g$ [g/g]	σ_g [g/g]
10	0.225	3.39E-2	0.481	2.42E-2	0.294	2.38E-2
20	0.378	2.13E-2	0.361	1.26E-2	0.261	2.84E-2
30	0.477	4.09E-2	0.311	7.57E-3	0.212	4.45E-2
50	0.466	3.58E-2	0.232	1.06E-2	0.302	3.99E-2
90	0.484	2.22E-2	0.196	2.42E-3	0.320	2.28E-2
120	0.495	3.38E-2	0.210	7.12E-3	0.295	2.71E-2
420°C						
Residence Time [s]	$\bar{\eta}_o$ [g/g]	σ_o [g/g]	$\bar{\eta}_s$ [g/g]	σ_s [g/g]	$\bar{\eta}_g$ [g/g]	σ_g [g/g]
10	0.325	6.11E-2	0.425	2.74E-2	0.250	8.22E-2
20	0.489	3.08E-2	0.273	1.25E-2	0.238	2.41E-2
30	0.480	3.91E-2	0.229	6.24E-3	0.291	4.54E-2
50	0.530	2.18E-2	0.197	1.80E-3	0.273	2.33E-2
90	0.518	3.49E-2	0.190	7.73E-3	0.292	3.45E-2
120	0.491	3.75E-2	0.209	2.59E-2	0.300	2.39E-2

4.7 Kline McClintock Instrumental Error Analysis Results

The instrumental error associated with the calculated yields was estimated using the methodology presented in Section 3.5. Calculated uncertainties from the Loblolly pine experiments are given in Table 4.6 and the uncertainties as a percentage of the average yields are given in Table 4.7.

Analysis of the results shows that as a percentage of the yield the instrumental error had the lowest impact on the solids. This was to be expected because fewer measurements are necessary to calculate a solids yield and among them only four are at the lower resolution of the mass balance. In the case of the oil yields, six measurements are at the lower resolution of the balance and this explains much of the increase in error. The gas yields nearly always have a higher percentage of error attributable to instrumental sources because the gas yield is calculated by difference between the deposited mass and the measured oil and residual solids masses. The largest instrumental error introduced is 4.8% in the case of the oil produced at a reactor temperature of 400°C and a residence time of 10 seconds. The lowest percentage of yield error was calculated to be 0.63% at a reactor temperature of 380°C and a residence time of 20 seconds.

Table 4.6: Experimental measurement uncertainty results for Loblolly pine

		380°C			390°C	
Residence Time [s]	$\Delta\eta_o$ [g/g]	$\Delta\eta_s$ [g/g]	$\Delta\eta_g$ [g/g]	$\Delta\eta_o$ [g/g]	$\Delta\eta_s$ [g/g]	$\Delta\eta_g$ [g/g]
10	4.98E-3	4.50E-3	6.71E-3	4.51E-3	3.82E-3	5.91E-3
20	4.45E-3	3.76E-3	5.82E-3	4.63E-3	3.25E-3	5.66E-3
30	4.66E-3	3.49E-3	5.83E-3	4.65E-3	3.01E-3	5.54E-3
50	4.71E-3	3.13E-3	5.65E-3	5.01E-3	2.68E-3	5.68E-3
90	5.05E-3	2.55E-3	5.66E-3	5.25E-3	2.05E-3	5.64E-3
120	5.00E-3	2.26E-3	5.49E-3	5.29E-3	1.82E-3	5.60E-3
300	5.28E-3	1.71E-3	5.55E-3	5.73E-3	1.64E-3	5.96E-3
		400°C			410°C	
Residence Time [s]	$\Delta\eta_o$ [g/g]	$\Delta\eta_s$ [g/g]	$\Delta\eta_g$ [g/g]	$\Delta\eta_o$ [g/g]	$\Delta\eta_s$ [g/g]	$\Delta\eta_g$ [g/g]
10	6.52E-3	5.14E-3	8.30E-3	4.73E-3	3.19E-3	5.71E-3
20	6.92E-3	4.08E-3	8.03E-3	4.89E-3	2.30E-3	5.41E-3
30	7.05E-3	3.39E-3	7.82E-3	5.48E-3	2.08E-3	5.86E-3
50	6.94E-3	2.44E-3	7.35E-3	5.23E-3	1.53E-3	5.45E-3
90	7.91E-3	2.28E-3	8.23E-3	6.89E-3	1.70E-3	7.09E-3
120	8.28E-3	2.16E-3	8.56E-3	5.40E-3	1.41E-3	5.58E-3
		420°C				
Residence Time [s]	$\Delta\eta_o$ [g/g]	$\Delta\eta_s$ [g/g]	$\Delta\eta_g$ [g/g]			
10	4.97E-3	2.82E-3	5.71E-3			
20	5.34E-3	1.78E-3	5.63E-3			
30	5.58E-3	1.59E-3	5.80E-3			
50	5.62E-3	1.35E-3	5.78E-3			
90	5.57E-3	1.31E-3	5.72E-3			
120	5.53E-3	1.45E-3	5.71E-3			

Table 4.7: Experimental measurement uncertainty results for Loblolly pine as a percentage of yield

	380°C			390°C		
Residence Time [s]	$\frac{\Delta\eta_o}{\eta_o}$ [%]	$\frac{\Delta\eta_s}{\eta_s}$ [%]	$\frac{\Delta\eta_g}{\eta_g}$ [%]	$\frac{\Delta\eta_o}{\eta_o}$ [%]	$\frac{\Delta\eta_s}{\eta_s}$ [%]	$\frac{\Delta\eta_g}{\eta_g}$ [%]
10	2.76	0.66	3.52	2.59	0.64	2.58
20	2.59	0.63	2.49	1.87	0.64	2.33
30	2.28	0.66	2.22	1.80	0.64	2.05
50	2.12	0.66	1.86	1.57	0.67	2.04
90	1.48	0.67	2.06	1.32	0.68	1.88
120	1.48	0.67	1.70	1.35	0.69	1.63
300	1.25	0.68	1.71	1.21	0.72	2.00
	400°C			410°C		
Residence Time [s]	$\frac{\Delta\eta_o}{\eta_o}$ [%]	$\frac{\Delta\eta_s}{\eta_s}$ [%]	$\frac{\Delta\eta_g}{\eta_g}$ [%]	$\frac{\Delta\eta_o}{\eta_o}$ [%]	$\frac{\Delta\eta_s}{\eta_s}$ [%]	$\frac{\Delta\eta_g}{\eta_g}$ [%]
10	4.80	0.98	2.46	2.10	0.66	1.94
20	2.37	0.97	2.78	1.30	0.64	2.07
30	1.79	0.93	3.22	1.15	0.67	2.76
50	1.61	0.91	2.45	1.12	0.66	1.81
90	1.62	1.00	2.87	1.42	0.87	2.22
120	1.67	1.05	2.86	1.09	0.67	1.89
	420°C					
Residence Time [s]	$\frac{\Delta\eta_o}{\eta_o}$ [%]	$\frac{\Delta\eta_s}{\eta_s}$ [%]	$\frac{\Delta\eta_g}{\eta_g}$ [%]			
10	1.53	0.66	2.28			
20	1.09	0.65	2.37			
30	1.16	0.70	1.99			
50	1.06	0.69	2.11			
90	1.08	0.69	1.96			
120	1.13	0.69	1.91			

4.8 Whole Wood Pyrolysis Model Fits

4.8.1 Single Component and Two Component Global Model Fits

The initial fit to the Loblolly pine pyrolysis data was performed by fitting a half-life degradation curve to each of the five reactor temperature data sets for both the single and two component models. The resultant coefficients are presented in Table 4.8 and the models plotted against the single variable statistics for the experimental results in Figures 4.4-4.8. Residuals plots are provided in Figures 4.9a-e.

Analysis of the single component fit reduced χ^2 values shows an initially very poor fit of the model to the data which improves as reactor temperature is increased. In contrast the two component model shows reduced χ^2 values nearly equal to 1 for both the 380 and 390°C fits with values for 400 and 410°C well below the reduced χ^2 values obtained for the single component fits. The 420°C results showed an equivalent fit quality between the single and two component fits indicating a negligible improvement. Over the five temperatures the χ^2 results indicate clearly that the two component model is a superior mechanism for describing the pyrolysis of Loblolly pine at the individual temperatures.

Examination of the residuals plots shows agreement with the conclusions drawn from the χ^2 values. For the single component model the residuals both decrease in magnitude and attain better symmetry about the 0-axis as the reactor temperature increases. Recall that a lack of symmetry indicates that the model has failed to capture some piece of information in the data. Within the single component model, fits at all temperatures demonstrate a failure to capture the lower residence time behavior. The two component model residuals plots, however, show improved symmetry across all reactor temperatures and even at the lowest residence times, showing that the two component model captures the observed pyrolysis phenomena well.

The c_1 and c_2 values show large variations between the individual temperature

Table 4.8: Individual temperature fit Loblolly pine single component and two component results with 95% confidence intervals

Single Component Fits										
Temp	380°C		390°C		400°C		410°C		420°C	
c [g/g]	0.605	± 0.041	0.674	$^{+0.022}_{-0.023}$	0.777	± 0.010	0.802	± 0.009	0.806	± 0.003
τ [s]	9.10	$^{+4.14}_{-2.84}$	10.6	± 0.8	12.0	± 0.8	9.45	$^{+1.16}_{-1.15}$	6.13	$^{+0.45}_{-0.48}$
χ^2	1279		401		128		121		22.9	
ν	18		18		15		15		15	
χ^2_ν	71.0		22.3		8.51		8.04		1.53	
Two Component Fits										
Temp	380°C		390°C		400°C		410°C		420°C	
c_1 [g/g]	0.439	± 0.010	0.397	$^{+0.014}_{-0.013}$	0.526	$^{+0.005}_{-0.011}$	0.430	± 0.007	0.035	± 0.005
c_2 [g/g]	0.314	± 0.006	0.383	± 0.005	0.268	$^{+0.006}_{-0.007}$	0.379	± 0.007	0.777	± 0.004
τ_1 [s]	52.5	$^{+2.4}_{-2.3}$	42.6	$^{+2.3}_{-2.1}$	16.5	± 0.8	15.4	± 1.7	22.1	$^{+8.9}_{-7.4}$
τ_2 [s]	2.06	$^{+0.58}_{-2.06}$	2.29	$^{+1.24}_{-0.00}$	0.834	$^{+3.62}_{-0.833}$	2.55	$^{+2.09}_{-2.55}$	5.38	$^{+1.00}_{-0.30}$
χ^2	15.9		17.9		33.8		36.0		19.7	
ν	16		16		13		13		13	
χ^2_ν	0.994		1.12		2.60		2.77		1.51	

fits. This is a result of the unconstrained nature of the fits and no attempt at correlating the fits between temperatures. This is addressed, however, in the global model best fits in which a single set of c_1 and c_2 values were fit to the entire set of data simultaneously.

Model best fits were also performed for both the single component global and two component global models. For the single component global model a best fit was also performed using only the upper three reactor temperatures tested (400, 410 and 420°C) because they showed significantly better individual fit results for the single component model. Additionally, the maximum convertible quantities (c values) were in good agreement between the three models but showed a large departure from the c values obtained for the 380 and 390°C fits. The results of the global fits are contained in Table 4.9 and are plotted against the experimental result mean values with two standard deviation error bars in Figures 4.10-4.14. Residuals for the curve fits are given in Figures 4.15a-e.

Graphical analysis confirms the conclusions drawn from the numerical results, that the global single component model is inadequate for describing the pyrolysis at 380

Table 4.9: Single component global fits for Loblolly pine with 95% confidence intervals

Global Fit to 380, 390, 400, 410 and 420°C Data									
Model	c [g/g]		E_a [kJ/mol]		A [1/s]		χ^2	ν	χ^2_ν
SC Global	0.786	±0.014	132	$^{+0.5}_{-0.6}$	1.19E9	$^{+0.13E9}_{-0.11E9}$	6722	92	73.1
TC Global Pt.1	0.453	±0.005	220	±0.2	3.82E15	$^{+0.17E15}_{-0.16E15}$	325	89	3.65
TC Global Pt.2	0.352	±0.004	185	$^{+1}_{-2}$	1.26E14	$^{+0.54E14}_{-0.27E14}$	325	89	3.65
Global Fit to 400, 410 and 420°C Data									
Model	c [g/g]		E_a [kJ/mol]		A [1/s]		χ^2	ν	χ^2_ν
SC Global	0.801	±0.006	157	±3	8.28E10	±0.45E10	419	50	8.39

and 390°C but shows better agreement with the higher temperatures tested (400, 410 and 420°C). The implications of this will be further demonstrated in Chapter 6. Two component models, however, demonstrated graphically good (as well as numerically superior) fits to the data across all temperatures. The graphically close fit to the experimental mean values is reflected in the relatively low reduced χ^2 value of the two component global fit.

Trends to be noticed within the two component global fit are that as the reactor temperature decreases the fits appear to over predict the final yield and as the reactor temperature is increased the fits appear to over predict the lower residence time yields (*e.g.* $t \leq 20$s).

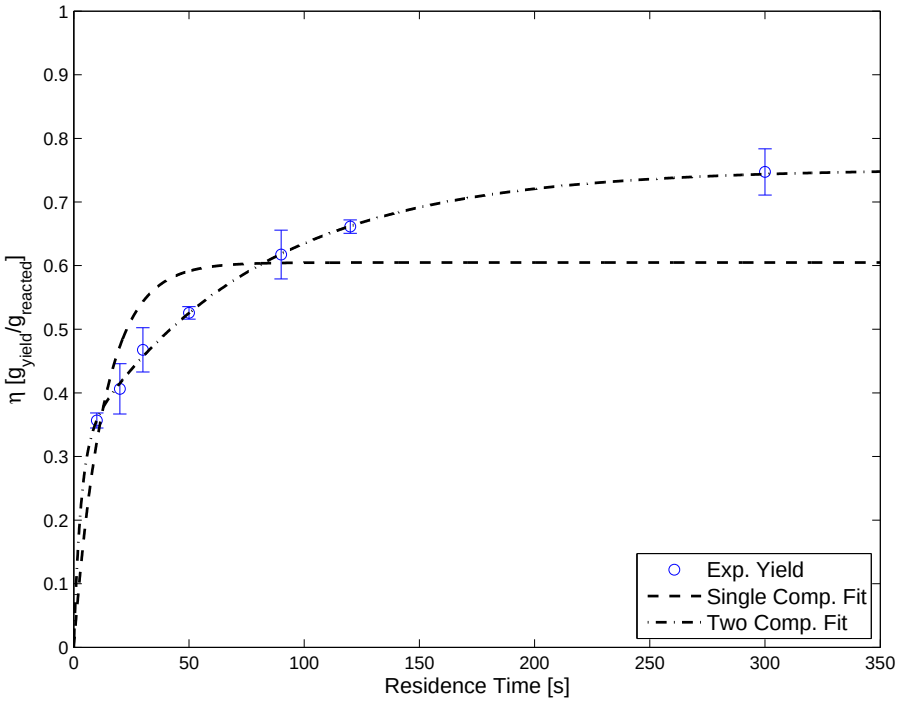

Figure 4.4: Single and two component half-life model curves fit to 380°C results plotted against the data mean values with two standard deviation error bars

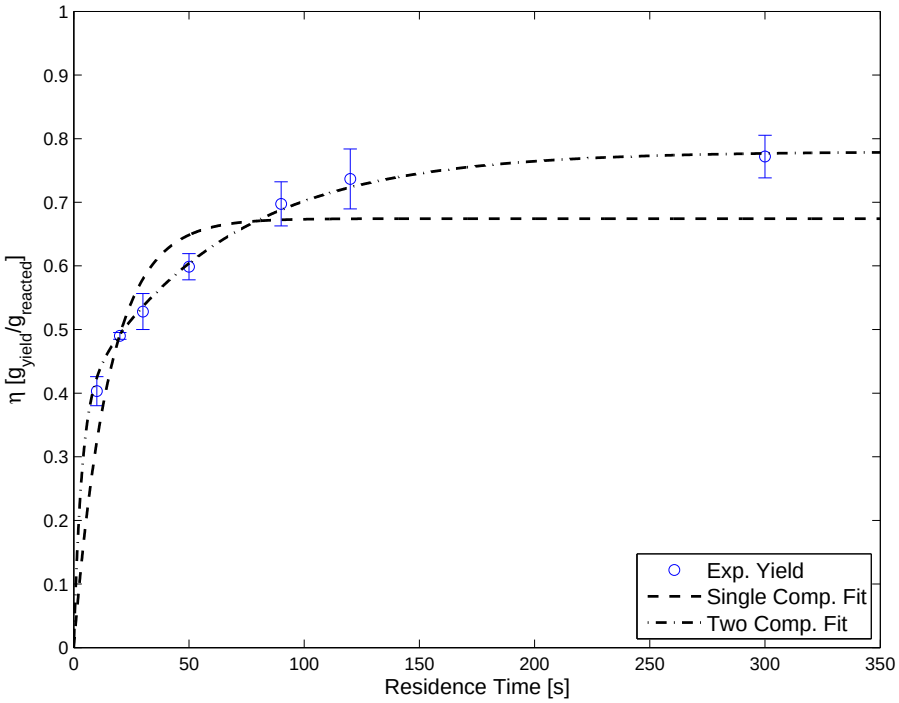

Figure 4.5: Single and two component half-life model curves fit to 390°C results plotted against the data mean values with two standard deviation error bars

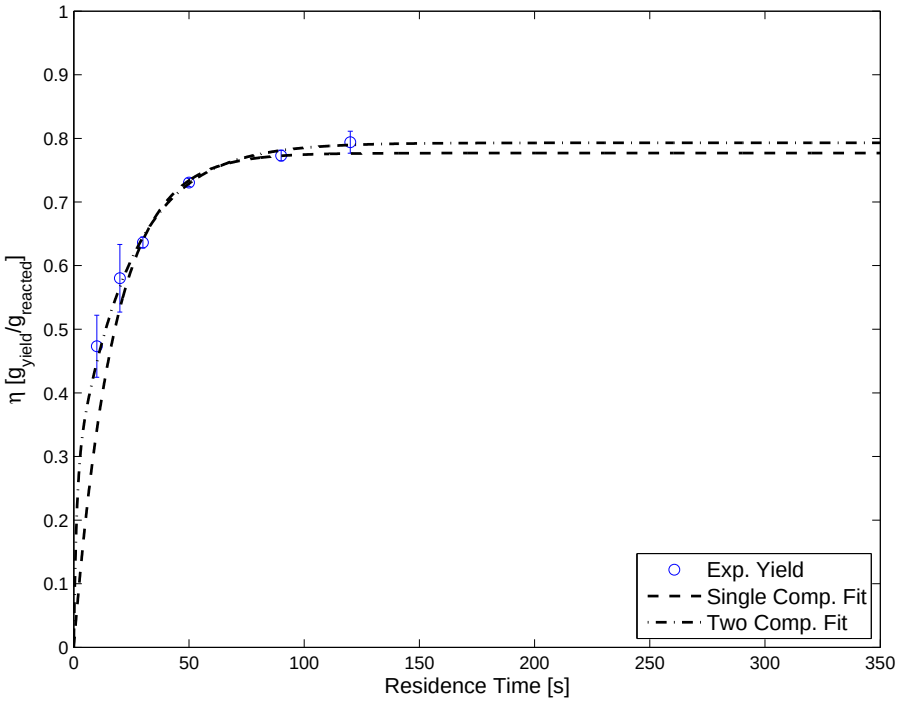

Figure 4.6: Single and two component half-life model curves fit to 400°C results plotted against the data mean values with two standard deviation error bars

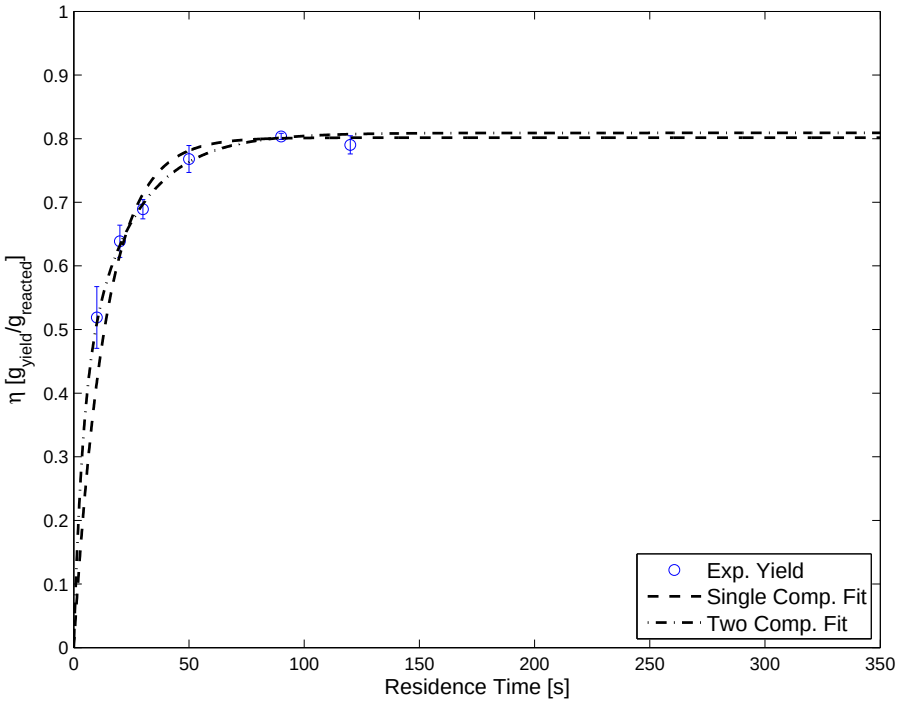

Figure 4.7: Single and two component half-life model curves fit to 410°C results plotted against the data mean values with two standard deviation error bars

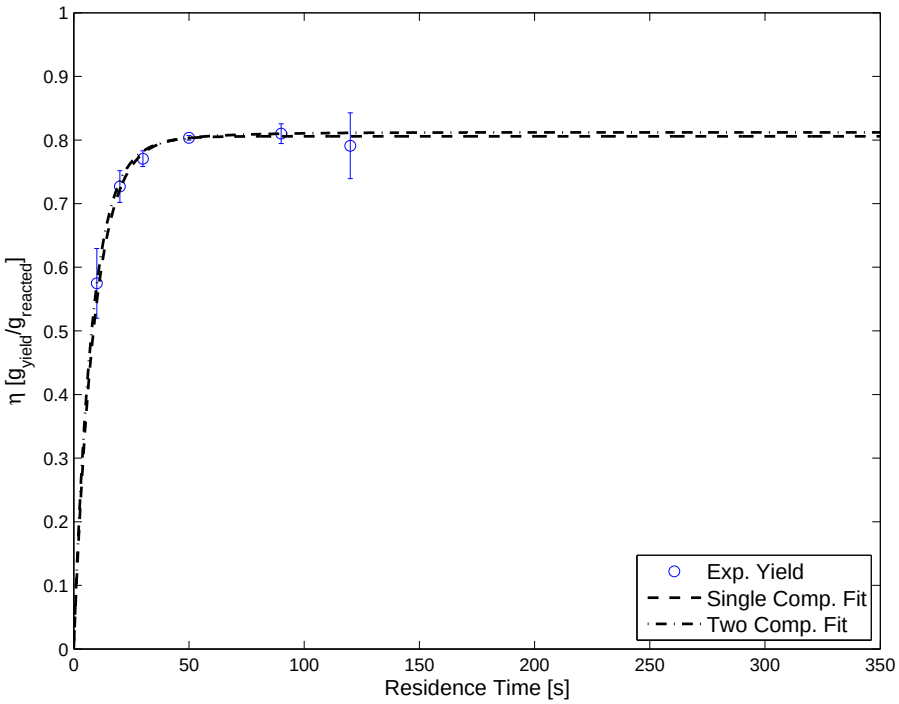

Figure 4.8: Single and two component half-life model curves fit to 420°C results plotted against the data mean values with two standard deviation error bars

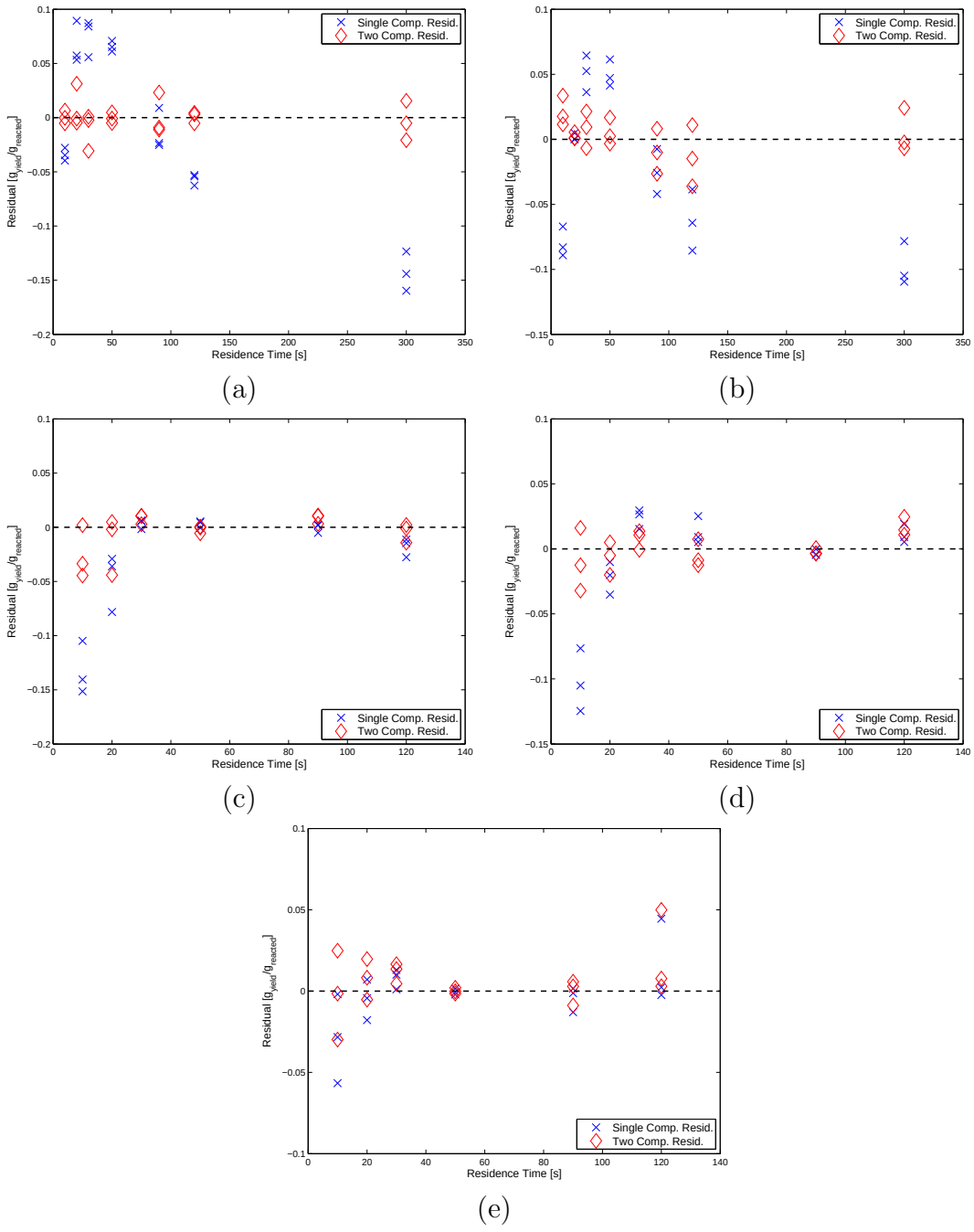

Figure 4.9: Single and two component individual temperature half-life model curve fit residuals for reactor temperatures of: (a) 380°C (b) 390°C (c) 400°C (d) 410°C (e) 420°C (NOTE: y-axis ranges change between plots)

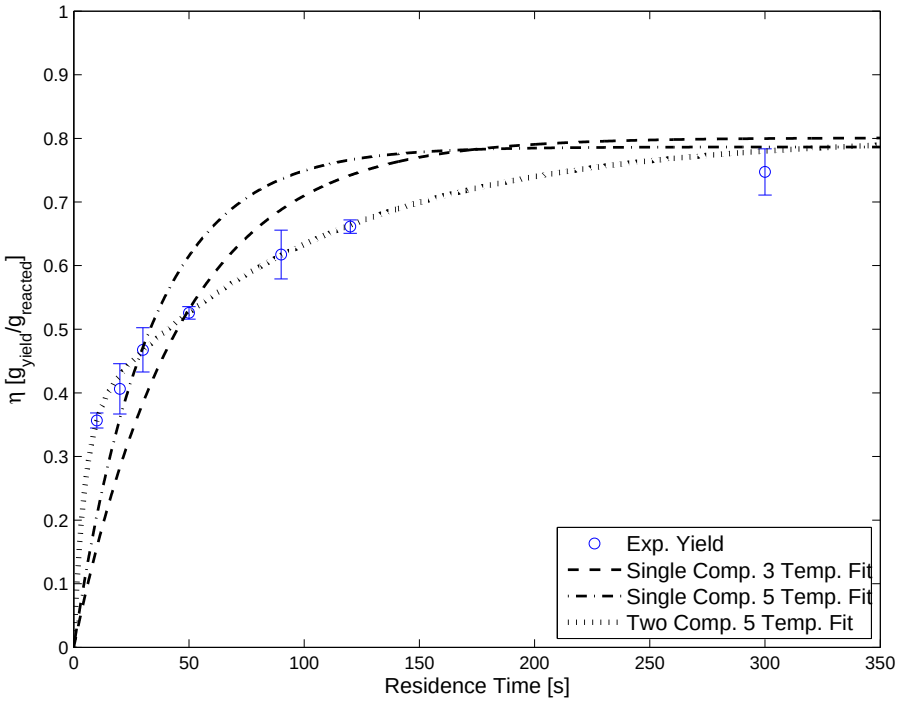

Figure 4.10: Single and two component model global fit results plotted against 380°C experimental mean values with two standard deviation error bars

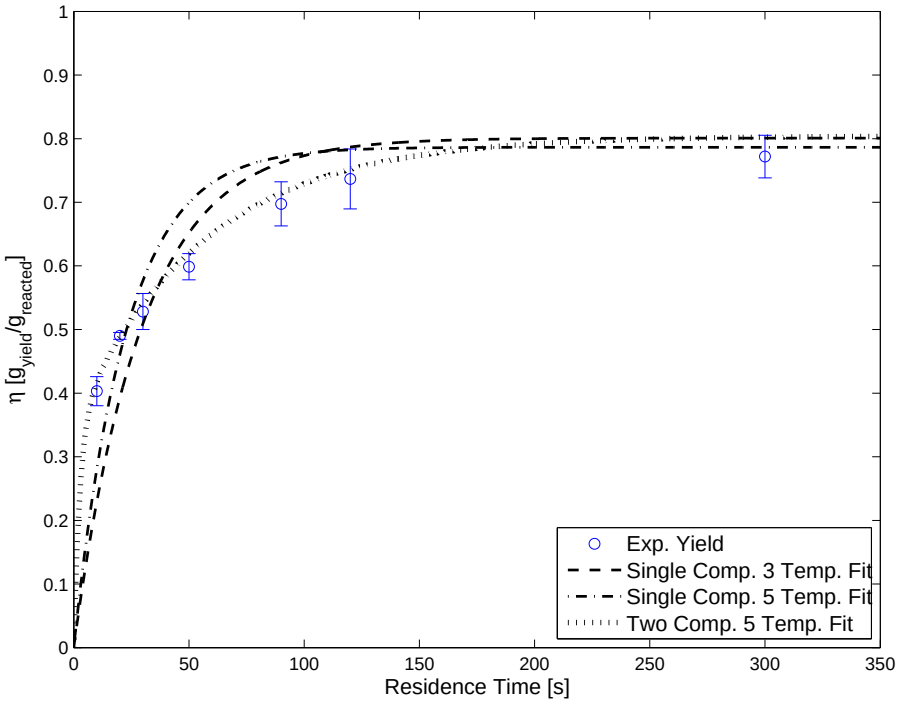

Figure 4.11: Single and two component model global fit results plotted against 390°C experimental mean values with two standard deviation error bars

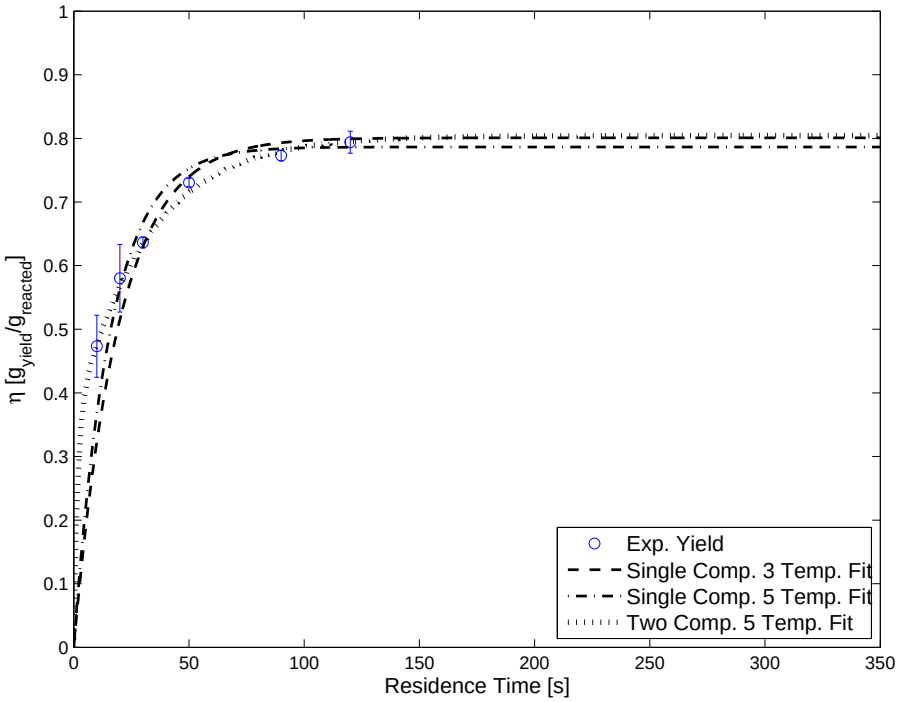

Figure 4.12: Single and two component model global fit results plotted against 400°C experimental mean values with two standard deviation error bars

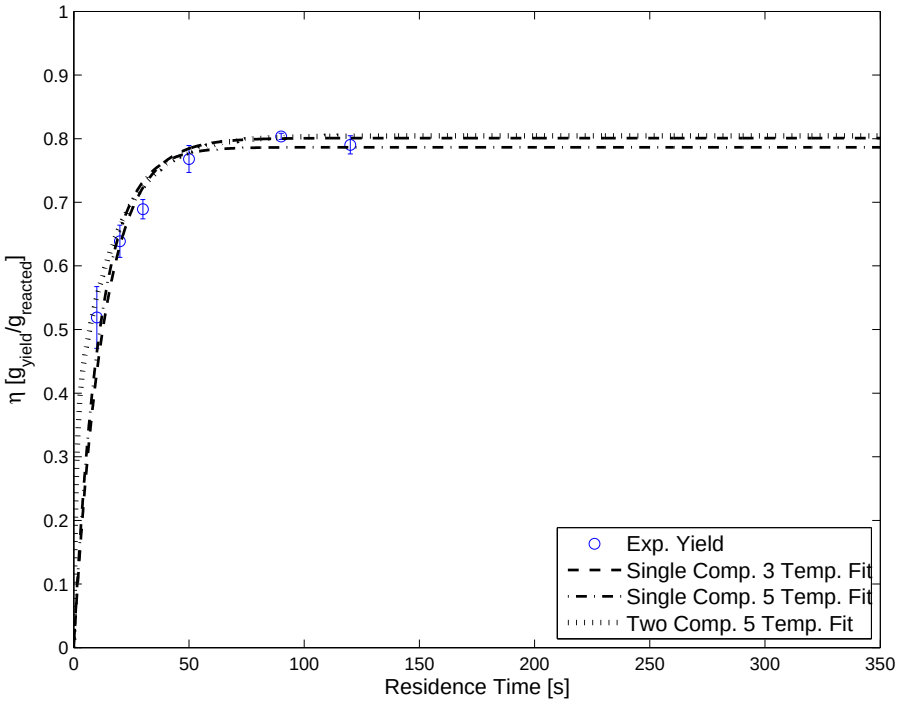

Figure 4.13: Single and two component model global fit results plotted against 410°C experimental mean values with two standard deviation error bars

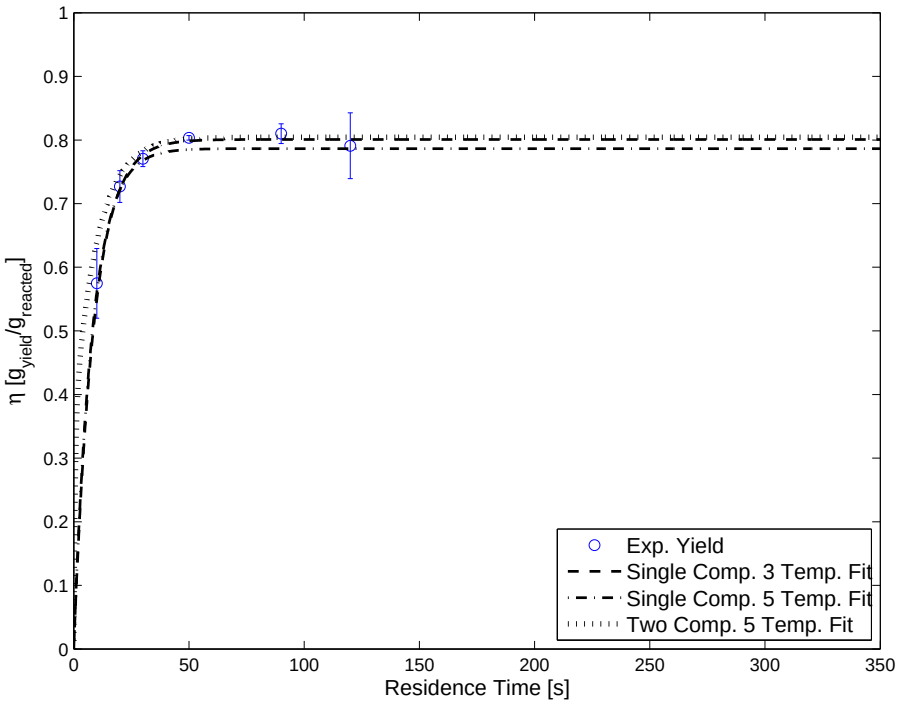

Figure 4.14: Single and two component model global fit results plotted against 420°C experimental mean values with two standard deviation error bars

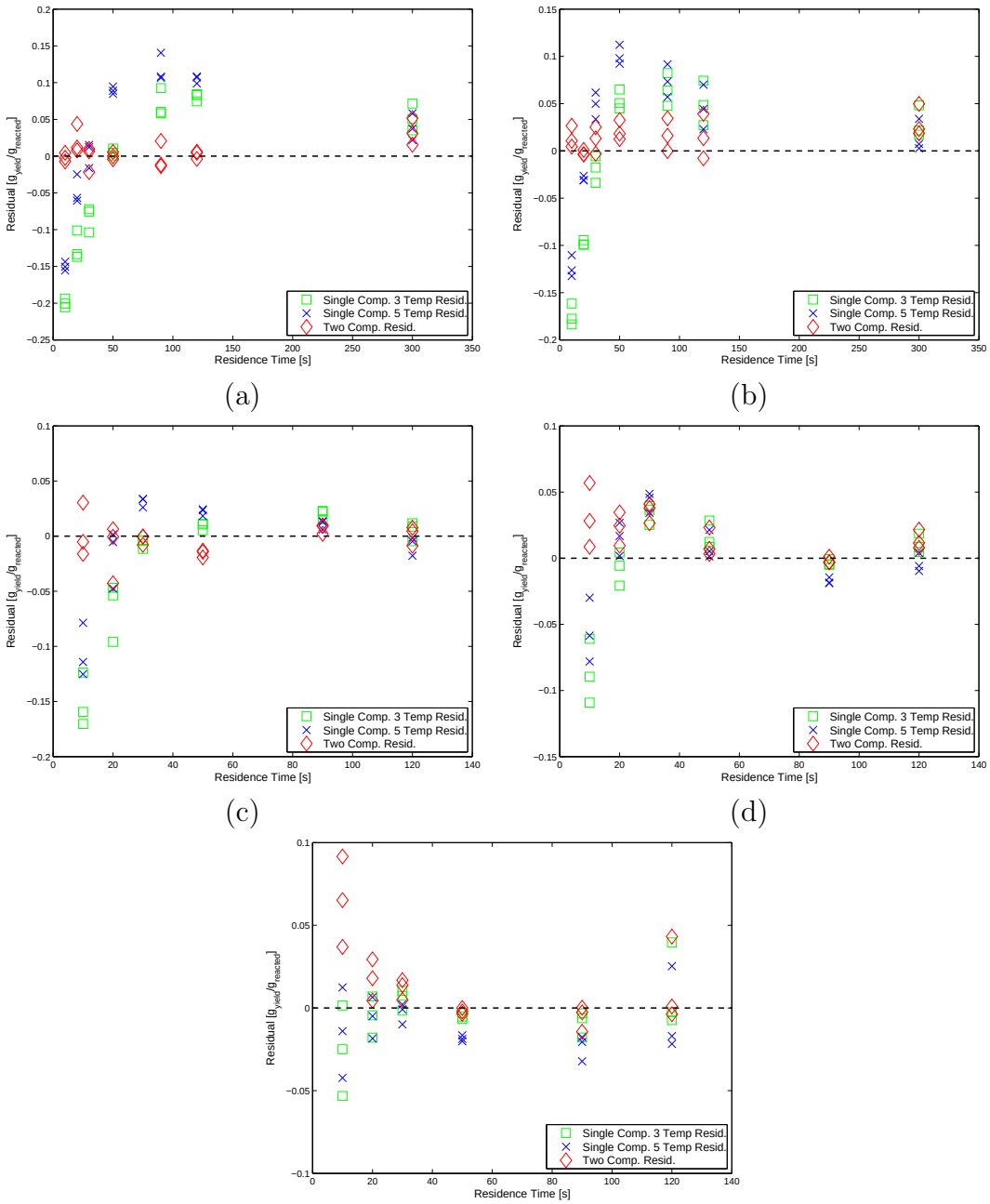

Figure 4.15: Three temperature and five temperature single component global fit residuals and two component global fit residuals for reactor temperatures of: (a) 380°C (b) 390°C (c) 400°C (d) 410°C (e) 420°C (NOTE: y-axis ranges change between plots)

4.8.2 Product Based Model Fits

Product based model fits were applied to the gas and oil yields based on the assumption that the char forms at the same rate as the total volatiles. Consequently, the char formation activation energy and pre-exponential term were taken from the single component global results using data from the upper three tested reactor temperatures on Loblolly pine because this model showed a significantly better fit than that for all the single component global model applied to all five tested reactor temperature results. The model results are summarized in Table 4.10 and plotted against the experimental data in Figures 4.16-4.18. Residuals from the product based model curve fits are presented in Figures 4.19a-c.

From graphical analysis of the figures it appears that the fit to the gas yields is better than that to the oil yields. Additionally, the model predictions appear to be better suited for the longer residence times at higher temperatures. The residuals plots reinforce this assessment, showing poor symmetry except at the higher temperatures and longer residence times.

Table 4.10: Loblolly pine high temperature product based model fit results

Model	E_a [kJ/mol]		A [1/s]		χ^2	ν	χ^2_ν
Loblolly pine SC Global	157	± 3	8.28E10	$\pm$0.45E10	419	50	8.39
Loblolly pine oil	218	$^{+0.3}_{-1}$	6.51E+15	$^{+1.55\text{E}15}_{-0.38\text{E}15}$	535	46	11.6
Loblolly pine gas	163	$^{+1}_{-0.4}$	3.00E+11	$^{+0.23\text{E}11}_{-0.69\text{E}11}$	535	46	11.6

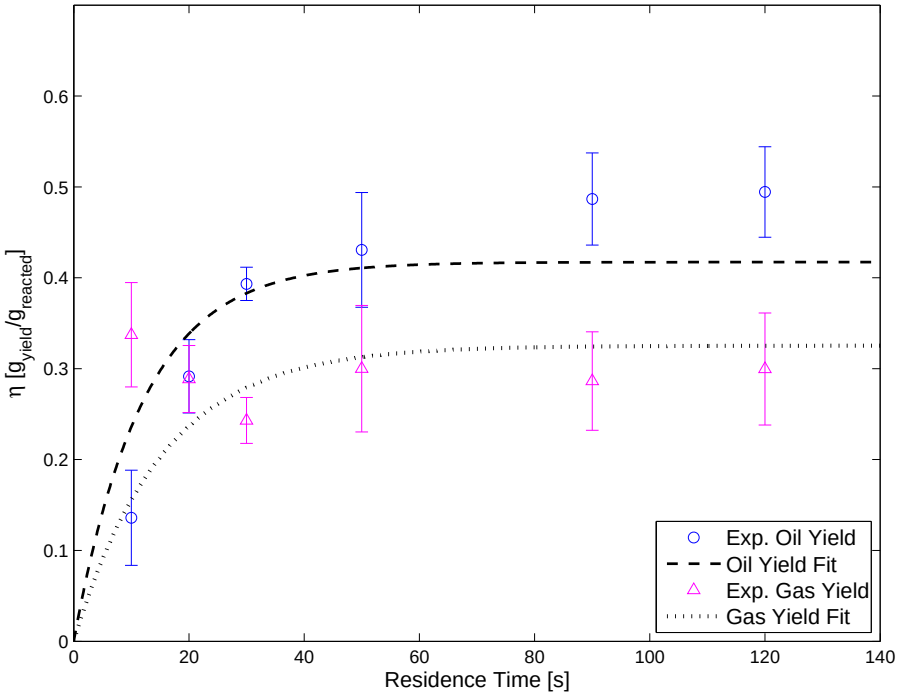

Figure 4.16: Loblolly pine product based global fit results plotted against 400°C experimental mean values with two standard deviation error bars

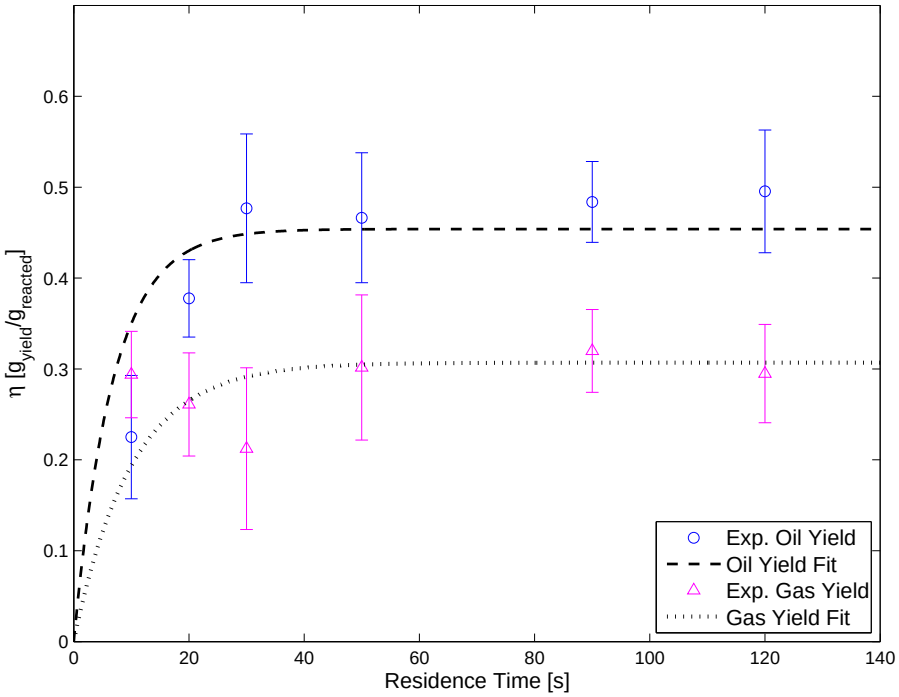

Figure 4.17: Loblolly pine product based global fit results plotted against 410°C experimental mean values with two standard deviation error bars

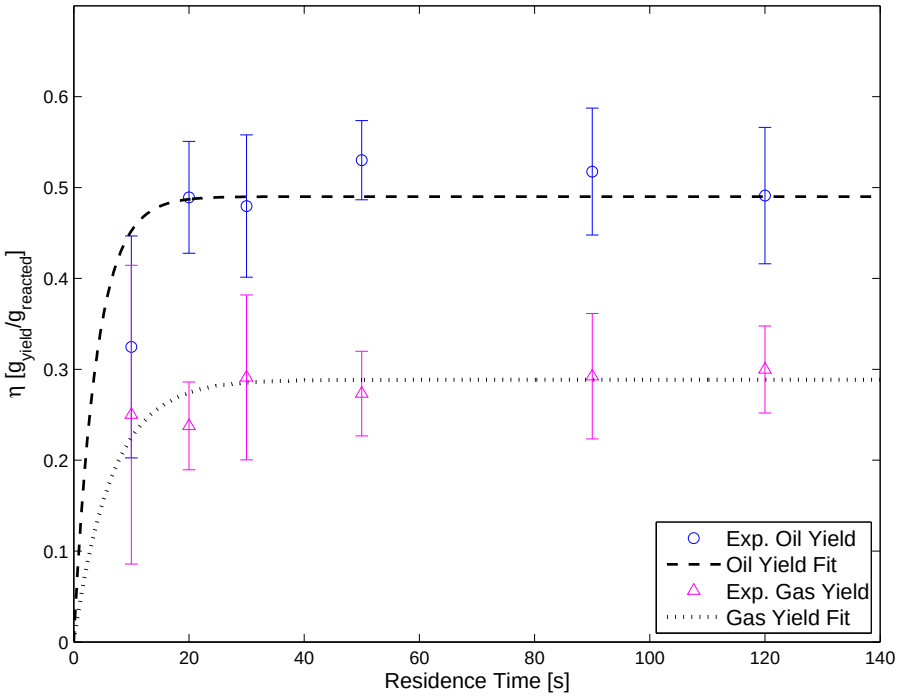

Figure 4.18: Loblolly pine product based global fit results plotted against 420°C experimental mean values with two standard deviation error bars

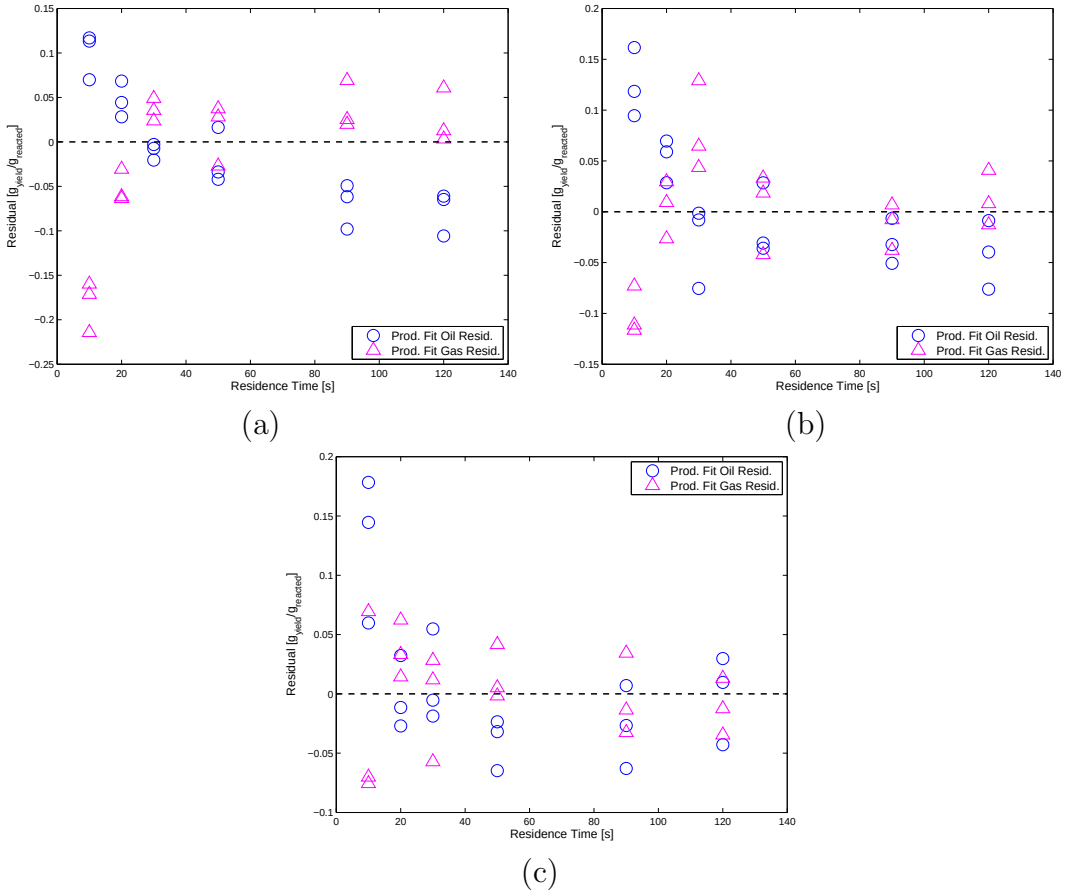

Figure 4.19: Product based model oil and gas yield residuals for reactor temperatures of: (a) 400°C (b) 410°C (c) 420°C (NOTE: y-axis ranges change between plots)

4.9 Discussion

The over prediction at higher temperatures and low residence times, within the single component and two component models, is possibly a product of continued reaction after pyrolysis products are removed from the reaction plate surface. If the residual solids are not cooling fast enough, as there was no active cooling implemented for the solids, the solids should continue to pyrolyze and produce some gaseous product during cooling. This would also help to explain the higher variability and non-uniform gas yield trends, shown in Figures 4.16 -4.18 for the product based model fits, in which the gas yield at lower residence times and higher temperatures first decreases before increasing.

A slight decrease in final yield as temperatures decreased from 400°C was observed. This follows the expected trend, based upon analysis of TGA data from Loblolly pine. Examination of the TGA derivative plot shown in Figure 6.13 shows that a turning point for the rate of mass loss exists around 380°C. Consequently, any deviation in temperature below that point would result in a rapidly decreasing rate of mass loss. This was observed in the decreasing final volatile yields (and simultaneous increasing char yields) at final residence times shown in Table 4.5. Overall, this confirms that the tested reaction temperatures are operating on a lower bound for complete conversion of the biomass, as was targeted.

The global fit residuals plots (Figure 4.15) show the same trend as observed within the individual single and two component models, that the symmetry of the residuals plots improves significantly with the addition of a second component. Residual results also show that at 410 and 420°C some low residence time data is not fully captured by the model nor are the 50 and 90 second data points well characterized for the 390°C reactor temperature results. High temperature and low residence time deviations are explicable by the previously discussed continuation of pyrolysis after solids removal from the reactor. Deviation in the predicted and experimental low temperature and

high residence time yields may be a result of operation near the aforementioned corner on the TGA derivative plot.

The decrease in yields from 90-120 second residence times at reactor temperatures of 410 and 420°C indicates a possible source of error. It is implausible that the actual yield would decrease, or as was actually measured, the amount of residual solids would increase, as the residence time increases. The 120 second residence time tests were part of the end of the testing matrix shown in Table 4.3 which could indicate a system variation. This would not be perceptible within the neighboring tests at 10 second residence times because those measurements were at the point of steepest ascent measured on the yield versus time curves. Nor would it be visible within the 380 and 390°C 300 second residence time tests because the pyrolysis was still far from completion at the preceding residence time measurement of 120 seconds. Consequently it is indeterminate but possible that system drift occurred.

4.10 Summary

Three different bulk pyrolysis models were presented, applied to fast pyrolysis experimental results and evaluated using a χ^2 goodness of fit parameter. Global best fit kinetic parameters were solved for using a particle swarm optimization algorithm and confidence intervals evaluated using an F-test. Kline-McClintoch instrumental error propagation estimations were presented for the pyrolysis yields.

The single component and two component bulk pyrolysis models were fit to both individual temperature results and the global set of temperature results. The fits in both cases demonstrated that the lower reactor temperatures tested (380 and 390°C) were not predicted well by the single component model but were well predicted by the two component model. Evaluation of the individual temperature fits shows that the single component model predictions improve significantly with the increase in temperature from 380 to 420°C and that the two component model converges to

the same goodness of fit as the single component model over the same temperature range. This means that as reactor temperatures increase single component models may provide predictions of the same quality as more complex kinetic schemes.

Residuals plots for the single and two component fits showed that the lowest residence time data (10s) was not fully captured using either model. This may be the result of continued reactions within the pyrolysis solids after removal from the reactor, which would also explain the unexpected gas yield trend for residence times $\leq$ 30s at reactor temperatures of 410 and 420°C. Overall, the two component global model showed a significantly better fit than the single component global model with a final reduced χ^2 value of 3.65.

The three temperature fit kinetic parameter results (using data from $400-420$°C) were implemented for the prediction of char production within the product based model based upon the superior fit of the single component model at higher temperatures. The product based model results showed a reduced χ^2 value of 11.6 for the oil and gas fits using the global single component three temperature fit.

Instrumental error propagation evaluation resulted in an average instrumentally induced deviation of 1.59% across all yields and instrumental error standard deviations of 1.71%, 0.73% and 2.26% for the oil, solid and gas yields respectively.

CHAPTER 5

INVESTIGATION OF KINETICS OF PSEUDO-COMPONENT BASED REACTION MECHANISMS

5.1 Introduction

In this chapter two pseudo-component based pyrolysis models will be evaluated. First, a superposition model of cellulose, hemicellulose and lignin will be presented. Second, a modified pseudo-component superposition model will be presented for which an intermediate solid compound is formed from the individual components along with the volatiles. This compound then pyrolyzes into volatiles and char. The pyrolysis of Avicel cellulose and Beechwood xylan is presented including the experimental bounding, experimental structure, and summary of the results. Kinetic parameters are then fit to cellulose and xylan assuming a single component reaction mechanism. Pseudo-component superposition is evaluated for the estimation of lignin parameters and the presence of component interactions is experimentally investigated. The global best fit of the pseudo-component and pseudo-component intermediate compound models is then evaluated against the whole wood Loblolly pine experimental pyrolysis results.

5.2 Salient Literature

Pseudo-component models are of particular interest because these models treat the individual constituents of biomass as independent pyrolyzing entities. The three fundamental biomass pseudo-components are cellulose, hemicellulose and lignin, which all woody cellulosic biomass is composed of in varying proportions. Consequently, modeling on the basis of these three compounds is viewed as a potentially widely

applicable generalized approach to biomass pyrolysis.

In 1971 Shafizadeh and McGinnis [77] presented the thermogravimetric analysis (TGA) and differential thermal analysis (DTA) of cotton wood and its extracted components and qualitatively evaluated the results. The authors concluded from qualitative analysis of the results that whole cottonwood DTA reflects the thermal behavior of its individual components. It was also noted that lignin is the dominant contributor to char and that the carbohydrates (cellulose, xylan and mannan were identified in this work) are the sources of the volatile products (oils and gases).

In 1985 Ward and Braslaw [19] formulated one of the earlier pseudo-component kinetic models by testing wild cherry wood and acid separated lignin using a TGA oven and an electric tube furnace. Cellulose kinetics were taken from a previously published study and hemicellulose kinetics were inferred by difference (*i.e.* the volatilization not accounted for by cellulose and lignin pyrolysis predictions). Both lignin and hemicellulose were modeled as three step consecutive reactions while cellulose was modeled as a single step. The model results were used to estimate wood compositions by fitting the pseudo-components to whole wood pyrolysis results. This study demonstrated an early attempt at using pseudo-component pyrolysis mechanisms in a summative independent parallel pyrolysis model, though not in a robust predictive way.

Bilbao *et al.* [78, 79] investigated the pyrolysis of xylan and lignin for the prediction of *Pinus pinaster* and barley straw pyrolysis on a pseudo-component basis with cellulose kinetics taken from literature. Xylan and lignin experimental data was gathered using a TGA oven at heating rates of 0.025, 0.33 and 1.33°C/s (1.5, 20 and 80°C/min). Pseudo-component fits showed only qualitatively good agreement with the data. The predicted conversion of *Pinus pinaster* showed modest agreement with the experimental results while the predicted conversion of barley straw showed very poor agreement with the experimental results. The fits were improved,however, with decreasing heating rate.

Varhegyi *et al.* [80] investigated the pyrolysis of cellulose and hemicellulose utilizing a TGA oven with a 0.17°C/s heating rate for the purpose of deriving kinetic descriptors. Modeling curves were fit to the TGA derivative curves using a least squares fit and results showed that cellulose can be well described by a single reaction kinetic scheme, whereas the hemicellulose samples tested showed a best fit to the TGA data with a two component sequential kinetic scheme. Five models were fit to the TGA results: single reaction model (Arrhenius), independent parallel reactions, competitive reactions, successive reactions, combined independent, and successive reactions. Least squared error best fit results showed that independent parallel reaction and successive reaction models gave nearly identical fits with similar kinetic parameters while overall cellulose was best fit with a single component model.

Antal and Varhegyi [81] investigated the validity of intermediate compounds in sequential pyrolysis models for cellulose using a TGA oven at heating rates from $0.033 - 1.3$°C/s ($2 - 80$°C/min). A thorough discussion of the history of cellulose pyrolysis kinetics was presented and published results compared to experimental results from Avicel cellulose. The authors concluded that despite the apparent complexity of cellulose pyrolysis, its decomposition is well described by a simple first order single component kinetic model with a high activation energy of 238kJ/mol. Additionally, lower activation energies reported from higher heating rate studies were attributed to thermal lag within the sample with respect to the reported oven temperatures.

Milosavljevic and Suuberg [20] studied the pyrolysis of cellulose specifically with respect to the impact of heating rate and final reactor temperature. Experiments were performed using a standard TGA oven with testing at both constant heating rate and ramp and hold conditions. Constant heating rate tests were performed at rates between 0.0015 and 0.016°C/s ($0.092 - 0.93$°C/min). Ramp and hold tests were performed in two sets with target temperatures between 265 and 375°C with heating rates between 0.017 and 1°C/s ($1 - 60$°C/min). Single component global models

were fit to the experimental results. The authors concluded that higher heating rate experiments which reached reactor temperatures above $\sim 325°C$ gave lower activation energies (140-155kJ/mol) while experiments at lower reactor temperatures gave a much higher activation energy of approximately 218kJ/mol.

Varhegyi *et al* [82] also used a TGA oven to investigate the effects of heating rate on cellulose pyrolysis and derive xylan and lignin kinetic parameters at heating rates between 0.033 and 1.33°C/s ($2-80°C$/min). Xylan from Beechwood was used to characterize hemicellulose pyrolysis. Competitive, successive and independent parallel reactions were evaluated for model fits with the model of successive reactions showing the best fit and agreement over all the tested heating rates. When pyrolyzing milled wood lignin the resultant activation energies were both low and over a broad range (34-65kJ/mol) with pre-exponential factors from $10^{0.3} - 10^{3}$. The authors attribute the cellulose activation energy ranges observed by Milosavljevic and Suuberg [20] to heat transfer limitations. An additional set of TGA experiments was used to check this with heating rates between 0.03 and 0.83°C/s and very small initial sample masses (0.3-0.5mg). The curve fits showed good agreement with a common activation energy of 240kJ/mol while the pre-exponential factor was allowed to vary from $10^{18.5} - 10^{18.1}$. Further cellulose tests demonstrated that a successive reaction scheme (using an intermediate component) appeared to collapse into a single component at higher heating rates. The authors attributed this to differing limiting reaction steps as pyrolysis temperatures increased.

Grønli *et al.* [67] conducted a thorough kinetic derivation study on four hardwoods, five softwoods and five lignin samples using a TGA oven at heating rates of 0.083°C/s (5°C/min). The lignin samples were chemically isolated from Beechwood, Redwood (using two different methods), Douglas Fir, and *Pinus pinea*. Results showed a fairly consistent pyrolysis behavior for the lignin samples (at least qualitatively) from which a common activation energy for lignin was approximated.

Using known cellulose and hemicellulose compositions of the nine wood samples a five component conversion model was fit to each TGA curve which included two departure function components. Best fit common activation energies were found and pre-exponential factors were allowed to vary between species. Results showed, however, that the pre-exponential factors experienced little variability despite the differences in component proportionality between species and the structural differences between softwoods and hardwoods.

Manyà *et al.* [83] utilized a TGA oven to pyrolyze sugarcane bagasse, mixed softwood waste, Kraft alkali lignin and Avicel cellulose at heating rates of $0.083 - 0.33$°C/s ($5 - 20$°C/min). Cellulose pyrolysis was used as a benchmark to evaluate the TGA oven performance with respect to previously published studies and showed good agreement. Lignin pyrolysis was used to determine a suitable reactor order for modeling its decomposition. The best fit model included first order Arrhenius models for both hemicellulose and cellulose and a third order Arrhenius model for lignin. Kinetic parameter values were determined by using a non-linear least squares method and showed good agreement between both the sugarcane bagasse and waste wood values.

Branca *et al.* [66] evaluated pseudo-component based as well as single and two component global models using a TGA oven at heating rates of $0.05 - 1.8$°C/s ($3 - 108$°C/min). The pseudo-component based model used TGA derived kinetics from the previously mentioned study by Grønli *et al.* [67] as well as best fit components to the experimental results as a comparison. The single component global model used two sets of kinetic parameters taken from literature, one with a high activation energy and one with a low activation energy. The two component model simply added an additional component to the single component model and separated the two according to cellulose+lignin and hemicellulose. Results showed that the pseudo-component model from literature only fit the heating rate conditions for which the

kinetic parameters were derived and deviated significantly at higher heating rates. The best fit coefficients based upon the experimental results showed good agreement amongst all tested temperatures. Overall, the pseudo-component and two component models provided nearly equivalent fits with much poorer fits obtained using the single component model.

Ramiah [84] utilized a TGA oven with an integrated differential thermal analyzer (DTA) to investigate the thermal degradation of isolated cellulose, hemicellulose and lignin at a heating rate of 0.07°C/s (4°C/min). Four isolated cellulose sample types were investigated (Avicel P_2, Cellulose R, Cellulose ICR-1 and Cellulose ICR-3), two types of hemicellulose (Birch xylan and Douglas Fir glucomannan) and two types of lignin (Spruce Periodate lignin and Douglas Fir Klason lignin). The results indicated that cellulose pyrolysis is an endothermic process followed by an exothermic process while both xylan and lignin degradation are dominantly exothermic processes. It was also confirmed that impurities in cellulose samples significantly affect the thermal analysis curves.

Yang *et al.* [85] tested fibrous cellulose, alkali lignin and Birchwood xylan (representative of hemicellulose) individually and in varying ratio mixtures in a TGA oven. The purpose was to evaluate the interactions between components in a pseudo-component superposition model. Biomass samples were then synthesized with varying proportions of each component between 0 and 100% by weight. The oven heating rate utilized was 0.17°C/s (10°C/min). The authors concluded that the pyrolysis of the component mixtures demonstrated negligible interactions and can be modeled as independent superimposed reactions. Deviations that do exist between superposition predictions and actual biomass pyrolysis were attributed to the presence of minerals. Though not explicitly stated, the implication is that the minerals have a catalytic effect.

Hosoya *et al.* [86] investigated cellulose-hemicellulose and cellulose-lignin interactions at an 800°C reaction temperature. To achieve higher heating rates than a TGA oven, a glass tube pre-loaded with the sample to be pyrolyzed was loaded into a pre-heated cylindrical oven. Mixtures of cellulose and xylan, cellulose and glucomanna, and cellulose and lignin were mixed in 2:1 ratios. Experimental results indicated that cellulose-hemicellulose interactions were not significant but that cellulose-lignin interactions resulted in decreased char yields and a shift in the solubility of the produced oils to a higher water soluble content. This shift indicates significant impacts upon the chemical composition of the produced oils.

Couhert *et al.* [87] also investigated the pyrolysis of cellulose, hemicellulose, and lignin individually and as mixtures of varying ratios. Gas compositions were quantitatively determined via gas chromatography (GC) and fourier transform infrared (FTIR) analysis and the ability to predict gaseous component outcome based upon component ratios was tested. Actual samples of Beechwood and a spruce/fir mix were tested for the evaluation of pseudo-component superposition predictions. It was found that the predicted gas products were very far from the measured outcomes.

5.3 Pseudo-Component Model Structures

The two pseudo-component model structures to be evaluated are shown in Figure 5.1. These are selected based upon literary precedent and, in theory, they offer the potential of providing robust, widely applicable predictive pyrolysis kinetic models. Within both models the reactions are assumed to be parallel and non-competing.

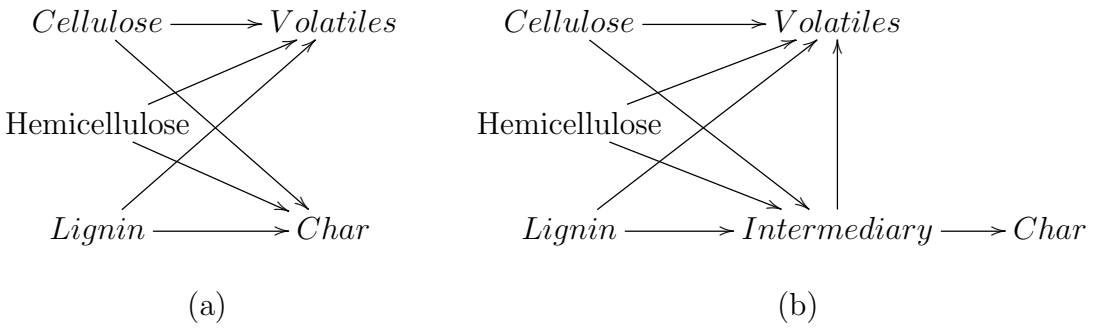

Figure 5.1: Pyrolysis model diagrams: (a) Pseudo-component (b) Intermediate solid

5.3.1 Pseudo-Component Based Model

The pseudo-component based model accounts for the simultaneous pyrolysis of cellulose, hemicellulose and lignin and subsequently requires three times as many Arrhenius kinetic terms as the single component global model. In 1985 Ward and Braslaw [19] formulated one of the earliest pseudo-component models by testing wild cherry wood and acid separated lignin using a TGA oven. Cellulose kinetics were taken from a previously published study and hemicellulose kinetics were inferred by difference. For the derivation of these parameters the following two assumptions will be made: 1. The pyrolysis reactions are independent and occur simultaneously (in parallel); 2. All extractives and ash can be lumped into the lignin pyrolysis term. The independent parallel reaction assumption allows for the estimation of the lignin pyroylsis behavior when two of the three component behaviors (cellulose and hemicellulose) can be accounted for along with whole wood pyrolysis. The estimation of lignin's pyrolysis behavior is necessary because the micro-reactor cannot effectively process lignin due to its phase change upon heating. Additionally, the estimation by difference allows for the lignin term to work as a departure function and allows for the second assumption to be applied (inclusion of extractives). The model is graphically depicted in Figure 5.1a.

The separation of carbohydrates into cellulose and hemicellulose was based upon

work by Navarro *et al.* [88] which states that cellulose is only anhydrous glucose and subsequently the remaining carbohydrates (xylose, mannose, galactose, rhamnose and arabinose) constitute hemicellulose. This convention is used here and the hemicellulose carbohydrate pyrolysis will be simulated by the pyrolysis of xylan derived from Beechwood. Xylan is frequently used as a representative of hemicellulose as a whole because it is either the first or second most abundant carbohydrate within wood by weight (amongst the hemicellulloses) and it is readily extractable. [89, 90, 87, 16, 48]

Volatilization rates for both the Avicel cellulose and Beechwood xylan are fitted with global single component models and kinetic parameters derived according to the method detailed in Equations 4.1 - 4.3. The predicted yield values (gas + oil) for each tested residence time and reactor temperature combination are subtracted from the corresponding whole wood experimental yield results as shown in Equation 5.1,

$$\phi_{lig}\eta_{lig}(t) = \eta_{wood}(t) - \phi_{cell}\eta_{cell} - \phi_{hemi}\eta_{xyl} \tag{5.1}$$

where ϕ indicates the fraction by mass of each component and subscripts lig, $cell$, $hemi$ and xyl refer to lignin, cellulose, hemicellulose and xylan respectively. Fractions of cellulose, hemicellulose and lignin were taken from published chemical compositions of Loblolly pine: $\phi_{cell} = 0.45$, $\phi_{xyl} = 0.26$, and $\phi_{lig} = 0.29$. [91]

The application of these coefficients, as they are from non-competing parallel reactions, is then similar to that for the global two component model of Section 4.3.2 but with three summed terms instead of two. The char and volatiles formation are predicted by in Equations 5.2 and 5.3.

$$\begin{aligned}\eta_c(t) =& \phi_{cell}c_{c,cell}\left(1 - \frac{1}{2}^{tk_{cell}(T)/\ln 2}\right) + \phi_{hemi}c_{c,xyl}\left(1 - \frac{1}{2}^{tk_{xyl}(T)/\ln 2}\right) \\ &+ \phi_{lig}c_{c,lig}\left(1 - \frac{1}{2}^{tk_{lig}(T)/\ln 2}\right)\end{aligned} \tag{5.2}$$

$$\eta_v(t) = \phi_{cell} c_{v,cell} \left(1 - \frac{1}{2}^{tk_{cell}(T)/\ln 2}\right) + \phi_{hemi} c_{v,xyl} \left(1 - \frac{1}{2}^{tk_{xyl}(T)/\ln 2}\right) + \phi_{lig} c_{v,lig} \left(1 - \frac{1}{2}^{tk_{lig}(T)/\ln 2}\right) \tag{5.3}$$

5.3.2 Intermediate Solid Model

Several previous studies have looked at the insertion of an intermediary for the improvement of model fits. [24, 80, 92] Typically this intermediary is represented by a solid compound which further reacts to form the final char and additional volatiles. The model schematic is given in Figure 5.1b.

Within the intermediary model the rate of formation of the final volatiles occurs according to Equation 5.4,

$$\frac{\partial \eta_v}{\partial t} = \phi_{cell} \frac{\partial \eta_{cell}}{\partial t} + \phi_{hemi} \frac{\partial \eta_{xyl}}{\partial t} + \phi_{lig} \frac{\partial \eta_{lig}}{\partial t} + k_I \eta_I \tag{5.4}$$

where k_I is the rate at which the intermediary compound pyrolyzes. Integration of the equation to determine η_v as a function of time, however, requires that η_I be known. The rate at which η_I is produced is given by Equation 5.5,

$$\frac{\partial \eta_I}{\partial t} = \phi_{cell} \frac{1 - c_{cell}}{c_{cell}} \frac{\partial \eta_{cell}}{\partial t} + \phi_{hemi} \frac{1 - c_{xyl}}{c_{xyl}} \frac{\partial \eta_{xyl}}{\partial t} + \phi_{lig} \frac{1 - c_{lig}}{c_{lig}} \frac{\partial \eta_{lig}}{\partial t} - k_I \eta_I \tag{5.5}$$

The terms $(1 - c_i)/c_i$ are the ratio of component i's produced char to produced volatiles. The ratios are required to evaluate the formation of char from the η values which give the total volatiles production as a function of time. The solution to Equation 5.5 is found by solving for both the particular and general solutions to the ODE. The particular component and its solution is given in Equations 5.6 and 5.7,

$$\frac{\partial \eta_{I,pt}}{\partial t} = \phi_c \frac{1-c_c}{c_c}\frac{\partial \eta_c}{\partial t} + \phi_x \frac{1-c_x}{c_x}\frac{\partial \eta_x}{\partial t} + \phi_L \frac{1-c_L}{c_L}\frac{\partial \eta_L}{\partial t} \tag{5.6}$$

$$\eta_{I,pt} = \phi_c \frac{1-c_c}{c_c}\eta_c + \phi_x \frac{1-c_x}{c_x}\eta_x + \phi_L \frac{1-c_L}{c_L}\eta_L + C_1 \tag{5.7}$$

where C_1 is the integration constant and the η_i terms are according to the pattern of Equation 4.1. The general solution is given in Equations 5.8 and 5.9,

$$\frac{\partial \eta_{I,gen}}{\partial t} = -k_v \eta_v \tag{5.8}$$

$$\eta_{I,gen} = C_2 e^{-k_I t} \tag{5.9}$$

where C_2 is the integration constant. The boundary conditions to solving for the constants are given in Equations 5.10 and 5.11,

$$\eta_I(t=0) = 0 \tag{5.10}$$

$$\eta_I(t \to \infty) = 0 \tag{5.11}$$

Solving for the constants C_1 and C_2 results in the final form of η_I given in Equation 5.12,

$$\begin{aligned}\eta_I =& \phi_c \frac{1-c_c}{c_c}\eta_c + \phi_x \frac{1-c_x}{c_x}\eta_x + \phi_L \frac{1-c_L}{c_L}\eta_L \\ &+ \left(e^{-k_I t} - 1\right)\left(\phi_c(1-c_c) + \phi_x(1-c_x) + \phi_L(1-c_L)\right)\end{aligned} \tag{5.12}$$

Equation 5.12 is then inserted into Equation 5.4 for the partial of η_v. Integrating this and applying the initial condition that $\eta_I(t=0) = 0$ results in Equation 5.13,

$$\begin{aligned}\eta_v \;=\; & \phi_c\eta_c + \phi_x\eta_x + \phi_L\eta_L + k_I c_I \Bigg(\phi_c(1-c_c)\left(\frac{e^{-k_c t}}{k_c} + t\right) + \phi_x(1-c_x)\left(\frac{e^{-k_x t}}{k_x} + t\right) \\ & + \phi_L(1-c_L)\left(\frac{e^{-k_L t}}{k_L} + t\right) + \left(-\frac{e^{-k_I t}}{k_I} - t\right)\left(\phi_c(1-c_c) + \phi_x(1-c_x) + \phi_L(1-c_L)\right)\Bigg) \\ & - c_I k_I \Bigg(\phi_c(1-c_c)\frac{1}{k_c} + \phi_x(1-c_x)\frac{1}{k_x} + \phi_L(1-c_L)\frac{1}{k_L} \\ & - \frac{1}{k_I}\left(\phi_c(1-c_c) + \phi_x(1-c_x) + \phi_L(1-c_L)\right)\Bigg)\end{aligned} \tag{5.13}$$

where the k terms are of the form given in Equation 4.3. The equation allows for twelve unknowns: c, E, and A for each component. To provide some bounding to the solution the c_{cell} and c_{xyl} values will be interposed from the psuedo-component based model solution.

5.4 Experimental Bounding

Within this work single component models were pursued for cellulose and xylan characterization and consequently less information needed to be extracted from the cellulose and xylan tests. As such, only three residence times were tested: the lowest (10s), the highest (120s) and a point in between (30s) with the intent of capturing some of the curvature of the volatilization versus time plot.

Initial tests for cellulose and xylan were performed at 410°C and results indicated that pyrolysis was occurring too rapidly for the progression of the reaction to be observed. Determination of suitable lower temperatures for the pyrolysis of cellulose and xylan required published kinetics to be used for bounding predictions. Examination of published kinetic parameters in cellulose pyrolysis shows a wide range of activation energies (pre-exponential terms are less often considered in comparison studies). Milosavljevic [20] attributes the variations to two pyrolysis regimes, one at lower temperatures and one at higher temperatures, as a result of heating rates. Antal, [22] however, attributes the variations to thermal lag within the TGA systems commonly utilized, temperature measurement error, and differences in cellulose samples (Antal noted up to a 30°C shift in TGA curves based upon the source of the cellulose). The thermal lag effect within TGA ovens was reported to be significantly more prominent at higher heating rates, as should be expected.

Cellulose pyrolysis kinetic approximations for experimental bounding were taken from work by Di Blasi and Lanzetta. [25] The system utilized was a radiantly heated

oven which achieved heating rates between $19 - 56°C/s$ which qualifies it as a fast pyrolysis device. Additionally, the authors performed temperature verification tests for the system as well as thermal lag experiments to ensure the temperature gradients within the sample were minimized. Sigma Aldrich Avicel cellulose was tested which is expected to be very similar to the GFC Avicel cellulose that will be utilized in the micro-reactor tests. This is in contrast to Whitman cellulose filter paper that is sometimes used for cellulose pyrolysis tests.

Xylan pyrolysis kinetic approximations were based upon kinetics experimentally derived by Lanzetta and Di Blasi. [24] Their kinetic parameters were derived using the same methodologies as those used in the cellulose derivation in reference [25]. Lanzetta and Di Blasi did, however, conclude that Xylan decomposes in two consecutive reactions, the first of which forms both volatiles and an intermediary species while the second reacts only the intermediary species following its complete formation. Both of these reactions were modeled within a predictive simulation for test parameter determination.

Reactor temperatures for cellulose and xylan were selected at 350, 360 and 370°C. Additionally, the reactor temperature of 340°C was added to the xylan experimental design midway through testing. This precautionary measure was taken because initial results at 370°C indicated that xylan pyrolysis may be occurring too quickly to be observed using the determined residence times. Final results showed that in fact the change in residual solids mass was observable (though small) and as a consequence the xylan results have a higher data resolution than the cellulose results with four tested reactor temperatures instead of three.

The cellulose and xylan operating temperatures and residence times are given in Table 5.1. All experiments were randomized and as previously noted the 340°C xylan tests were introduced into a re-randomized matrix mid-way through the cellulose and xylan testing.

Table 5.1: Selected operating temperatures and residence times for cellulose and xylan fast pyrolysis experimentation

Species	Residence Time [s]	Reactor Temperature [°C]
Beechwood Xylan	10, 30, 120	340, 350, 360, 370
Avicel Cellulose	10, 30, 120	350, 360, 370
50/50 & 60/40 mixtures	15, 45, 135	350, 410

Verification tests for the impact of pseudo-component mixtures were conducted by testing 50/50 and 60/40 cellulose/xylan mixtures. These were tested at 350 and 410°C to correspond to temperatures in the middle of the temperature ranges for which the pseudo-components themselves were tested and the Loblolly pine was tested. Residence times of 15, 45 and 135 seconds were selected so as to not directly correspond with residence times for which the species were derived. A summary of these settings is contained in Table 5.1.

5.5 Sample Preparation and Experimental Structure

The pseudo-component based model will utilize commercially obtained cellulose and xylan samples. Lignin will be approximated by difference using the component results and the bulk wood results from Loblolly pine. Avicel cellulose samples were obtained from Sigma-Aldrich and Beechwood xylan obtained from GFC Chemical. The randomized experimental test sequence utilized is given in Table 5.2.

An evaluation of pseudo-component superposition will be performed on a mixture of isolated cellulose and xylan. The samples were mixed in proportions of 50/50 and 60/40 (cellulose/xylan) and prepared in 10g batches. The combined components were added to a plastic mixing tube along with 17 stainless steel ball bearings which varied in size from 1/8" diameter to 1/4" diameter. The samples were mixed by placing the mixing tube inside a tumbler at 46rpm for a minimum of 3 hours. The ball bearings were then removed and the mixed samples stored within the desiccator. The measured masses of each component are contained in Table 5.3 along with the exact mass ratios,

which indicate that nearly perfect ratios were obtained. The mixture testing matrix is given in Table 5.4.

Table 5.2: Testing matrix for Avicel cellulose and Beechwood xylan pyrolysis tests at 340, 350, 360 and 370°C

Test	Species	Residence Time [s]	Reactor Temp [°C]	Test	Species	Residence Time [s]	Reactor Temp [°C]
1	Cellulose	30	370	33	Xylan	10	340
2	Xylan	30	350	34	Xylan	120	360
3	Cellulose	10	350	35	Xylan	10	370
4	Cellulose	120	350	36	Cellulose	10	350
5	Xylan	10	350	37	Cellulose	120	370
6	Xylan	30	370	38	Xylan	120	370
7	Cellulose	30	350	39	Xylan	30	340
8	Xylan	120	360	40	Xylan	120	340
9	Cellulose	10	360	41	Xylan	120	340
10	Cellulose	10	360	42	Xylan	30	340
11	Cellulose	10	370	43	Xylan	30	360
12	Xylan	10	370	44	Cellulose	30	350
13	Xylan	120	370	45	Xylan	120	350
14	Xylan	30	370	46	Cellulose	30	370
15	Cellulose	30	360	47	Xylan	30	340
16	Xylan	120	350	48	Xylan	30	350
17	Xylan	30	370	49	Cellulose	30	350
18	Xylan	30	360	50	Cellulose	30	360
19	Cellulose	120	350	51	Cellulose	10	360
20	Cellulose	10	370	52	Xylan	10	350
21	Xylan	10	350	53	Cellulose	10	350
22	Cellulose	120	370	54	Xylan	120	350
23	Xylan	30	350	55	Cellulose	120	370
24	Xylan	10	360	56	Cellulose	120	350
25	Cellulose	30	360	57	Xylan	10	360
26	Cellulose	30	370	58	Cellulose	120	360
27	Xylan	120	340	59	Cellulose	120	360
28	Xylan	30	360	60	Xylan	10	370
29	Xylan	120	360	61	Cellulose	10	370
30	Xylan	10	340	62	Cellulose	120	360
31	Xylan	10	340	63	Xylan	120	370
32	Xylan	10	360				

Table 5.3: Exact compositions and ratios of targeted 50/50 and 60/40 cellulose/xylan mixtures

	50/50 mix	60/40 mix
Avicel cellulose [g]	5.0001	6.0032
Beechwood xylan [g]	5.0026	4.0013
Exact Ratio c/x	49.975/50	60.013/40

Table 5.4: Testing matrix for Avicel cellulose and Beechwood xylan mixtures (cellulose/xylan) pyrolysis tests at 350 and 410°C

Test	Species	Residence Time [s]	Reactor Temp [°C]	Test	Species	Residence Time [s]	Reactor Temp [°C]
1	50/50	135	350	19	60/40	45	410
2	50/50	45	410	20	50/50	45	410
3	60/40	15	350	21	60/40	15	410
4	50/50	15	410	22	60/40	135	410
5	60/40	45	350	23	60/40	15	350
6	60/40	135	350	24	60/40	135	410
7	60/40	45	410	25	60/40	15	350
8	50/50	45	350	26	60/40	45	350
9	50/50	15	350	27	60/40	45	350
10	50/50	15	350	28	50/50	15	410
11	60/40	45	410	29	60/40	135	350
12	50/50	135	350	30	50/50	135	410
13	60/40	135	350	31	50/50	45	410
14	50/50	45	350	32	50/50	135	350
15	50/50	45	350	33	50/50	135	410
16	60/40	135	410	34	50/50	135	410
17	50/50	15	350	35	50/50	15	410
18	60/40	15	410	36	60/40	15	410

5.6 Experimental Yields

The calculated pyrolysis yields from the cellulose, xylan and mixture tests are given in Tables 5.5-5.8. The tabulated results show the expected trends with the exception of a reported negative yield for Avicel cellulose oil at a 10 second residence time and 350°C reactor temperature. This seemingly errant data point will be addressed within Section 5.9.

Table 5.5: Avicel Cellulose pyrolysis average product yields and standard deviations for 350, 360 and 370°C reactor temperatures with gas yields calculated by difference

350°C						
Residence Time [s]	$\bar{\eta}_o$ [g/g]	σ_o [g/g]	$\bar{\eta}_s$ [g/g]	σ_s [g/g]	$\bar{\eta}_g$ [g/g]	σ_g [g/g]
10	-0.007	1.70E-1	0.628	2.52E-2	0.379	1.45E-1
30	0.125	1.64E-1	0.440	8.54E-3	0.435	1.56E-1
120	0.395	1.49E-1	0.108	9.83E-3	0.497	1.49E-1
360°C						
Residence Time [s]	$\bar{\eta}_o$ [g/g]	σ_o [g/g]	$\bar{\eta}_s$ [g/g]	σ_s [g/g]	$\bar{\eta}_g$ [g/g]	σ_g [g/g]
10	0.189	2.96E-2	0.531	2.21E-2	0.279	2.90E-2
30	0.129	1.11E-1	0.305	3.09E-3	0.567	1.08E-1
120	0.313	7.54E-2	0.050	6.76E-3	0.637	7.56E-2
370°C						
Residence Time [s]	$\bar{\eta}_o$ [g/g]	σ_o [g/g]	$\bar{\eta}_s$ [g/g]	σ_s [g/g]	$\bar{\eta}_g$ [g/g]	σ_g [g/g]
10	0.180	1.40E-1	0.383	3.13E-2	0.437	1.10E-1
30	0.283	1.03E-1	0.139	1.99E-2	0.578	9.12E-2
120	0.335	6.98E-2	0.029	1.13E-2	0.636	7.14E-2

Table 5.6: Beechwood Xylan pyrolysis average product yields and standard deviations for 340, 350, 360 and 370°C reactor temperatures with gas yields calculated by difference

340°C						
Residence Time [s]	$\bar{\eta}_o$ [g/g]	σ_o [g/g]	$\bar{\eta}_s$ [g/g]	σ_s [g/g]	$\bar{\eta}_g$ [g/g]	σ_g [g/g]
10	0.146	6.56E-2	0.404	1.37E-2	0.450	6.12E-2
30	0.193	4.82E-2	0.328	8.39E-3	0.480	5.66E-2
120	0.262	2.19E-2	0.308	4.04E-3	0.431	1.80E-2
350°C						
Residence Time [s]	$\bar{\eta}_o$ [g/g]	σ_o [g/g]	$\bar{\eta}_s$ [g/g]	σ_s [g/g]	$\bar{\eta}_g$ [g/g]	σ_g [g/g]
10	0.339	1.25E-1	0.352	1.06E-2	0.309	1.34E-1
30	0.318	1.38E-1	0.297	4.26E-3	0.386	1.42E-1
120	0.319	5.60E-2	0.288	1.12E-2	0.393	4.66E-2
360°C						
Residence Time [s]	$\bar{\eta}_o$ [g/g]	σ_o [g/g]	$\bar{\eta}_s$ [g/g]	σ_s [g/g]	$\bar{\eta}_g$ [g/g]	σ_g [g/g]
10	0.293	3.85E-2	0.316	1.16E-2	0.391	5.02E-2
30	0.308	4.83E-2	0.284	2.24E-2	0.408	6.42E-2
120	0.335	1.34E-1	0.281	1.06E-2	0.383	1.43E-1
370°C						
Residence Time [s]	$\bar{\eta}_o$ [g/g]	σ_o [g/g]	$\bar{\eta}_s$ [g/g]	σ_s [g/g]	$\bar{\eta}_g$ [g/g]	σ_g [g/g]
10	0.355	1.11E-1	0.294	8.03E-3	0.351	1.18E-1
30	0.478	4.40E-2	0.284	8.98E-3	0.237	4.74E-2
120	0.377	1.30E-1	0.270	3.47E-3	0.353	1.32E-1

Table 5.7: Cellulose/Xylan 50/50 mix pyrolysis average product yields and standard deviations for 360 and 410°C reactor temperatures with gas yields calculated by difference

350°C						
Residence Time [s]	$\bar{\eta}_o$ [g/g]	σ_o [g/g]	$\bar{\eta}_s$ [g/g]	σ_s [g/g]	$\bar{\eta}_g$ [g/g]	σ_g [g/g]
15	0.165	3.15E-2	0.494	2.07E-2	0.340	1.51E-2
45	0.187	8.66E-2	0.431	1.14E-2	0.378	7.89E-2
135	0.303	5.65E-2	0.353	6.08E-3	0.344	5.80E-2
410°C						
Residence Time [s]	$\bar{\eta}_o$ [g/g]	σ_o [g/g]	$\bar{\eta}_s$ [g/g]	σ_s [g/g]	$\bar{\eta}_g$ [g/g]	σ_g [g/g]
15	0.472	6.89E-2	0.223	1.06E-2	0.305	6.78E-2
45	0.486	3.18E-2	0.212	3.21E-3	0.302	3.03E-2
135	0.537	2.20E-2	0.208	2.52E-3	0.255	2.45E-2

Table 5.8: Cellulose/Xylan 60/40 mix pyrolysis average product yields and standard deviations for 360 and 410°C reactor temperatures with gas yields calculated by difference

350°C						
Residence Time [s]	$\bar{\eta}_o$ [g/g]	σ_o [g/g]	$\bar{\eta}_s$ [g/g]	σ_s [g/g]	$\bar{\eta}_g$ [g/g]	σ_g [g/g]
15	0.037	2.11E-2	0.554	1.39E-2	0.409	3.51E-2
45	0.142	1.53E-2	0.465	3.61E-3	0.393	1.20E-2
135	0.275	4.69E-2	0.381	6.08E-3	0.344	4.14E-2
410°C						
Residence Time [s]	$\bar{\eta}_o$ [g/g]	σ_o [g/g]	$\bar{\eta}_s$ [g/g]	σ_s [g/g]	$\bar{\eta}_g$ [g/g]	σ_g [g/g]
15	0.496	1.56E-2	0.227	1.15E-2	0.277	1.95E-2
45	0.482	8.81E-2	0.200	4.93E-3	0.318	8.36E-2
135	0.443	6.56E-2	0.189	1.73E-3	0.368	6.59E-2

5.7 Kline McClintock Instrumental Error Analysis Results

The instrumental error associated with the calculated yields was estimated using the methodology presented in Section 3.5. Calculated uncertainties from the Avicel cellulose and Beechwood xylan experiments are given in Table 5.9 and the uncertainties as a percentage of the average yields are given in Table 5.10.

Table 5.9: Experimental measurement uncertainty results for Avicel cellulose and Beechwood xylan

Avicel Cellulose						
	350°C			360°C		
Residence Time [s]	$\Delta\eta_o$ [g/g]	$\Delta\eta_s$ [g/g]	$\Delta\eta_g$ [g/g]	$\Delta\eta_o$ [g/g]	$\Delta\eta_s$ [g/g]	$\Delta\eta_g$ [g/g]
10	7.94E-3	7.18E-3	1.07E-2	7.87E-3	5.93E-3	9.86E-3
30	8.47E-3	5.35E-3	1.00E-2	7.79E-3	3.48E-3	8.53E-3
120	8.70E-3	1.39E-3	8.81E-3	8.78E-3	9.87E-4	8.83E-3
	370°C					
Residence Time [s]	$\Delta\eta_o$ [g/g]	$\Delta\eta_s$ [g/g]	$\Delta\eta_g$ [g/g]			
10	7.68E-3	4.36E-3	8.83E-3			
30	7.67E-3	1.67E-3	7.85E-3			
120	9.35E-3	9.28E-4	9.40E-3			
Beechwood Xylan						
	340°C			350°C		
Residence Time [s]	$\Delta\eta_o$ [g/g]	$\Delta\eta_s$ [g/g]	$\Delta\eta_g$ [g/g]	$\Delta\eta_o$ [g/g]	$\Delta\eta_s$ [g/g]	$\Delta\eta_g$ [g/g]
10	6.43E-3	3.74E-3	7.44E-3	7.16E-3	3.35E-3	7.91E-3
30	6.98E-3	3.27E-3	7.70E-3	7.04E-3	2.84E-3	7.59E-3
120	7.44E-3	3.20E-3	8.10E-3	7.48E-3	2.97E-3	8.04E-3
	360°C			370°C		
Residence Time [s]	$\Delta\eta_o$ [g/g]	$\Delta\eta_s$ [g/g]	$\Delta\eta_g$ [g/g]	$\Delta\eta_o$ [g/g]	$\Delta\eta_s$ [g/g]	$\Delta\eta_g$ [g/g]
10	7.22E-3	3.12E-3	7.91E-3	7.09E-3	2.77E-3	7.91E-3
30	6.73E-3	2.63E-3	7.59E-3	7.01E-3	2.44E-3	7.59E-3
120	7.05E-3	2.65E-3	8.04E-3	7.47E-3	2.67E-3	8.04E-3

Table 5.10: Experimental measurement uncertainty results for Avicel cellulose and Beechwood xylan as a percentage of yield

Avicel Cellulose						
	350°C			360°C		
Residence Time [s]	$\frac{\Delta\eta_o}{\eta_o}$ [%]	$\frac{\Delta\eta_s}{\eta_s}$ [%]	$\frac{\Delta\eta_g}{\eta_g}$ [%]	$\frac{\Delta\eta_o}{\eta_o}$ [%]	$\frac{\Delta\eta_s}{\eta_s}$ [%]	$\frac{\Delta\eta_g}{\eta_g}$ [%]
10	119	1.14	2.83	4.16	1.12	3.53
30	6.77	1.22	2.31	6.05	1.14	1.51
120	2.20	1.29	1.77	2.80	1.98	1.39
	370°C					
Residence Time [s]	$\frac{\Delta\eta_o}{\eta_o}$ [%]	$\frac{\Delta\eta_s}{\eta_s}$ [%]	$\frac{\Delta\eta_g}{\eta_g}$ [%]			
10	4.27	1.14	2.02			
30	2.71	1.21	1.36			
120	2.79	3.21	1.48			
Beechwood Xylan						
	340°C			350°C		
Residence Time [s]	$\frac{\Delta\eta_o}{\eta_o}$ [%]	$\frac{\Delta\eta_s}{\eta_s}$ [%]	$\frac{\Delta\eta_g}{\eta_g}$ [%]	$\frac{\Delta\eta_o}{\eta_o}$ [%]	$\frac{\Delta\eta_s}{\eta_s}$ [%]	$\frac{\Delta\eta_g}{\eta_g}$ [%]
10	4.42	0.93	1.65	2.11	0.95	2.56
30	3.62	1.00	1.61	2.22	0.96	1.97
120	2.84	1.04	1.88	2.34	1.03	2.05
	340°C			350°C		
Residence Time [s]	$\frac{\Delta\eta_o}{\eta_o}$ [%]	$\frac{\Delta\eta_s}{\eta_s}$ [%]	$\frac{\Delta\eta_g}{\eta_g}$ [%]	$\frac{\Delta\eta_o}{\eta_o}$ [%]	$\frac{\Delta\eta_s}{\eta_s}$ [%]	$\frac{\Delta\eta_g}{\eta_g}$ [%]
10	2.47	0.99	2.02	2.00	0.94	2.25
30	2.19	0.92	1.86	1.47	0.86	3.20
120	2.10	0.94	2.10	1.98	0.99	2.28

5.8 Component Based Pyrolysis Model Fits

5.8.1 Pseudo-Component Model Fits

The global single component fits for the pyrolysis of Avicel cellulose and Beechwood xylan are presented in Table 5.11. Plots of the best fit curves and experimental yield mean values with two standard deviation error bars are contained in Figures 5.2-5.8. Residual plots for the fitted cellulose and xylan curves are contained in Figures 5.9a-c and 5.10a-d, respectively. Graphically, both models capture the trends observed in the data with the exception of the 10 second residence time mean experimental yields for Avicel cellulose, which were underpredicted by 36%, 27% and 23% at reactor temperatures of 350, 360 and 370°C respectively.

Several published cellulose and xylan kinetic values from literature are contained

in Tables 5.12 and 5.13 for comparison to the model fit results.

Table 5.11: Avicel cellulose and Beechwood xylan single component global best-fit results

Component	c [g/g]		E_a [kJ/mol]		A [1/s]		χ^2	ν	χ^2_ν
Avicel Cellulose	0.947	$\pm$0.020	145	$\pm$0.3	4.52E10	$^{+0.26E9}_{-0.24E9}$	328	23	14.2
Beechwood Xylan	0.710	$\pm$0.009	107	$\pm$1	2.08E 8	$^{+0.59E8}_{-0.36E8}$	243	32	7.6

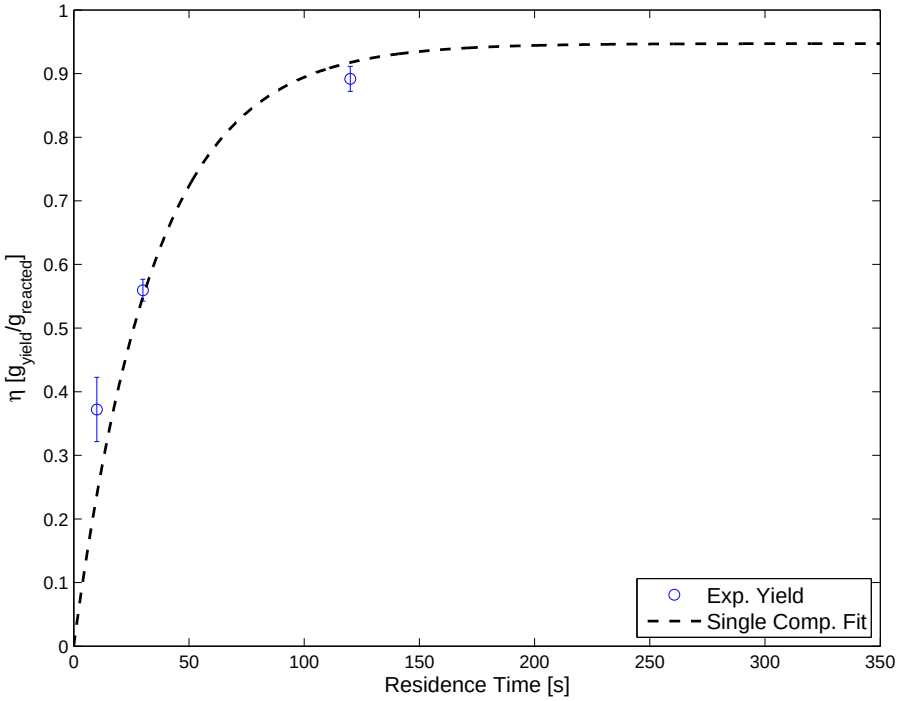

Figure 5.2: Avicel cellulose single component model global fit results plotted against 350°C experimental mean values with two standard deviation error bars

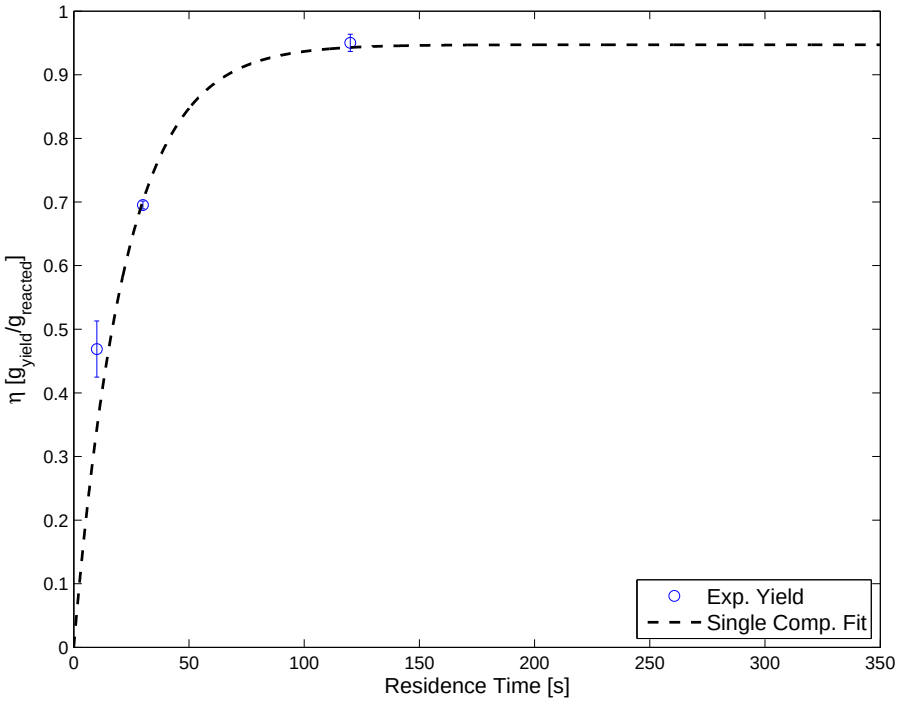

Figure 5.3: Avicel cellulose single component model global fit results plotted against 360°C experimental mean values with two standard deviation error bars

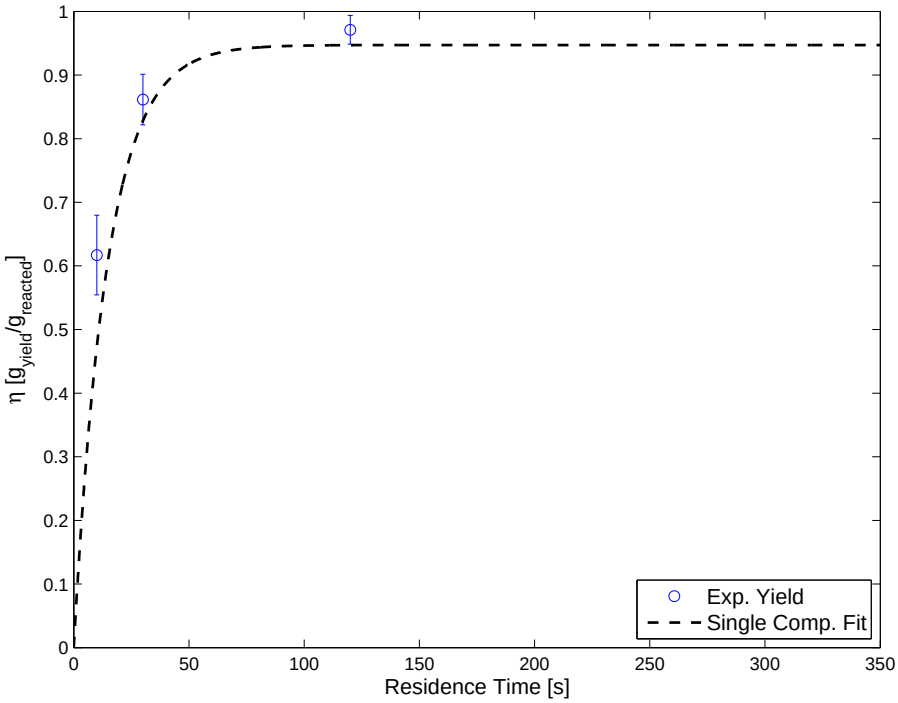

Figure 5.4: Avicel cellulose single component model global fit results plotted against 370°C experimental mean values with two standard deviation error bars

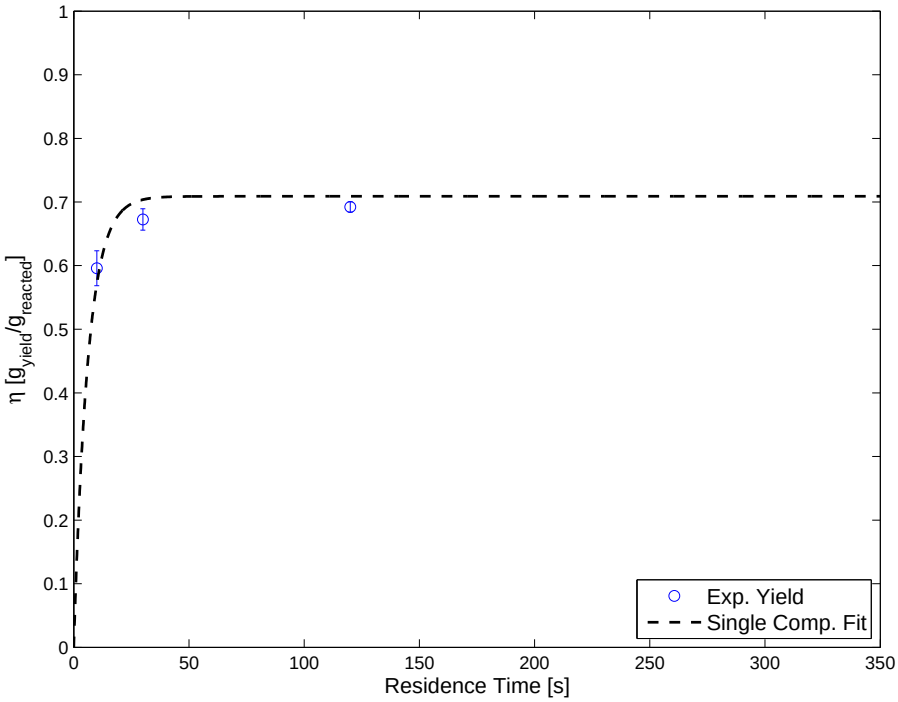

Figure 5.5: Beechwood xylan single component model global fit results plotted against 340°C experimental mean values with two standard deviation error bars

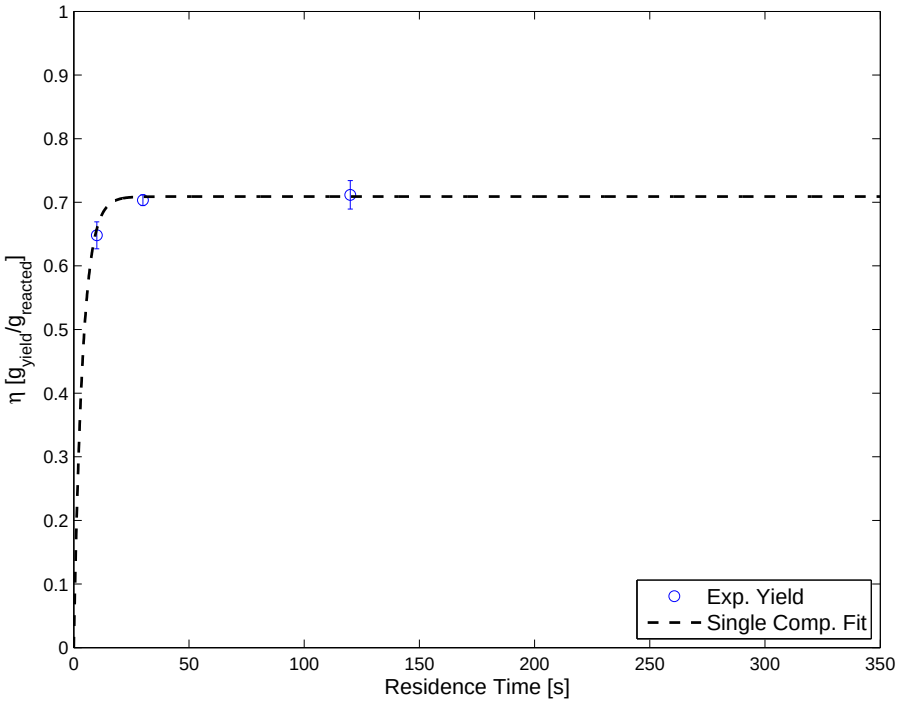

Figure 5.6: Beechwood xylan single component model global fit results plotted against 350°C experimental mean values with two standard deviation error bars

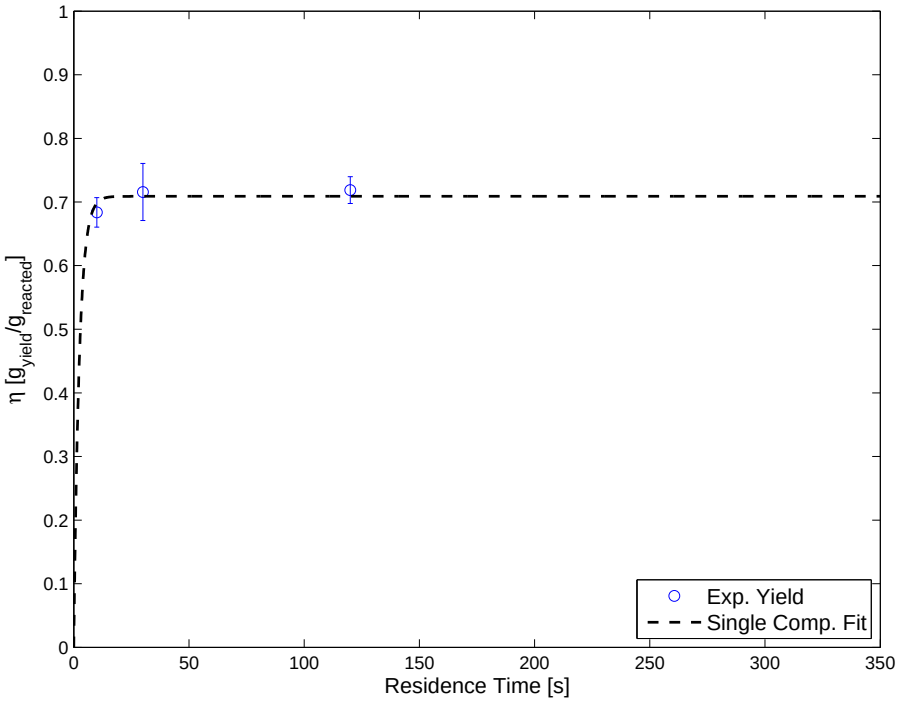

Figure 5.7: Beechwood xylan single component model global fit results plotted against 360°C experimental mean values with two standard deviation error bars

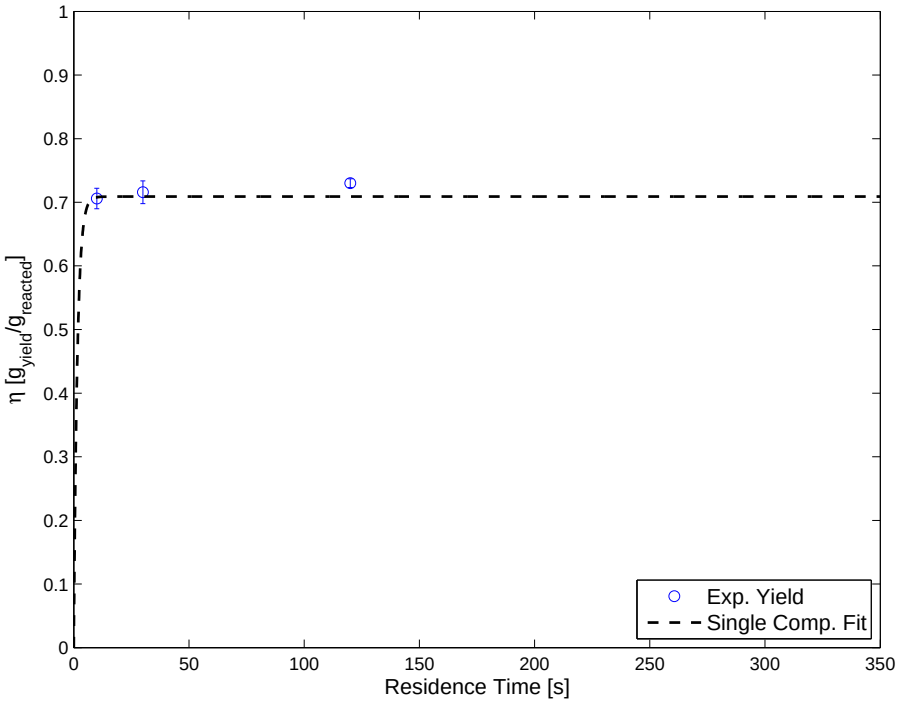

Figure 5.8: Beechwood xylan single component model global fit results plotted against 370°C experimental mean values with two standard deviation error bars

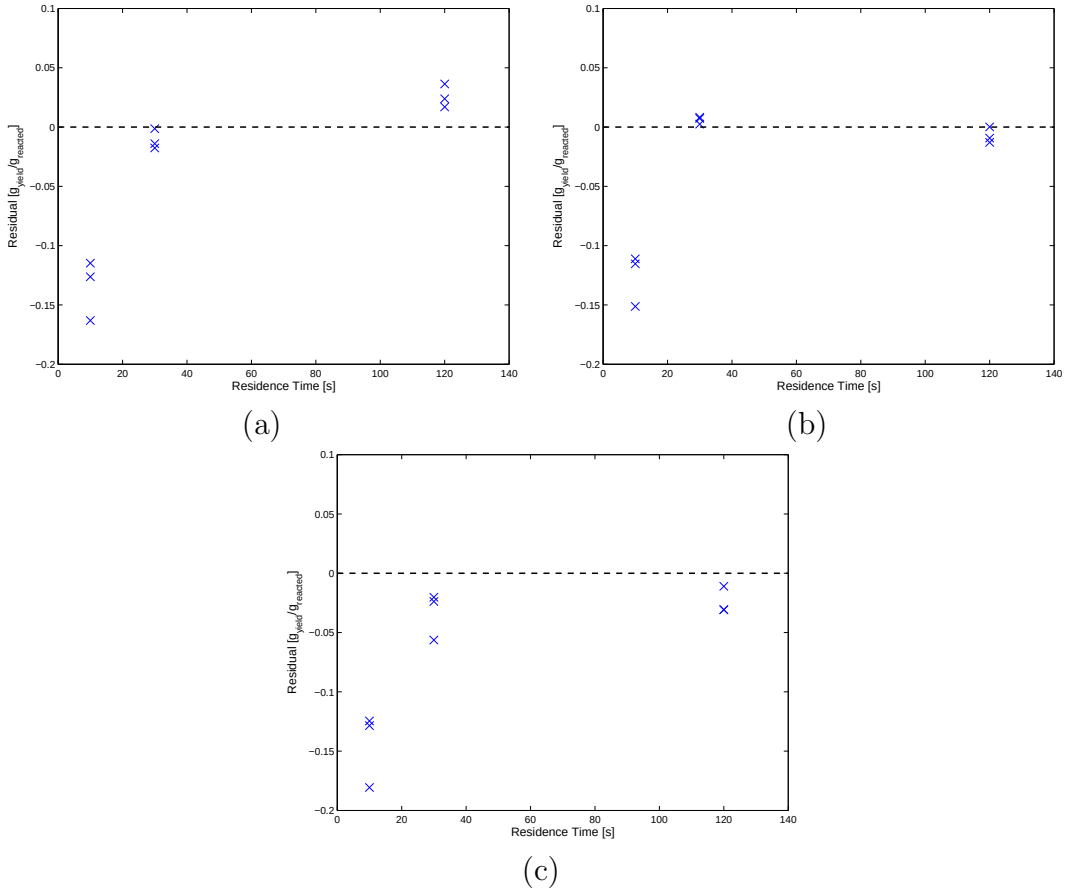

Figure 5.9: Avicel cellulose single component global fit residuals for reactor temperatures of: (a) 350°C (b) 360°C (c) 370°C

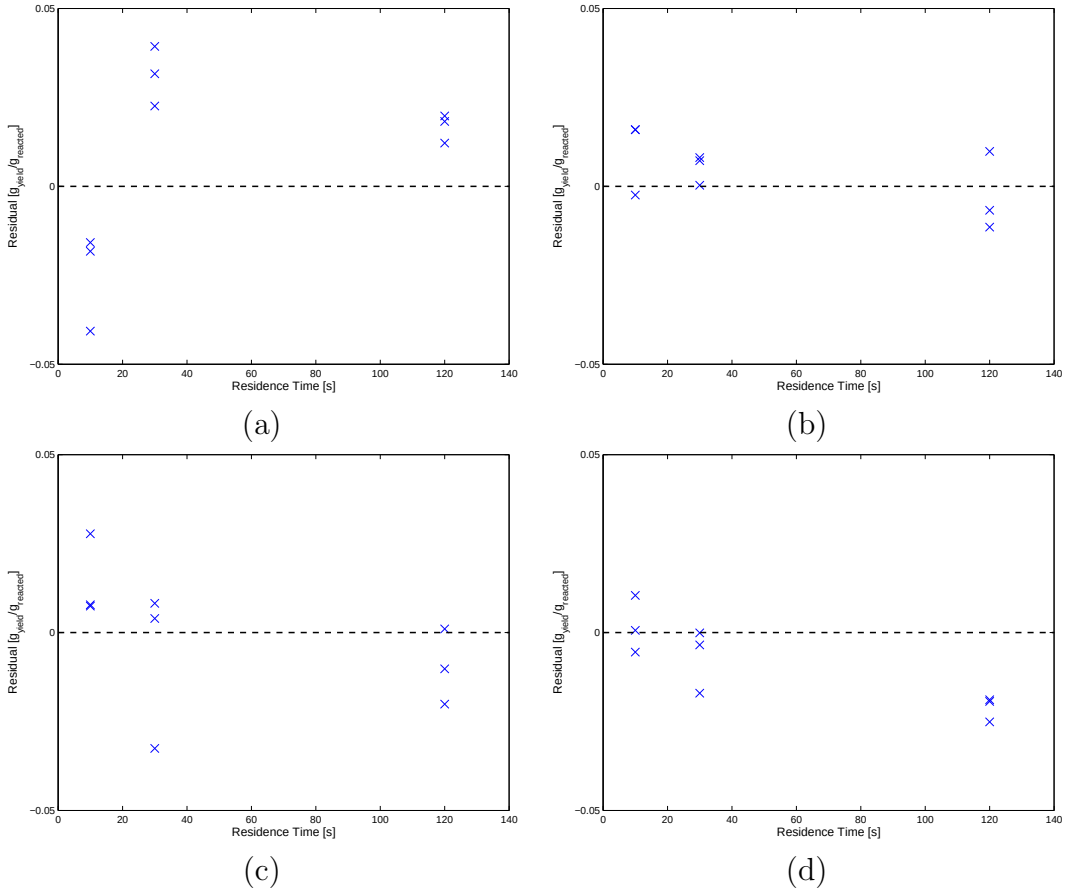

Figure 5.10: Beechwood Xylan single component global fit residuals forreactor temperatures of: (a) 340°C (b) 350°C (c) 360°C (d) 370°C

A key portion of the pseudo-component model is the estimation of the volatilized quantity of the biomass attributable to lignin at each residence time. This is calculated by subtracting the predicted quantity of converted cellulose and hemi-cellulose (approximated by xylan in this study) from the actual measured converted quantity of whole wood, as described in Equation 5.1 in Section 5.3.1.

Conversion predictions were made by applying the Arrhenius coefficient results contained in Table 5.11 at the reactor temperature for which the raw wood results were obtained. The resultant data points for predicted yields attributed to lignin ($\phi_{Lig}\eta_{Lig}(t)$) are shown in Figure 5.11.

Product lignin yields for residence times of 90 seconds and below show negative yields, clearly an impossibility. What this indicates is that there is a restriction that is limiting the conversion of the individual components when they are pyrolyzing as a part of whole wood. This restriction could be the result of one of two things: 1. The pyrolysis of whole wood is kinetically limited and pseudo-component reactions are not independent but are in fact competing or interacting; 2. The pyrolysis of the whole wood tested using the micro-reactor is inhibited by heat or mass transfer limitations resulting in an apparent slowing of the reaction.

A scaling analysis was performed to examine the possibility that the observed whole wood pyrolysis is heat or mass transfer limited rather than kinetically limited. If the pyrolysis is heat or mass transfer limited this would explain the inability to

Table 5.12: Published cellulose kinetic parameters from literature

Comp.	E_a [kJ/mol]	A [1/s]	c [g/g]	Conditions	Reference
1	234	3.98E17	0.93	TGA 10°C/min	[80]
1	205	1.26E15	0.94	TGA 80°C/min	[80]
1	218	2.51E17-3.16E18	-	TGA 1°C/min	[20]
1	218	5.01E17-2.51E19	-	TGA 60°C/min $T < 327$°C	[20]
1	140	1.26E10-3.16E14	-	TGA 60°C/min $T > 327$°C	[20]
1	214	1.26E17	-	Radiant Heating $19 - 56$°C/s	[25]
1	234	5.01E17	-	TGA 10°C/min	[81]

Table 5.13: Published xylan pyrolysis kinetic parameters from literature

Comp.	E_a [kJ/mol]	A [1/s]	c [g/g]	Conditions	Reference
1/2	193	7.94E16	0.43	TGA 10°C/min	[80]
2/2	95	5.01E6	0.56	TGA 10°C/min	[80]
1/2	76.6	3.63E5	0.63	Radiant Heating 40 – 70°C/s	[24]
2/2	51.8	3.80E2	0.28	Radiant Heating 40 – 70°C/s	[24]
1	258.8	2.00E22	-	TGA 5°C/min	[93]
1	257.2	2.51E21	-	TGA 20°C/min	[93]
1	194	3.16E15	-	TGA 40°C/min	[93]
1	125.1	1.62E9	-	TGA 80°C/min	[93]

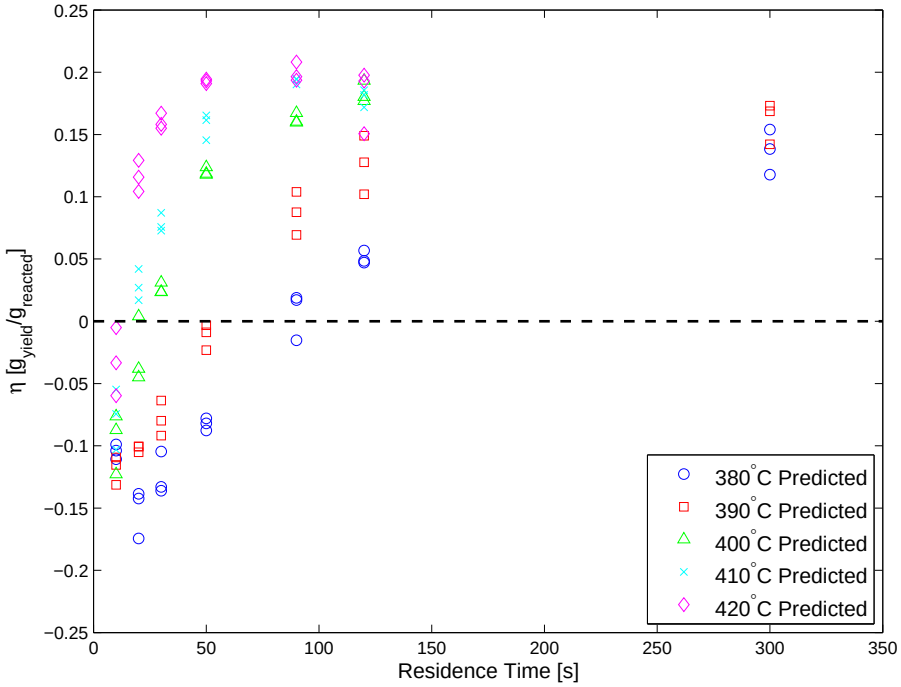

Figure 5.11: Predicted pyrolysis yields from lignin based upon a subtraction of xylan and cellulose yields from whole wood pyrolysis yields

superimpose independent cellulose, lignin and xylan kinetics for fast pyrolysis predictions because the kinetics are not accurately described in the whole wood pyrolysis tests. If the pyrolysis is not heat or mass transfer limited then the whole wood pyrolysis results do provide for whole wood pyrolysis kinetics and the lignin yield predictions indicate that the superposition of pseudo-components is not a suitable fast pyrolysis model.

Previous studies have utilized a non-dimensional pyrolysis number (Py) to describe the relative rates of pyrolysis and heat transfer for the purpose of predicting governing phenomena transition points in particle sizing. [94, 95, 96] The pyrolysis number is built upon scale analysis in which the characteristic times for the pyrolysis reaction and that for heat transfer are related through a ratio of the two. The characteristic time for the pyrolysis reaction itself is given by $\tau^*_{py} = 1/k$ where k is the rate of reaction. The characteristic time for heat transfer is given by $\tau^*_{heat} = \alpha/d^2$ where α is the thermal diffusivity of the pyrolyzing biomass and d is the characteristic dimension. In the micro-reactor bed the characteristic dimension is equal to the particle bed height, which is estimated to be 400μm based upon the nominal sieve opening for the #40 mesh used within the Wiley mill particle grinder. [58] This results in a pyrolysis number given by Equation 5.14,

$$Py = \frac{\tau^*_{py}}{\tau^*_{heat}} = \frac{\alpha}{kd^2} \tag{5.14}$$

Following the same methodologies for mass transfer as for heat transfer a pyrolysis number can be defined for diffusion as the ratio between the pyrolysis time constant and the diffusion time constant according to Equation 5.15,

$$Py_{diff} = \frac{\tau^*_{py}}{\tau^*_{diff}} = \frac{D}{kd^2} \tag{5.15}$$

where D is the mass diffusivity of the pyrolysis products.

The thermal diffusivity was evaluated at $\alpha = 1.23\text{E} - 6\text{m}^2/\text{s}$ based upon a wood

temperature of 400°C.[54] The mass diffusion coefficient was taken to be $D = 1\text{E} - 6\text{m}^2/\text{s}$ [97] which is a more conservative value among those found in literature. The rate of pyrolysis was calculated to be $k = 0.0468\text{s}^{-1}$ using the kinetic parameters reported in Table 4.9 for the single component global model at 400°C. The resulting Pyrolysis numbers for heat and mass transfer are then $Py = 164$ and $Py_{diff} = 134$.

Because the pyrolysis numbers are much greater than 1, the pyrolysis of raw wood within the micro-reactor is reaction limited and neither heat nor mass transfer limited. This means that the characterization of the pyrolysis of raw wood within the micro-reactor is, as previously claimed, a characterization of the fast pyrolysis kinetics governing the volatilization of the raw wood. Based upon the previous cellulose and xylan superposition results, the fast pyrolysis of Loblolly pine is not a set of independent parallel reactions but is clearly a set of dependent reactions either competing or in sequence due to interactions.

An additional set of experiments was performed to further test for the presence of interactions. Two mixtures of Avicel cellulose and Beechwood xylan were pyrolyzed at ratios of 50/50 and 60/40 (cellulose/xylan). A ratio of 60/40 was chosen because it is very close to the ratios of cellulose to hemicellulose found in pines and spruces. [91] A ratio of 50/50 was chosen simply because it was an even proportioned mix. Homogeneous mixtures were made by first combining a total of 10g of sample (cellulose+xylan) in the proper proportions. The combination was then mixed in a ball bearing filled tumbler for a minimum of three hours at a rotation rate of 46rpm. Two temperatures and three residence times were selected to evaluate the impact of the combined mixture versus the pseudo-component superposition. Residence times of 15, 45, and 135 seconds were chosen so as to not directly coincide with experimental results used to derived the kinetic parameters. Reactor temperatures of 350 and 410°C were selected to test the mixtures within the temperature ranges of both the pure xylan and cellulose experiments and the whole wood experiments.

Experimental results and theoretical predictive curves for the mixture tests are shown in Figures 5.12-5.15. The low temperature results (Figures 5.12 and 5.14) show a clear over-prediction of the rate of pyrolysis which is in agreement with the lignin predictions of Figure 5.11. The over-prediction indicates a significant retardation to the rate of pyrolysis. Further testing is required to accurately quantify this, but for the sake of verification these plots demonstrate that interactions are occurring to alter the pyrolysis reaction when multiple components are present. The high temperature results (Figures 5.13 and 5.15) indicate that agreement between the final yields can be reached.

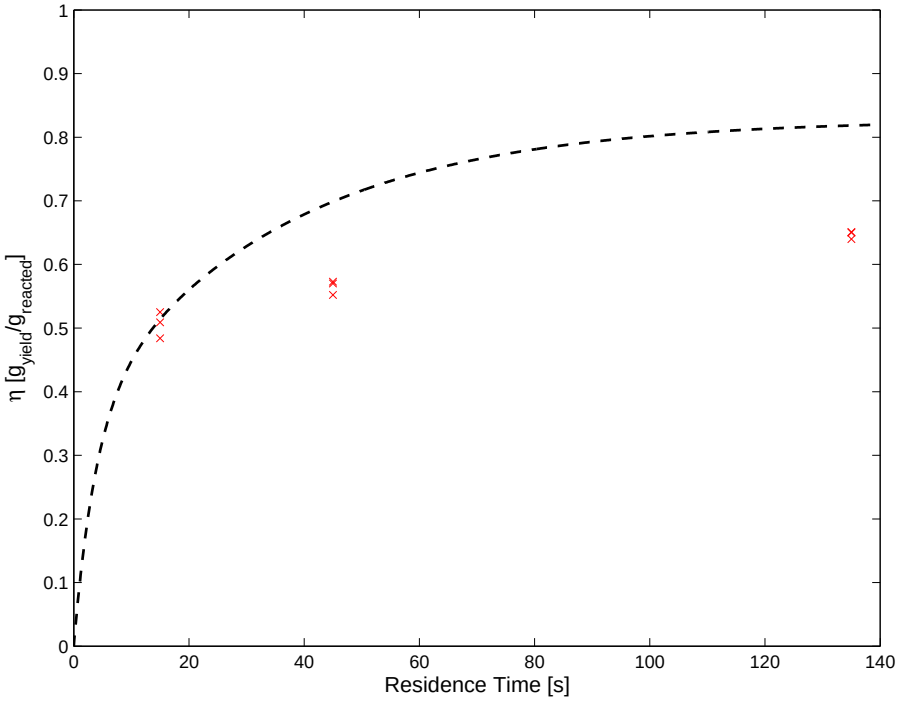

Figure 5.12: Cellulose and xylan 50/50 mix 350°C theoretical prediction and experimental results

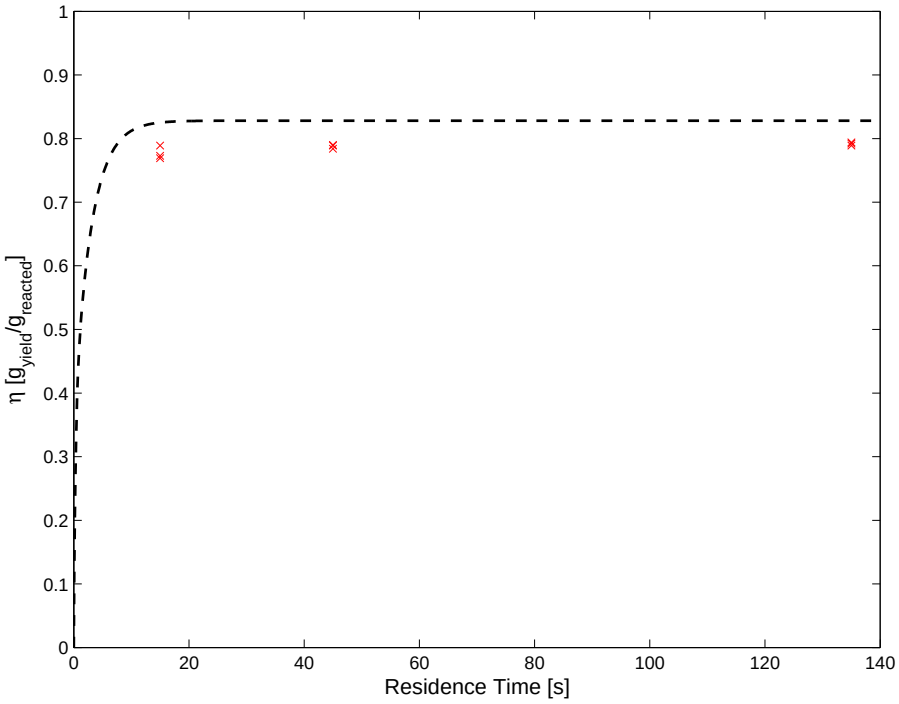

Figure 5.13: Cellulose and xylan 50/50 mix 410°C theoretical prediction and experimental results

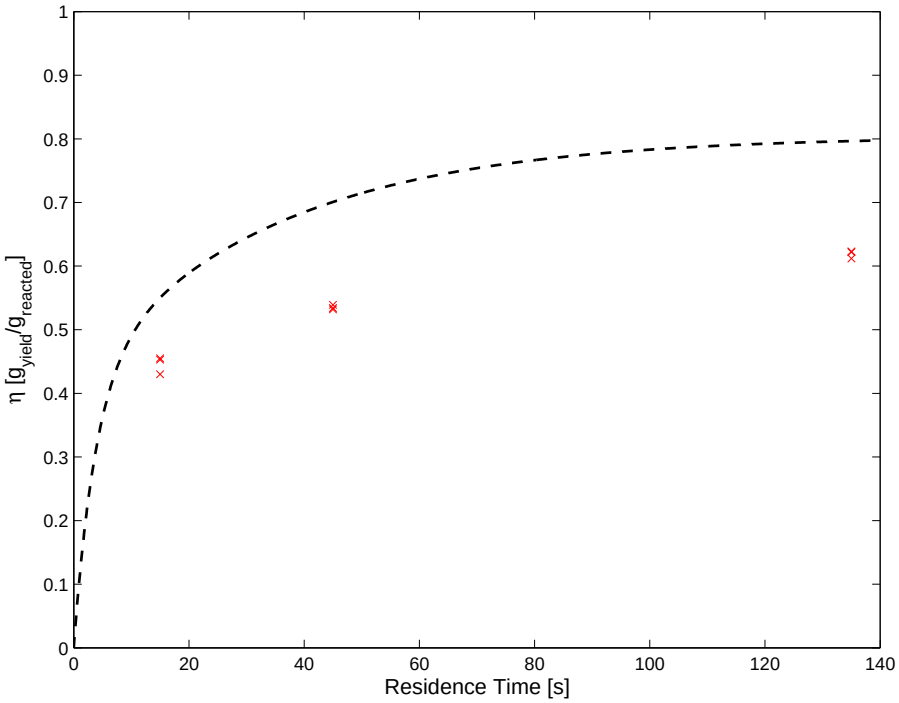

Figure 5.14: Cellulose and xylan 60/40 mix 350°C theoretical prediction and experimental results

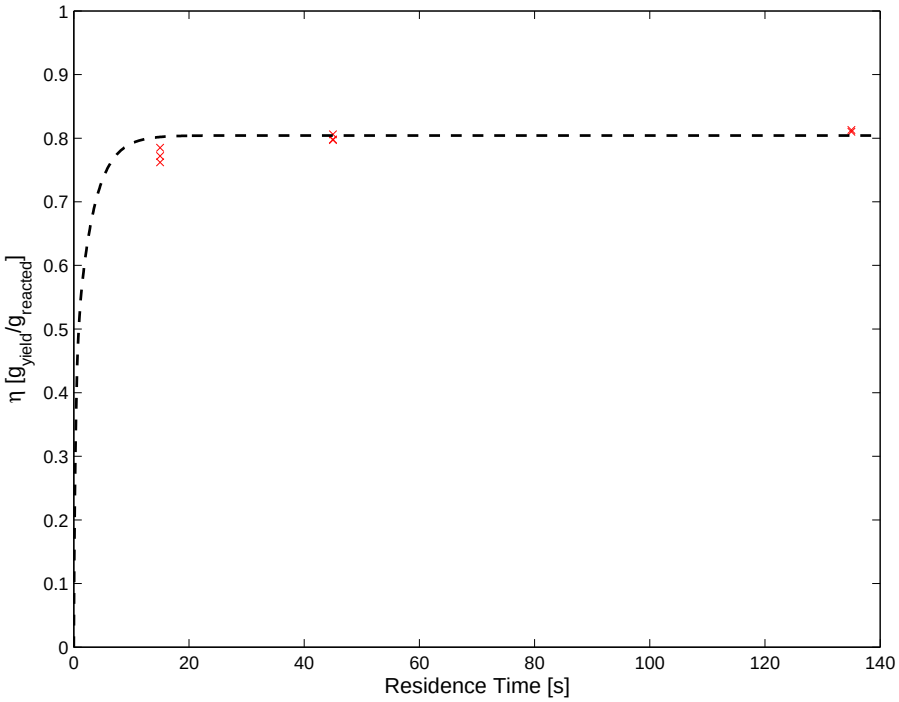

Figure 5.15: Cellulose and xylan 60/40 mix 410°C theoretical prediction and experimental results

The pseudo-component model using the isolated cellulose and xylan kinetic parameters will still be used to evaluate its applicability to predicting the pyrolysis of other species because of its wide acceptance in literature. To do so, however, will require the application of lignin kinetics from other published works. Three lignin values were selected from literature and are presented in Table 5.14. Two of the selected parameters were obtained through experimentation using TGA ovens (Organosolv lignin and Hydrolytic lignin). The parameters for Milled wood lignin were obtained through fast pyrolysis using an electric screen heater.

Table 5.14: Selected lignin kinetic parameter values from literature obtained using TGA ovens

Source	c [g/g]	E_a [kJ/mol]	A [1/s]
Hydrolytic Lignin from Softwood [98]	0.78	1.52E2	1.3E10
Organosolv Lignin from Hardwood [98]	0.70	1.44E2	2.4E9
Milled Wood Lignin [30]	0.93	6.91E4	3.4E4

5.8.2 Global Best Fit Results

The pure pseudo-component model and intermediate solid model were fit to the five Loblolly pine experimental results sets using globally optimized kinetic parameters as per the methods of Section 4.4. The resultant reduced χ^2 were 3.60 and 3.48 for the pure pseudo-component and intermediate solid models respectively. The best-fit coefficients are summarized in Table 5.15 and the best-fit model results are plotted against the experimental yield mean values with two standard deviation error bars in Figures 5.16-5.20. Residuals plots for both models are given in Figures 5.21a-e.

Table 5.15: Loblolly pine pseudo-component and intermediate solid model best fit results

Component	c [g/g]		E_a [kJ/mol]		A [1/s]		χ^2	ν	χ^2_ν
Pseudo-Component Model									
Cellulose	0.995	± 0.012	216	± 0.3	1.89E15	$^{+0.10\text{E}15}_{-0.09\text{E}15}$	317	88	3.60
Hemicellulose	0.712	$^{+0.017}_{-0.018}$	86.9	$^{+57.7}_{-86.9}$	6.90E10	$^{+\infty}_{-6.90\text{E}10}$	317	88	3.60
Lignin	0.594	$^{+0.016}_{-0.015}$	107	$^{+2}_{-3}$	4.70E7	$^{+2.92\text{E}7}_{-1.27\text{E}7}$	317	88	3.60
Intermediate Solid Model									
Cellulose	0.990	± 0.012	213	± 0.3	1.14E15	± 0.06E15	296	85	3.48
Hemicellulose	0.800	$^{+0.017}_{-0.018}$	188	$^{+134}_{-188}$	1.00E25	$^{+\infty}_{-1.00\text{E}25}$	296	85	3.48
Lignin	0.527	± 0.014	150	$^{+2}_{-3}$	1.36E11	$^{+1.13\text{E}11}_{-0.44\text{E}11}$	296	85	3.48
Intermediate Product	0.165	$^{+0.109}_{-0.105}$	487	$^{+5}_{-3}$	6.38E34	$^{+5.30\text{E}34}_{-3.63\text{E}34}$	296	85	3.48

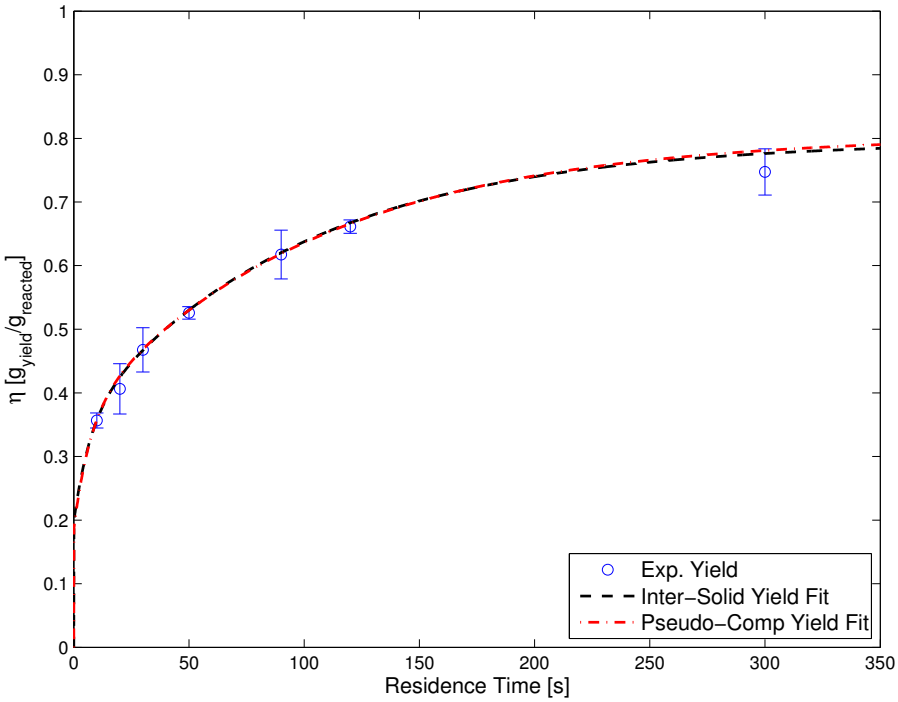

Figure 5.16: Loblolly pine Intermediate solid global fit results plotted against 380°C experimental mean values with two standard deviation error bars

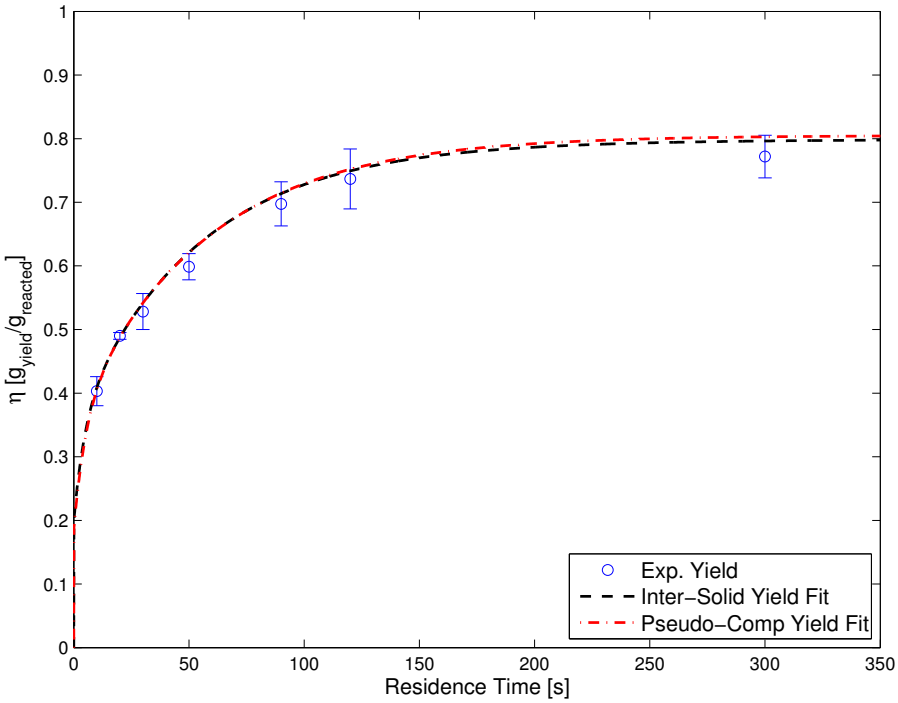

Figure 5.17: Loblolly pine Intermediate solid global fit results plotted against 390°C experimental mean values with two standard deviation error bars

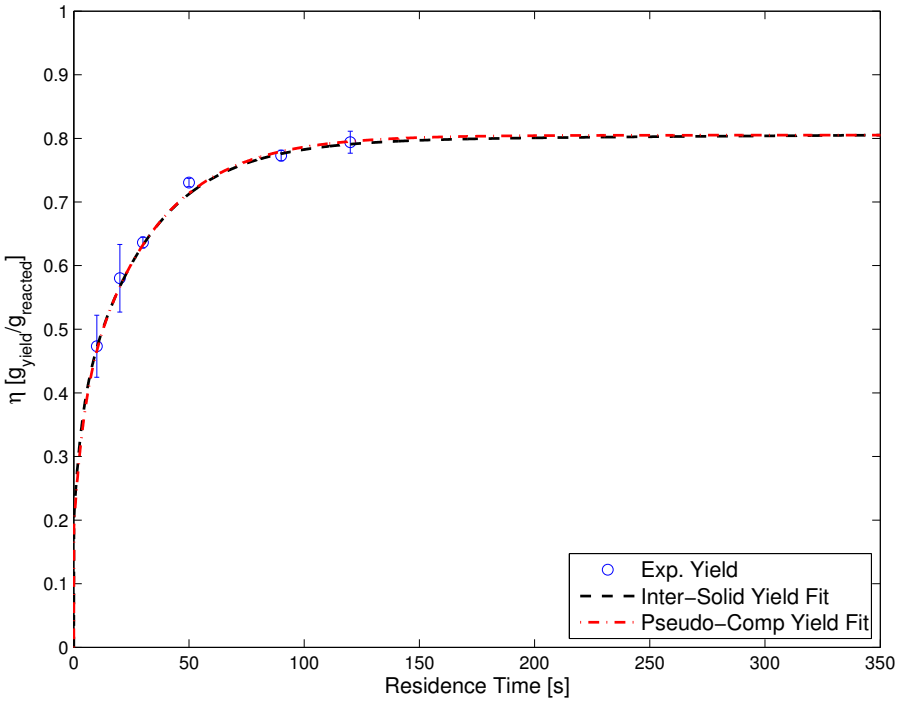

Figure 5.18: Loblolly pine Intermediate solid global fit results plotted against 400°C experimental mean values with two standard deviation error bars

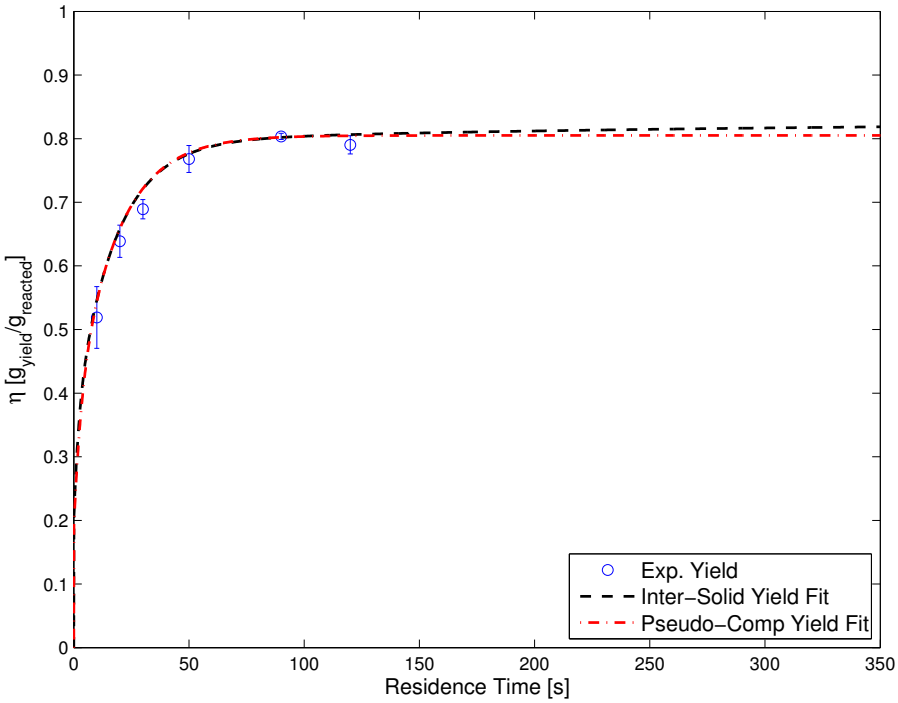

Figure 5.19: Loblolly pine Intermediate solid global fit results plotted against 410°C experimental mean values with two standard deviation error bars

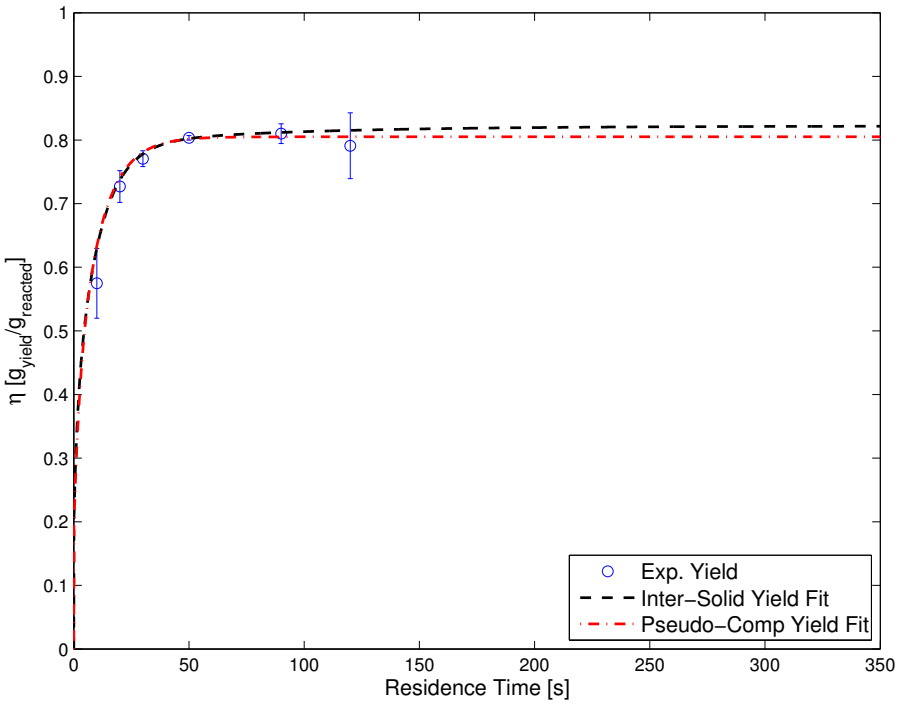

Figure 5.20: Loblolly pine Intermediate solid global fit results plotted against 420°C experimental mean values with two standard deviation error bars

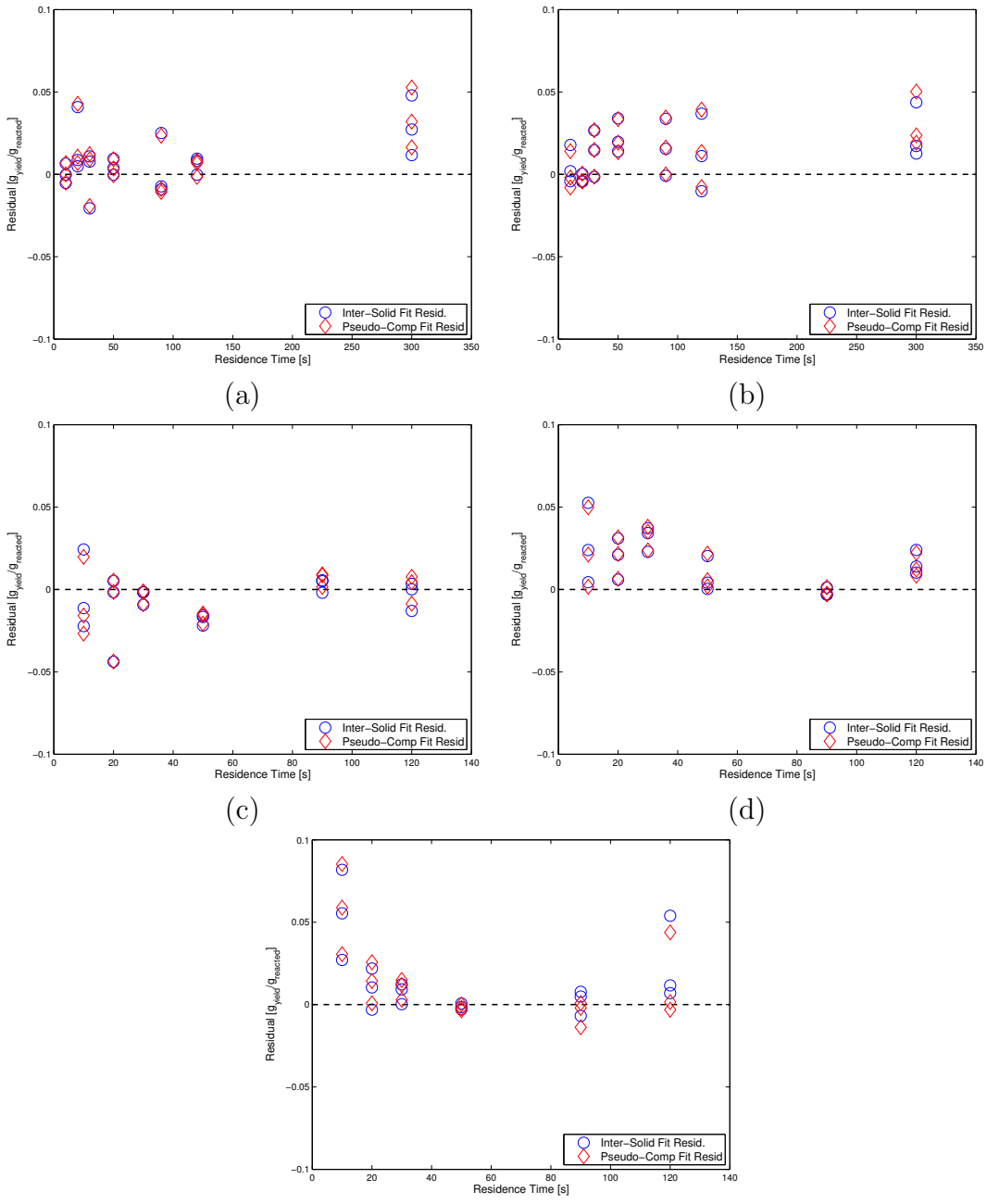

Figure 5.21: Intermediate solid model best fit curve residuals for reactor temperatures of: (a) 380°C (b) 390°C (c) 400°C (d) 410°C (e) 420°C

5.9 Discussion

The average instrumental error as a percentage of yield is 6.76% for the cellulose tests and 1.85% for the xylan tests. Within the cellulose results, the lowest instrumental error percentage is 1.12% and the highest is 119%. This high value corresponds to the negative oil yield data point for the 10 second residence time and 350°C reactor temperature. The instrumental error at that point was calculated to be 0.0079g/g. Compared to the measured oil yield of -0.007g/g, it is evident that the negative yield can come about by having a near zero oil yield combined with less than one standard deviation of propagated instrumental error.

The maximum and minimum xylan instrumental errors as a percentage of yield are 4.42% and 0.86% respectively. The lower error percentage among the xylan yields as opposed to the cellulose yields is due to the faster observed rate of pyrolysis of xylan. This increased conversion rate results in, on average, higher oil and gas yields which by nature of the experimental system have inherently higher instrumental errors than the solid yields. The subsequent result is a larger denominator for the percentage error calculation.

Analysis of the values reported in Table 5.12 shows that the cellulose activation energy and the pre-exponential term are in closest agreement with results from Milosavljevic and Suuberg [20] for the higher temperature portion of their tests. The reason for the agreement is most likely because all other studies looked only at the lower temperature portion of cellulose pyrolysis TGA plots. The root cause is that at lower low heating rates nearly all of the sample is consumed before higher temperatures can be reached. The study by Lanzetta and Di Blasi, [25] while testing heating rates 19-56 times higher than Milosavljevic and Suuberg, [20] only tested up to 350°C but observed fractional conversion quantities (c values) very close to that reported here. It is then likely that Lanzetta and Di Blasi did not observe the lower activation energy because their experimental method precluded reaching higher temperatures.

The lower temperature kinetic results by Milosavljevic and Suuberg also support this as both the activation energy and pre-exponential factor are in good agreement with the study by Lanzetta and Di Blasi.

In comparison to literature, the xylan activation energy and pre-exponential best fit results appear to be approached by the results of Williams and Besler. [93] Within their study the heating rate of the TGA oven was varied from 5 to 80°C/min. Over this range the values reported for both the activation energy and pre-exponential values trend toward the best fit results presented here. Higher heating rate results reported by Di Blasi and Lanzetta [24] do not agree with those presented here. Di Blasi and Lanzetta's tests, though, stopped at 340°C, so it is plausible that much like the cellulose samples, xylan exhibits a different behavior as higher temperatures are reached. With respect to two component models for xylan pyrolysis modeling, [80, 24] the application of such a model was attempted here but produced coefficients with confidence intervals of -100% to $+\infty$. This is a result of a lack of very low residence time data ($<$ 10s) to capture the steepest part of the conversion curves at the tested temperatures.

The demonstration of interactions observed in the pseudo-component mixture tests are in disagreement with previous studies evaluating the pyrolysis of isolated pseudo-component mixtures, most likely due to the low rates of heating utilized in other superposition studies. Raveendran *et al.* [99] tested isolated pseudo-components, whole biomass and synthesized biomass (based upon pseudo-component mixtures) in a TGA oven and tubular radiant reactor. From both reactor configuration results the authors concluded that an additive superposition scheme is an accurate predictor of whole biomass and furthermore that interactions are insignificant between pseudo-components. Yang *et al.* [85] concluded from testing various proportions of the isolated pseudo-components in a TGA oven, that interaction effects were negligible and that any deviation between predicted biomass pyrolysis yields and actual biomass

yields was due to the presence of mineral content. The results here, however, indicate a significant level of interactions taking place and retarding the reaction. Tests by Yang *et al.* and Raveendran were performed at low heating rates and consequently the rate effects may have not been observable, as stated above.

The results of Miller and Bellan [100] showed some agreement with the results presented here. In their study a sequential kinetics scheme was employed for each pseudo-component with kinetic parameters being compiled from multiple literature sources. The predictive results produced TGA derivative curves of similar shape to experimental curves but which quantitatively both over predicted the conversion and predicted a shift in the rate of mass loss (dm/dt) curve to lower temperatures. This rate curve shift indicates a predicted faster conversion than was experimentally measured for whole wood, which is akin to the trend seen in Figure 5.11. The authors attributed the departure from the superposition model to the presence of minerals within the raw biomass having a catalytic effect.

Both graphically and numerically the global best fit pseudo-component and intermediate solid model results are in good agreement with the experimental data. The confidence intervals for hemicellulose and lignin kinetic coefficients, however are very large for both models. Hemicellulose and lignin constitute significantly smaller fractions of Loblolly pine at 0.26 and 0.29g/g respectively, as opposed to cellulose at 0.45g/g. Consequently, the fluctuation of the rate of pyrolysis of hemicellulose and lignin components will have a much smaller impact on overall pyrolysis rates. As a result, a large range of activation energy and pre-exponential values are possible to fulfill the F-test criterion for confidence intervals given by Equation 4.17.

Model coefficient results also indicate that the intermediate product is mostly insignificant. Considering the mass fraction of each pseudo-component and multiplying those by their respective c-values from Table 5.15, the volatile yield attributed to

the primary pyrolysis of the pseudo-components is 0.776g/g. The resultant yield attributed to the intermediate products is simply the intermediate c-value multiplied by 1 minus the pseudo-component yields (*e.g.* $c_I(1 - \phi_c c_c - \phi_x c_x - \phi_L c_L)$). This results in 0.037g/g of yield attributed to the intermediate solid devolatilizing. In addition, the pure pseudo-component model fit shows an increase in the reduced χ^2 value of only 0.12 over the intermediate solid model. Therefore if an experimenter is limited in the number of independent test samples attainable, it may become statistically economical to utilize a pure pseudo-component model as opposed to an intermediate solid model which requires an additional three degrees of freedom for fitting.

5.10 Summary

Two pseudo-component pyrolysis models were presented, a superposition model consisting of cellulose, hemicellulose and lignin as well as a superposition model like the first but with an included intermediary solid compound. Experimental results were presented for the pyrolysis of Avicel cellulose and Beechwood xylan (represtative of hemicellulose) and the instrumental uncertainty analysis evaluated. The experimental yield results were used for the pure pseudo-component superposition model. The intermediate solid model used component ratios taken from literature and allowed the remainder of the kinetic parameters to be adjusted for a best fit.

Propagated instrumental error analysis results showed that the average instrumental error within the xylan yields is 1.85% and for the cellulose yields is 6.76%. An unexpected negative yield within the cellulose oil results was explained by its corresponding instrumental error which accounted on a percentage basis for119% of the measured yield. This indicates that the propagated instrumental error is detrimental to the measurement of very low yields, however, this was the case for only 1 of the 351 yield values reported for the cellulose, xylan and Loblolly pine pyrolysis results.

The xylan fit was significantly better than the cellulose fit with reduced χ^2 values

of 7.6 and 14.2 respectively. The derived kinetic parameters for cellulose agreed with results from literature when higher reactor temperatures were considered (*e.g.* $> 340°C$). Xylan kinetic parameters did not show direct agreement with literature values but results from Williams and Besler [93] approached those presented here as the heating rate was increased. Both these results indicate that Milosavljevic and Suuberg's [20] conclusions about multiple cellulose kinetics existing as a function of temperature regime also apply to the pyrolysis of xylan.

Pyrolysis yields attributable to lignin were estimated by subtracting the predicted cellulose and hemicellulose yields from whole wood pyrolysis results. The predicted lignin yields were evaluated to be negative at lower residence times indicating that some retardation of the reaction was occurring that is not accounted for in the pure superposition model. This demonstrates that strictly additive methods can not be applied to accurately predict the fast pyrolysis of Loblolly pine. Additional investigations were conducted into the possible limiting factors within the observed whole wood pyrolysis. A scaling analysis was performed which showed that the reaction is clearly rate limited based upon the governing time scales for the heat transfer, mass transfer and pyrolysis reaction kinetics. An experimental set was tested to evaluate possible interactions between pseudo-components simultaneously pyrolyzing. Both 50/50 and 60/40 mixtures of cellulose/xylan (on a mass basis) showed that the combined substance had a significantly retarded rate of pyrolysis. The final volatilized quantities, however, were very close to those predicted by superposition. This is the first experimental demonstration of the interaction between pseudo-components undergoing fast pyrolysis. It is most likely the affect of low heating rates employed by previous studies that results in the retardation of the pyrolysis reaction not been observed. This also demonstrates that the presence of catalytic minerals is not the only source of predictive errors in pseudo-component models, as is typically concluded. [99, 85, 100, 66]

The intermediate solid model produced a fit to the data with a reduced χ^2 value of 3.48. Within the intermediate solid model, however, the intermediate term was determined to be mostly insignificant. Refitting to the data with the removal of the term results in an increase in the reduced χ^2 value by only 0.12. It is therefore recommended that in situations of limited experimentation, the pure pseudo-component model may be more suitable as it requires fewer degrees of freedom.

CHAPTER 6

COMPARISON OF FAST PYROLYSIS MECHANISM PREDICTIVE POWER

6.1 Introduction

The purpose of this chapter is to demonstrate the need for fast pyrolysis derived kinetic parameters. To do this, however, it is necessary to first evaluate the kinetic models derived in Chapters 4 and 5 against a set of verification data. Additionally, the extensibility of the models to alternate species of biomass will be evaluated. Comparative evaluations of kinetic model descriptive power have been primarily left to review studies, which typically tabulate the works of others and attempt to draw conclusions regarding kinetics from dissimilar experimental configurations. [101, 16, 102, 68] The variability between reactor heating methodologies, product removal pathways, feedstocks and feedstock preparation methods presents a significant barrier to comparative analysis. Therefore, the effective evaluation and comparison of kinetic model suitabilities is addressed here using a common data set for all derived models.

Fast pyrolysis and slow pyrolysis derived kinetic parameters are compared on an $\ln k$ versus $1/T$ plot for graphical evidence of dissimilarity. The projected yields using both fast and slow pyrolysis kinetic parameters are also compared.

Two evaluation species are pyrolyzed, Norway spruce (*Picea abies*) and Scots pine (*Pinus sylvestris*), for model extensibility evaluation. The five previously derived kinetic models are compared along with several key models from literature. Quality of fit according to reduced χ^2 parameters will be used as the predictive power metric. As was previously stated, χ^2 values are implemented so that the spread of the data can be included within the error estimate and to then provide a numerical means

of comparison between models. It is not expected that a reduced χ^2 value of 1 (indicating an ideal fit) will be obtained but that the resultant reduced χ^2 values will allow inter-model comparisons.

6.2 Fast Pyrolysis Model Validation

The derived pyrolysis models from Chapters 4 and 5 were evaluated against an additional independent set of Loblolly pine experimental results. Experiments were performed using a randomized set of tests at 400°C and residence times of 16, 64 and 256 seconds in triplicate. The residence times were selected so as to not directly coincide with the residence times used for kinetic parameter derivation tests while also providing a long residence time check for the evaluation of convergence. The complete randomized verification testing matrix is contained in Table 6.1.

Table 6.1: Testing matrix for verification tests on Loblolly pine

Test	Residence Time [s]	Reactor Temp [°C]
1	16	400
2	256	400
3	256	400
4	64	400
5	16	400
6	256	400
7	64	400
8	16	400
9	64	400

Predicted conversions at 400°C are plotted against the verification data in Figure 6.1 for the single and two component models, Figure 6.2 for the intermediate component and pseudo-component models and Figure 6.3 for the product based model. The percentage error of each model is given in Table 6.2.

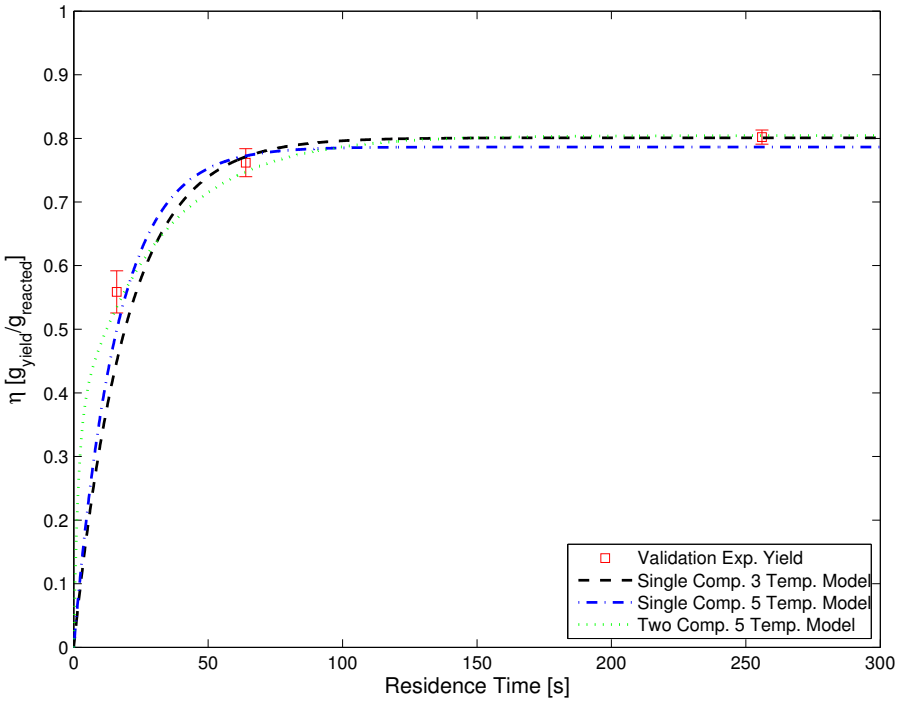

Figure 6.1: Single and two component model predictions at 400°C plotted against verification data taken at 16, 64 and 256 seconds

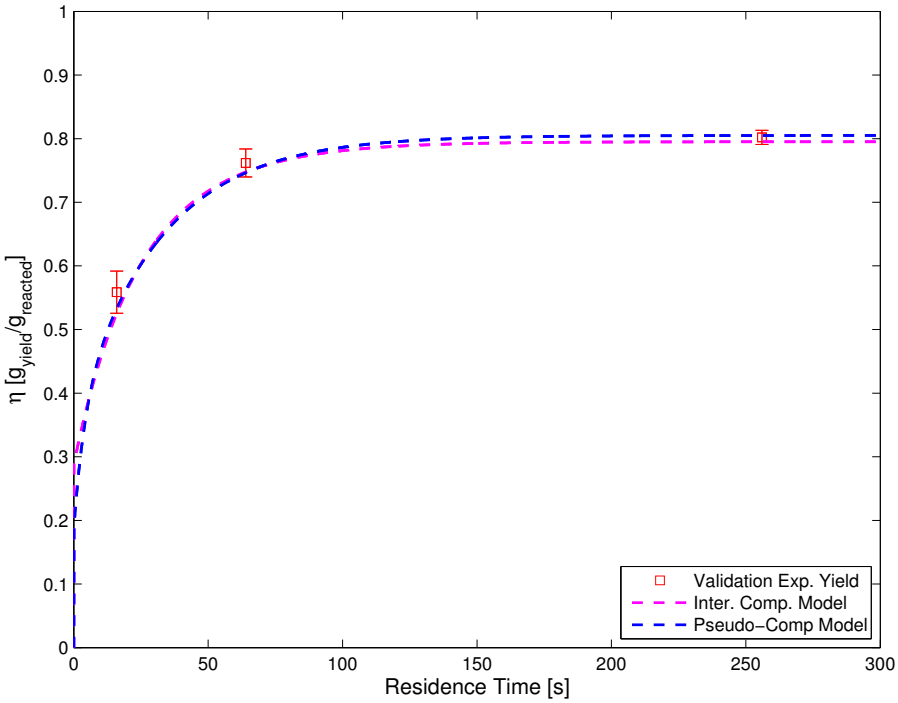

Figure 6.2: Pseudo-component and intermediate solid model predictions at 400°C plotted against verification data taken at 16, 64 and 256 seconds

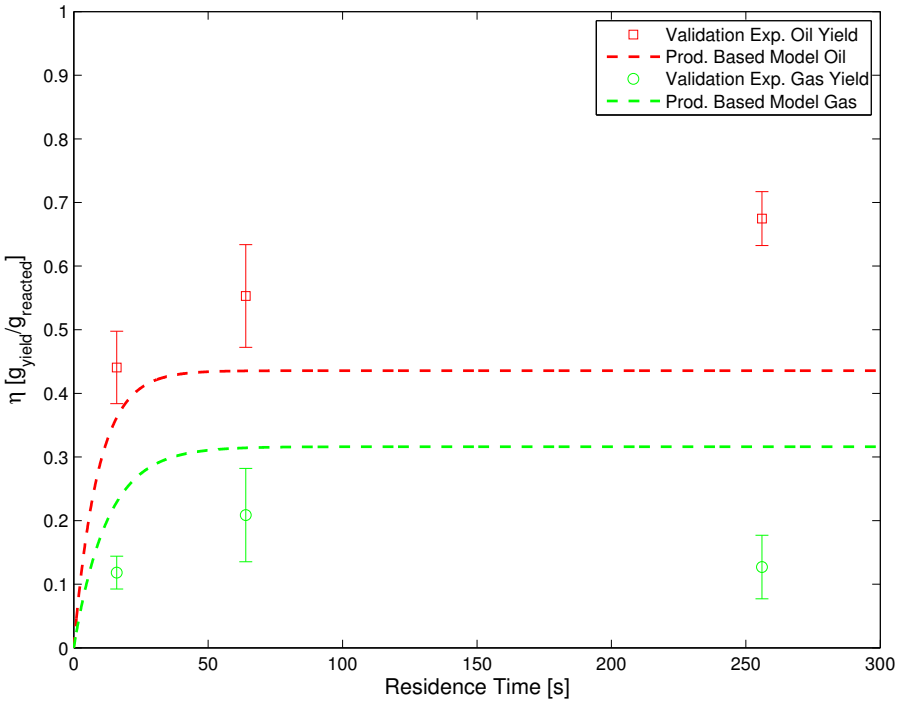

Figure 6.3: Product based model predictions at 400°C plotted against verification data taken at 16, 64 and 256 seconds

Table 6.2: Percentage error of each model at each individual residence time and the average across all three residence times

Residence Time [s]	16	64	256	Ave.
Single Comp. 3Temp	-19.6%	1.24%	-0.14%	-6.17%
Single Comp. 5Temp	-10.7%	1.41%	1.93%	3.73%
Two Comp.	-4.25%	-1.84%	0.29%	-1.94%
Intermediate Comp.	-5.96%	-1.87%	-0.86%	-2.90%
Pseudo-Comp.	-4.63%	-2.00%	0.36%	-2.09%
Prod. Based Oil	-17.9%	-21.3%	-35.4%	-24.9%
Prod. Based Gas	93.6%	50.6%	149%	97.7%

6.3 Fast Pyrolysis Model Extensibility Experimental Testing and Results

Model extensibility evaluations and the subsequent model comparisons were performed on two additional softwoods: Scots pine (*Pinus sylvestris*) and Norway spruce (*Picea abies*). Tests were conducted at reactor temperatures of 405 and 415°C and residence times of 15, 45 ad 135 seconds so as to not directly coincide with the Loblolly pine test conditions. The alternate species were chosen because they are common softwoods with similar pseudo-component compositions to Loblolly pine and have been used in previously published pyrolysis studies. The Scots pine and Norway spruce feedstock were obtained as standard wood samples (1/2"x3"x6" block) from a wood products distributor and processed using the same Wiley mill and drying process as the Loblolly pine samples. The moisture content of Scots pine and Norway spruce is assumed to be equivalent to that measured for the Loblolly pine (3.57% by mass). The randomized testing matrix for the pyrolysis of the alternate species is presented in Table 6.3. The mean yield and standard deviation results are contained in Tables 6.4 and 6.5.

Table 6.3: Testing matrix for extensibility species (Scots pine and Norway spruce) pyrolysis tests at 405 and 415°C

Test	Species	Residence Time [s]	Reactor Temp [°C]	Test	Species	Residence Time [s]	Reactor Temp [°C]
1	Abies	45	405	19	Abies	135	415
2	Sylvestris	15	415	20	Abies	45	415
3	Sylvestris	15	405	21	Abies	135	405
4	Abies	45	415	22	Sylvestris	15	415
5	Sylvestris	45	405	23	Sylvestris	45	415
6	Sylvestris	15	405	24	Abies	15	405
7	Abies	45	405	25	Sylvestris	135	405
8	Sylvestris	45	405	26	Sylvestris	45	405
9	Sylvestris	135	415	27	Abies	45	415
10	Abies	135	405	28	Abies	135	415
11	Sylvestris	135	405	29	Sylvestris	45	415
12	Abies	15	415	30	Sylvestris	135	405
13	Sylvestris	135	415	31	Sylvestris	15	405
14	Abies	45	405	32	Abies	15	405
15	Abies	15	405	33	Sylvestris	45	415
16	Abies	15	415	34	Abies	15	415
17	Abies	135	415	35	Abies	135	405
18	Sylvestris	135	415	36	Sylvestris	15	415

Table 6.4: Scots pine pyrolysis average product yields and standard deviations for 405 and 415°C reactor temperatures with gas yields calculated by difference

405°C						
Residence Time [s]	$\bar{\eta}_o$ [g/g]	σ_o [g/g]	$\bar{\eta}_s$ [g/g]	σ_s [g/g]	$\bar{\eta}_g$ [g/g]	σ_g [g/g]
15	0.338	6.29E-3	0.435	1.47E-2	0.227	9.60E-3
45	0.433	2.43E-2	0.243	2.09E-2	0.324	4.42E-2
135	0.504	6.01E-2	0.179	7.14E-3	0.317	5.96E-2
415°C						
Residence Time [s]	$\bar{\eta}_o$ [g/g]	σ_o [g/g]	$\bar{\eta}_s$ [g/g]	σ_s [g/g]	$\bar{\eta}_g$ [g/g]	σ_g [g/g]
15	0.372	3.51E-2	0.372	3.14E-3	0.256	3.75E-2
45	0.474	6.79E-2	0.200	1.16E-2	0.326	6.78E-2
135	0.554	4.02E-2	0.172	5.24E-3	0.274	4.46E-2

Table 6.5: Norway spruce pyrolysis average product yields and standard deviations for 405 and 415°C reactor temperatures with gas yields calculated by difference

405°C						
Residence Time [s]	$\bar{\eta}_o$ [g/g]	σ_o [g/g]	$\bar{\eta}_s$ [g/g]	σ_s [g/g]	$\bar{\eta}_g$ [g/g]	σ_g [g/g]
15	0.262	8.37E-2	0.400	1.98E-2	0.337	6.46E-2
45	0.381	7.24E-2	0.223	1.73E-2	0.397	8.65E-2
135	0.450	4.67E-2	0.171	2.67E-2	0.379	6.06E-2
415°C						
Residence Time [s]	$\bar{\eta}_o$ [g/g]	σ_o [g/g]	$\bar{\eta}_s$ [g/g]	σ_s [g/g]	$\bar{\eta}_g$ [g/g]	σ_g [g/g]
15	0.388	5.89E-2	0.304	2.22E-2	0.308	7.98E-2
45	0.404	6.75E-2	0.171	1.72E-2	0.425	6.37E-2
135	0.521	8.55E-2	0.174	2.75E-3	0.305	8.81E-2

6.4 Tabulation of Models for Comparison

Nine published pyrolysis models were selected for comparison to the derived models of Chapters 4 and 5. These were selected from key studies which are either frequently referenced works considered a baseline within the field or works which provide a unique approach and perspective to the field. The kinetic parameter values are summarized in Tables 6.6-6.8 along with those derived in this work.

Whole wood pyrolysis kinetic parameters were taken from three different studies all of which used different experimental apparati and different feedstocks. Wagenaar *et al.* [103] investigated the pyrolysis of pine sawdust (from an unspecified species) for the purpose of deriving a first order global pyrolysis model and a product based model. Tests were performed with both a drop-tube furnace and a TGA oven, though heating rates were not reported for either reactor. Results showed successful application of the TGA data to the derivation of a single component model fit, which was said to fit other experimental results well for temperatures below 400°C.This study was selected because it is a commonly referenced study within the field. Nunn *et al.* [30] pyrolyzed powdered Sweetgum hardwood using an electric screen heater reactor for the derivation of single component global kinetics. Batches of 100mg of sample

were pyrolyzed with heating rates of up to 100°C/s reported with target temperatures between 330 and 1130°C. Once peak temperatures were reached, the system was quenched at an average cooling rate of 200°C/s. Conversion estimates were based upon the residual char within the mesh screen. Di Blasi and Branca [26] conducted a kinetics study using two different experimental reactors for the pyrolysis of Beechwood. A fluidized bed reactor was used to measure product quantities (char, gas and oil) while a radiantly heated tubular quartz furnace with integrated thermobalance and *in situ* thermocouple was used to measure volatilization rates. Reactor temperates from $\sim 315 - 450$°C were tested and both single component global and product based models were derived from Beechwood pyrolysis experimental results. Heating rates of 16.7°C/s were reported for the radiant tube reactor. The derived models were shown to qualitatively fit the experimental results in the determined kinetically controlled regime for the tested reactors (≤ 435°C). The studies by Nunn *et al.* and Di Blasi and Branca were selected because of the higher heating rates used in their experimental efforts. The product based pyrolysis models provided by Wagenaar *et al.* and by Di Blasi and Branca will be used for comparison to the product based model derived here.

Lignin kinetic parameter values were selected from literature to complete the predictive pseudo-component model using cellulose and xylan parameters from Section 5.8.1. The values were selected from studies which used three different extraction methods for obtaining the tested lignin. The first of the methods produces Organolov lignin using an "organic solvent such as methanol or ethanol containing a suitable catalyst such as HCl...to break the linkages with polysaccharides and the lignin fragments dissolve." [104] In the second method, to obtain Milled wood lignin, "[wood] is milled in a ball-mill for tens of hours to mechanically break the linkages with polysaccharides. The lignin fragments become soluble in some solvents such as 0.2 mol/L NaOH solution and then the dissolved lignin is separated by extraction

using dioxanewater mixture."[104] The third method, to produce Hydrolytic lignin, uses dilute acid "to hydrolyze most of the polysaccharides to produce fermentable sugars, leaving lignin as a solid by-product" [104] The pyrolysis of Hydrolytic lignin is less common within literature but was selected specifically because it was derived from a softwood within the study cited.

Jiang *et al.* [104] pyrolyzed Organosolv lignin from an unspecified hardwood and Hydrolytic lignin from an unspecified softwood using a TGA oven. Seven different heating rates were investigated between 0.033 and 3.3°C/s ($2 - 200$°C/min) and kinetic parameters fit to the complete set of results. Milled wood lignin kinetics were taken from work by Nunn *et al.* [105] in which an electric screen heater was used at nominal heating rates of 1000°C/s to pyrolyze the sample. The Milled wood lignin was obtained from Sweetgum.

Two additional pseudo-component studies were selected for comparison. Grønli *et al.* [67] tested four hardwoods, five softwoods and five lignin samples using a TGA oven. Best fit common activation energies were found and pre-exponential factors were allowed to vary between species. Results showed, however, that the pre-exponential factors experienced little variability despite the differences in component proportionality between species and the structural differences between softwoods and hardwoods. Manyà *et al.* [83] utilized a TGA oven to pyrolyze sugarcane bagasse, mixed softwood waste, Kraft alkali lignin and Avicel cellulose. Kinetic parameter values were obtained by using a non-linear least squares method and showed good agreement between both the sugarcane bagasse and mixed softwood waste values.

Pseudo-component makeups for Scots pine and Norway spruce were taken from values published by the United States Department of Agriculture Forrest Products Division [54] and work by Navarro *et al.* [88]. For Scots pine: $\phi_c = 0.44$; $\phi_x = 0.27$; $\phi_L = 0.29$. For Norway spruce: $\phi_c = 0.43$; $\phi_x = 0.26$; $\phi_L = 0.31$.

Table 6.6: Model coefficients for bulk kinetic pyrolysis models derived in this work and selected pyrolysis models from literature to be used for model comparisons

Micro-Reactor Derived Model Values					
Source	Component	Apparatus	E_a[kJ/mol]	A[1/s]	c[g/g]
SC 3 Temp Model [a]	Whole Wood	MR ($\sim 400°C/s$)	157	8.28E10	0.801
SC 5 Temp Model	Whole Wood	MR ($\sim 400°C/s$)	132	1.19E9	0.786
TC Model Pt 1	Whole Wood	MR ($\sim 400°C/s$)	220	3.82E15	0.453
TC Model Pt 2			185	1.26E14	0.352
Literature Model Values					
Source	Component	Apparatus	E_a[kJ/mol]	A[1/s]	c[g/g]
Wagenaar *et al.* [103]	Whole Wood (Pine)	TGA and Entrained Flow Reactor [b]	150	1.40E10	0.95
Di Blasi and Branca [26]	Whole Wood (Beech)	Radiant Thermo-balance ($16.7°C/s$)	141	4.38E9	0.88
Nunn *et al.* [30]	Whole Wood (Sweetgum)	Electric Screen Heater ($100°C/s$)	69.1	3.39E4	0.93

[a]Fitted to results from reactor temperatures of 400, 410 and 420°C
[b]No heating rate reported

Table 6.7: Model coefficients for pseudo-component pyrolysis models derived in this work and selected pyrolysis models from literature to be used for model comparison

Micro-Reactor Derived Model Values					
Source	Component	Apparatus	E_a[kJ/mol]	A[1/s]	c[g/g]
SC Model	Avicel Cellulose	MR ($\sim 400°C/s$)	145	4.52E10	0.947
SC Model	Beechwood Xylan	MR ($\sim 400°C/s$)	151	1.19E12	0.709
Intermediate	Cellulose	MR ($\sim 400°C/s$)	213	1.14E15	0.99
Component	Hemicellulose		188	1.00E25	0.8
Model	Lignin		150	1.36E11	0.527
	Intermediate		487	6.38E34	0.165
Pseudo-component	Cellulose	MR ($\sim 400°C/s$)	216	1.89E15	0.995
Model	Hemicellulose		86.9	6.90E10	0.712
	Lignin		107	4.70E7	0.594
Literature Model Values					
Source	Component	Apparatus	E_a[kJ/mol]	A[1/s]	c[g/g]
Nunn *et al.* [105]	Milled Wood Lignin	Electric Screen Heater ($100°C/s$)	82.1	3.39E5	0.8435
Jiang *et al.* [104]	Hydrolytic Lignin	TGA	142	1.28E10	0.78
	Organosolv Lignin	($0.033 - 3.3°C/s$)	144	2.37E9	0.7
Grønli *et al.* [67][a]	Hemicellulose	TGA ($0.083°C/s$)	100	2.29E6	0.34
Scots pine	Cellulose		236	2.51E17	0.35
	Lignin		46	3.39E0	0.11
Grønli *et al.* [67] [a]	Hemicellulose	TGA ($0.083°C/s$)	100	2.51E6	0.33
Norway spruce	Cellulose		236	2.69E17	0.32
	Lignin		46	3.80E0	0.14
Manyà *et al.* [83] [a]	Hemicellulose	TGA	197	4.7E15	0.119
Mixed softwood	Cellullose	($0.083 - 0.33°C/s$)	246	1E18	0.295
	Lignin		51.4	1.01E1	0.275

[a]Here c represents the contribution to total volatiles by that component

Table 6.8: Model coefficients for product based pyrolysis models derived in this work and selected pyrolysis models from literature to be used for model comparisons

Micro-Reactor Derived Model Values					
Source	Component	Apparatus	E_a[kJ/mol]	A[1/s]	c[g/g][b]
Product Based	Char [a]	MR ($\sim$ 400°C/s)	157	8.28E10	-
Model	Oil		218	6.51E15	-
	Gas		163	3.00E11	-
Literature Model Values					
Source	Component	Apparatus	E_a[kJ/mol]	A[1/s]	c[g/g][b]
Di Blasi and	Char	Fluidized Bed	112	3.27E6	-
Branca [26]	Gas (Beech)	and Radiant Thermo-	153	4.38E9	-
	Oil	balance (16.7°C/s)	148	1.08E10	-
Wagenaar	Char	TGA and Entrained	125	3.05E7	-
et al. [103]	Gas (Pine)	Flow Reactor	177	1.11E11	-
	Oil		149	9.28E9	

[a]Values taken from the single component global three temperature result
[b]Universal$c$-values do not apply because the reactions are competing

6.5 Comparison Results

The implementation of the derived and the selected literature models contained in Tables 6.6-6.8 is provided in Figures 6.4-6.11 plotted against the Scots pine and Norway spruce experimental mean values with two standard deviation error bars. The agreement with the alternate species data is evaluated using a weighted least squared error (WLSE) term. This is calculated according to Equation 6.1,

$$WLSE = \frac{1}{\nu}\sum_{i=1}^{n}\left(\frac{\eta_i(t,T) - \eta_{model}(t,T)}{\sigma(t,T)}\right)^2 \tag{6.1}$$

where ν is the number of degrees of freedom, equal to the number of tests minus 1 because the model coefficients are not dependent upon the data points collected for *abies* and *sylvestris*. A WLSE was calculated for comparison of the models because it considers both the squared error and the standard deviation associated with the data point for which the squared error is calculated. This metric results in a weighting of the data according to the scatter in the experimental results.

WLSE values are contained in Tables 6.9 and 6.10 along with an average WLSE

Table 6.9: Norway spruce (NP) and Scots pine (SP) weighted least squared error (WLSE) results evaluated for Loblolly pine based models and literature models with average weighted least squared error ($\overline{\text{WLSE}}$) and normalized weighted least squared error ($\widehat{\text{WLSE}}$)

Model	NS WLSE	SP WLSE	$\overline{\text{WLSE}}$	$\widehat{\text{WLSE}}$
Single Comp. 3 Temp Global Fit	25.1	18.3	21.7	1.25
Two Comp. Global Fit	14.0	24.5	19.2	1.10
Inter. Solid Model Global Fit	21.2	13.6	17.4	1.00
Pseudo-comp Model Global Fit	24.5	21.7	23.1	1.33
Pseudo-comp Model w/ Milled Wood Lignin [105]	52.2	877	465	26.7
Pseudo-comp Model w/ Hydrolytic Lignin [104]	28.3	747	388	22.3
Pseudo-comp Model w/ Organosolv Lignin [104]	20.2	58.9	39.5	2.27
Single Comp. from Wagenaar [103]	384	286	335	19.3
Single Comp. from Di Blasi [26]	74.6	41.3	57.9	3.33
Single Comp. from Nunn [30]	313	1330	822	47.2
Pseudo-comp Model from Grønli [67]	623	293	458	26.3
Pseudo-comp Model from Manyà [83]	3450	2490	2970	171

and normalized WLSE according to the best numerical result. Final char yield predictions for the product based models are contained in Table 6.11 with % error calculations. Recall that the char yields are only useful for evaluation on a final yield basis because it is not possible to directly measure the amount of char present until the reaction is complete.

Table 6.10: Norway spruce (NP) and Scots pine (SP) WLSE results evaluated for Loblolly pine product based models and literature product based models with average weighted least squared error ($\overline{\text{WLSE}}$) and normalized weighted least squared error ($\widehat{\text{WLSE}}$)

Model	NS WLSE	SP WLSE	$\overline{\text{WLSE}}$	$\widehat{\text{WLSE}}$
Prod. Based Model Global Fit Oil	3.14	3.46	3.30	1.62
Prod. Based Model Global Fit Gas	2.44	1.63	2.04	1.00
Prod. Based Model from Di Blasi [26] Oil	11.0	30.3	23.2	11.4
Prod. Based Model from Di Blasi [26] Gas	15.1	1360	688	337
Prod. Based Model from Wagenaar [103] Oil	9.76	27.1	18.4	9.02
Prod. Based Model from Wagenaar [103] Gas	20.0	1610	815	400

Table 6.11: Final char yield predictions, measured values and % error

Scots pine				
	405°C		415°C	
Model	c_c	% Error	c_c	% Error
Measured	0.179	-	0.172	-
Prod. Based Model Final Char	0.248	38.6	0.230	33.7
Prod. Based Final Char - Di Blasi [26]	0.133	-25.7	0.123	-28.5
Prod. Based Final Char - Wagenaar [103]	0.176	-1.68	0.167	-2.91
Norway spruce				
	405°C		415°C	
Model	c_c	% Error	c_c	% Error
Measured	0.171	-	0.174	-
Prod. Based Model Final Char	0.248	45.0	0.230	32.2
Prod. Based Final Char - Di Blasi [26]	0.133	-22.2	0.123	-29.3
Prod. Based Final Char - Wagenaar [103]	0.176	2.92	0.167	-4.02

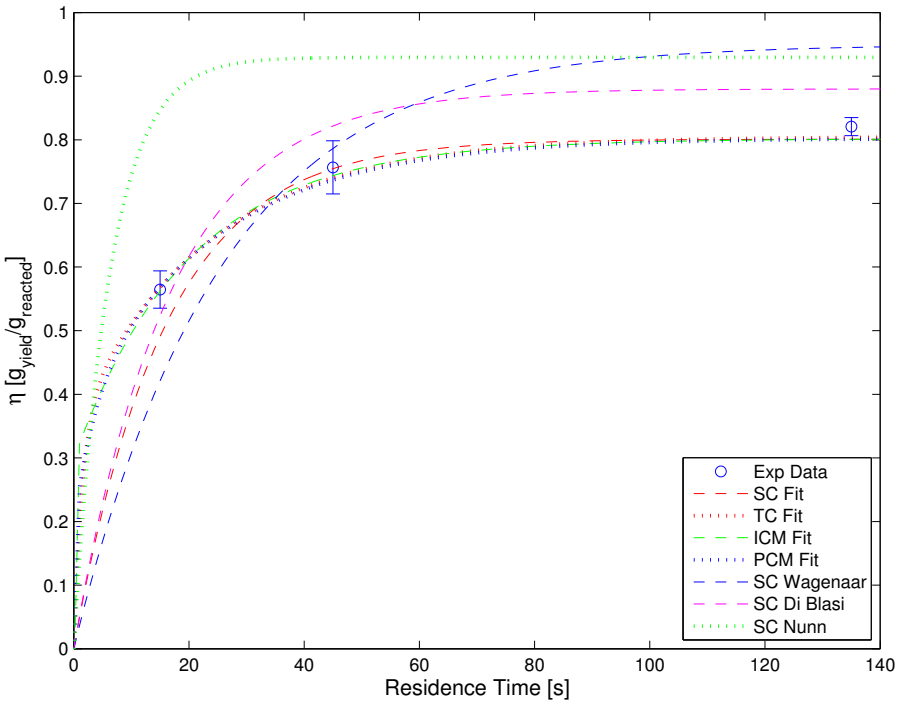

(a)

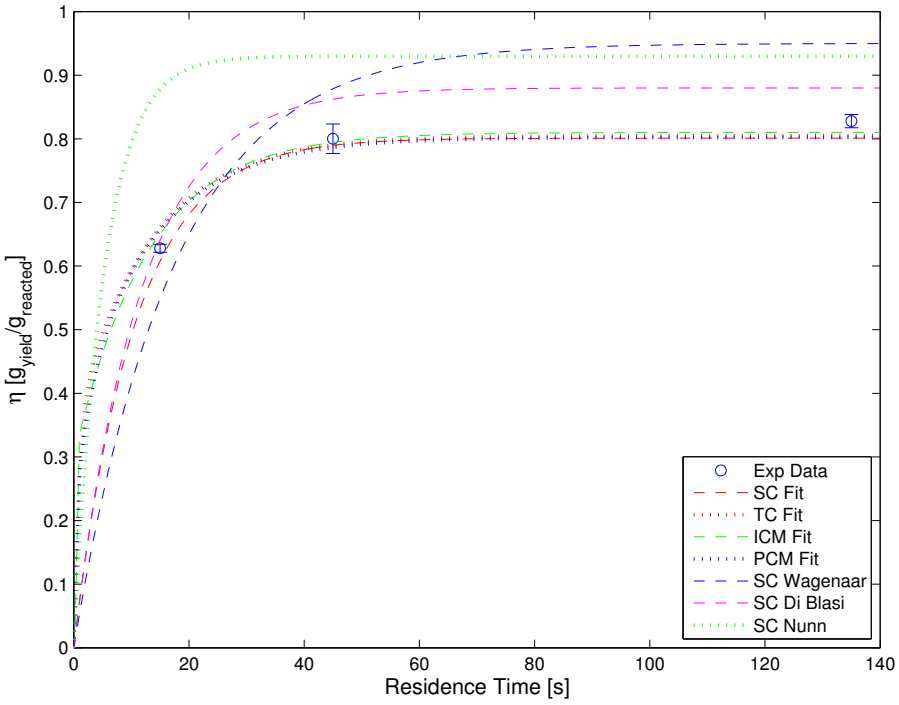

(b)

Figure 6.4: Scots pine (a) 405°C and (b) 415°C experimental mean total yield values with two standard deviation error bars plotted against the Loblolly pine single component global three temperature fit (SC), two component global fit (TC), intermediary compound model fit (ICM) and the pure pseudo-component model fit (PCM) as well as published single component global models from Di Blasi and Branca [26] and Nunn *et al.* [30].

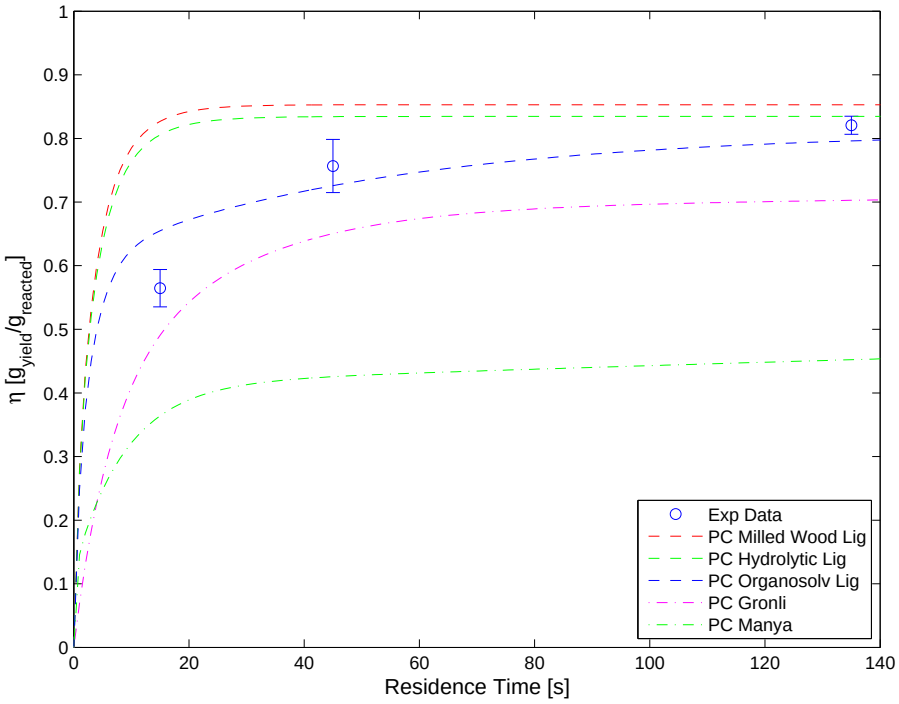

(a)

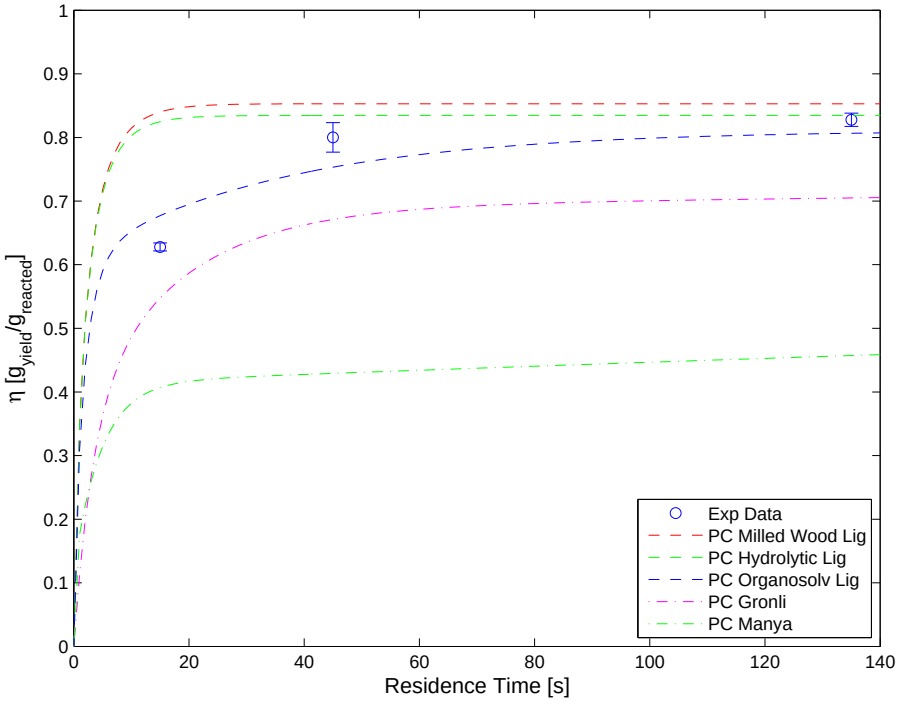

(b)

Figure 6.5: Scots pine (a) 405°C and (b) 415°C experimental mean total yield values with two standard deviation error bars plotted against the Loblolly pine pseudo-component (PC) model with three types of lignin from Refs [105] and [104] as well as published pseudo-component models from Grønli *et al.* [67] and Manya *et al.* [83]

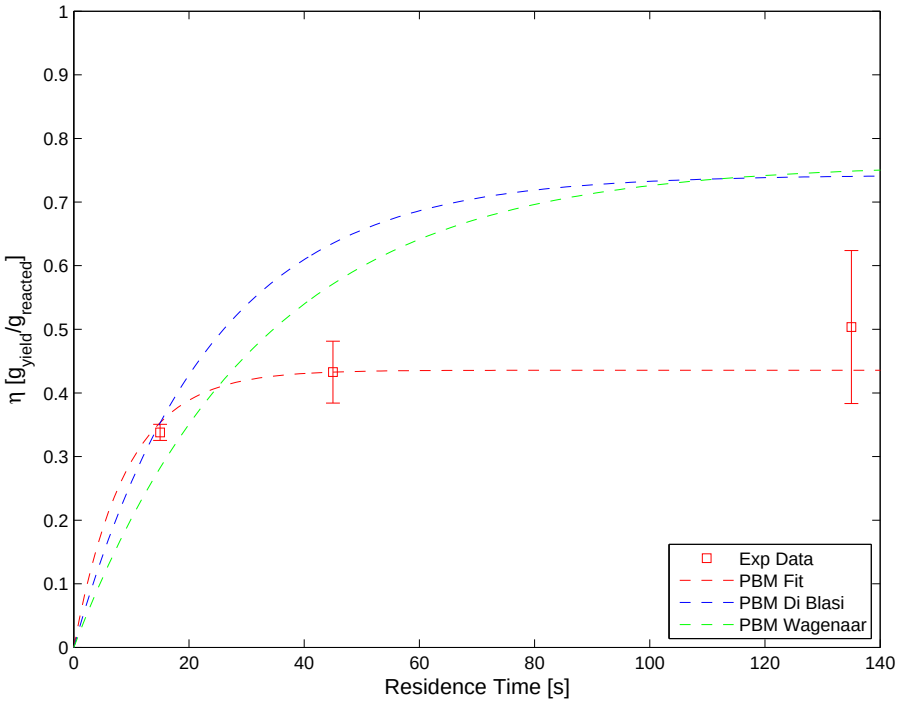

(a)

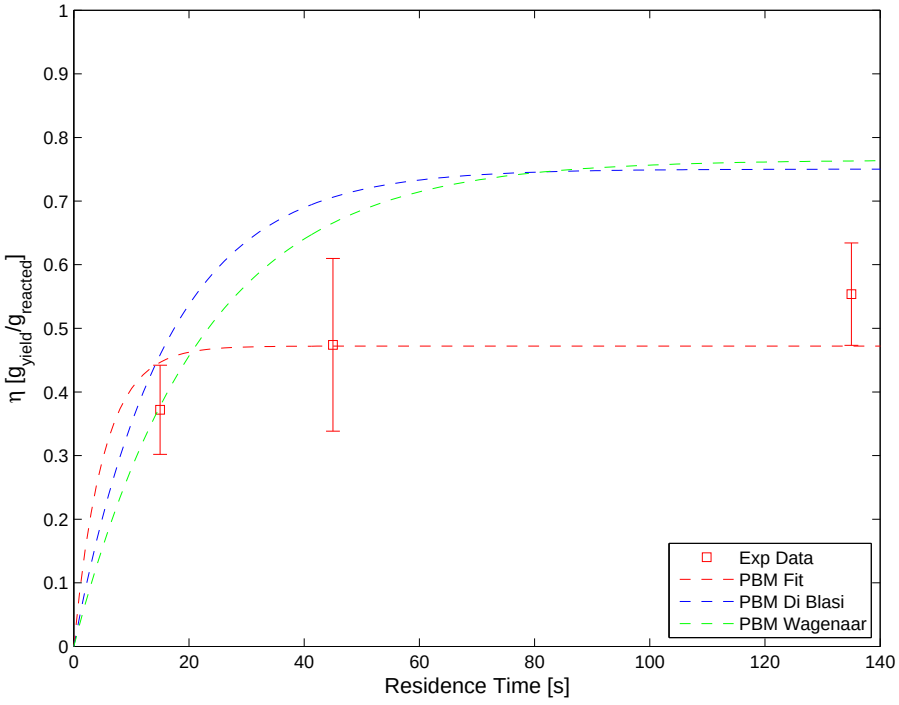

(b)

Figure 6.6: Scots pine (a) 405°C and (b) 415°C experimental mean oil yield values with two standard deviation error bars plotted against the Loblolly pine product based model (PBM) as well as published pseudo-component models from Di Blasi and Branca [67] and Wagenaar *et al.* [103]

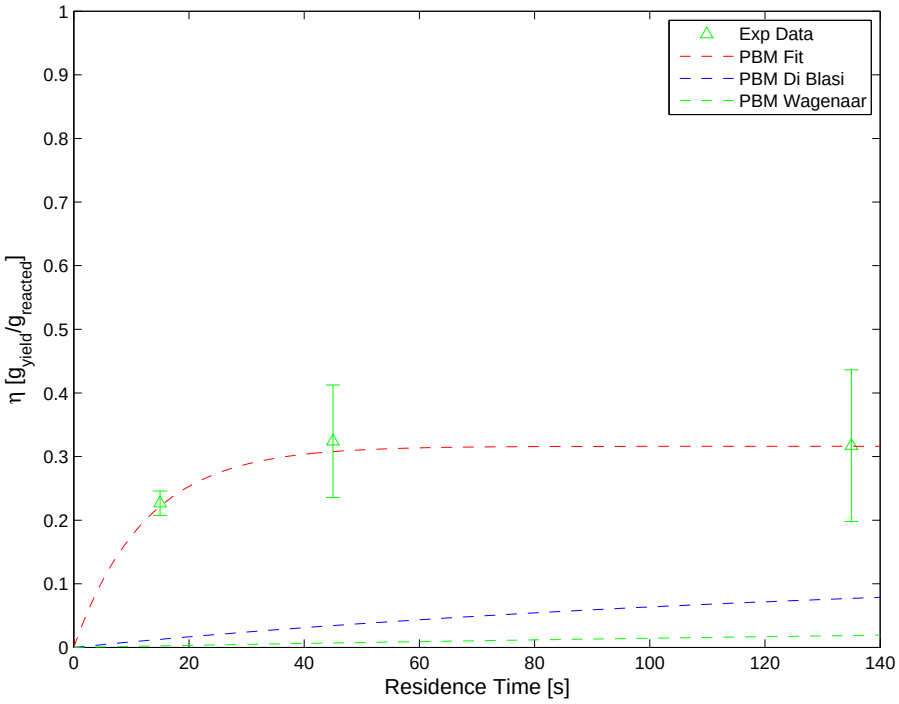

(a)

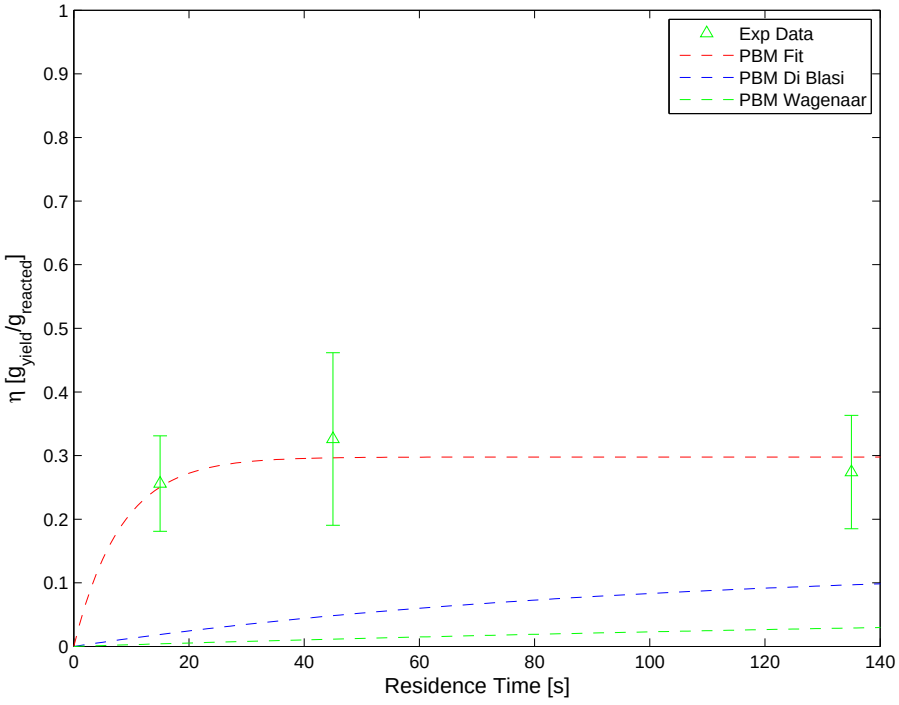

(b)

Figure 6.7: Scots pine (a) 405°C and (b) 415°C experimental mean gas yield values with two standard deviation error bars plotted against the Loblolly pine product based model (PBM) as well as published pseudo-component models from Di Blasi and Branca [67] and Wagenaar *et al.* [103]

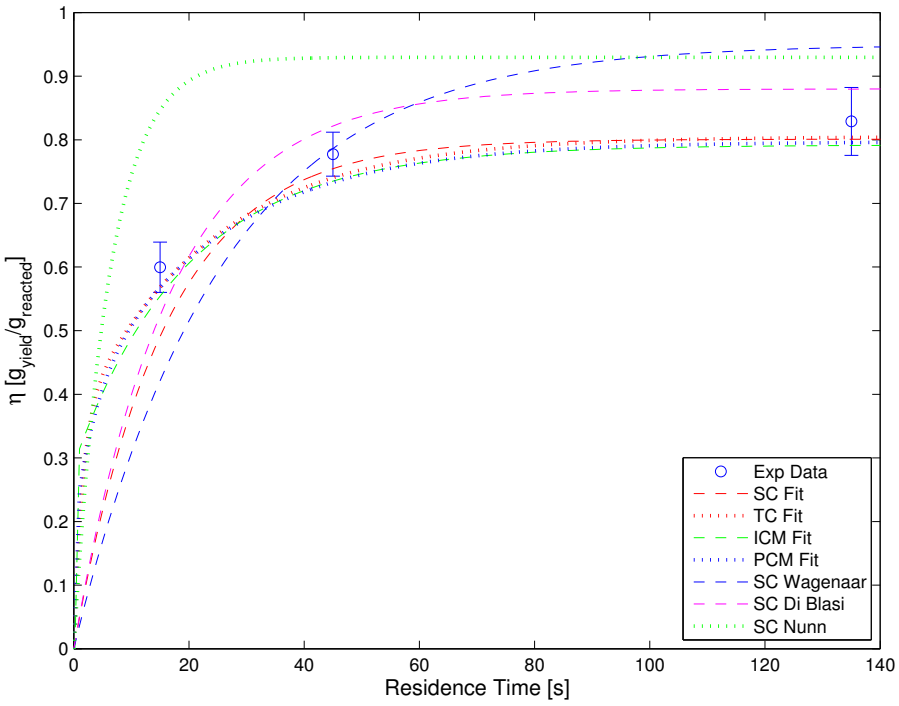

(a)

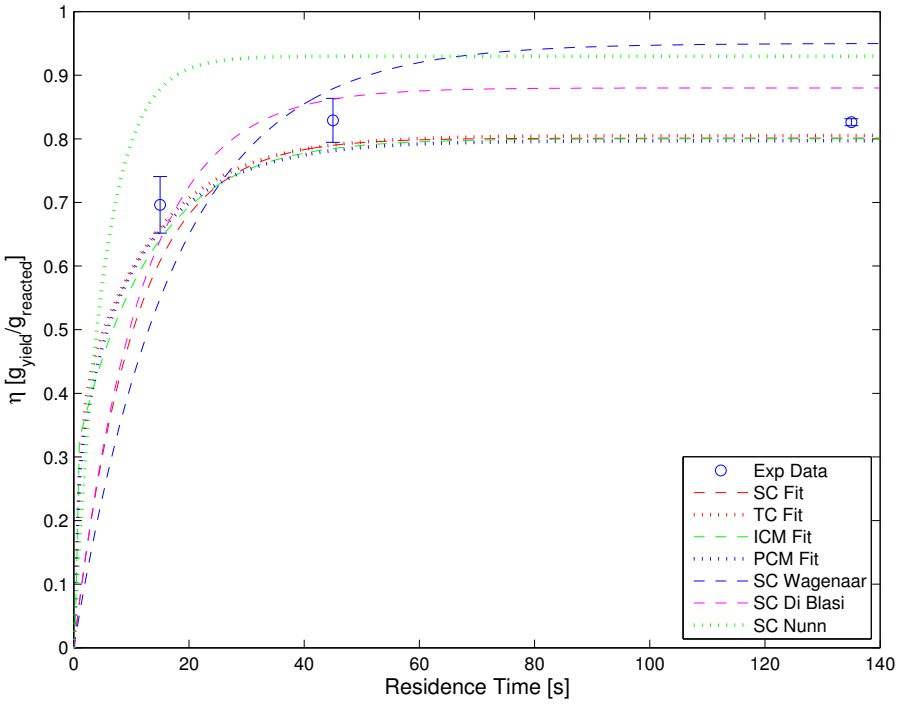

(b)

Figure 6.8: Norway spruce (a) 405°C and (b) 415°C experimental mean total yield values with two standard deviation error bars plotted against the Loblolly pine single component global three temperature fit (SC), two component global fit (TC), intermediary compound model fit (ICM) and the pure pseudo-component model fit (PCM) as well as published single component global models from Di Blasi and Branca [26] and Nunn *et al.* [30]

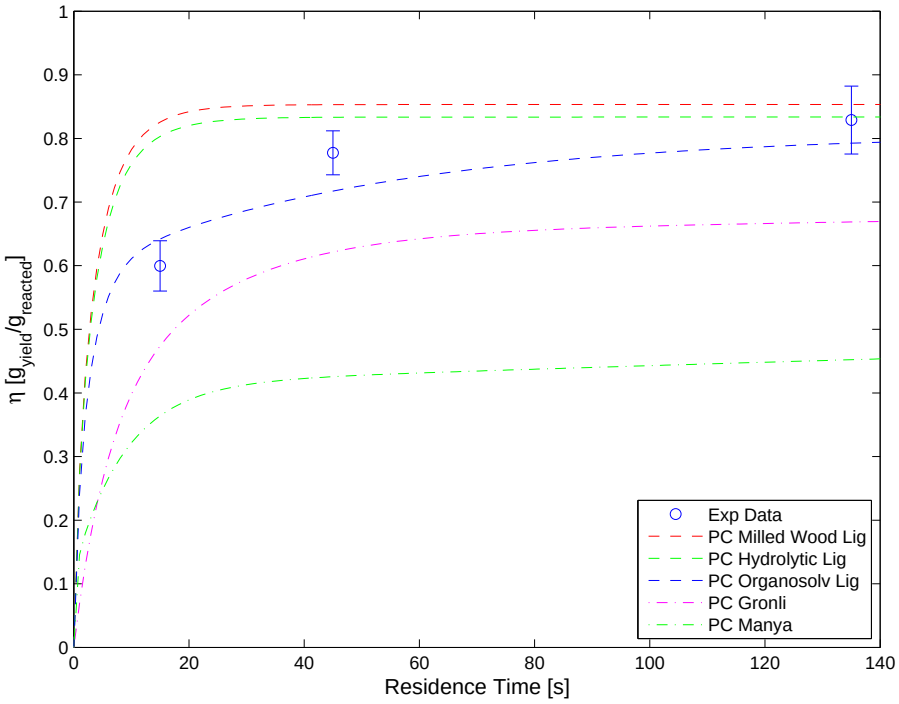

(a)

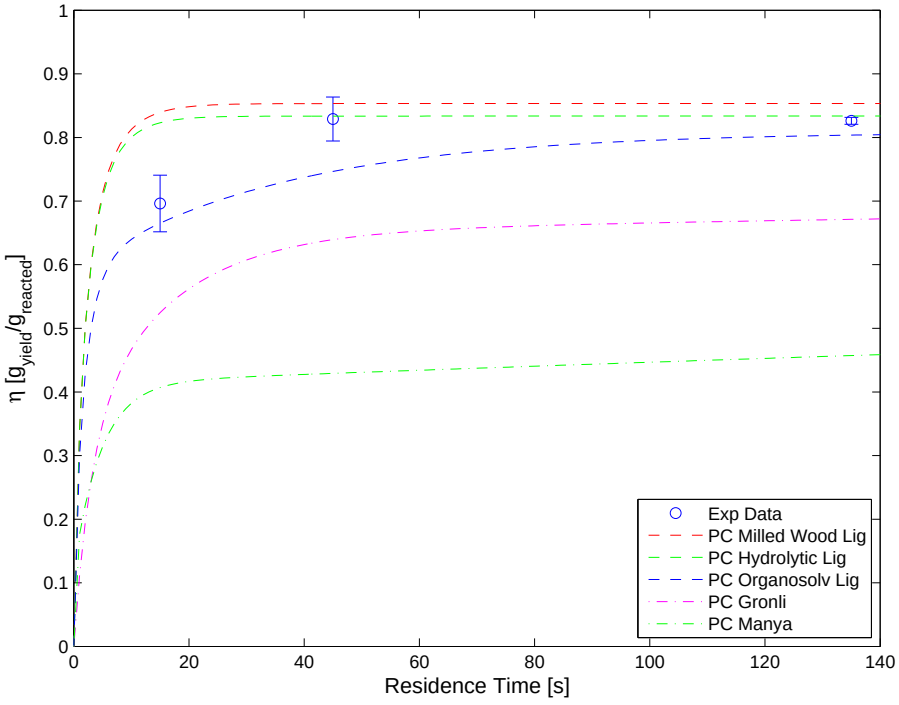

(b)

Figure 6.9: Norway spruce (a) 405°C and (b) 415°C experimental mean total yield values with two standard deviation error bars plotted against the Loblolly pine pseudo-component model with three types of lignin from Refs [105] and [104] as well as published pseudo-component models from Grønli *et al.* [67] and Manya *et al.* [83]

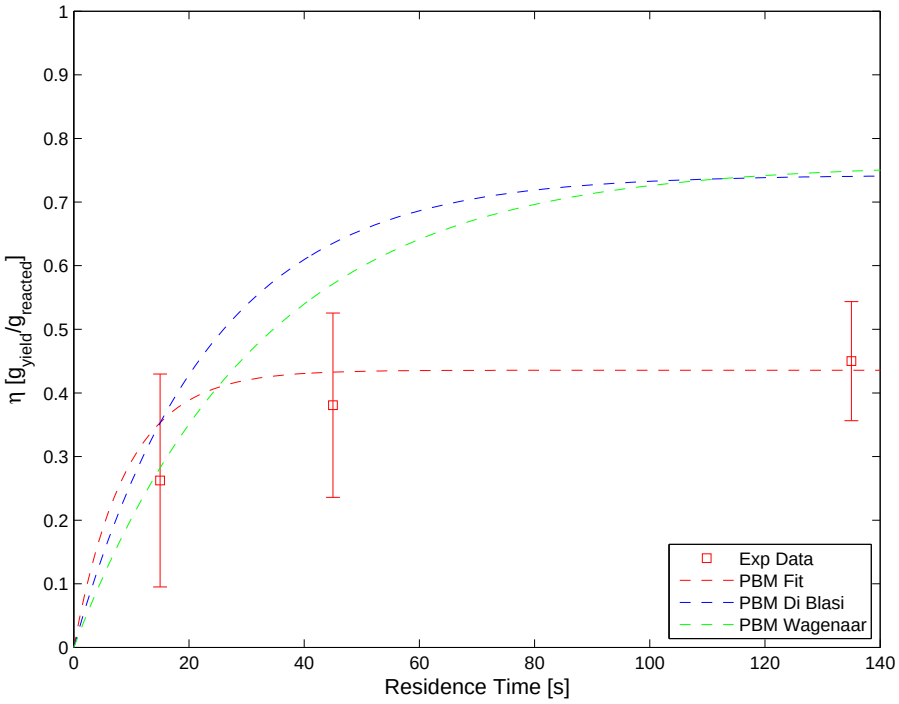

(a)

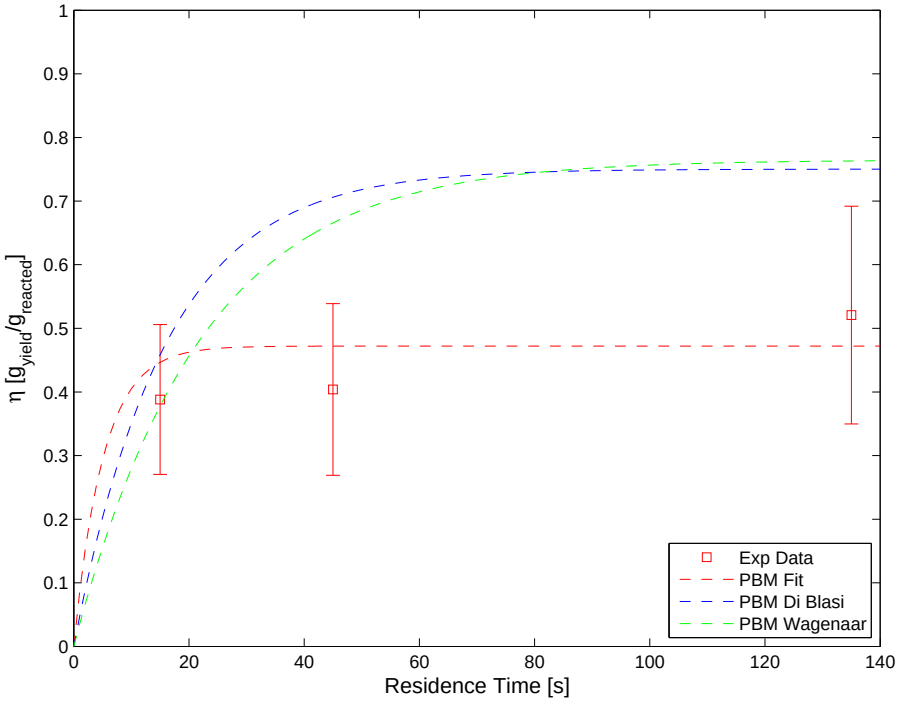

(b)

Figure 6.10: Norway spruce (a) 405°C and (b) 415°C experimental mean oil yield values with two standard deviation error bars plotted against the Loblolly pine product based model (PBM) as well as published pseudo-component models from Di Blasi and Branca [67] and Wagenaar *et al.* [103]

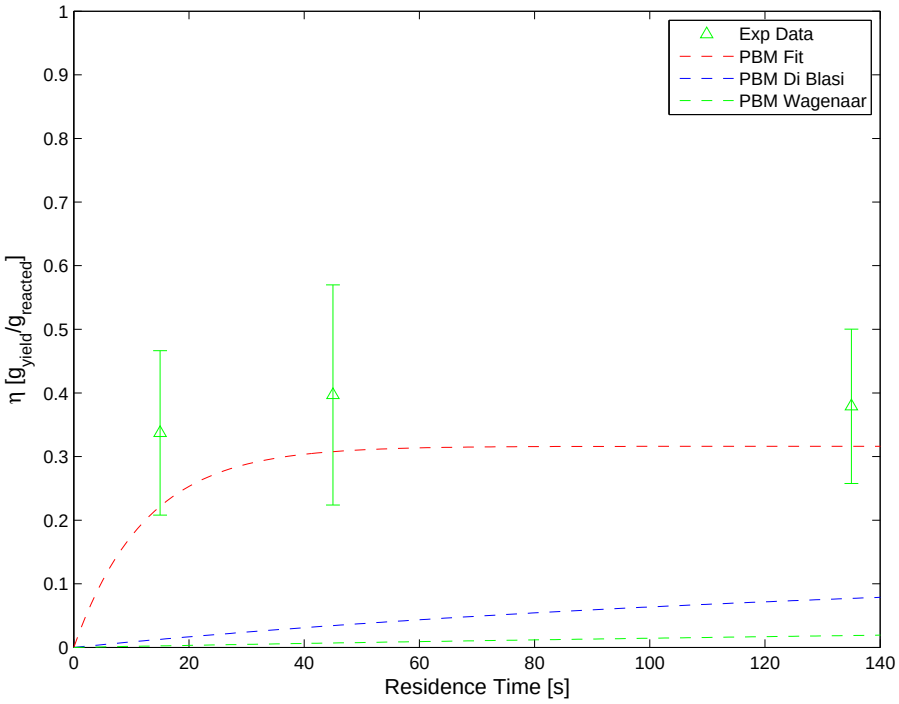

(a)

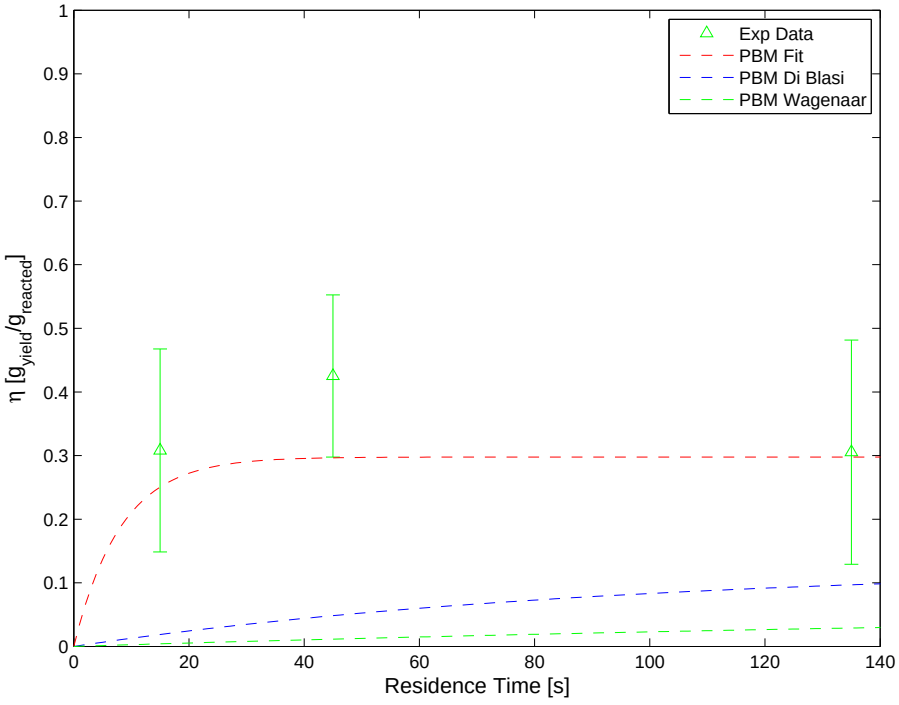

(b)

Figure 6.11: Norway spruce (a) 405°C and (b) 415°C experimental mean gas yield values with two standard deviation error bars plotted against the Loblolly pine product based model (PBM) as well as published pseudo-component models from Di Blasi and Branca [67] and Wagenaar *et al.* [103]

6.6 Fast and Slow Pyrolysis Kinetic Comparison

Within kinetic derivation studies several issues have been identified which make the case that fast and slow pyrolysis kinetics are not interchangeable:

- The wide range of activation energies reported for whole wood pyrolysis (89-175kJ/mol) has been attributed to varied heating conditions within the tested reactors [26]
- The failure in some studies to account for particle size results in the combining of heat and mass transfer effects with perceived kinetic rates [27, 106, 92]
- The temperature histories inherent in low heating rate studies are frequently left unaddressed [27, 103]

6.6.1 Slow Pyrolysis Methods and Results

Effective comparison between slow and fast pyrolysis derived kinetic parameters requires that the same feedstock be used to derive both the fast and slow pyrolysis results. An evaluation of the slow pyrolysis of Loblolly pine will be performed using a TA instruments Q50 thermogravimetric analysis oven (TGA). A constant heating rate of 0.167°C/s (10.0°C/min) was used and an initial sample mass of 8.4mg reacted. The oven temperature range tested was from 25°C to 600°C. The inert environment is provided using a nitrogen purge. The TGA sampling rate was by default 2Hz which resulted in significant noise within the TGA derivative plots due to overlapping thermocouple and mass balance measurement noise. Signal filtering was performed using a zero phase finite impulse response (FIR) filter. This type of filter is well suited to the decay of the biomass during pyrolysis because it continuously adjusts for the dynamic bias of the signal. The zero phase element is accomplished by filtering the signal both forwards and backwards. By doing so, the resultant filtered signal is not shifted in the time domain, and in this case subsequently the temperature domain.

The filter was applied using the Matlab *filtfilt* function. [107]

The residual mass as a percentage is calculated using Equation 6.2,

$$R = \frac{m_T}{m_0} \tag{6.2}$$

where m_T is the mass remaining at temperature T and m_0 is the initial mass. The instantaneous rate of pyrolysis at any given temperature is evaluated using Equation 6.3,

$$k = \frac{-(dm/dt)|_T}{m_T - m_{char}} \tag{6.3}$$

where m_{char} is the final mass of residual char. These results can then be plotted on a traditional $\ln k$ versus $1/T$ Arrhenius plot. Kinetic parameters of an Arrhenius form were extracted from the locally linear regions of the Arrhenius plot and then correlated to the typically assigned pseudo-components based upon literature. [18] On an Arrhenius plot a linear segment correlates to Equation 6.4,

$$\ln k = \ln A - \frac{E_a}{RT} \tag{6.4}$$

Thus the slope of any linear region of the TGA rate curve is the effective activation energy divided by the negative of the reciprocal of the universal gas constant (*i.e.* slope $= -E_a/R$). The corresponding vertical axis intercept is the natural logarithm of the pre-exponential factor (*i.e.* $\ln A$). This theoretically corresponds to the maximum rate of reaction when an infinite amount of thermal energy is supplied.

TGA oven results as a percentage of starting mass are shown in Figure 6.12 with the subsequent derivative curve in Figure 6.13. The derivative plot shows both the unfiltered and filtered results overlaid to demonstrate the effect of the finite impulse filter on the data.

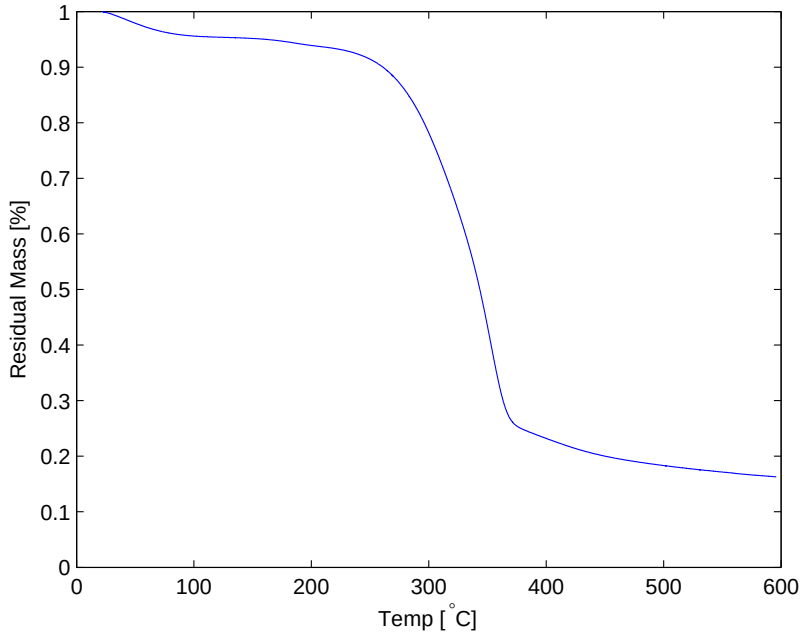

Figure 6.12: Loblolly pine TGA oven residual mass results as a function of temperature, normalized to the initial mass value

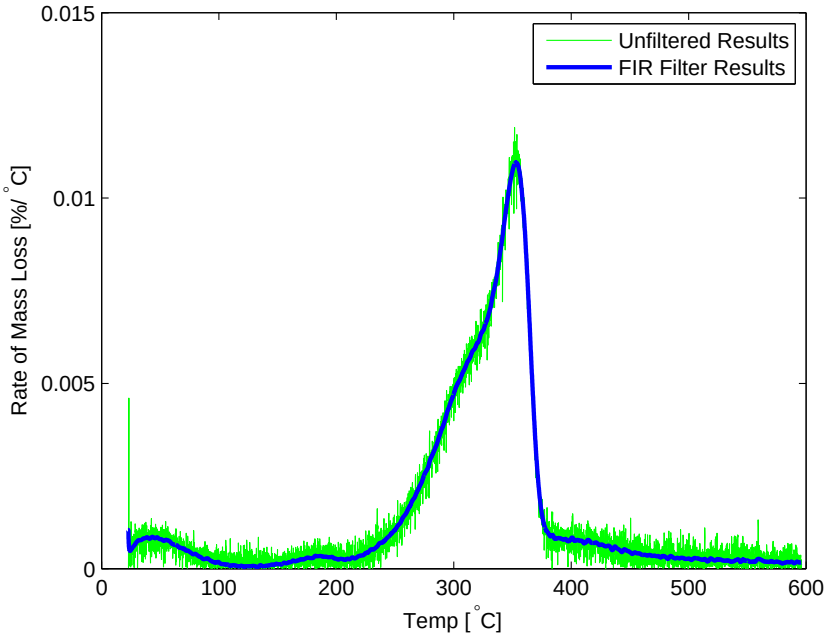

Figure 6.13: Loblolly pine TGA oven derivative curves as functions of temperature showing both the filtered and unfiltered results

6.6.2 The Comparison and Overlay of Slow and Fast Pyrolysis Kinetic Parameters

The kinetic rates determined from TGA results for Loblolly pine and micro-reactor single component global model results for Loblolly pine are plotted in Figure 6.14a. TGA data obtained for temperatures below 200°C was omitted from the Arrhenius plot because any mass loss observed before this point is associated with loss of water and extractives, not pyrolysis. Data above 500°C was omitted from the Arrhenius plot because the derivative plot in Figure 6.13 shows that the reaction has nearly ceased and the data is dominated by noise despite the applied filtering.

Each of the three linear regions on the TGA derived $\ln k$ versus $1/T$ plot are typically correlated (from right to left) with hemicellulose, cellulose, and lignin. [18] The linear regions for kinetic parameter approximation were bounded by qualitative graphical analysis. The hemicellulose pyrolysis region was bounded from $230 - 300$°C. The cellulose pyrolysis region was bounded from $340 - 360$°C. The lignin pyrolysis region had appreciable noise associated with it even after filtering, so the first semi-linear segment ($390 - 430$°C) was used for kinetic parameter approximation. Performing least squares regression fits on the respective linear regions yielded the coefficients of an Arrhenius form given in Table 6.12. Of particular note is the low pre-exponential value calculated for Lignin. This is, however, in agreement with results published by Grønli [18] from the TGA pyrolysis of Scots Pine with a calculated pre-exponential of $4.79\text{E} - 1\text{s}^{-1}$. Projections of the best fits to the linear regions of the TGA kinetic results are shown in Figure 6.14b with the three temperature single component best fit line overlaid.

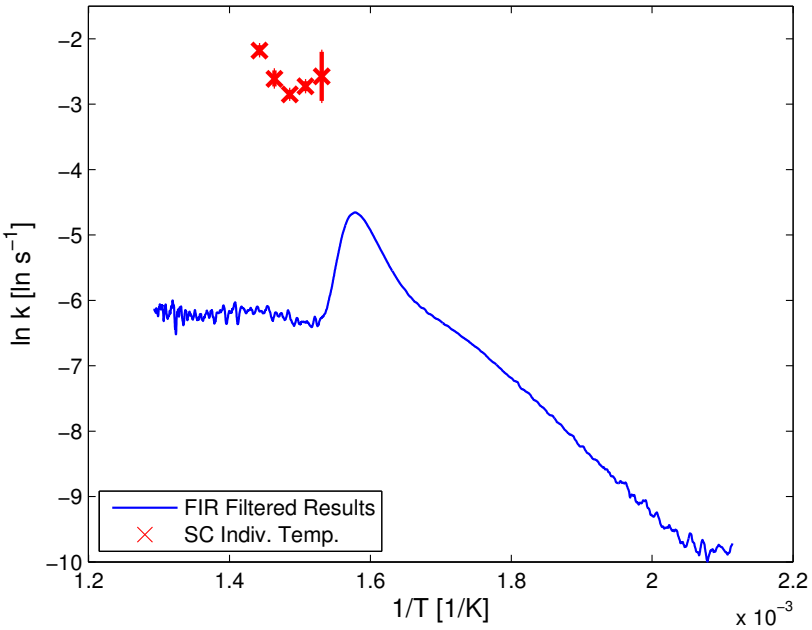

(a)

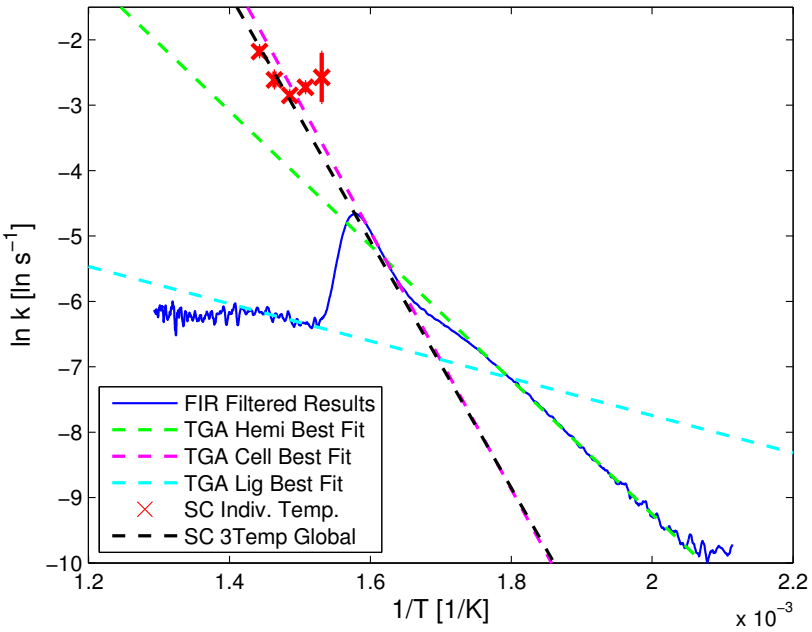

(b)

Figure 6.14: Arrhenius plots of slow and fast pyrolysis experimentally determined fits: (a) Single component (SC) data points for individual temperatures are plotted with 95% confidence intervals indicated. (b) The rate curve from TGA is plotted with best fit lines to the corresponding pseudo-component semi-linear regimes (from right to left: hemicellulose, cellulose and lignin). The three temperature single component fit to fast pyrolysis results is also plotted.

Table 6.12: Kinetic coefficients of an Arrhenius form derived from slow pyrolysis TGA results correlated to expected pseudo-component pyrolysis regimes

	TGA		
Component	A [1/s]	E_a [kJ/mol]	R^2
Hemicellulose	8.12E4	85.5	0.999
Cellulose	3.46E11	164	0.999
Lignin	1.29E-1	23.7	0.707

Further evaluation of slow and fast pyrolysis kinetic parameter interchangeability was performed by comparing the predicted conversions against verification data from 400°C fast pyrolysis tests. The single component three temperature fit of Chapter 4 was used and the slow pyrolysis kinetic parameters of Table 6.12 were applied to Equation 6.5 for the prediction of pyrolysis yields,

$$\eta_{wood} = \phi_{cell}\eta_{cell} + \phi_{hemi}\eta_{xyl} + \phi_{lig}\eta_{lig} \tag{6.5}$$

The predicted conversions and verification data are plotted in Figure 6.15.

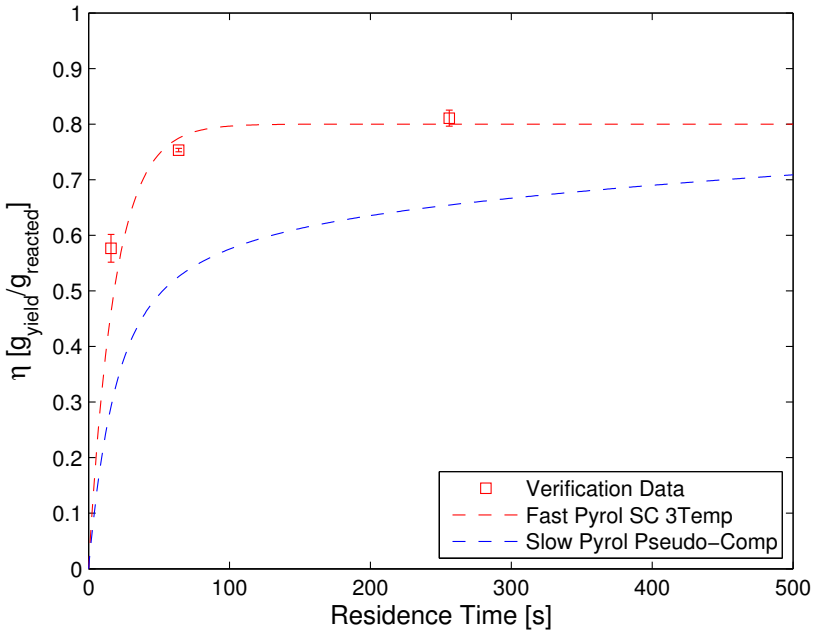

Figure 6.15: Predicted pyrolysis yields using fast and slow pyrolysis derived kinetic parameters plotted against fast pyrolysis verification data at 400°C

6.7 Discussion

Model validation percentage error results show that the two component model provided for the lowest average absolute error at 1.94% followed by the pseudo-component best fit model at 2.09%. The intermediate solid model produced an error of 2.9%, significantly greater than that for the two component and pseudo-component models, an unexpected departure from the superior fit observed in Chapter 5. The product based model provided very poor predictions with absolute average errors of 24.9% and 97.7% for the oil and gas predictions respectively.

The intermediate solid model showed the most predictive capability among the alternate species predictions for total volatiles with an average weighted least squared error (WLSE) of 17.4. This best value was then used as a normalization factor for comparison between the models. The next best predictors were the two component global and single component global models with normalized weighted least squared error values of 1.10 and 1.25 respectively. The intermediate solid model, however,

was also the mechanism requiring the greatest number of terms.

The product based oil and gas predictions derived from Loblolly pine produced significantly improved fits compared to the original fits for which the models were derived. The average WLSE values for the oil and gas were 3.30 and 2.04 respectively. The predicted final char yields from Table 6.11, however, show that the product based model over-predicted the char yields by an average of 33.7%. This is in contrast to the results from the model fits in Chapter 4 in which the global kinetic parameters used for solids predictions (from the three temperature Loblolly pine single component results) produced a significantly better fit than the gas and oil results.

The best global single component model from literature, and best overall literature model, was from Di Blasi and Branca [26]. The kinetic parameters were derived under well controlled and well validated pyrolysis conditions, though on a dissimilar species of biomass and at moderate heating rates (16.7°C/s). Both product based models from Di Blasi and Wagenaar proved to have normalized WLSE values of the same order. In both cases, the predicted oil yields were significantly higher and the predicted gas yields significantly lower than those measured. The model by Wagenaar, however, produced the best prediction of final char values with only 2.91% and 4.02% absolute error for the Scots pine and Norway spruce respectively. The over prediction of oil yields and under prediction of gas yields is likely due to differing condensation methods between studies. Condenser configurations used are very infrequently disclosed in literature. The actual condenser operating temperatures are also not reported. For the pyrolysis of small samples within the micro-reactor, the condenser effectiveness was impeded by the need to decrease the overall mass. Consequently, a longer (and heavier) condenser may have allowed for more product collection and better agreement between yields, at least by final yield values.

The pseudo-component models showed very poor predictive power, both amongst the isolated pseudo-component model derived in this work (with multiple lignin values

from literature) and pseudo-component models from literature. The experimentally rigorous model by Grønli, derived from multiple species, showed poor predictive power with WLSE values of 623 and 293 for Norway spruce and Scots pine respectively. This model, however, relied on the typical TGA methods discussed earlier for which large departures were observed between the TGA derived slow pyrolysis kinetics and the micro-reactor derived fast pyrolysis kinetics from Loblolly pine. Manyã's TGA derived results from isolated pseudo-components proved to provide even worse fits than those obtained using Grønli's model with an average WLSE value of 2970. The poor predictive power should not be solely attributed to the instrument used but also to the apparent interactions between pseudo-components under fast pyrolysis conditions, as was demonstrated in Section 5.8.1.

Graphical evaluation of Figure 6.14a shows clearly that the slow and fast pyrolysis kinetic parameters are distinctly different based upon the lack of observed overlap in the kinetic rate values measured within the micro-reactor and the TGA. Partial agreement between the slow and fast pyrolysis kinetic values is only attainable by projecting the semi-linear TGA region typically attributed to cellulose pyrolysis up to the tested micro-reactor temperatures, as shown in Figure 6.14b. Comparison of the activation energies ($E_{a,TGA,cell}$ = 164kJ/mol and $E_{a,MR,Loblolly}$ = 157kJ/mol) shows a 4.5% difference while the pre-expontial factors ($A_{TGA,cell}$ = 3.46E11s^{-1} and $A_{MR,Loblolly}$ = 8.28E10s^{-1}) differ by more than a factor of 3. The impact of this approximately 5% difference in activation energy values will be quantified in Section 7.11.

Comparison of the attributed cellulose region of the TGA rate curve to that projected by the fast pyrolysis cellulose results shows an even more significant disagreement. The micro-reactor fast pyrolysis results for cellulose ($E_{a,MR,cell}$ = 145kJ/mol and $A_{MR,cell}$ = 4.52E10s^{-1}) differ from the TGA cellulose region results by 12% for the activation energy and by a factor of 6.7 for the pre-exponential factor. The

TGA hemi-cellulose attributed region results differ from micro-reactor xylan kinetic parameters by 25% between the activation energies ($E_{a,TGA,hemi} = 85.5$kJ/mol and $E_{a,MR,xyl} = 107$kJ/mol) and by four orders of magnitude between the pre-exponential factors ($A_{TGA,hemi} = 8.12\text{E}4\text{s}^{-1}$ and $A_{MR,xyl} = 2.08\text{E}8\text{s}^{-1}$). The disagreement between the TGA rate curve region attributed to cellulose and the tested Avicel cellulose may be due to sample isolation techniques [22] or residual mineral content within the isolated samples. The comparison to TGA pyrolyzed Avicel cellulose results in literature presented in Section 5.8.1, however, indicates that the disagreement is more likely the result of reactor thermal conditions. The same argument can be made for the comparison between the hemicellulose semi-linear region and the the Beechwood xylan micro-reactor results with the additional consideration that hemicellulose is actually composed of multiple carbohydrate components. [88]

The 380°C and 390°C fast pyrolysis kinetic rate values (the two rightmost x's of Figure 6.14a) fall well outside of the line formed by the $400 - 420$°C results even with the 95% confidence intervals considered. This is in agreement with assessments made in Section 4.8.1 that the single component fit is not suitable for the tested reactor temperatures below 400°C.

6.8 Summary

The fitted models of Chapters 4 and 5 were evaluated using both validation data from Loblolly pine pyrolysis and extensibility data from the fast pyrolysis of Norway spruce and Scots pine. The validation results showed that the two component model produced the best predictive result with an absolute average error of 1.94%, followed by the pseudo-component model with an absolute average error of 2.09% and the intermediate component model at 2.90%.

The intermediate component model proved to be the best predictor of alternate species and the pseudo-component and single and two component global models are

nearly equally good predictors. Additionally, the global single component kinetic model proposed by Di Blasi and Branca [26] was determined to be the best literature model evaluated. This is attributed to the well controlled experimental conditions within that study, which are most similar to the fast pyrolysis conditions observed here. Specifically, the separation of heat and mass transfer pathways in accompaniment with significantly increased heating rates over TGA (16.7°C/s).

The pseudo-component models based upon isolated pseudo-component kinetic values showed poor fit qualities overall. This can be attributed to the interactions taking place between pseudo-components and the commonly cited presence of mineral content acting as a catalyzing agent. The stark disagreement between predictions made using slow pyrolysis derived pseudo-component kinetic parameters is attributed to what appears to be a different set of kinetic pathways. This is supported by the observations made in Chapter 5 in which the pyrolysis of isolated pseudo-component mixtures showed a significant retardation of the pyrolysis reaction which was not previously observed in slow pyrolysis pseudo-component mixture studies.

The product based model presented in Chapter 4 proved to be a better fit to the alternate species oil and gas data than the initial Loblolly pine fits with an order of magnitude improvement in the fit quality. The final char yields, though, were over predicted by nearly 35%.

For future application, the single component or two component global models are likely to be the most practically implementable due primarily to simplicity and similarity of the predictive result qualities to the more complicated intermediate solid model.

Fast pyrolysis kinetic parameter results were plotted against slow pyrolysis kinetic rate results from a TGA oven. The disagreement between the TGA derived slow pyrolysis rate results and those for fast pyrolysis shows very clearly that the observed kinetic rates are not the same. This indicates that a different series of kinetic

mechanisms is likely taking place when the temperature history typically encountered under slow pyrolysis conditions is not followed. Furthermore, the large discrepancies between kinetic values is indicative of errors introduced by applying kinetic parameters to models far outside the range of thermal conditions for which the parameters were derived. These conclusions are in agreement with previous studies. [26, 108] This is, however, the first graphical demonstration of this type and the first time this has been demonstrated under such diametrically opposed thermal conditions using the exact same feedstock.

CHAPTER 7

APPLICATION OF KINETIC DESCRIPTORS TO PARTICLE BED PYROLYSIS MODELING

7.1 Introduction

The purpose of this chapter is to demonstrate the application of fast pyrolysis kinetics to the simulation of fast pyrolysis within a moving bed vacuum pyrolysis reactor. The model scope is constrained to one-dimensional transport with two boundary conditions, which is a reasonable approximation for modeling along the smallest dimension of a low aspect ratio bed (H/L). The model is applied for the prediction of temperature profiles, heating rates, specific heating power requirements (on a raw wood feedstock basis) and pyrolysis yields as a function of time. The model has been developed as a design tool that provides an evaluation of key parameters in a fast computationally efficient manner. The model is applied to the prediction of pyrolysis yields within the micro-reactor and compared to experimental results. Additionally, the extensibility of the model to the sizing of a moving bed reactor is demonstrated and the impact of activation energy variations evaluated.

7.2 Nomenclature

a	Internal Wetted Surface Area	Re	Reynold Number
c	Specific Heat	S	Product Source Term
g	Gravitational Acceleration	T	Temperature
h_{loc}	Local Internal Convection Coeff	V	Volume
k	Pyrolysis Kinetic Rate	w	Width
m	Mass	α	Thermal Diffusivity
n	Node Number	ϵ	Emissivity
p	Pressure	$\hat{\epsilon}$	Porosity
t	Time	κ	Thermal Conductivity
v_0	Superficial Velocity	μ	Viscosity
x, y, z	Spacial Positions	ξ	Particle Shape Factor
A	Area	ρ	Density
B	Constant for Blake-Kozeny Eq	σ	Stephan Boltzman Constant
D	Mass Diffusivity	τ^*	Characteristic Time Scale
E	Internal Energy	ψ_v	Pyrolysis Volatile Fraction
H_{bed}	Particle Bed Height	ΔH_{py}	Heat of Pyrolysis
Fo	Fourier Number		
K	Permeability		*Subscripts*
L	Length	ad	Advection
L_c	Characteristic Length	c	Char
M	Molecular Weight	$cond$	Conduction
N	Last Node in FD Array	$conv$	Convection
N''	Number of Particles	g	Gas
Nu	Nusselt Number	gen	Generation
P	Perimeter	s	Solid
Pr	Prandtl Number	w	Wood
R	Universal Gas Constant	Δp	Pressure Driven

7.3 Salient Literature

7.3.1 Vacuum Fast Pyrolysis Systems

Few scaled vacuum fast pyrolysis systems have been published. In 1997 Roy *et al.* [109] presented a stirred moving bed vacuum pyrolysis reactor. This technology was later patented and scaled up for production under the company name Pyrovac. [110] The results from the large scale application of this technology are unknown as the company later encountered financial troubles and eventually collapsed. Further research has since been conducted on the technology initially presented by Roy *et al.*.

Yang *et al.* [111] studied the overall heat transfer coefficient of the particles within a stirred bed looking at both the moving bed configuration proposed by Roy and a stirred bed rotary reactor. Gupta *et al.* [112] investigated the characterization of the flow within moving and stirred beds of the configuration proposed by Roy. Beyond these few studies, there are no other published works pertaining to moving bed fast pyrolysis reactors.

7.3.2 Pyrolysis Modeling

The modeling of fast pyrolysis is of interest for reactor design and optimization efforts with the goal of producing bio-oil end products. The modeling of pyrolysis requires the use of general kinetic descriptors for conversion rate predictions due to the complexity of the pyrolysis process. Additionally, property evaluations are required for the multitude of physical parameters necessary to model the pyrolysis process. Many property values used are estimations that have been shown to be effective within pyrolysis models but have not yet been measured. This is due to the difficulties in measuring properties such as diffusivity, thermal conductivity and molecular weight in volatile and unstable products such as those produced during pyrolysis.

Pyrolysis models have been demonstrated to accurately predict pyrolysis outcomes within specific configurations using a combination of measured and derived physical parameters. [113, 100, 114, 115, 18] Additionally, some models have also helped to better identify property values and their variations under changing thermal conditions by fitting to experimental results.

In the aforementioned study by Bamford *et al.*, [61] pyrolysis was studied as a step in the combustion of individual wood particles providing the first known pyrolysis model. The pyrolysis was treated as a single component devolatilization mechanism following a first order Arrhenius reaction mechanism. Heat transfer through the particle was considered and diffusion within the biomass was assumed to occur at a

rate equal to the rate of pyrolysis. All properties were assumed constant. Though significant simplifications were made, modest agreement with experimental particle temperature measurements was shown.

In the aforementioned study by Roberts and Clough, [17] the radial heat transfer within wood cylinders was modeled and pyrolysis experiments were conducted on radiantly heated cylinders of Beechwood with embedded thermocouples. The purpose of the study was to evaluate the suitability of first order kinetics in modeling wood pyrolysis and estimate the enthalpy change as a result of pyrolysis product formation, commonly referred to as the heat of pyrolysis. Through the application of the heat transfer model the authors concluded that the heat of pyrolysis was exothermic and is a result of the presence of secondary reactions between trapped volatiles and residual solids.

Kansa *et al.* [113] formulated a one dimensional pyrolysis model for the transient charring of wood slabs. The impact of wood porosity on volatile flow and removal was considered in addition to the accounting for heat transfer with a radiant boundary condition. The results showed modest agreement with published experimental values at low heat fluxes and poor agreement at higher heat flux boundary conditions.

Pyle and Zaror [94] investigated the applicability of non-dimensional scale analysis ratios to the prediction of limiting phenomena during the pyrolysis of biomass. The Biot number ($Bi = hL_c/\kappa$) was used to evaluate the ratios of external convective heat transfer to internal conduction. Two pyrolysis numbers were defined ($Py = \alpha/kL_c^2$ and $Py' = h/k\rho c_p L_c$) to evaluate the ratio of internal conduction to the rate of pyrolysis and the ratio of external convection to the rate of pyrolysis. The non-dimensional numbers were then used to classify pyrolysis processes by controlling factors: External heat transfer limited; Kinetically limited; or Internal heat transfer limited. Verification experiments were conducted in a tubular TGA furnace on pine cylinders of varying diameter with embedded thermocouples. The results showed

that the limiting phenomena was accurately predicted using the non-dimensional scale factors.

Miller and Bellan [100] formulated both a kinetically limited model and a heat and mass transfer pyrolysis model based upon modified pseudo-component superposition kinetics. Within the kinetically limited model, agreement was shown to be highly dependent upon the reaction conditions (*i.e.* heating rate and final temperature). The heat and mass transfer model assumed that biomass particles can be modeled as spheres and employed the full momentum conservation equation instead of applying Darcy's law, which was noted as the typical simplification. Qualitative agreement with literature was demonstrated and quantitative agreement was shown for small particle sizes and high reactor temperatures. Appropriate property selection was noted as begin very important to the model's predictive accuracy.

Di Blasi [114] constructed a heat and mass transfer pyrolysis model for radiantly heated samples, but included the impact of temperature dependency of property values. Specifically, the change in the solid phase with the production of char and consumption of wood as well as the change in the volatiles as a product of secondary reactions. The shrinkage of the particle and subsequent decrease in the available internal volume was also accounted for. Particle shrinkage impacted both the effective thermal conductivity and the internal pressure of the pyrolyzing biomass. Qualitative agreement with literature was shown. Quantitative departures were stated to be the result of poorly characterized properties for char and partially charred wood.

The work of Di Blasi was later built upon by Grønli and Melaaen, [115, 18] who included the effects of high initial water content within large biomass particles. This required the inclusion of the enthalpy of vaporization as well as accounting for simultaneous water and volatile species transport. Grønli *et al.* noted [115] that the most difficult task was the correct selection of a reaction model and its kinetic parameters. The model showed good predictive power to the radiant heating of large

biomass particles. A sensitivity analysis revealed that mass transfer effects were only significant in predicting secondary reactions.

Bharadwaj *et al.* [116] built upon the works of Grønli and Di Blasi by considering the devolatilization and combustion of biomass in a boiler system. Good agreement was demonstrated between model results and experimental results for millimeter sized particles within a multifuel combustor. The authors concluded that neither lumped capacitance models nor simple internal heat transfer models adequately predict the mass loss of the biomass particles. Accounting for both heat and mass transfer effects in high moisture content particles delayed the predicted completion of pyrolysis but provided significantly more accurate results than simpler models not considering initial moisture content.

Babu and Chaurasia [12] constructed a comprehensive one-dimensional heat and mass transfer model for large particles considering varying thermal and transport properties. All three modes of heat transfer were accounted for within the particle (convection, conduction and radiation) and convective and diffusive transport of volatile species, variable pressure and velocity within the sample were included. Local thermal equilibrium between gaseous and solid components was assumed as well as a negligible particle moisture content. Model simplifications were also evaluated considering first the neglect of bulk gaseous motion within the particle pores and second that heat transfer only occurs by conduction within the particle and particle porosity is negligible. Model comparison results showed that the assumptions had minimal impact upon mass conversion predictions. Only one previous study was used in the evaluation of model results, however.

Papadikis *et al.* [117, 118] modeled the pyrolysis of biomass in fluidized sand bed reactors while accounting for particle shrinkage. The intent of the model was to provide a greater understanding of the fluid-particle interactions and the impact of shrinking particles on the transport. Heat transfer and pyrolysis kinetics were

accounted for as well as the fluid particle interactions. Biomass particles were treated as spheres (though the authors acknowledged that in practice particles are definitely not spherical). The release of pyrolysis volatiles was ignored due to its insignificance on a mass basis with respect to the circulating fluid volume. Model results showed that particle shrinkage has a negligible impact on the flow of the particle within the reactor and the effect on the overall heat transfer and subsequent rate of pyrolysis was insignificant.

Each of the previous studies contributed to the fundamental understanding of or modeling of biomass pyrolysis. The general predictive power of each model type, however, is difficult to ascertain due to the variability of conditions between studies. Not only are the tested species different in most cases, the system thermal conditions modeled range from screen heaters [30] (rapid direct contact heating) to radiant tube furnaces (slow or fast irradiant heating) [26] to TGA ovens (slow natural convective heating) [83, 67, 80, 19] to fluidized beds (fast convective and direct contact heating) [117, 118, 36, 37, 35]. As a consequence, until a comprehensive thermodynamic understanding of pyrolysis reactions can be formulated, kinetic modeling and pyrolysis reactor modeling should be restricted by thermal conditions (heating rate and temperature range) and particle specifications (size and species).

Pyrolysis modeling typically centers on either large particle pyrolysis heat and mass transfer models or fluidized bed/entrained flow systems. Work is yet to be done for systems providing the separation of heat and mass transport pathways. This configuration provides for not only lower process gas loads, and subsequent lower heating and cooling loads, but provides for the minimization of secondary reactions. This minimization is because products can be removed quickly from the production zone and transported while simultaneously cooled, thus preventing secondary reactions. Moving bed reactors offer the possibility of heat and mass transfer separation and as such should be further investigated through modeling.

In this work a pyrolysis model was developed for the prediction of pyrolysis yields as a function of time under separated heat and mass transfer conditions. The application of the model will be discussed with respect to a moving bed reactor because this design offers a continuous operation implementation of separate heat and mass transfer pathways. This separation is desirable because it both prevents secondary reactions, which result in increased char and tar formation, and can provide for lower process energy costs as compared to fluidized bed systems. Within fluidized bed systems large volumes of carrier gas are used to transport the products (both volatiles and solids) and in the case of bubbling fluidized beds the carrier gas is also the primary means of heating the biomass being pyrolyzed. The cooling of the carrier gases for volatiles condensation and the subsequent reheating of the gases represents a significant energy expenditure which can be drastically reduced by separating the product transport from the thermal energy transport. Moving beds can heat by either direct contact with a pre-heated reaction plate surface or through irradiance from a source above the bed. The chamber can then be either evacuated by vacuum pump or purged with an inert gas to remove the volatile pyrolysis products.

7.4 Packed Bed Fast Pyrolysis Model Overview

The pyrolysis of biomass within a moving packed bed was modeled as a continuous porous medium. Heat transfer within both the gas and solid phases were considered as well as the conservation of the volatiles as a single species throughout the bed. The bottom of the packed bed rests upon an impermeable and isothermal reactor plate. The top of the packed bed radiatively exchanges heat with the reactor ceiling and pyrolysis products are ejected into the evacuated chamber. This configuration is favorable for pyrolysis reactors because convective heat losses as a result of the carrier gas are eliminated. Additionally, lower volatile partial pressures improve condenser effectiveness downstream. Alternate boundary conditions could also be implemented

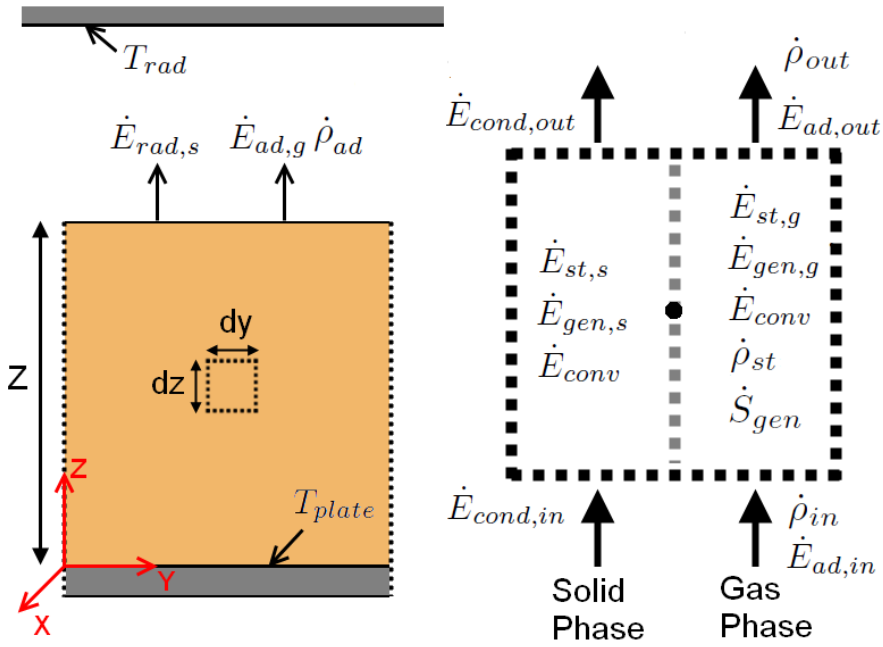

Figure 7.1: Heat and mass transfer model diagram for a packed bed of particles

within the model, however, the additional problem of detailed boundary condition evaluations within a moving bed reactor is beyond the scope of this work. A diagram of the particle bed is shown in Figure 7.1 with an infinitesimal cell energy balance and boundary conditions indicated.

The complete set of assumptions for model simplification are as follows:

1. Transport (both heat and mass) only occurs in the z-direction (*i.e.* $Z \ll W$ and $Z \ll L$)

2. Conduction within the gas phase is negligible with respect to advection (*i.e.* $Le \ll 1$)

3. Solid phase internal radiation heat exchange is insignificant

4. Char and unreacted wood are always at local thermal equilibrium

5. The biomass particles can be approximated as cylinders

6. Diffusive mass flux is insignificant with respect to pressure driven flow in the gas phase ($\tau^*_{diff} \gg \tau^*_{\Delta p}$)

The particle bed within the representative pack bed is stipulated to be much thinner in the z-direction than both its width and length (Assumption 1).Diffusion in the gas phase is expected to occur at a much higher rate than conduction. The Lewis number ($Le = \alpha/D$) was calculated based upon the properties of the volatiles presented in Section 7.7. The thermal diffusivity of the volatiles is approximately 0.19E-6m^2/s at 400°C and the mass diffusivity is approximately 2E-5m^2/s. This results in a Lewis number of $Le = 0.0095$ indicating that mass diffusion happens much faster than the transfer of heat through the volatiles and that advective heat transfer is then dominant over conductive heat transfer within the gas phase (Assumption 2). Local thermal gradients within the packed bed are anticipated to be low and as a consequence radiation within the bed is ignored (Assumption 3). Char and unreacted wood within the bed are assumed to always be at local thermal equilibrium because the two are one continuous substance which makes up the solid phase (Assumption 4. The particles are assumed to be cylindrical for the evaluation of internal convection coefficients (Assumption 5). This is evaluated in Section 7.7.1.

7.4.1 Scaling Analysis

A scaling analysis was performed to determine the dominant transport mode of the volatilized products within the packed bed. The two modes of mass transfer, diffusion and pressure driven flow, are accounted for in the conservation of species equation in the density form presented in Equation 7.1,

$$\frac{\partial \rho_g}{\partial t} = -v_0 \frac{\partial \rho_g}{\partial z} + D \frac{\partial^2 \rho_g}{\partial z^2} + \dot{S}_{gen} \tag{7.1}$$

where ρ_g is the density of the volatiles within the bed gas phase, v_0 is the superficial velocity of the volatiles within the bed, D is the diffusivity of the volatiles and $\dot{S}_{gen}$

is the volatiles generation rate (source term). Temporarily, the product generation rate will be ignored to compare the time scales of diffusion and bulk flow through the bed.

Scaling analyses are predicated upon characteristic dimensions. The characteristic height of the bed will be referred to as H_{bed} and the characteristic time scale referred to as τ^*. The characteristic density gradient will be generically called $\Delta\rho$. Substitution of the characteristic dimensions into Equation 7.1 gives Equation 7.2,

$$\frac{\Delta\rho}{\tau^*} = -v_0\frac{\Delta\rho}{H_{bed}} + D\frac{\Delta\rho}{H_{bed}^2} \tag{7.2}$$

The individual characteristic time scales for diffusion and bulk flow are then given by Equations 7.3 and 7.4,

$$\tau^*_{diff} = \frac{H_{bed}^2}{D} \tag{7.3}$$

$$\tau^*_{\Delta p} = \frac{H_{bed}}{v_0} \tag{7.4}$$

The height of the bed will be evaluated in the top of the range to be investigated with this model, 5E-3m. The previously introduced diffusivity will be used where $D = 2\text{E-}5\text{m}^2/\text{s}$. The characteristic time scale for diffusion is then $\tau^*_{diff} = 1.25\text{s}$.

The superficial velocity is defined as the flow velocity perpendicular to the cross-section of the bed. The superficial velocity within porous media is commonly solved for using Darcy's law given in Equation 7.5, [119]

$$v_0 = -\frac{K}{\mu}(\bigtriangledown p - \rho g) \tag{7.5}$$

where K is the permeability of the porous medium, μ is the viscosity of the volatiles, p is pressure and g is gravitational acceleration. Permeabilities are, however, empirically determined values ranging from $10^{-12} - 10^{-4}$ for various packed beds. [120] In the

case of packed beds with unknown permeabilities, the Blake-Kozeny equation can be applied. This correlation is based upon an empirically derived modification to the friction factor for internal flow within circular tubes. This is correlation is given by Equation 7.6,

$$v_0 = -\frac{L_c^2}{150\mu}\frac{\hat{\epsilon}^3}{(1-\hat{\epsilon})^2}\frac{dp}{dz} \tag{7.6}$$

where $\hat{\epsilon}$ is the porosity (volumetric void fraction) of the bed and L_c is the characteristic length of the particle given in Section 7.7.1. Assuming ideal gas behavior within the volatiles allows for an expression of the Blake-Kozeny equation in terms of the density as shown in Equation 7.7,

$$v_0 = -\frac{L_c^2}{150\mu}\frac{\hat{\epsilon}^3}{(1-\hat{\epsilon})^2}\frac{RT_v}{M}\frac{d\rho_v}{dz} \tag{7.7}$$

where M is the molecular weight of the volatile products and R is the universal gas constant. The correlation has been demonstrated to produce good predictions for systems with $\hat{\epsilon} < 0.5$ and where $L_c\rho v_0/(\mu(1-\hat{\epsilon})) < 10$. [119]

The superficial velocity can now be estimated using the viscosity, characteristic length and porosity from the properties table presented in Section 7.7. The density differential, for the evaluation of the superficial velocity, will be approximated by looking at the first 0.1 seconds of pyrolysis. A rate of pyrolysis of $k = 0.0540\text{s}^{-1}$ is calculated using the kinetic rate coefficients from the single component global pyrolysis model (given in Table 6.6) at 400°C. Based upon the measured intitial bulk density of the bed of 340kg/m^3 (this measurement is discussed in Section 7.7) the resulting initial formation rate of volatiles will be approximately $14.7\text{kgm}^{-3}\text{s}^{-1}$. A density differential of 0.147kg/m^3 will then develop with respect to the evacuated space above the bed, assuming the production occurs prior to the initiation of flow. The superficial velocity is then 12.1m/s and the characteristic time scale for pressure drive flow is $\tau^*_{\Delta p} = 4.1\text{E}-4\text{s}$. Therefore, the pressure driven flow is the dominant mass transport

phenomena and consequently diffusive mass transport can be neglected (Assumption 6).

7.5 Analytical Formulation of Conservation Equations

The general energy balance and mass balance (on a unit volume basis) in accordance with Figure 7.1 are given in Equations 7.8-7.10,

$$\dot{E}_{st,s} = \dot{E}_{cond,in} - \dot{E}_{cond,out} + \dot{E}_{gen,s} - \dot{E}_{conv} \tag{7.8}$$

$$\dot{E}_{st,g} = \dot{E}_{ad,in} - \dot{E}_{ad,out} + \dot{E}_{gen,g} + \dot{E}_{conv} \tag{7.9}$$

$$\dot{\rho}_{st} = \dot{\rho}_{\Delta p,in} - \dot{\rho}_{\Delta p,out} + \dot{S}_{gen} \tag{7.10}$$

The gas and solid phase energy conservation equations are modeled as separate and interacting because of the gas phase density dependent transport. Expansions of the energy balances for the solid and gas phases within the porous bed are given in Equations 7.11 and 7.12,

$$\rho_s c_s \frac{\partial T_s}{\partial t} = \frac{\partial}{\partial z}\left(\kappa_s \frac{\partial T_s}{\partial z}\right) + \rho_w k \Delta H_{py} - h_{loc} a (T_s - T_g) \tag{7.11}$$

$$\rho_g c_{p,g} \frac{\partial T_g}{\partial t} = -v_0 \frac{\partial \rho_g}{\partial z} c_{p,g} T_g + \psi_v \rho_w k c_{p,g,(T=T_s)} T_s + h_{loc} a (T_s - T_g) \tag{7.12}$$

where κ is thermal conductivity, k is the pyrolysis rate coefficient solved for as function of the solids temperature, c is specific heat, ρ is density, ψ_v is the fraction of pyrolyzed wood that converts to volatiles, h_{loc} is the local internal convection coefficient, a is the internal wetted surface area per unit volume, D is the diffusivity of pyrolysis volatiles and ΔH_{py} is the enthalpy of pyrolysis. The subscript w is for wood, c denotes char, s denotes solids and g denotes gas.

The bulk solid density (ρ_s), bulk solid thermal conductivity (κ) and the bulk solid specific heat (c_s) are functions of both the solid phase and char phase present within the bed. Gas properties are simply the corresponding volatile property values evaluated for the local gas temperature with the exception of ($c_{p,g,(T=T_s)}$). This term corresponds to volatiles added to the gas phase through pyrolysis which enter at the temperature of the pyrolyzing solid.

Within a thermally transient system the density of char and unreacted wood present are path dependent variables. The governing equations for the wood density, char density, bulk solid density times the specific heat, and thermal conductivity are given in Equations 7.13-7.16,

$$\rho_w = \rho_{w,(t=0)} - \int_0^t \rho_w k dt \tag{7.13}$$

$$\rho_c = (1 - \psi_v) \int_0^t \rho_w k dt \tag{7.14}$$

$$\rho_s c_s = \rho_w c_w + \rho_c c_c \tag{7.15}$$

$$\kappa_s = \frac{\rho_w \kappa_w + \rho_c \kappa_c}{\rho_w + \rho_c} \tag{7.16}$$

where c, k, and κ are all temperature dependent quantities and $\rho_{w,0}$ is the initial bulk density of the wood particles within the bed. The internal wetted surface area is given by Equation 7.17,

$$a = \frac{N'' \bar{A}_{particle}}{V_{bed}(1 - \hat{\epsilon})} = \frac{\rho_{w,0} \bar{A}_{particle}}{\bar{m}_{particle}(1 - \hat{\epsilon})} \tag{7.17}$$

where N'' is the number of particles within the bed volume, $\bar{A}_{particle}$ is the average surface area of a particle, V_{bed} is the particle bed volume and $\bar{m}_{particle}$ is the average mass of a particle. The internal local convection coefficient (h_{loc}) can then be

calculated using Equation 7.18, [119]

$$Nu_{loc} = \frac{h_{loc} L_c}{\kappa_g} = 2.19(RePr)^{1/3} \tag{7.18}$$

Equation 7.18 can be rearranged to yield Equation 7.19,

$$h_{loc} = \frac{\kappa_g}{L_c} 2.19(RePr)^{1/3} \tag{7.19}$$

where Pr is the Prandtl number and L_c is the characteristic length given by Equation 7.20,

$$L_c = \frac{6\xi}{a} \tag{7.20}$$

where ξ is a shape factor which is 1 for spheres and 0.92 for cylinders based upon an empirical fit. [119] The constant of 6 present within Equation 7.20 is chosen so that the characteristic length for spheres is exactly equal to the spherical particle diameter. The Reynolds number (Re) is given by Equation 7.21, [119]

$$Re = \frac{L_c v_0 \rho_g}{\mu} \tag{7.21}$$

where μ is the viscosity of the volatiles and the superficial velocity (v_0) is calculated according to Equation 7.7.

The full form mass conservation formula on a density basis is given by Equation 7.22,

$$\begin{aligned} \frac{\partial \rho_g}{\partial t} &= -v_0 \frac{\partial \rho_g}{\partial z} + \psi_v \rho_w k \\ &= \frac{L_c^2}{150\mu} \frac{\hat{\epsilon}^3}{(1-\hat{\epsilon})^2} \frac{RT_g}{M} \left(\frac{\partial \rho_g}{\partial z} \right)^2 + \psi_v \rho_w k \end{aligned} \tag{7.22}$$

Assembling the constant terms within Equation 7.22 and substituting the constant B results in the simpler form of Equation 7.23,

$$\frac{\partial \rho_g}{\partial t} = BT_g \left(\frac{\partial \rho_g}{\partial z} \right)^2 + \psi_v \rho_w k \tag{7.23}$$
$$B = \frac{L_c^2}{150\mu} \frac{\hat{\epsilon}^3}{(1-\hat{\epsilon})^2} \frac{R}{M}$$

The initial conditions for all three conservation equations are given in Equations 7.24 - 7.26,

$$T_s = T_0 \tag{7.24}$$

$$T_g = T_0 \tag{7.25}$$

$$\rho_g = 0 \tag{7.26}$$

where T_0 is equal to ambient temperature (22°C). The boundary conditions for the solid phase energy conservation equation (7.11) are given in Equations 7.27 7.28,

$$T_s(z=0) = T_{plate} \tag{7.27}$$

$$-\kappa_s \frac{\partial T_s}{\partial z}\Big|_{z=Z} = \sigma \epsilon_w (T^4_{s,(z=Z)} - T^4_{rad}) \tag{7.28}$$

Equation 7.27 states that the temperature at the bottom of the bed is equal to the temperature of the reaction plate surface. Equation 7.28 states that the rate of conductive heat transfer at the top of the bed is equal to the radiative heat loss from the top of the bed to the reactor wall at T_{rad}.

The boundary conditions for the conservation of species and the gaseous phase energy conservation are shared. This is because the heat transfer in the gaseous phase is only by advection, as per the Lewis number calculation of Section 7.4. The

boundary conditions for the gas phase heat and mass conservation equations (7.12 and 7.23) are given in Equations 7.29 and 7.30,

$$\frac{\partial \rho_g}{\partial z}\Big|_{z=0} = 0 \tag{7.29}$$

$$\rho_g(z = Z) = 0 \tag{7.30}$$

Equation 7.29 states that the density gradient at the bottom of the bed is equal to zero and subsequently that no mass transfer occurs at that boundary. The implication to the conservation of energy in the gas phase is that no energy is advected into or out of the gas at the plate boundary. Equation 7.30 states that the density of the product at the surface of the bed is equal to zero. This is a consequence of the assumed vacuum within the reaction chamber.

7.6 Finite Difference Formulation of Conservation Equations

The particle bed and its governing equations must first be discretized for implementation into a finite difference solution method. The discretized particle bed is shown in Figure 7.2. The representative element shown in Figure 7.1 is defined with a height of dz, width of dy and depth into the page of dx. A series of representative elements stacked atop one another makeup the bed model. This is a center-node model in which each cell volume is identical and the cell's properties are treated as homogeneous with the cell.

The complete development and simplification of the finite difference equations is given in Appendix C. The final forms of the three conservation equations for implementation into a finite difference simulation are given in Equations 7.31-7.33,

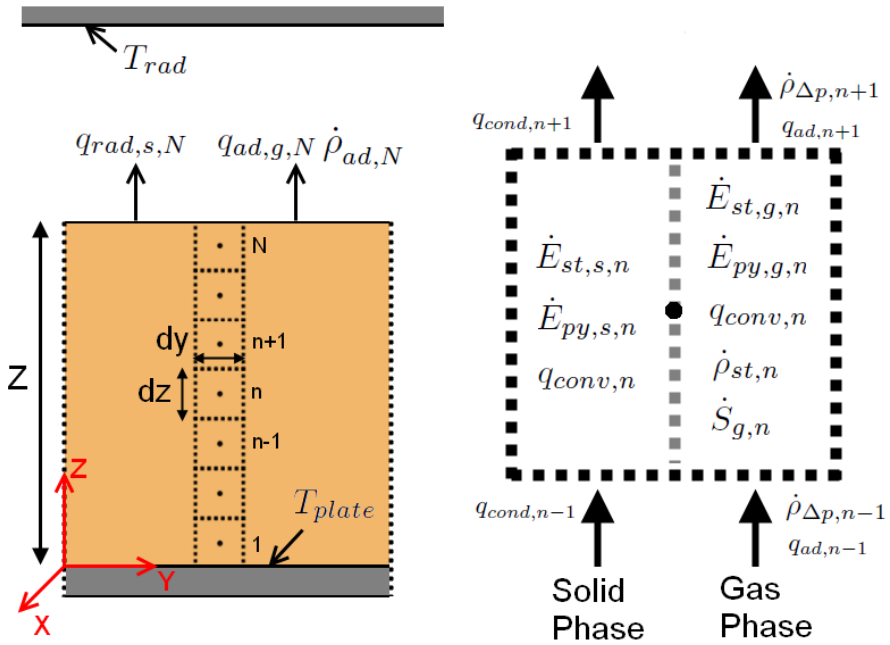

Figure 7.2: Discretized porous bed diagram for finite difference solution of the pyrolysis model

$$T_{s,n}^{t+1} = \left[\frac{\kappa_{s,n-1}^{t}}{(\Delta z)^2}T_{s,n-1} - \left(\frac{\kappa_{s,n-1}^{t}}{(\Delta z)^2} + \frac{\kappa_{s,n}^{t}}{(\Delta z)^2} + h_{loc,n}^{t}a\right)T_{s,n}^{t} + \frac{\kappa_{s,n}^{t}}{(\Delta z)^2}T_{s,n+1} + h_{loc,n}^{t}aT_{g,n}^{t} + \rho_{w,n}^{t}k(T_{s,n}^{t})\Delta H_{py}\right]\frac{\Delta t}{(\rho c)_{s,n}^{t}} + T_{s,n}^{t} \tag{7.31}$$

$$T_{g,n}^{t+1} = \left[\dot{\rho}_{\Delta p,n-1}^{t}(c_p)_{g,n-1}^{t}T_{g,n-1}^{t} + \dot{\rho}_{\Delta p,n+1}^{t}(c_p)_{g,n}^{t}T_{g,n}^{t} + \dot{S}_{g,n}^{t}(c_p)_{g,n}^{t}T_{s,n}^{t} - h_{loc,n}^{t}a(T_{g,n}^{t} - T_{s,n}^{t})\right]\frac{\Delta t}{(\rho c_p)_{g,n}^{t}} + T_{g,n}^{t} \tag{7.32}$$

$$\rho_{n}^{t+1} = \left[\frac{BT_{g,n}^{t}}{(\Delta z)^2}(\rho_{n-1}^{t})^2 - \frac{2BT_{g,n}^{t}}{(\Delta z)^2}(\rho_{n}^{t})^2 + \frac{BT_{g,n}^{t}}{(\Delta z)^2}(\rho_{n+1}^{t})^2 + \dot{S}_{g,n}^{t}\right]\Delta t + \rho_{n}^{t} \tag{7.33}$$

where the source term ($\dot{S}_{g,n}^{t}$) is given by Equation 7.34

$$\dot{S}_{g,n}^{t} = \psi_v \rho_w^{t} k(T_{s,n}^{t}) \tag{7.34}$$

The boundary cell equations for the solid phase are given in Equations 7.35 and 7.36,

$$T_{s,n=1}^{t+1} = \Bigg[\left(-\frac{\kappa_{s,n=1}^{t}}{(\Delta z/2)^2} - \frac{\kappa_{s,n=1}^{t}}{\Delta z^2} - h_{loc,n=1}^{t} a \right) T_{s,n=1}^{t} + \frac{\kappa_{s,n=1}}{\Delta z^2} T_{s,n=2} + \frac{\kappa_{s,n=1}^{t}}{(\Delta z/2)^2} T_{plate} + h_{loc,N}^{t} a T_{g,n=1} + \rho_{w,n=1}^{t} k(T_{s,n=1}^{t}) \Delta H_{py} \Bigg] \frac{\Delta t}{(\rho c)_{s,n=1}^{t}} + T_{s,n=1}^{t} \tag{7.35}$$

$$T_{s,N}^{t+1} = \Bigg[\frac{\kappa}{\Delta z^2} T_{s,N-1}^{t} + \left(-\frac{\kappa_{s,N-1}}{\Delta z^2} - h_{loc,N}^{t} a \right) T_{s,N}^{t} - \frac{\sigma \epsilon_w}{\Delta z} (T_{s,N}^{t})^4 + h_{loc,N}^{t} a T_{g,N}^{t} + \rho_{w,N}^{t} k(T_{s,N}^{t}) \Delta H_{py} + \frac{\sigma \epsilon_w}{\Delta z} T_{rad}^{4} \Bigg] \frac{\Delta t}{(\rho c)_{s,N}^{t}} + T_{s,N}^{t} \tag{7.36}$$

The boundary cell conditions for the gaseous phase are given in Equations 7.37 and 7.38,

$$T_{g,n=1}^{t+1} = \Bigg[\left(-h_{loc,n=1}^{t} a + \dot{\rho}_{\Delta p,n=2}^{t} c_{p,g,n=1}^{t} \right) T_{g,n=1} + h_{loc,n=1}^{t} a T_{s,n=1}^{t} + \dot{S}_{g,n}^{t} c_{p,g,n=1}^{t} T_{s,n=1}^{t} \Bigg] \frac{\Delta t}{(\rho c_p)_{g,n=1}} + T_{g,n=1}^{t} \tag{7.37}$$

$$T_{g,N}^{t+1} = \Bigg[\dot{\rho}_{\Delta p,N-1}^{t} c_{p,g,N-1}^{t} T_{g,N-1}^{t} + \left(\dot{\rho}_{\Delta p,N+1}^{t} c_{p,g,N}^{t} - h_{loc,N}^{t} a \right) T_{g,N}^{t} + h_{loc,N} a T_{s,N}^{t} + \dot{S}_{g,N}^{t} c_{p,g,N}^{t} T_{s,N}^{t} \Bigg] \frac{\Delta t}{(\rho c_p)_{g,N}} + T_{g,N}^{t} \tag{7.38}$$

The boundary cell equations for the conservation of species are given in Equations 7.39 and 7.40,

$$\rho_{n=1}^{t+1} = \left[-\frac{BT_{g,n}^{t}}{(\Delta z)^2} (\rho_{n=1}^{t})^2 + \frac{BT_{g,n}^{t}}{(\Delta z)^2} (\rho_{n=2}^{t})^2 + \dot{S}_{g,n}^{t} \right] \Delta t + \rho_{n=1}^{t} \tag{7.39}$$

$$\rho_N^{t+1} = \left[\frac{BT_{g,N}^t}{(\Delta z)^2}(\rho_{N-1}^t)^2 - \frac{BT_{g,N}^t}{(\Delta z)^2}\left(\frac{1}{(\Delta z)^2} + \frac{1}{(\Delta z/2)^2}\right)(\rho_N^t)^2 + \frac{BT_{g,N}^t}{(\Delta z)^2}(\rho_{N+1}^t)^2 + \dot{S}_{g,N}^t \right] \Delta t + \rho_N^t \tag{7.40}$$

7.7 Selection of Published Physical Property Values

Properties for the packed bed model were selected from literature for most parameter values with the exception of bed density, bed porosity and moisture content of the wood. Properties such as the enthalpy of pyrolysis could be approximated if the chemical composition of Loblolly pine and the exact pyrolysis products obtained were definitively known. Published values are necessary, though, because molecular definitions of the products and virgin wood are not known. Within literature many properties are debated to lie within a large range of values. For example, Milosavljevic *et al.* [121] documented the range of heats of reaction (also called heat of pyrolysis) for the pyrolysis of cellulose to lie between -2100kJ/kg (highly endothermic) and 2510kJ/kg (highly exothermic). The primary reason for such large variations is reaction conditions which could provide for very slow pyrolysis with char being the dominant product (typically deemed exothermic) to very fast pyrolysis with oil being the dominant product (typically deemed endothermic). With this consideration, properties for the implementation of the packed bed model were selected from studies with like conditions wherever possible. Additionally, some properties are yet to be measured. The diffusivity of pyrolysis volatiles is estimated either using correlations from *Perry's Chemical Engineering Handbook* [122] based upon estimated molecular weight of the products, [12, 123] or based upon commonly accepted values which provide for good model and experimental agreement. [124, 97, 116] Again, properties from like studies will be used wherever possible.

The physical properties utilized in the packed bed pyrolysis model are contained

in Table 7.1. Wood specific heat, thermal conductivity and dried density were taken from tabulated values by the United States Department of Agriculture [54]. Functions for the specific heats of the char and volatiles (noted as g because it exists in the gaseous phase within the transport model) were taken from work by Grønli [18]. The functions were derived based upon previously published data and have been applied to pyrolysis modeling with good agreement to experimental results. [116, 115] The thermal conductivity of the gaseous volatiles was taken from a study by Kansa *et al.* [113] and has been used to good effect in more recent fast pyrolysis models. [125, 126] The char thermal conductivity was taken from work by Koufopanos *et al.* [92] because it was one of the few models in literature which provided for a temperature dependence. It was successfully applied by Babu and Charasia [12, 127] within their multiphysics pyrolysis models. The emissivity of the wood is typically taken to be 0.92 or 0.95. [128, 12, 18, 129, 124] To provide a more conservative boundary condition the larger value was used. The enthalpy of pyrolysis was selected from studies which successfully applied the parameter to modeling pyrolysis under like conditions, as previously stated was necessary. The enthalpy of pyrolysis value presented in Table 7.1 was first presented by Koufopanos *et al.* [92] and was applied in fast pyrolysis models by Babu and Charasia [12, 127] and Papadikis *et al.* [117] and is assumed to be constant over all temperatures. The molecular weight for the volatiles was averaged from those presented by Grønli [18] for both the condensed oil and permanent gas products. A weighted average was applied, however, accounting for the ratio of condensed oil and gas products from Loblolly pine experimental results presented in Chapter 4. The diffusion coefficient was taken from a frequently applied value which showed good model and experimental agreement [124, 114, 130].

The measured property values included the bed porosity, packed bed density and moisture content. The packed bed density was measured by vibrating a known mass

Table 7.1: Physical properties utilized in the packed bed pyrolysis model

Property	Value/Function		Source
c_c	$420 + 2.09T_s + 6.85\text{E} - 4T_s^2$	[J/kgK]	[18]
$c_{p,g}$	$-100 + 4.4T_g - 0.00157T_g^2$	[J/kgK]	[18]
c_w	$(103.1 + 3.867T_s)$	[J/kgK]	[54]
D	$2\text{E} - 5$	[m^2/s]	[124, 114, 130]
$f_{moisture}$	0.036	[g/g]	Measured
$\bar{M}_{wt}$	83	[g/mol]	Averaged From [115]
ΔH_{py}	-255	[kJ/kg]	[92]
ϵ	0.95	-	[128, 12]
κ_c	$0.08 - 0.0001T_s$	[W/mK]	[92]
κ_g	0.026	[W/mK]	[113]
κ_w	$(\rho(0.1941 + 0.004064f_{moisture})$ $+0.01864)(1.02^{(T_s-300)/20})$	[W/mK]	[54]
ρ_w	510	[kg/m^3]	[54]
ρ_{bed}	340	[kg/m^3]	Measured
$\hat{\epsilon}$	0.33	-	Measured

of particulate within a graduated container under the same conditions as are experimentally provided (frequency and amplitude). The known mass divided by the final volume yielded the packed bed density. The porosity was then calculated according to equation 7.41,

$$\hat{\epsilon} = \frac{\rho_w - \rho_{bed}}{\rho_w} \tag{7.41}$$

Sample moisture content was determined using a Mettler Toledo HR73 moisture balance. This device works by massing the target sample, heating it up to 105°C and holding it there until the mass of the sample ceases to change. The change in mass divided by the initial sample mass is the moisture content on a g/g basis.

7.7.1 Particle Size Characterization

Particle sizes and shapes were evaluated by taking photographs of dispersed particles and using an image processing software to analyze the photographs. The camera used was a Sony SSC-C374 and the image processing software was *Leica QWin Standard V2.3*. Measurement calibration was performed by first imaging a flat scale ruler and

adjusting the software calibration accordingly.

For each image particles were dispersed on a white piece of paper by dropping from a height of approximately 5cm. The dispersed particles were then imaged. The image was imported into the QWin software which performed the following sequence of tasks: edge finding; skeleton formation; triple point identification for overlap adjustment; particle measurement. The particle measurements included computing the number of particles in the image (N_p), calculating the percentage of the image obscured by the particles ($O\%$), average skeleton length ($\bar{L}_s$ based upon the longest dimension), average skeleton aspect ratio ($\bar{AR}$), average particle area ($\bar{A}$) and average particle perimeter ($\bar{P}$). The results from 29 image evaluations are contained in Table 7.2. The mean and standard deviations of each measurement weighted by number of particles are also included at the base of the table.

Of particular interest for the pyrolysis model is the effective shape of the particle (rectangular, ellipsoidal, cylindrical). To do this the measured perimeter and cross-sectional area were analyzed and volumetric estimations and the impact of shape were evaluated.

The weighted mean particle width (based upon the weighted mean particle length and aspect ratio) is calculated to be $\bar{w}_p^* = 180\mu$m. Mean weighted values will henceforth be noted with an asterisk (*). For a rectangular or cylindrical long-axis cross-section the perimeter and area are trivial and are simply $P = 2L + 2w$ and $A = wL$. For an ellipsoid, however, the long-axis cross-sectional perimeter and area are given by Equations 7.42 and 7.43,

$$P = 2\pi \left[\frac{(L/2)^2 + (w/2)^2}{2} \right]^{1/2} \tag{7.42}$$

$$A = \pi w L \tag{7.43}$$

The comparative results are summarized in Table 7.3 using the weighted mean

Table 7.2: Particle size imaging results by image number with weighted mean and standard deviation values

Image	N	$O\%$	$\bar{A}$[mm^2]	$\bar{L}_p$ [mm]	$\bar{P}$ [mm]	$\bar{AR}$
1	137	8.8	0.0763	0.35	1.06	1.79
2	132	7.6	0.0696	0.36	1.04	1.82
3	183	7.0	0.0483	0.29	0.86	1.74
4	155	8.1	0.0587	0.31	0.91	1.81
5	134	4.4	0.0391	0.26	0.76	1.84
6	135	7.4	0.0572	0.32	0.93	1.87
7	120	4.2	0.0424	0.29	0.81	1.88
8	112	4.1	0.0473	0.31	0.88	1.98
9	208	10.8	0.0633	0.32	0.91	1.86
10	137	8.8	0.0801	0.37	1.06	1.82
11	392	16.3	0.0473	0.27	0.80	1.71
12	170	7.2	0.0497	0.28	0.82	1.74
13	136	7.0	0.0596	0.29	0.89	1.67
14	208	12.1	0.0632	0.33	0.96	1.86
15	228	14.8	0.0778	0.37	1.10	1.80
16	229	10.8	0.0544	0.33	0.94	1.88
17	161	9.5	0.0692	0.37	1.04	1.95
18	180	10.0	0.0648	0.35	1.01	1.80
19	92	4.8	0.0583	0.31	0.89	1.75
20	201	9.8	0.0558	0.28	0.83	1.73
21	197	10.4	0.0583	0.31	0.91	1.76
22	295	15.7	0.0613	0.32	0.95	1.81
23	295	18.7	0.0756	0.34	1.02	1.74
24	252	14.6	0.0705	0.34	1.01	1.78
25	205	10.1	0.0577	0.33	0.94	1.86
26	244	15.9	0.0771	0.36	1.06	1.76
27	307	18.4	0.0699	0.31	0.94	1.66
28	305	18.7	0.0711	0.33	0.98	1.76
29	210	12.9	0.0731	0.35	1.03	1.77
Wtd $\bar{\mu}$	223	12.0	0.0628	0.32	0.95	1.79
Wtd σ	-	1.94E1	1.15E-4	9.05E-4	7.63E-3	4.97E-3
Wtd $\sigma/\bar{\mu}$ [%]	-	161%	0.18%	0.28%	0.81%	0.28%

Table 7.3: Comparison on longitudinal cross-section perimeter and area between theoretical particle morphology and measured particle morphology

Shape	P[mm]	A[mm^2]
Rectangular/Cylindrical	1.00	0.058
Ellipsoidal	0.82	0.046
Measured	0.95	0.063

particle width and length results from Table 7.2. From the results it is clear that the particles are either rectangular or cylindrical based upon the similarity between both perimeter and area theoretical and experimental results. The actual three-dimensional shape, however, is necessary to approximate for implementation into the packed bed model, particularly for the shape factor ξ used here. It is very unlikely that either perfect rectangular prisms or cylinders are produced given the nature of the Wiley milling process used to form the chips. The remaining factor of significance is the total surface area of the particle because it impacts the characteristic length used to estimate the local convection coefficient in Equation 7.19. Calculation of the surface area values yields: $A_{s,rect} = 0.30\text{mm}^2$ and $A_{s,cyl} = 0.23\text{mm}^2$. The values differ by 21% (before rounding). The surface area of the particles will then be approximated by an average of the two surface areas.

7.8 Model Implementation Methodology

The model solution followed the iterative approach outlined in Figure 7.3. The physical properties of each cell were evaluated within the iterative loop to account for variations in thermal conductivity, specific heat and changes in the composition of the solid. Additionally, the rate of pyrolysis was evaluated locally within each cell for each time step. The predicted temperature and density changes were then calculated and added to the current values. The time step was incremented and the loop repeated until the set simulation time was reached.

Time step sizing is typically performed based upon the heat and mass transfer

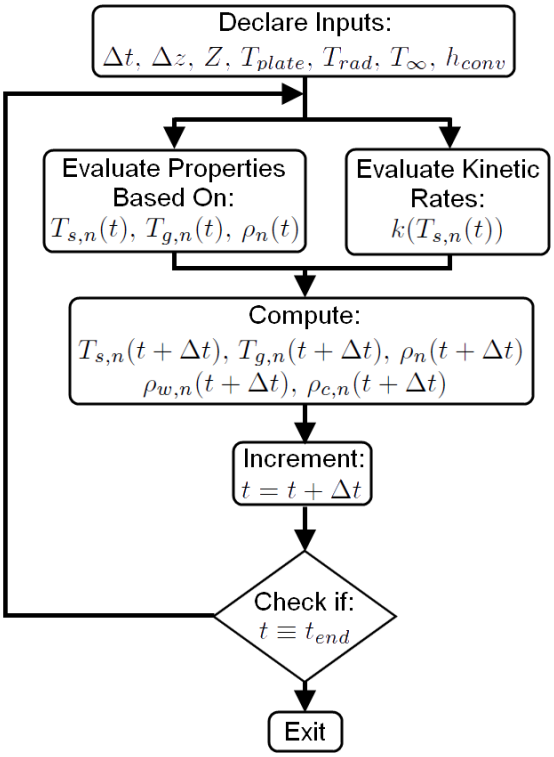

Figure 7.3: Finite difference explicit solution methodology flow chart

Fourier numbers given in Equations 7.44 and 7.45, [55]

$$Fo = \frac{\alpha t}{L^2} \tag{7.44}$$

$$Fo_m = \frac{Dt}{L^2} \tag{7.45}$$

where L is half the length of a cell (the distance between the $n = 1$ node and the hot plate underneath. With pressure driven flow, however, an equivalent non-dimensional time scale must be substituted for the diffusivity based mass transfer Fourier number. This timescale can be taken from the scaling analysis of Equations 7.2-7.7. The subsequent pressure driven flow Fourier number is given by Equation 7.46,

$$Fo = \frac{v_0 t}{L} \tag{7.46}$$

Thermal diffusivity was evaluated at the reaction plate temperature, which would

be the maximum thermal diffusivity encountered during the simulation. The superficial velocity was estimated based upon the initial rate of pyrolysis volatiles production presented in Section 7.4. For a one-dimensional finite difference solution, the maximum time step should be based on a Fourier number less than or equal to 0.5 to ensure stability of the model.[55] To provide a more conservative time step, a maximum Fourier number of 0.25 will be used here. The model time step (Δt) was set based upon the lower of the two values determined from the Fourier number analysis. The thermal diffusivity was evaluated at 400°C using the properties listed in Section 7.7. The superficial velocity was evaluated at $v_0 = 12.1$m/s taken from the scaling analysis estimate of Section 7.4.1. A cell size of 100μm was selected resulting in a characteristic cell length of $L = 50\mu$m. The limiting time steps were rounded down to $1\text{E}-3$s for heat transfer and $1\text{E}-6$s for mass transfer. The rounded pressure driven flow time step is only valid for superficial velocities less than or equal to 12.5m/s. If internal flow velocities above this are encountered, the simulation may go unstable resulting in divergence. An additional source of instability encountered was the rate of heat transfer between the solid and gas phases as a result of gaseous flow within the bed. Convection coefficients were encountered on the order of 100W/m^{2}K producing large instabilities in the system without further time step reduction. The impact of the heat exchange, however, is to simply bring the solid and gas phases into local thermal equilibrium on a cell by cell basis. As a consequence, a simplification to the numerical simulation was made providing for local thermal equilibrium at the end of each time step based upon the solid and gas phase energy contents for each cell.

7.9 Packed Bed Multi-Physics Model Results

Heat and mass transfer simulations were performed at the conditions listed in Table 7.4 using the finite difference model structure presented in Section 7.6. The results from the simulation include for each cell the solid phase temperature, the gas phase

Table 7.4: Finite difference simulation parameters

T_{plate}	450°C	Δz	100μm
H_{bed}	$1\text{E}-3$m	Δt	$1e-6$s
t_{end}	60s		

temperature, the concentration of pyrolysis volatiles and the cumulative release of volatiles all as functions of time. These results are plotted in Figures 7.4-7.7.

Three key metrics for the evaluation of a heating configuration are the time to reach 90% of the maximum convertible quantity of volatiles ($t_{90\%}$), the specific energy requirement on a per kg of input feedstock basis to reach 90% of the maximum yield ($\bar{e}_{90\%}$) and the specific power requirement over the time to reach 90% conversion ($\bar{p}$). The specific power requirement must be taken as an average within the finite difference simulations and not a maximum. This is because in the initial heating of the biomass layer, the bottom most cell interacts with the plate over a finite distance of $\Delta z/2$ and with an initial temperature differential of $T_{plate} - T_0$. The initial heat flux according to Fourier's law is then determined based upon a large instantaneous temperature differential and a very short heat transfer pathway. Therefore, an average specific heating requirement over the first second of heat transfer is reported. The result is not affected by the initial spike in heat flux when averaged over a time scale much larger than the simulation time step.

The above simulation was repeated for three reactor temperatures and three particle bed heights to demonstrate model capability and application to the comparison of system configurations. These results are shown in Table 7.5.

7.10 Comparison to Experimental Results Using the Micro-Reactor

The predictive capabilities of the model solid phase simulation were validated against experimental results obtained using the micro-reactor. Only the solid phase transport was simulated because the biomass layer thickness of 400μm within the micro-reactor

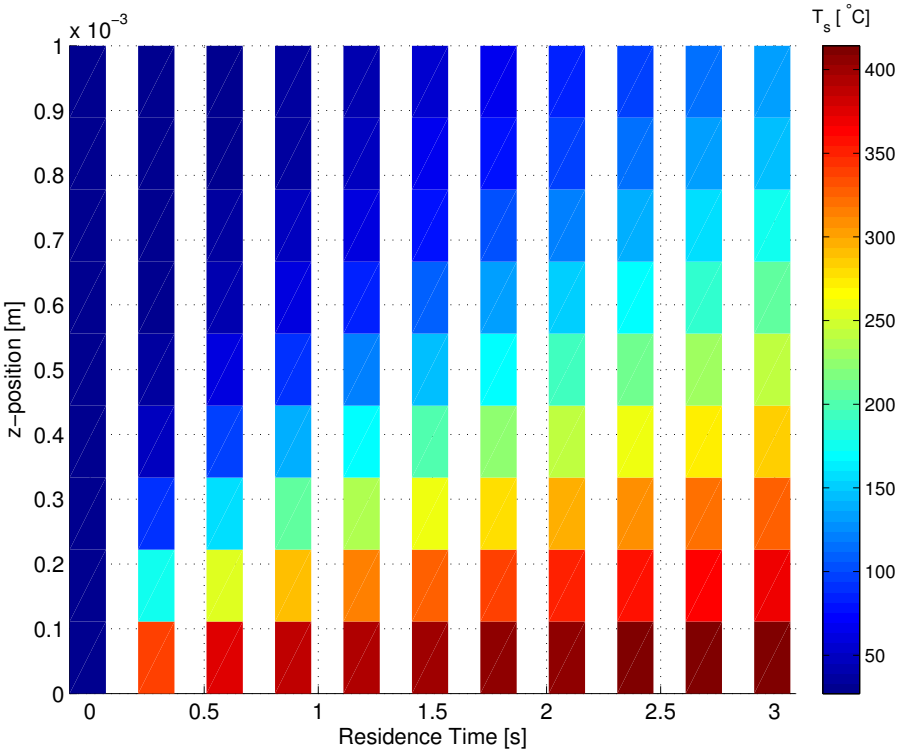

(a)

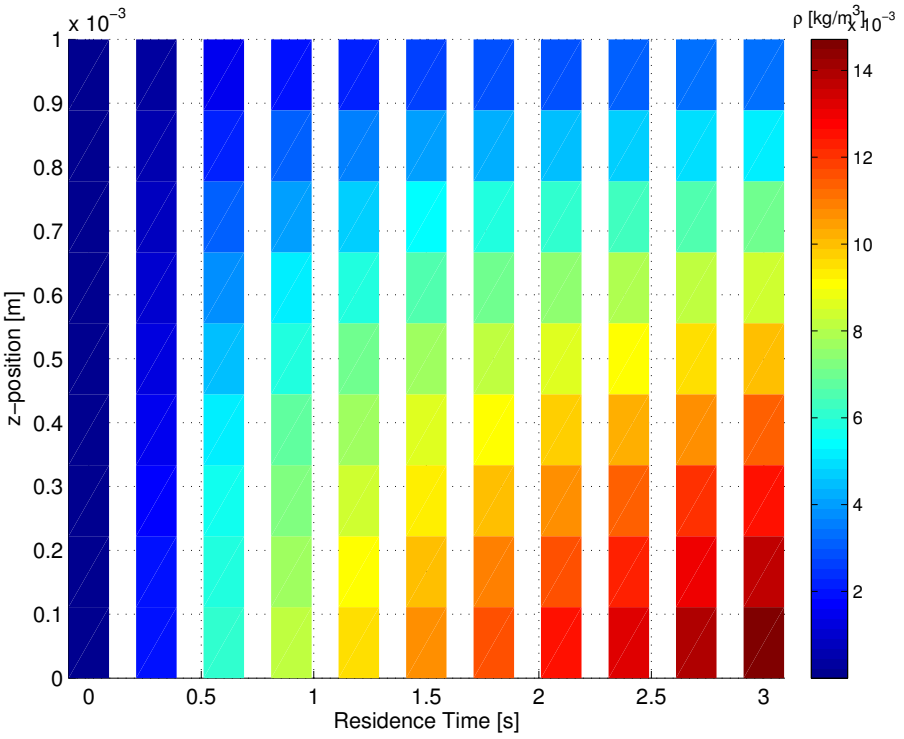

(b)

Figure 7.4: Multi-physics pyrolysis simulation results for a 1mm thick bed and reactor plate temperature of 450°C: (a) Time-space temperature plot for the solid phase transients (b) Time-space density plot for the products within the gas phase

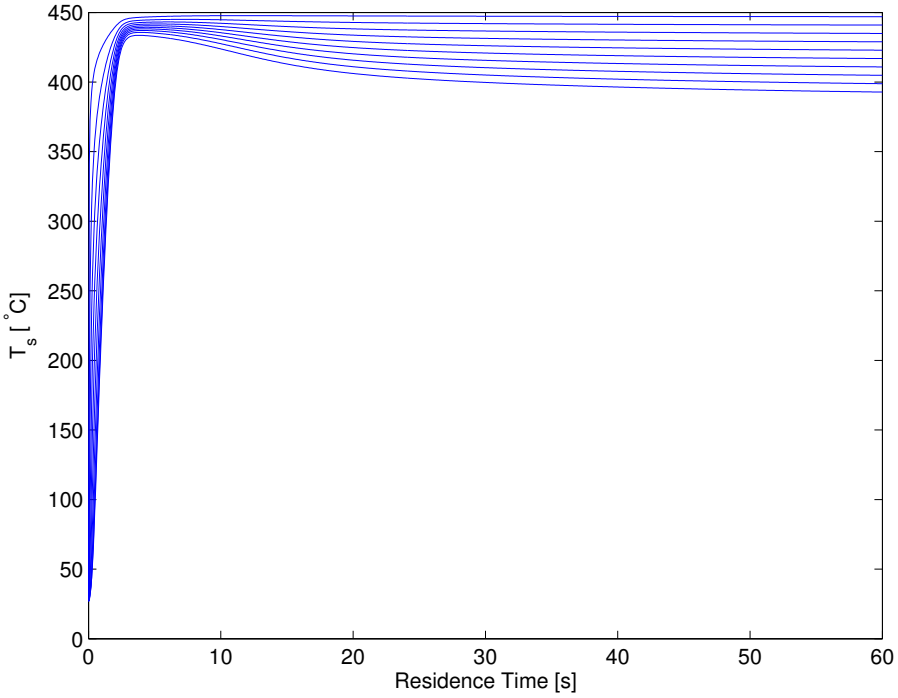

(a)

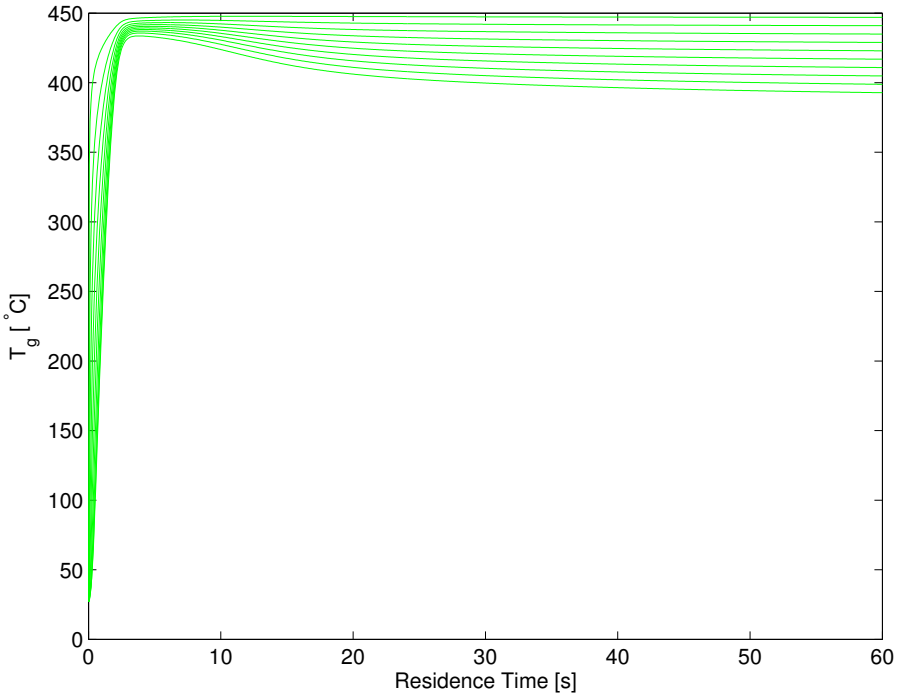

(b)

Figure 7.5: Multi-physics pyrolysis simulation results for a 1mm thick bed and reactor plate temperature of 450°C: (a) Solid phase cell temperatures from the bottom of the bed (top line) to the top of the bed (bottom line) (b) Gas phase cell temperatures for all nodes with top and bottom nodes indicated

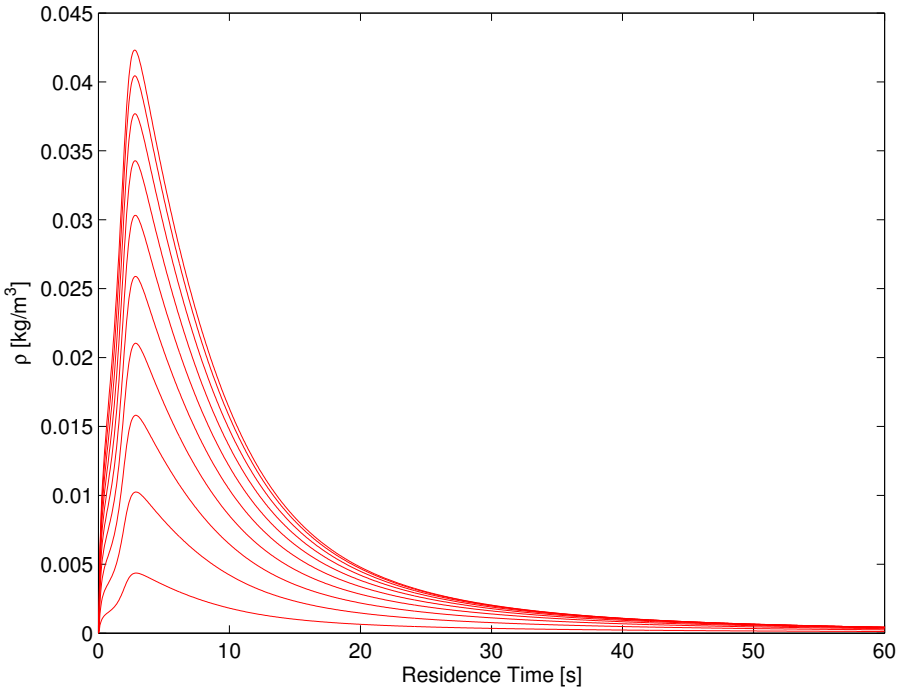

(a)

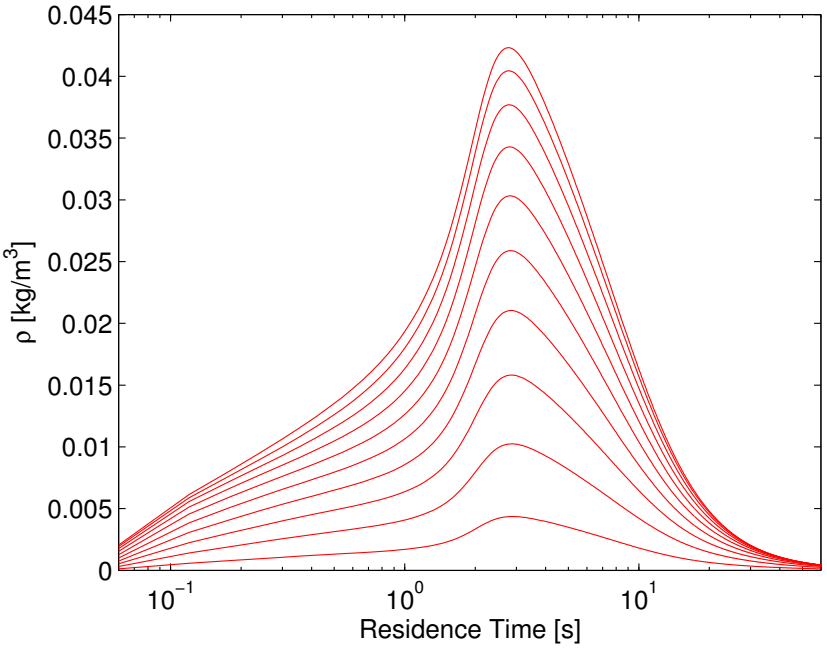

(b)

Figure 7.6: Multi-physics pyrolysis simulation results for a 1mm thick bed and reactor plate temperature of 450°C: Product density on a cell by cell basis from the bottom of the bed (top line) to the top of the bed (bottom line) on both (a) linear and (b) semi-log plots

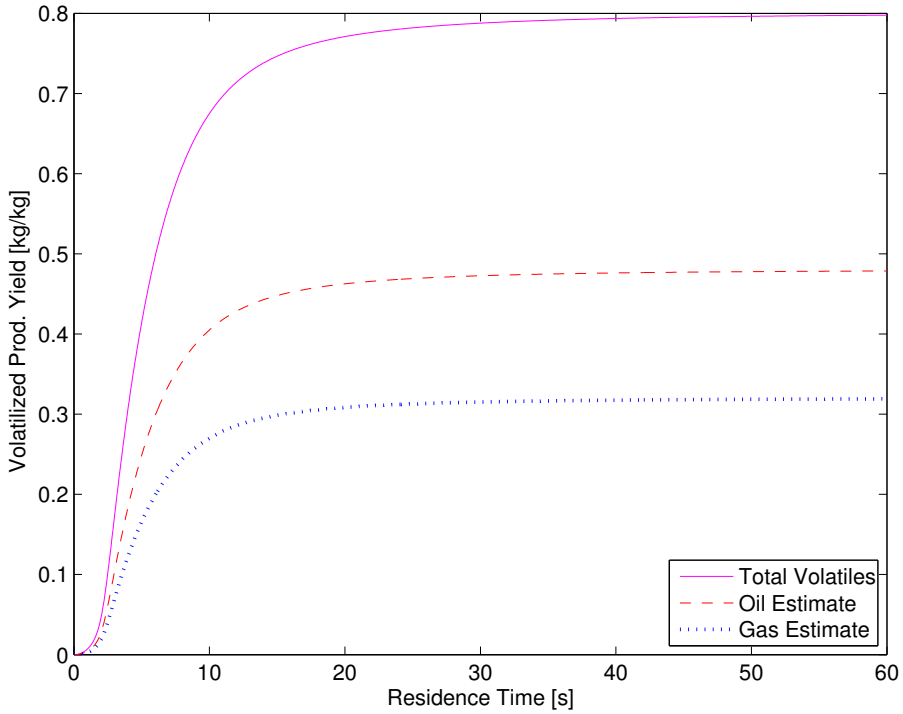

Figure 7.7: Multi-physics pyrolysis simulation results for a 1mm thick bed and reactor plate temperature of 450°C: Predicted volatile yields on a per kg of input feedstock basis

Table 7.5: Key parameter results from simulations run under nine different configurations

		425°C	
	1mm	3mm	5mm
$t_{90\%}$ [s]	30.5	35.3	38.8
$\bar{e}_{90\%}$ [kJ/kg]	1130	729	659
$\bar{p}$ [kW/kg]	37.0	20.7	17.0
		450°C	
	1mm	3mm	5mm
$t_{90\%}$ [s]	12.4	15.9	19.1
$\bar{e}_{90\%}$ [kJ/kg]	975	720	671
$\bar{p}$ [kW/kg]	78.6	45.3	35.1
		475°C	
	1mm	3mm	5mm
$t_{90\%}$ [s]	5.76	8.70	11.2
$\bar{e}_{90\%}$ [kJ/kg]	918	729	689
$\bar{p}$ [kW/kg]	159	83.8	61.5

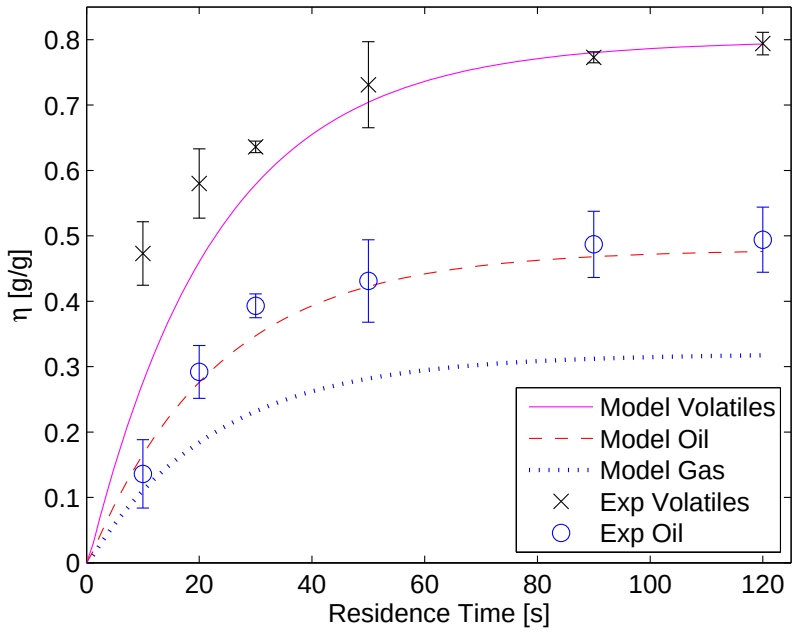

Figure 7.8: Micro-reactor experimental total yield and oil yield results plotted against the predictive results using the finite difference simulation

represents a layer of only 1-2 biomass particles which does not provide a significant resistance to product flow out of the bed. Therefore the gas phase transport correlations do not apply and the produced products are expected to escape nearly instantaneously. A comparison of the predicted and experimental results is shown in Figure 7.8. The average predictive error is 12.7% for the total yield and 8.0% for the oil yield. The largest error observed is for the total yield predictions at a residence time of 10 seconds, underpredicting by 42%. The smallest error observed is for the total yield predictions at a residence time of 90 seconds, underpredicting by 0.9%.

7.11 Extension of Model Results to the Sizing of Moving Beds

Moving bed reactor design parameters can now be guided based upon the predictive outputs of the packed bed simulations. Consider the simplified moving bed shown in Figure 7.9. For a specified bed height (H) and reaction plate temperature (T_{plate}) the

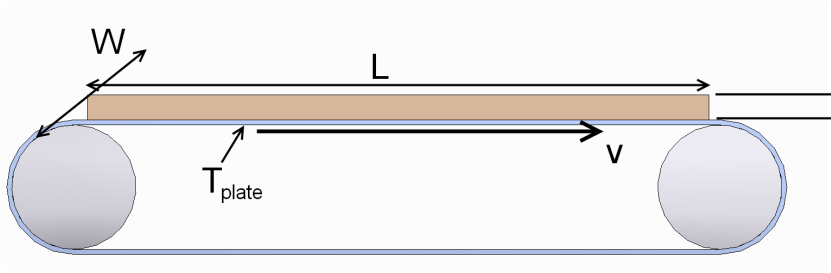

Figure 7.9: Simplified moving bed pyrolysis reactor diagram with key parameters identified

time to reach 90% conversion, energy required from the reaction plate and the initial specific heating load can be predicted.

A key design parameter for any commercial reactor is the maximum throughput ($\dot{m}$). The required heating power is related to the throughput by the specific energy requirement ($\bar{e}_{90\%}$) as shown in Equation 7.47,

$$P = \dot{m}\bar{e}_{90\%} \tag{7.47}$$

The maximum throughput is also related to the bed dimensions and the bed density by Equation 7.48,

$$\dot{m} = v_{bed}H_{bed}w_{bed}\rho_{bed} \tag{7.48}$$

The length of the bed and the velocity at the belt surface are related by the residence time requirement of the particles. Assuming a targeted 90% completion of pyrolysis Equation 7.49 relates the three parameters,

$$v_{bed} = \frac{L_{bed}}{t_{90\%}} \tag{7.49}$$

The key design parameters for moving bed reactor sizing are now related by Equations 7.47-7.49.

Consider, for example, a 20ton/day pilot plant using 10 parallel moving bed reactors for which the reactor plate temperature is set at $T_{plate} = 475°C$ and the bed

height is fixed at H_{bed} = 3mm. The time to 90% completion of pyrolysis is 8.70 seconds and the specific energy required for heating the biomass during this time period is 729kJ/kg, taken from the results contained in Table 7.5. The heating power requirement for each moving bed reaction plate is then 8.37kW. The bed sizing can be performed by specifying either the bed width, length or belt velocity and applying them to Equations 7.48 and 7.49. Specifying a 2m long belt results in a belt surface velocity of 0.230m/s (13.8m/min) and a belt width of 0.10m, per reactor.

The simulation activation energy was varied to evaluate the impact of kinetic parameter error propagation and demonstrate the necessity for accurate kinetic parameter determination. Recall from Chapter 6 that the impact of a 5% difference in activation energies remained to be evaluated. The multi-physics simulation was then rerun for a reactor plate temperature of 425°C and a bed height of 3mm with a 5% decrease in the activation energy while all other properties remained unchanged. The adjusted time to reach 90% conversion is 4.50 seconds and the specific energy required for heating the biomass is 678kJ/kg. The new heating power requirement is 15.0kW per moving bed reaction plate, an increase by nearly a factor of two. The adjusted belt surface velocity is 0.44m/s (26.7m/min) and the new belt width is 0.047m per reactor.

7.12 Discussion

Multi-physics temperature prediction results show a rapid development of the temperature profile within the packed bed with pseudo-steady-state reached by 5 seconds in the 425°C 1mm bed simulation. This rapid development is the result of convective heat exchange between the hot pyrolysis gases and the cooler solids as the gases pass through the upper portions of the bed. The solid and gas phase temperature results show the expected heating trends and clearly illustrate the thermal gradient over the height of the bed. The yields plot indicates that by 8.7s, 90% of the volatiles have

been pyrolyzed. The density plot (Figure 7.6) shows the anticipated trend of higher densities at the bottom cells (upper lines) than the top cells (lower lines). The maximum densities encountered within each cell show a peak shift starting with the top most cell and ending with the bottom most cell. This peak shift is a product of the high rate of heat transfer through the bed and resulting kinetically limited reaction.

Within Table 7.5, the required time to reach 90% conversion follows the anticipated trends of increasing times as bed height increases and decreasing times as reactor plate temperature increases. The energy requirements show a decrease in the required specific process energy with increasing bed height. This is a result of the bed acting as an insulator and thus the losses from the top of the bed are decreased with the decreasing bed-top temperature. A transition is observed in the required specific process energy, however, as the reactor plate temperature is increased. For the 1mm bed height, the required specific process energy decreases with increasing reactor plate temperature. The trend for the 3mm bed height is a decreasing and then increasing energy requirement. For the 5mm bed height, the trend is a continually increasing process energy. These trends show that there is a non-linear response of the required specific process energy to the variation of the two control parameters: bed height and reactor plate temperature. Therefore, the designer of a fast pyrolysis moving bed vacuum reactor should characterize the response surface surrounding the desired operating point. This will allow the impact of variations in process parameters (controlled or uncontrolled) to be estimated and proper design accommodations made.

The calculated specific energy requirements shown in Table 7.5 indicate a small energy investment with respect to the potential product energy content outcomes. A moderate lower heating value for pyrolysis oils is 20MJ/kg. [131, 132] At 90% conversion 0.42kg/kg of oil/feed should be produced. This results in an estimated 8460kJ/kg of oil energy content on a feed in basis, a significant increase over the

maximum 1130kJ/kg specific energy input reported in Table 7.5

Predictive results compared to the micro-reactor experimental results provided an initial verification of the model solid phase and actual pyrolysis reaction properties. The results demonstrated oil predictions within 8% of the experimentally measured mean values and total conversion predictions within 12.7% of the experimentally measured mean values. The under-prediction of the total yields is attributable to imperfect physical property values. Specifically, the magnitude of the heat of pyrolysis, the thermal conductivity or the specific heat of the biomass or char could be to blame. Over-predicting either the magnitude of the heat of pyrolysis or the specific heat of the solids would result in a thermal lag. The same effect would be observed by under-predicting the thermal conductivity of the solids. The prediction error is anticipated to be reduced through tuning of the model with additional experimental data, considering thicker biomass particle beds.

The vacuum pyrolysis moving bed sizing analysis represents a simple application to the simulation predictions presented here. The extensions of this model are, however, far reaching. In particular the detailed evaluation of boundary conditions within moving bed reactors could provide for high fidelity predictions of pyrolysis results.

The 5% decrease in the activation energy was shown to produce significant variations in reactor sizing predictions. The time required to reach 90% conversion was reduced by 48%. The impact of this predicted residence time reduction was a near doubling of the power requirement and a halving of the belt width. Miscalculations on this order demonstrate the necessity of accurate kinetics in pyrolysis modeling for the design of fast pyrolysis reactors.

7.13 Summary

A coupled pyrolysis kinetics, heat and mass transfer finite difference simulation was presented for the prediction of biomass fast pyrolysis within packed beds. The multi-physics model accounted for conductive heat transfer within the solid phase, the generation of pyrolysis products from raw wood and resultant thermal effects, pressure driven flow of pyrolysis products in the gaseous phase and the advective heat transfer as a consequence of the pressure driven flow. The analytical and finite difference conservation equations were developed in detail. Model time scales were evaluated using Fourier non-dimensional time approximations.

The simulation results for a reactor plate temperature of 450°C and bed height of 1mm were presented demonstrating the model capabilities in producing results plots for solid and gas phase temperatures, volatilized product as a function of time, product densities and spacio-temporal plots for temperature and pyrolysis products. Additionally, key reactor design parameters of time to reach 90% conversion and the required specific process energy and and average specific power were calculated. These parameters were then presented for nine reactor configurations varying the particle bed height and reactor plate temperature and the impact on design parameters analyzed.

A case considering the simulation of pyrolysis within the micro-reactor was evaluated neglecting the gas-solid phase heat exchange due to the thin micro-reactor bed height. The results showed that the oil yield as a function of time was predicted to within 8% of the experimental values. The error is most likely the result of imperfect physical property evaluations.

The full multi-physics simulation was then applied to the sizing of a moving bed vacuum pyrolysis reactor and the impact of a 5% reduction in the activation energy for the pyrolysis reaction evaluated. The results showed that the necessary

residence time nearly doubles with the activation energy change and the energy requirement decreases by only 7%. The 20ton/day pilot plant sizing analysis showed significant repercussions from the change in activation energy with the belt width more than halved and the power requirement nearly doubled. These large variations demonstrated the necessity of accurate kinetics for the design of moving bed vacuum pyrolysis systems.

CHAPTER 8

CONCLUSIONS

This thesis has addressed the development, evaluation and application of kinetic parameters for the description of biomass fast pyrolysis. Specifically, the fast pyrolysis of Loblolly pine was investigated. Isothermal pyrolysis yields were obtained using a novel micro-reactor developed for this study. Kinetic parameters following five different kinetic mechanisms were derived from the yield results using a particle swarm optimization χ^2 minimization procedure. The best fit kinetic parameters were then compared for predictive capabilities on alternate species. A predictive pyrolysis simulation for the advancement of packed bed reactor design was developed utilizing the kinetic parameters previously derived and evaluated. Five research objectives were stated at the beginning of this work. Each of those objectives will now be addressed and conclusions resulting from the pursuit of the objectives discussed. Key research contributions will then be highlighted and discussed. Finally, recommendations for future work will be made.

8.1 Summary and Conclusions

A novel micro-reactor was developed to facilitate the isothermal fast pyrolysis of biomass. The reactor system demonstrated the ability to control reactor plate temperature, particle residence time and remove pyrolysis products. Heating rates on the order of 400°C/s were projected based upon heat transfer simulations and experimental measurements of wood wafer heating rates. Particle distribution was also investigated using image analysis and an ANOVA to find the operating parameters which provided the best distribution of biomass over the reaction plate surface. Yield results obtained using the micro-reactor were then applied to the derivation of kinetic

parameters.

Fast pyrolysis derived kinetic parameters were shown to be substantially different from those derived using slow pyrolysis techniques. A graphical analysis was performed using an Arrhenius $\ln k$ versus $1/T$ plot with overlaid rate results from both a TGA oven and the micro-reactor. Fast pyrolysis rates showed partial agreement with the segment of the slow pyrolysis rate curve attributed to cellulose devolatilization. The majority of the rate curve, however, was in disagreement with the fast pyrolysis predicted rates. This challenges the commonly accepted interchangeability of slow and fast pyrolysis kinetics seen in literature, demonstrated through the use of slow pyrolysis kinetics in fast pyrolysis models.

Five kinetic mechanisms were evaluated using experimentally obtained yields from the micro-reactor. The intermediate solid compound model showed the best fit to Loblolly pine experimental results as well as the highest predictive power for alternate species tests. The two component global pyrolysis model showed comparable results for both the Loblolly pine yields and the predictive comparison study. The single component global pyrolysis model also showed good predictive results for the alternate species tests. The product based model derived from Loblolly pine showed good predictive capabilities for the alternate species oil and gas results but departed from the experimental solids yield by approximately 35%. The psuedo-component model showed poor predictive fits for the reasons sited under Objective 3.

The superposition of pseudo-components was unable to predict the rate of pyrolysis of Loblolly pine. Fast pyrolysis kinetic parameters were derived for isolated pseudo-components for cellulose and xylan (a representative hemicellulose carbohydrate) testing using the micro-reactor. The conversion of lignin was then predicted based upon a subtraction of the projected cellulose and hemicellulose conversion using published pseudo-component ratios for Loblolly pine. The results showed negative lignin yields for the first 50 seconds of pyrolysis. This indicates that some retardation

of the whole wood pyrolysis must be occurring.

The interaction of pseudo-components was concluded to be a contributor to the retardation of the pyrolysis reaction as compared to the predicted pseudo-component superposition. Two cellulose and xylan mixtures of differing ratios were pyrolyzed and the experimental yield results compared to the superposition predictions. The results showed an over prediction of the rate of pyrolysis using the superposition model with an eventual convergence on the final yields obtained. This demonstrates that interactions play a role in the departure between pseudo-component superposition and whole biomass pyrolysis. This differs from the common conclusion in literature that the departure is solely a result of the presence of mineral content in whole biomass. Scaling analyses were also performed to show that heat and mass transfer are not the rate limiting factors for the pyrolysis of biomass within the micro-reactor.

A multi-physics kinetics heat and mass-transfer model was developed for the prediction of fast pyrolysis in a moving bed vacuum pyrolysis reactor. The conservation equations were analytically developed and implemented within a finite-difference solution scheme. Simulation results provided both temperature and product density spacio-temporal profiles within the bed as well as product volatilization as a function of time. These results were used for the evaluation of key reaction design parameters: the time to reach 90% conversion and the specific energy and power requirements over this time period. These parameters were evaluated for nine reactor configurations varying the particle bed height and reaction plate temperature. The implications of the observed trends was then discussed. Simulation design parameter results were then applied to the sizing of a moving bed vacuum pyrolysis reactor and the impact of a 5% decrease in the pyrolysis activation energy evaluated.

Pursuant to the research reported in this thesis, and summarized above, the following conclusions can be drawn:

1. Mass conversion yields for biomass were measured to an average experimental

uncertainty of 0.003g/g for solid yields, 0.006g/g for oil yields and 0.007g/g for gas yields.

2. Low heating rate derived kinetic parameters are not interchangeable with high heating rate derived kinetic parameters for biomass pyrolysis.

3. Pseudo-component mechanisms limit the applicability of pseudo-component models to the prediction of whole whole wood fast pyrolysis.

4. Two component global kinetic mechanisms described the pyrolysis of Loblolly pine with equivalent predictive power to complex intermediate solid pseudo-component kinetic mechanisms, based upon a difference in reduced χ^2 goodness of fit values of 0.17.

5. Single component mechanisms for the pyrolysis of Loblolly pine provide equivalent predictive power to two component bulk kinetic mechanisms as reactor temperatures increase from $400 - 420°C$. The predictive power gained in the complexity of the two component models collapses as the reaction temperature increases, converging at 420°C with a reduced χ^2 difference of 0.02.

6. A multi-physics pyrolysis model was demonstrated to predict the oil yield to 8% for the fast pyrolysis of Loblolly pine.

7. Variations in the kinetic rate parameters significantly impact the predicted residence time and energy intensity of moving bed vacuum pyrolysis reactors.

8.2 Contributions

• A new experimental isothermal fast pyrolysis micro-reactor

The reactor design has been presented along with its development process and transient thermal analyses used in validating the reactor's biomass heating rate performance. The reactor provides for the control of feedstock residence time within the

reactor, allowing for the derivation of conversion rates as a function of residence time. The use of conduction as the primary mode of heat transfer allowed for the separation of heat transfer and product removal pathways. This in turn facilitated the use of a low temperature carrier gas resulting in product quenching and the minimization of secondary reactions within pyrolysis products. The separation of heat transfer and pyrolysis product removal mechanisms also allowed for the collection of separate solid and liquid pyrolysis products without the need for additional separation equipment. Heating rates for biomass within the reactor were projected to be on the order of 400°C/s. This reactor design has advanced the study of fast pyrolysis and provides a pathway to high fidelity isothermal pyrolysis yield data.

• A method for the determination of kinetic parameters using the χ^2 goodness of fit and particle swarm optimization

The computational methods for extracting pyrolysis yields from the micro-reactor result were presented providing a pathway to high fidelity isothermal pyrolysis data. These methods were then applied for the evaluation of pyrolysis yields as a function of both reactor temperature and residence time. A robust fitting methodology was presented which uses the χ^2 goodness of fit parameter as the evaluation of model descriptive power. The use of the χ^2 parameter allows for the consideration of the scatter within experimental data and also adjusts the goodness of fit according to the number of model parameters solved for. Global best fit kinetic parameters were solved for using a particle swarm optimization algorithm and confidence intervals evaluated using an F-test. Both the use of χ^2 parameters as a fit criterion and the particle swarm methodology for pyrolysis kinetic parameter derivation are firsts within the field.

• The comparative evaluation of pyrolysis models from a common data set

Five different model kinetic schemes were applied to the same core set of data

from Loblolly pine, Avicel cellulose and Beechwood xylan pyrolysis. The models were: single component; two component; product based; pseudo-component; and pseudo-component with an intermediate solid compound. The reduced χ^2 results showed that the intermediate char model is the best fit to the Loblolly pine pyrolysis data with a χ^2_ν value of 3.48. The two component global model showed the next best fit with a χ^2_ν value of 3.65. Predictive evaluations for Norway spruce and Scots pine produced average χ^2_ν values of 17.4, 19.2 and 21.7 for the intermediate solid model, two component model and single component models respectively. The pseudo-component model produced large departures in the predicted char and the pseudo-component model was the worst predictor with average χ^2_ν values ranging from 39.5-465 depending upon the source of the lignin kinetics. The single component and two component global pyrolysis models are, however, more suitable predictors for pyrolysis simulations than the more complicated intermediate solid model as approximately equivalent predictive fits were obtained with a much simpler form.

• The demonstration of fast and slow pyrolysis kinetic dissimilarities

Slow and fast pyrolysis kinetics were demonstrated to be different based upon a graphical analysis using an Arrhenius $\ln k$ versus $1/T$ plot. Kinetic rates as a function of temperature were extracted from thermogravimetric analysis results for the slow pyrolysis of Loblolly pine. The predicted fast pyrolysis rates from the previously derived single component global models for Loblolly pine, Avicel cellulose and Beechwood xylan were then overlaid on the Arrhenius plot. Fast pyrolysis rates showed partial agreement with the segment of the slow pyrolysis rate curve attributed to cellulose devolatilization. The majority of the rate curve, however, was in disagreement with the fast pyrolysis predicted rates. This challenges the commonly accepted notion of slow and fast pyrolysis kinetic interchangeability.

• The development of a packed bed pyrolysis model as a design tool

A packed bed pyrolysis model was developed providing detailed predictions of pyrolysis yields as well as temperature and product density profiles within the packed bed. The use of this model as a process parameter investigatory tool was also demonstrated. This represents a significant step in the modeling of fast pyrolysis reactors with separate heat and mass transfer pathways.

• The following papers have been published or are currently under review:

1. Williams, A., and Mayor, J. R., 2010. "A micro-reactor system for the analysis of the fast pyrolysis of biomass". Journal of Thermal Science and Engineering Applications, 2(3).

2. Mayor, J. R., and Williams, A., 2010. "Investigation into the effects of reaction duration on the isothermal fast pyrolysis of biomass". Journal of Energy Resources Technology, 132(4).

3. David, K., Williams, A., Mayor, R., Muzzy, J., and Ragauskas, A., 2009. "31p nmr analysis of bio-oils obtained from the pyrolysis of biomass". Biofuels, 1(6).

4. Mayor, J. R., and Williams, A., 2008. "Design, development and characterization of a micro-reactor for fast pyrolysis of biomass feedstocks". Presented at the Engineering Systems Design and Analysis Conference, Haifa, Israel, July 7-9.

5. Mayor, J. R., and Williams, A., 2009. "Investigation into the effects of reaction duration on the isothermal fast pyrolysis of biomass". Presented at the 3rd International Conference on Energy Sustainability 2009, San Francisco, CA USA, July 19-23, 2009.

6. Mayor, J. R., and Williams, A., 2010. "Experimentally derived Arrhenius coefficients for the reaction modeling of fast pyrolysis". Presented at the ASME

2010 4th International Conference on Energy Sustainability, Phoenix, AZ USA, May 17-22.

8.3 Recommendations for Future Work

During the course of this study several extensions and additions to the work were considered, and are presented in this section as recommendations for future work.

• Micro-Reactor Modifications

The quench cooling of solids should be considered to stop the continued reaction of solids within the solids trap discussed in Section 4.9. This could be accomplished by adding a cold plate to the bottom of the solids trap or by adding a purge flow of cold inert gas directly into the solids trap. The latter method would, however, alter the flow of gases within the reactor.

The addition of an automated semi-continuous deposit mechanism would simplify micro-reactor testing and provide for a significant reduction in the hands-on time required by the operator. This could be accomplished through either a hopper system with stop at the base or a screw feed mechanism. An automated feed system would also simplify increasing the number of deposits for increased oil production for further analysis.

• Additional Product Analyses

A process parameter study investigating the effects of reactor temperature, residence time and particle size on oil quality would provide useful process planning information for reactor design. The oil quality metrics would be lower heating value, viscosity and oil stability (by change in viscosity over time at a set temperature). Product composition studies would also be useful examining the micro-reactor gas and liquid products using GC/MS and HPLC. If integrated into the process parameter study the change in key compounds or groups of compounds could then be related back to operating parameters.

• Extensions to Kinetic Modeling Efforts

Alternate feedstocks should be evaluated using the micro-reactor. In particular herbaceous biomass such as switchgrass and miscanthus are of particular interest due to their fast growth and high annual yields. Hardwoods should also be considered to investigate the extensibility of the derived kinetic parameters from Loblolly pine to markedly dissimilar species of trees.

The tested temperature range should be extended. It would be of great interest to continue to populate the Arrhenius $\ln k$ versus $1/T$ plot with additional individual temperature data points from fast pyrolysis single component fits. This would serve to both further investigate the relationship between slow and fast pyrolysis and provide a larger data set and subsequent better evaluation for the global kinetic parameters.

• Extensions to Reactor Design

A critical evaluation of boundary conditions within packed bed reactors should be conducted. The trade offs between vacuum pyrolysis and cross flow conditions would need to be considered. Cross flow configurations in particular would require careful evaluation of duct sizing, purge gas flow rates, volatilization rates of pyrolysis products and the induced flow in the top of the porous bed as a result of cross flow above the bed.

Improved evaluations of pyrolysis properties are necessary for the improvement of model accuracies. The evaluation of properties such as char thermal conductivity and specific heat as well as volatile diffusivity, thermal conductivity and specific heat are yet to be thoroughly characterized. This is of course a formidable challenge due to the unstable nature of pyrolysis products, but it is a key element for the advancement of reactor design.

Finally, a higher throughput fast pyrolysis reactor should be designed around the principle of separate heat and mass transfer pathways. This would allow for larger quantities of oil to be collected for less operator time. The design should be guided

by the packed bed pyrolysis model contained within this work.

APPENDIX A

VIBRATORY ASSISTED SPREADING IMAGE RESULTS

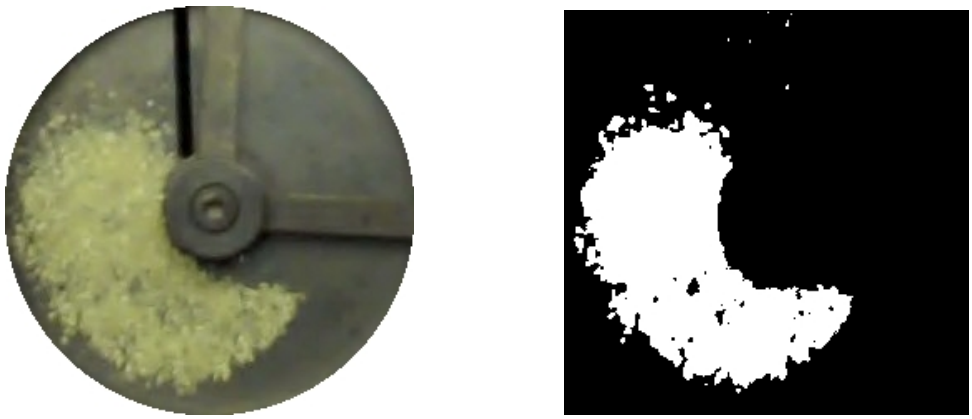

(a) (b)

Figure A.1: Run 1 raw spreading image (a) and contrast modified image (b) utilized in vibratory assisted particle spreading image processing

(a) (b)

Figure A.2: Run 2 raw spreading image (a) and contrast modified image (b) utilized in vibratory assisted particle spreading image processing

(a) (b)

Figure A.3: Run 3 raw spreading image (a) and contrast modified image (b) utilized in vibratory assisted particle spreading image processing

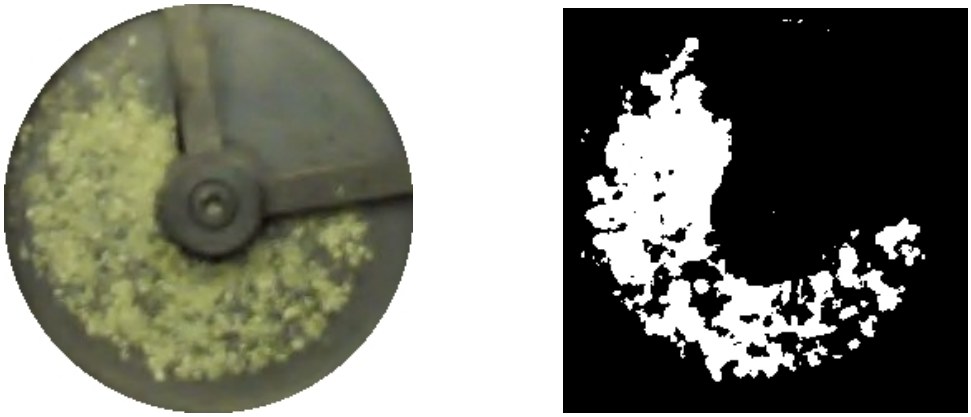

(a) (b)

Figure A.4: Run 4 raw spreading image (a) and contrast modified image (b) utilized in vibratory assisted particle spreading image processing

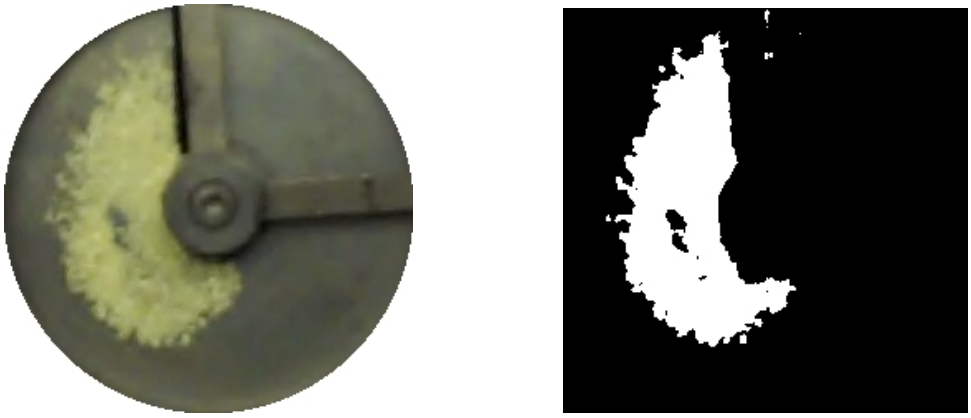

(a) (b)

Figure A.5: Run 5 raw spreading image (a) and contrast modified image (b) utilized in vibratory assisted particle spreading image processing

(a) (b)

Figure A.6: Run 6 raw spreading image (a) and contrast modified image (b) utilized in vibratory assisted particle spreading image processing

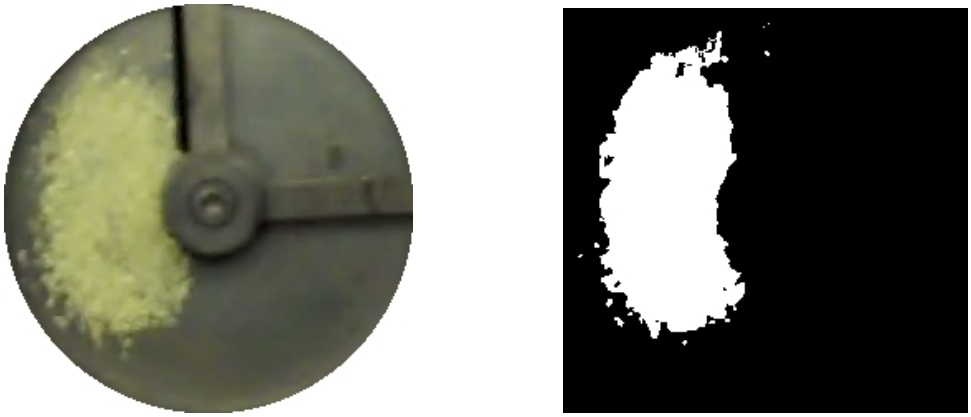

(a) (b)

Figure A.7: Run 7 raw spreading image (a) and contrast modified image (b) utilized in vibratory assisted particle spreading image processing

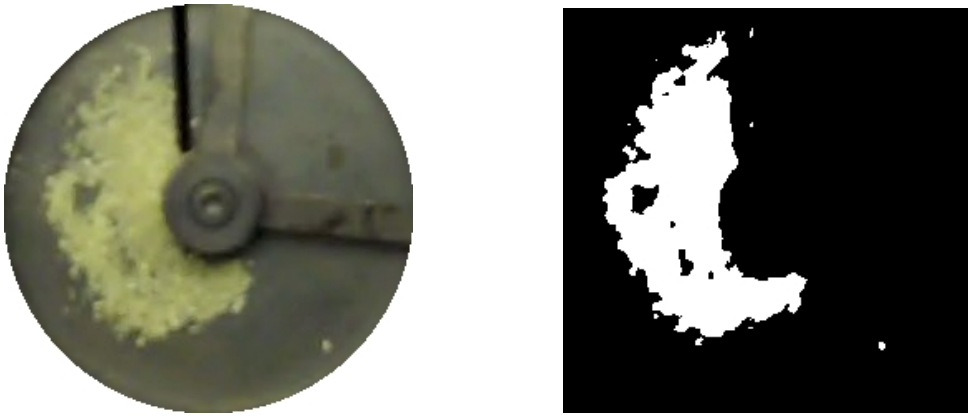

(a) (b)

Figure A.8: Run 8 raw spreading image (a) and contrast modified image (b) utilized in vibratory assisted particle spreading image processing

(a) (b)

Figure A.9: Run 9 raw spreading image (a) and contrast modified image (b) utilized in vibratory assisted particle spreading image processing

(a) (b)

Figure A.10: Run 10 raw spreading image (a) and contrast modified image (b) utilized in vibratory assisted particle spreading image processing

(a) (b)

Figure A.11: Run 11 raw spreading image (a) and contrast modified image (b) utilized in vibratory assisted particle spreading image processing

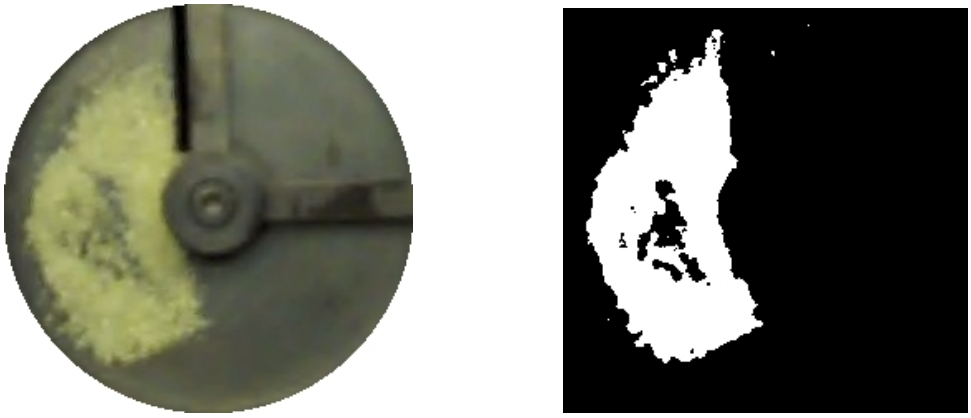

(a) (b)

Figure A.12: Run 12 raw spreading image (a) and contrast modified image (b) utilized in vibratory assisted particle spreading image processing

(a) (b)

Figure A.13: Run 13 raw spreading image (a) and contrast modified image (b) utilized in vibratory assisted particle spreading image processing

(a) (b)

Figure A.14: Run 14 raw spreading image (a) and contrast modified image (b) utilized in vibratory assisted particle spreading image processing

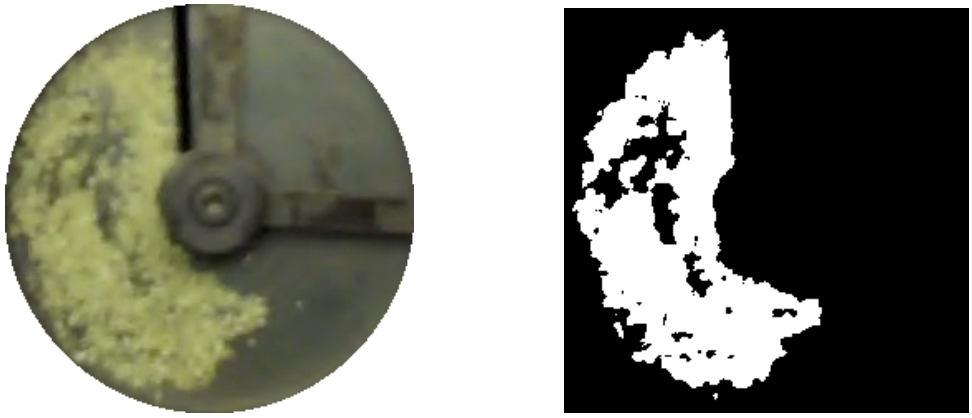

(a) (b)

Figure A.15: Run 15 raw spreading image (a) and contrast modified image (b) utilized in vibratory assisted particle spreading image processing

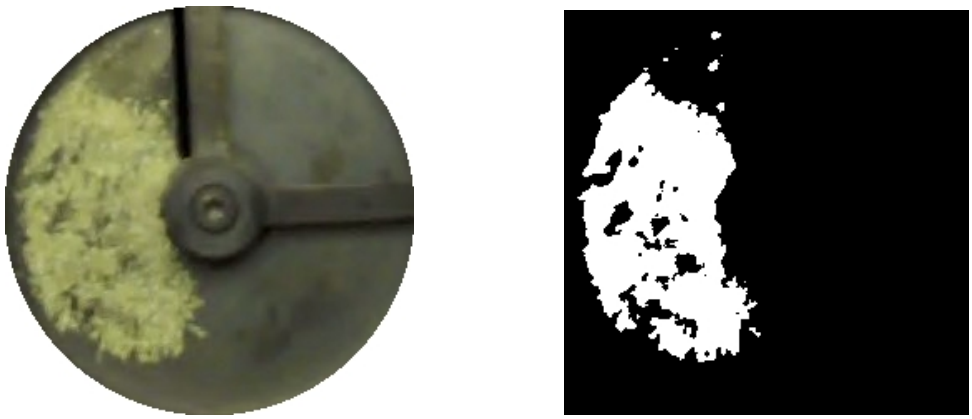

(a) (b)

Figure A.16: Run 16 raw spreading image (a) and contrast modified image (b) utilized in vibratory assisted particle spreading image processing

(a) (b)

Figure A.17: Run 17 raw spreading image (a) and contrast modified image (b) utilized in vibratory assisted particle spreading image processing

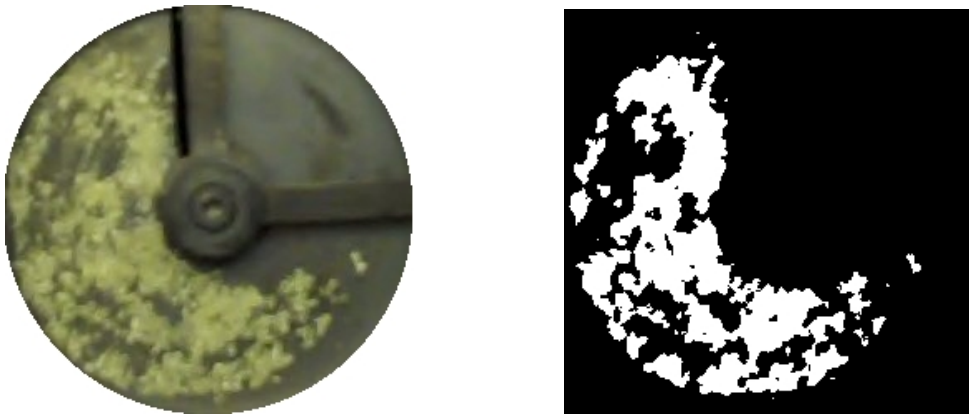

(a) (b)

Figure A.18: Run 18 raw spreading image (a) and contrast modified image (b) utilized in vibratory assisted particle spreading image processing

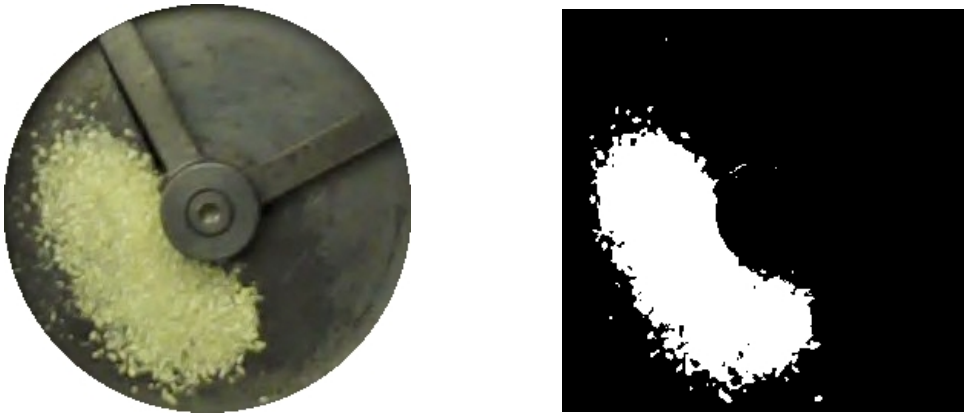

(a) (b)

Figure A.19: Run 19 raw spreading image (a) and contrast modified image (b) utilized in vibratory assisted particle spreading image processing

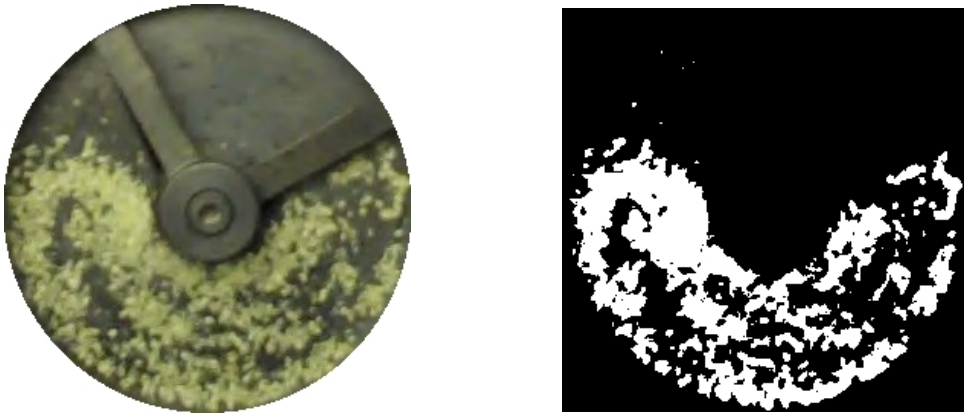

(a) (b)

Figure A.20: Run 20 raw spreading image (a) and contrast modified image (b) utilized in vibratory assisted particle spreading image processing

(a) (b)

Figure A.21: Run 21 raw spreading image (a) and contrast modified image (b) utilized in vibratory assisted particle spreading image processing

(a) (b)

Figure A.22: Run 22 raw spreading image (a) and contrast modified image (b) utilized in vibratory assisted particle spreading image processing

(a) (b)

Figure A.23: Run 23 raw spreading image (a) and contrast modified image (b) utilized in vibratory assisted particle spreading image processing

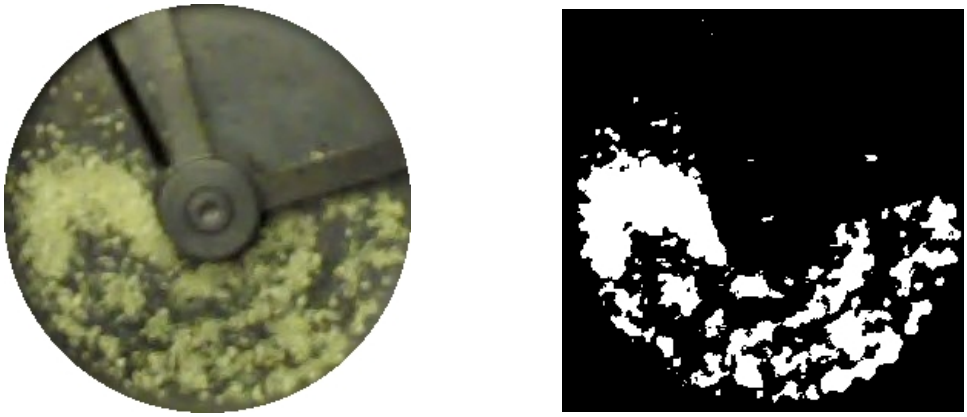

(a) (b)

Figure A.24: Run 24 raw spreading image (a) and contrast modified image (b) utilized in vibratory assisted particle spreading image processing

APPENDIX B

MICRO-REACTOR TEST DOCUMENTATION FORM AND DATA SHEET

Micro-Reactor Pyrolysis Test Structure TG2.3.1

Experiment #: _____ Date: _____

Feedstock: _____
Treatment: _____
Milling Equpment: _____ Particle Size: _____
Drying Temp: _____ ˚C Drying Time: _____

Purge Gas: _____ Chamber Flow Rate: _____
Dwell Time: _____ sec _____
Reaction Temperature: _____ ˚C

Purpose: To facilitate a fast pyrolysis reaction of biomass and recover the reaction product for mass balance and chemical analysis.

Equipment: Mass Balance: Model #: _____
Serial #: _____

Procedure:

i. Mass Seperately and record the mass of the components.
ii. Set Spread, Dwell, and Scrape times in Basic Stamp program.
iii. Activate He flow and set to 1680 cc/min.
iv. Reassemble reactor and preheat to set temperature with flow hood activated.
v Insert condenser and connect to reactor lid.
vi. After 5 minutes add liquid nitrogen to dewar.
vii. Mass weighing vessel for sample deposit and record value.
viii. Zero balance, mass out sample and record value.
ix. Pour sample in Stopcock chip drop.
x. Zero balance and remass weighing vessel.
xi. Activate automated testing system and rotate Stopcock.
xii. Repeat steps vii. through xi. until predetermined number of drops are processed.
xiii. Disconnect condenser and plug ends.
xiv. Turn off reactor heating elements.
xv. Disconnect chip catch.
xvi. Remove reactor cover and stopcock chip drop.
xvii. Once at room temperature, dry off condenser with compressed air and mass.
xviii. Once at room temperature mass the remaining components.
xix. Move collected byproducts to storage viles.
xx. Ensure flow hood and helium flow are turned off.

Heater Start Time: _____
Heater Stop Time: _____

Object	Before (g)	After (g)	Difference (g)	Adjusted % Mass
Stopcock Chip Drop				-
Chip Catch				
Turb Cold Trap+Plugs				
Unaccounted for Reacted Mass				

Sample	Paper Before (g)	Sample Before(g)	Paper After (g)	Paper Change (g)	Actual Deposit (g)
1					
2					
3					
4					
5					
6					
7					
8					
9					
10					
11					
12					
13					
14					
15					
16					
17					
18					
19					
20					
				Total Dep:	

Deposited - Stopcock Diff. (g)	

Vile	Specimen	Before (g)	After (g)	Difference (g)
1				
2				

APPENDIX C

DERIVATION OF CONSERVATION EQUATIONS IN FINITE DIFFERENCE FORM

The conservation equations were rewritten for implementation into a finite difference explicit solution model scheme. The heat transfer within the solid is given by Equation C.1,

$$\dot{E}^t_{st,s,n} = q^t_{cond,n-1} + q^t_{cond,n+1} + q^t_{conv,n} + \dot{E}^t_{py,s,n} \tag{C.1}$$

where $\dot{E}_{st}$ is the rate of energy storage in any given discretized cell, $q_{cond,n-1}$ is the heat conducted from the $n-1$ cell, $q_{cond,n+1}$ is the heat conducted from the $n+1$ cell and $\dot{E}_{pyr}$ is the heat sink due to the enthalpy of pyrolysis. The individual terms are then presented in Equations C.2 - C.6,

$$\dot{E}^t_{st,s,n} = (\rho c_p)^t_{s,n} \frac{T^{t+1}_{s,n} - T^t_{s,n}}{\Delta t} \Delta x \Delta y \Delta z \tag{C.2}$$

$$q^t_{cond,n-1} = \kappa^t_{s,n-1} \frac{T^t_{s,n-1} - T^t_{s,n}}{\Delta z} \Delta x \Delta y \tag{C.3}$$

$$q^t_{cond,n+1} = \kappa^t_{s,n} \frac{T^t_{s,n+1} - T^t_{s,n}}{\Delta z} \Delta x \Delta y \tag{C.4}$$

$$q^t_{conv,n} = h^t_{loc,n} a \Delta x \Delta y \Delta z (T^t_{g,n} - T^t_{s,n}) \tag{C.5}$$

$$\dot{E}^t_{py,s,n} = \rho^t_{w,n} k^t (T^t_{s,n}) \Delta H_{py} \Delta x \Delta y \Delta z \tag{C.6}$$

The discrete time step solutions for wood and char densities, the solids ρc term and the solids thermal conductivity are given by Equations C.7-C.10,

$$\rho_w^{t+1} = \rho_w^t - \rho_w^t k(T_{s,n}^t)\Delta t \tag{C.7}$$

$$\rho_c^{t+1} = \rho_c^t + (1-\psi_v)\rho_w^t k(T_{s,n}^t)\Delta t \tag{C.8}$$

$$(\rho c_p)_{s,n}^t = \rho_{w,n}^t c_w(T_n^t) + \rho_{c,n}^t c_c(T_n^t) \tag{C.9}$$

$$\kappa_{s,n}^t = \frac{\rho_{w,n}^t \kappa_w(T_n^t) + \rho_{c,n}^t \kappa_c(T_n^t)}{\rho_{w,n}^t + \rho_{c,n}^t} \tag{C.10}$$

The discretized energy balance for the gas phase is given in Equations C.11,

$$\dot{E}_{st,g,n}^t = q_{ad,n-1}^t + q_{ad,n+1}^t - q_{conv,n}^t + \dot{E}_{py,g,n}^t \tag{C.11}$$

where q_{ad} is the heat advected (either in to or out of the unit cell) by the diffusing pyrolysis products within the continuum. The individual terms are then broken down in Equations C.12 - C.16,

$$\dot{E}_{st,g,n}^t = (\rho c_p)_{g,n}^t \frac{T_{g,n}^{t+1} - T_{g,n}^t}{\Delta t}\Delta x \Delta y \Delta z \tag{C.12}$$

$$q_{ad,n-1}^t = \dot{\rho}_{\Delta p,n-1}^t (c_p)_{g,n-1}^t \Delta x \Delta y \Delta z T_{g,n-1}^t \tag{C.13}$$

$$q_{ad,n+1}^t = \dot{\rho}_{\Delta p,n+1}^t (c_p)_{g,n}^t \Delta x \Delta y \Delta z T_{g,n}^t \tag{C.14}$$

$$\dot{E}_{py,n}^t = \dot{S}_{g,n}^t (c_p)_{g,n}^t T_{s,n}^t \Delta x \Delta y \Delta z \tag{C.15}$$

$$\dot{S}^t_{g,n} = \psi_v \rho^t_w k(T^t_{s,n}) \tag{C.16}$$

The discretized conservation of species for the unit cell is described by Equation C.17,

$$\dot{\rho}^t_{g,n} = \dot{\rho}^t_{\Delta p,n-1} + \dot{\rho}^t_{\Delta p,n+1} + \dot{S}^t_{g,n} \tag{C.17}$$

The individual terms are then given by Equations C.18 - C.20,

$$\dot{\rho}^t_{g,n} = \frac{\rho^{t+1}_n - \rho^t_n}{\Delta t} \tag{C.18}$$

$$\dot{\rho}^t_{\Delta p,n-1} = BT^t_{g,n} \left(\frac{\rho^t_{n-1} - \rho^t_n}{\Delta z} \right)^2 \tag{C.19}$$

$$\dot{\rho}^t_{\Delta p,n+1} = BT^t_{g,n} \left(\frac{\rho^t_{n+1} - \rho^t_n}{\Delta z} \right)^2 \tag{C.20}$$

The subsequent superficial velocities for the Reynolds number and local convection coefficient calculations are given by Equation C.21,

$$v^t_{0,n} = \frac{\dot{\rho}^t_{\Delta p,n+1} + \dot{\rho}^t_{\Delta p,n-1}}{2\rho^t_{g,n}} \tag{C.21}$$

The boundary conditions for implementation into the finite difference model are given by Equations C.22-C.27,

$$q_{cond,s,n=0} = \kappa \frac{T_{plate} - T_{s,n=1}}{\Delta z/2} \Delta x \Delta y \tag{C.22}$$

$$-\kappa \left(\frac{T_{s,N} - T_{s,N-1}}{\Delta z} \right) = \sigma \epsilon_w (T^4_{s,N} - T^4_{glass}) \tag{C.23}$$

$$q_{ad,g,n=0} = 0 \tag{C.24}$$

$$q_{ad,N+1} = \dot{\rho}^t_{\Delta p,N+1}(c_p)_{g,N}T_{g,N}\Delta x\Delta y\Delta z \tag{C.25}$$

$$\rho^t_{g,n=0} - \rho^t_{n=1} = 0 \tag{C.26}$$

$$\rho_{g,N+1} = \rho_\infty \tag{C.27}$$

The discretized initial conditions are given by Equations C.28-C.30,

$$T_s^{t=0} = T_0 \tag{C.28}$$

$$T_g^{t=0} = T_0 \tag{C.29}$$

$$\rho_g^{t=0} = 0 \tag{C.30}$$

The combined full form discretized equations are shown in Equations C.31-C.33

$$\begin{aligned}(\rho c)^t_s\frac{T^{t+1}_{s,n} - T^t_{s,n}}{\Delta t}\Delta x\Delta y\Delta z =&\kappa^t_{s,n-1}\frac{T^t_{s,n-1} - T^t_{s,n}}{\Delta z}\Delta x\Delta y + \kappa^t_{s,n}\frac{T^t_{s,n+1} - T^t_{s,n}}{\Delta z}\Delta x\Delta y\\ &+ h^t_{loc,n}a\Delta x\Delta y\Delta z(T^t_{g,n} - T^t_{s,n})\\ &+ \rho^t_{w,n}k(T^t_{s,n})\Delta H_{py}\Delta x\Delta y\Delta z\end{aligned} \tag{C.31}$$

$$\begin{aligned}(\rho c_p)^t_{g,n}\frac{T^{t+1}_{g,n} - T^t_{g,n}}{\Delta t}\Delta x\Delta y\Delta z =&\dot{\rho}^t_{\Delta p,n-1}(c_p)^t_{g,n-1}T^t_{g,n-1}\Delta x\Delta y\Delta z\\ &+ \dot{\rho}^t_{\Delta p,n+1}(\rho c_p)^t_{g,m@(n)}T^t_{g,n}\Delta x\Delta y\Delta z\\ &- h^t_{loc,n}a\Delta x\Delta y\Delta z(T^t_{g,n} - T^t_{s,n})\\ &+ \dot{S}^t_{g,n}(c_p)^t_{g,n}T^t_{s,n}\Delta x\Delta y\Delta z\end{aligned} \tag{C.32}$$

$$\frac{\rho_n^{t+1}-\rho_n^t}{\Delta t} = BT_{g,n}^t\left(\frac{\rho_{n-1}^t-\rho_n^t}{\Delta z}\right)^2 + BT_{g,n}^t\left(\frac{\rho_{n+1}^t-\rho_n^t}{\Delta z}\right)^2 + \dot{S}_{py,n}^t \tag{C.33}$$

Simplification yields Equations C.34-C.36,

$$\begin{aligned}(\rho c)_{s,n}^t\frac{T_{s,n}^{t+1}-T_{s,n}^t}{\Delta t} =&\kappa_{s,n-1}^t\frac{T_{n-1,s}^t-T_{n,s}^t}{(\Delta z)^2} + \kappa_{s,n}^t\frac{T_{n+1,s}^t-T_{n,s}^t}{(\Delta z)^2}\\ &+ h_{loc,n}^t a(T_{g,n}^t - T_{s,n}^t) + \rho_{w,n}^t k(T_{s,n}^t)\Delta H_{py}\end{aligned} \tag{C.34}$$

$$\begin{aligned}(\rho c_p)_{g,n}^t\frac{T_{g,n}^{t+1}-T_{g,n}^t}{\Delta t} =&\dot{\rho}_{\Delta p,n-1}^t(c_p)_{g,n-1}^t T_{g,n-1}^t + \dot{\rho}_{\Delta p,n+1}^t(c_p)_{g,n}^t T_{g,n}^t\\ &- h_{loc,n}^t a(T_{g,n}^t - T_{s,n}^t) + \dot{S}_{g,n}^t(c_p)_{g,n}^t T_{s,n}^t\end{aligned} \tag{C.35}$$

$$\frac{\rho_n^{t+1}-\rho_n^t}{\Delta t} = \frac{BT_{g,n}^t}{(\Delta z)^2}\left((\rho_{n-1}^t)^2 - 2(\rho_n^t)^2 + (\rho_{n+1}^t)^2\right) + \dot{S}_{g,n}^t \tag{C.36}$$

Further separation for implementation within an explicit solution methodology produces Equations C.37-C.39,

$$\begin{aligned}T_{s,n}^{t+1} =&\left[\frac{\kappa_{s,n-1}^t}{(\Delta z)^2}T_{s,n-1} - \left(\frac{\kappa_{s,n-1}^t}{(\Delta z)^2} + \frac{\kappa_{s,n}^t}{(\Delta z)^2} + h_{loc,n}^t a\right)T_{s,n}^t + \frac{\kappa_{s,n}^t}{(\Delta z)^2}T_{s,n+1}\right.\\ &\left.+ h_{loc,n}^t a T_{g,n}^t + \rho_{w,n}^t k(T_{s,n}^t)\Delta H_{py}\right]\frac{\Delta t}{(\rho c)_{s,n}^t} + T_{s,n}^t\end{aligned} \tag{C.37}$$

$$\begin{aligned}T_{g,n}^{t+1} =&\Big[\dot{\rho}_{\Delta p,n-1}^t(c_p)_{g,n-1}^t T_{g,n-1}^t + \dot{\rho}_{\Delta p,n+1}^t(c_p)_{g,n}^t T_{g,n}^t + \dot{S}_{g,n}^t(c_p)_{g,n}^t T_{s,n}^t\\ &- h_{loc,n}^t a(T_{g,n}^t - T_{s,n}^t)\Big]\frac{\Delta t}{(\rho c_p)_{g,n}^t} + T_{g,n}^t\end{aligned} \tag{C.38}$$

$$\rho_n^{t+1} = \left[\frac{BT_{g,n}^t}{(\Delta z)^2}(\rho_{n-1}^t)^2 - \frac{2BT_{g,n}^t}{(\Delta z)^2}(\rho_n^t)^2 + \frac{BT_{g,n}^t}{(\Delta z)^2}(\rho_{n+1}^t)^2 + \dot{S}_{g,n}^t\right]\Delta t + \rho_n^t \tag{C.39}$$

The boundary cell equations for the solid phase are given in Equations C.40 and C.41,

$$T_{s,n=1}^{t+1} = \Bigg[\left(-\frac{\kappa_{s,n=1}^{t}}{\Delta z^2/2} - \frac{\kappa_{s,n=1}^{t}}{\Delta z^2} - h_{loc,n=1}^{t} a \right) T_{s,n=1}^{t} + \frac{\kappa_{s,n=1}}{\Delta z^2} T_{s,n=2} + \frac{\kappa_{s,n=1}^{t}}{\Delta z^2/2} T_{plate} + h_{loc,N}^{t} a T_{g,n=1} + \rho_{w,n=1}^{t} k(T_{s,n=1}^{t}) \Delta H_{py} \Bigg] \frac{\Delta t}{(\rho c)_{s,n=1}^{t}} + T_{s,n=1}^{t} \tag{C.40}$$

$$T_{s,N}^{t+1} = \Bigg[\frac{\kappa}{\Delta z^2} T_{s,N-1}^{t} + \left(-\frac{\kappa_{s,N-1}}{\Delta z^2} - h_{loc,N}^{t} a \right) T_{s,N}^{t} - \frac{\sigma \epsilon_w}{\Delta z} (T_{s,N}^{t})^4 + h_{loc,N}^{t} a T_{g,N}^{t} + \rho_{w,N}^{t} k(T_{s,N}^{t}) \Delta H_{py} + \frac{\sigma \epsilon_w}{\Delta z} T_{rad}^{4} \Bigg] \frac{\Delta t}{(\rho c)_{s,N}^{t}} + T_{s,N}^{t} \tag{C.41}$$

The boundary cell conditions for the gaseous phase are given in Equations C.42 and C.43,

$$T_{g,n=1}^{t+1} = \Bigg[\left(-h_{loc,n=1}^{t} a + \dot{\rho}_{\Delta p,n=2}^{t} c_{p,g,n=1}^{t} \right) T_{g,n=1} + h_{loc,n=1}^{t} a T_{s,n=1}^{t} + \dot{S}_{g,n}^{t} c_{p,g,n=1}^{t} T_{s,n=1}^{t} \Bigg] \frac{\Delta t}{(\rho c_p)_{g,n=1}} + T_{g,n=1}^{t} \tag{C.42}$$

$$T_{g,N}^{t+1} = \Bigg[\dot{\rho}_{\Delta p,N-1}^{t} c_{p,g,N-1}^{t} T_{g,N-1}^{t} + \left(\dot{\rho}_{\Delta p,N+1}^{t} c_{p,g,N}^{t} - h_{loc,N}^{t} a \right) T_{g,N}^{t} + h_{loc,N} a T_{s,N}^{t} + \dot{S}_{g,N}^{t} c_{p,g,N}^{t} T_{s,N}^{t} \Bigg] \frac{\Delta t}{(\rho c_p)_{g,N}} + T_{g,N}^{t} \tag{C.43}$$

The boundary cell equations for the conservation of species are given in Equations C.44 and C.45,

$$\rho_{n=1}^{t+1} = \left[-\frac{BT_{g,n}^{t}}{(\Delta z)^2} (\rho_{n=1}^{t})^2 + \frac{BT_{g,n}^{t}}{(\Delta z)^2} (\rho_{n=2}^{t})^2 + \dot{S}_{g,n}^{t} \right] \Delta t + \rho_{n=1}^{t} \tag{C.44}$$

$$\rho_{N}^{t+1} = \Big[\frac{BT_{g,N}^{t}}{(\Delta z)^2} (\rho_{N-1}^{t})^2 - \frac{BT_{g,N}^{t}}{(\Delta z)^2} \left(\frac{1}{(\Delta z)^2} + \frac{1}{(\Delta z/2)^2} \right) (\rho_{N}^{t})^2 + \frac{BT_{g,N}^{t}}{(\Delta z)^2} (\rho_{N+1}^{t})^2 + \dot{S}_{g,N}^{t} \Big] \Delta t + \rho_{N}^{t} \tag{C.45}$$

REFERENCES

[1] United States Environmental Protection Agency, 2010. Renewable fuel standards. www.epa.gov/otaq/fuels/renewablefuels/index.htm.

[2] Directive 2009/28/EC of the european parliament and of the council of 23 April 2009. http://eur-lex.europa.eu/LexUriServ/LexUriServ.do?uri=OJ:L:2009:140:0016:0062:en:PDF.

[3] Perlack, R. D., Wright, L. L., Turhollow, A. F., Graham, R. L., Stokes, B. J., and Erbach, D. C., 2005. Biomass as a feestock for a bioenergy and bioproducts industry: The technical feasibility of a billion-ton annual supply.

[4] Wear, D. N., and Greis, J. G., 2002. Southern forest resource assessment - technical report.

[5] Scott, D. A., and Dean, T. J., 2006. "Energy trade-offs between intensive biomass utilization, site productivity loss, and ameliorative treatments in loblolly pine plantations". *Biomass and Bioenergy,* **30**(12), pp. 1001–1010.

[6] Flynn, P., and Kumar, A., 2005. Trip report site visit to Alholmens 240 MW power plant.

[7] Cunningham, K., Barry, J., and Walkingstick, T., 2008. Managing loblolly pine stands...from a to z. Tech. Rep. FSA5023, University of Arkansas.

[8] Bridgwater, A. V., and Peacocke, G. V. C., 2000. "Fast pyrolysis processes for biomass". *Renewable & sustainable energy reviews,* **4**(1), pp. 1–73.

[9] Mohan, D., Jr., C. U. P., and Steele, P. H., 2006. "Pyrolysis of wood/biomass for bio-oil: A critical review". *Energy and Fuels,* **20**, pp. 848–889.

[10] Bridgwater, A. V., 1990. "Economics of primary fuels production from biomass". Vol. 5 of *Proceedings of the Intersociety Energy Conversion Engineering Conference*, Publ by IEEE, pp. 107–112.

[11] Branca, C., and Di Blasi, C., 2003. "Kinetics of the isothermal degradation of wood in the temperature range 528-708 k". *Journal of Analytical and Applied Pyrolysis,* **67**(2), pp. 207–219.

[12] Babu, B., and Chaurasia, A., 2004. "Pyrolysis of biomass: Improved models for simultaneous kinetics transport of heat, mass, and momentum". *Energy Conversion and Management,* **45**, pp. 1297–1327.

[13] Maschio, G., Lucchesi, A., and Stoppato, G., 1994. "Production of syngas from biomass". *Bioresource Technology,* **48**(2), pp. 119–126.

[14] Maschio, G., Koufopanos, C., and Lucchesi, A., 1992. "Pyrolysis, a promising route for biomass utilization". *Bioresource Technology,* **42**(3), pp. 219–231.

[15] Demirbas, A., and Arin, G., 2002. "An overview of biomass pyrolysis". *Energy Sources,* **24**(5), pp. 471–482.

[16] Di Blasi, C., 2008. "Modeling chemical and physical processes of wood and biomass pyrolysis". *Progress in Energy and Combustion Science,* **34**, pp. 47–90.

[17] Roberts, A. F., and Clough, G., 1963. "Thermal decomposition of wood in an inert atmosphere". *Symposium (International) on Combustion,* **9**(1), pp. 158–166.

[18] Gronli, M. G., 1996. "A theoretical and experimental study of the thermal degradation of biomass". Doctoral thesis.

[19] Ward, S. M., and Braslaw, J., 1985. "Experimental weight loss kinetics of wood pyrolysis under vacuum". *Combustion and Flame,* **61**(3), pp. 261–269.

[20] Milosavljevic, I., and Suuberg, E. M., 1995. "Cellulose thermal decomposition kinetics: Global mass loss kinetics". *Industrial & Engineering Chemistry Research,* **34**(4), pp. 1081–1091.

[21] Chornet, E., and Roy, C., 1980. "Compensation effect in the thermal decomposition of cellulosic materials". *Thermochimica Acta,* **35**(3), pp. 389–393.

[22] Antal Jr, M. J., Varhegyi, G., and Jakab, E., 1998. "Cellulose pyrolysis kinetics: Revisited". *Industrial and Engineering Chemistry Research,* **37**(4), pp. 1267–1275.

[23] Gronli, M., Antal Jr, M. J., and Varhegyi, G., 1999. "A round-robin study of cellulose pyrolysis kinetics by thermogravimetry". *Industrial and Engineering Chemistry Research,* **38**(6), pp. 2238–2244.

[24] Di Blasi, C., and Lanzetta, M., 1997. "Intrinsic kinetics of isothermal xylan degradation in inert atmosphere". *Journal of Analytical and Applied Pyrolysis,* **40-41**, pp. 287–303.

[25] Lanzetta, M., Di Blasi, C., and Buonanno, F., 1997. "An experimental investigation of heat-transfer limitations in the flash pyrolysis of cellulose". *Industrial & Engineering Chemistry Research,* **36**(3), pp. 542–552.

[26] Di Blasi, C., and Branca, C., 2001. "Kinetics of primary product formation from wood pyrolysis". *Industrial & Engineering Chemistry Research,* **40**(23), pp. 5547–5556.

[27] Thurner, F., and Mann, U., 1981. "Kinetic investigation of wood pyrolysis". *Industrial & Engineering Chemistry Process Design and Development,* **20**(3), pp. 482–488.

[28] Jensen, P. A., Frandsen, F. J., Dam-Johansen, K., and Sander, B., 2000. "Experimental investigation of the transformation and release to gas phase of potassium and chlorine during straw pyrolysis". *Energy and Fuels,* **14**, p. 6.

[29] Zhang, J., Toghiani, H., Mohan, D., Charles U. Pittman, J., and Toghiani, R. K., 2007. "Product analysis and thermodynamic simulations from the pyrolysis of several biomass feedstocks". *Energy and Fuels,* **21**, pp. 2373–2385.

[30] Nunn, T. R., Howard, J. B., Longwell, J. P., and Peters, W. A., 1985. "Product compositions and kinetics in the rapid pyrolysis of sweet gum hardwood". *Industrial & Engineering Chemistry Process Design and Development,* **24**(3), pp. 836–844.

[31] Westerhof, R. J. M., Brilman, D. W. F., van Swaaij, W. P. M., and Kersten, S. R. A., 2010. "Effect of temperature in fluidized bed fast pyrolysis of biomass: Oil quality assessment in test units". *Industrial & Engineering Chemistry Research,* **49**(3), pp. 1160–1168.

[32] Scott, D. S., Piskorz, J., Bergougnou, M. A., Graham, R., and Overend, R. P., 1988. "The role of temperature in the fast pyrolysis of cellulose and wood". *Industrial & Engineering Chemistry Research,* **27**(1), pp. 8–15.

[33] Scott, D. S., Piskorz, J., Majerski, P., Radlein, D., and Bridgwater, A. V., 1998. "Fast pyrolysis of sweet sorghum and sweet sorghum bagasse". *Journal of Analytical and Applied Pyrolysis,* **46**(1), pp. 15–29.

[34] Samolada, M. C., and Vasalos, I. A., 1991. "A kinetic approach to the flash pyrolysis of biomass in a fluidized bed reactor". *Fuel,* **70**(7), pp. 883–889.

[35] DeSisto, W. J., Hill, N., Beis, S. H., Mukkamala, S., Joseph, J., Baker, C., Ong, T.-H., Stemmler, E. A., Wheeler, M. C., Frederick, B. G., and van Heiningen, A., 2010. "Fast pyrolysis of pine sawdust in a fluidized-bed reactor". *Energy & Fuels,* **24**(4), pp. 2642–2651.

[36] Boukis, I. P., Grammelis, P., Bezergianni, S., and Bridgwater, A. V., 2007. "CFB air-blown flash pyrolysis. part i: Engineering design and cold model performance". *Fuel,* **86**(10-11), pp. 1372–1386.

[37] Boukis, I. P., Bezergianni, S., Grammelis, P., and Bridgwater, A. V., 2007. "Cfb air-blown flash pyrolysis. part ii: Operation and experimental results". *Fuel,* **86**(10-11), pp. 1387–1395.

[38] Gorton, C. W., Kovac, R. J., Knight, J. A., and Nygaard, T. I., 1990. "Modeling pyrolysis oil production in an entrained-flow reactor". *Biomass,* **21**(1), pp. 1–10.

[39] Knight, J. A., and Gorton, C. W., 1985. "Oil production via entrained flow pyrolysis of biomass". Proceedings of the Intersociety Energy Conversion Engineering Conference, SAE (P-164), pp. 569–572.

[40] Knight, J. A., Gorton, C. W., and Kovac, R. J., 1984. "Oil production by entrained flow pyrolysis of biomass". *Biomass,* **6**(1-2), pp. 69–76.

[41] Knight, J. A., Gorton, C. W., and Kovac, R. J. "Entrained flow pyrolysis of biomass". In 15th Biomass Thermochemical Conversion Contractor's Meeting, pp. 409–419.

[42] Lin, Y.-C., Cho, J., Tompsett, G. A., Westmoreland, P. R., and Huber, G. W., 2009. "Kinetics and mechanism of cellulose pyrolysis". *The Journal of Physical Chemistry C,* **113**(46), pp. 20097–20107.

[43] Boateng, A. A., 2007. "Characterization and thermal conversion of charcoal derived from fluidized-bed fast pyrolysis oil production of switchgrass". *Industrial & Engineering Chemistry Research,* **46**(26), pp. 8857–8862.

[44] Janse, A. M. C., de Jong, X. A., Prins, W., and van Swaaij, W., 1999. "Heat transfer coefficients in the rotating cone reactor". *Powder Technology,* **106**, pp. 168–175.

[45] Wagenaar, B. M., Prins, W., and van Swaaij, W. P. M., 1994. "Pyrolysis of biomass in the rotating cone reactor: modeling and experimental justification". *Chemical Engineering Science,* **49**(24, Part 2), pp. 5109–5126.

[46] Peacocke, G. V. C., and Bridgwater, A. V., 1994. "Ablative plate pyrolysis of biomass for liquids". *Biomass & Bioenergy,* **7**(1-6), pp. 147–154.

[47] Peacocke, G. V. C., Madrali, E. S., Li, C. Z., Guell, A. J., Wu, F., Kandiyoti, R., and Bridgwater, A. V., 1994. "Effect of reactor configuration on the yields and structures of pine-wood derived pyrolysis liquids: a comparison between ablative and wire-mesh pyrolysis". *Biomass & Bioenergy,* **7**(1-6), pp. 155–167.

[48] Ingram, L., Mohan, D., Bricka, M., Steele, P., Strobel, D., Crocker, D., Mitchell, B., Mohammad, J., Cantrell, K., and Jr., C. U. P., 2008. "Pyrolysis of wood and bark in an auger reactor: Physical properties and chemical analysis of the produced bio-oils". *Energy and Fuels,* **22**, pp. 614–625.

[49] Mohan, D., Pittman Jr, C. U., Bricka, M., Smith, F., Yancey, B., Mohammad, J., Steele, P. H., Alexandre-Franco, M. F., Gomez-Serrano, V., and Gong, H., 2007. "Sorption of arsenic, cadmium, and lead by chars produced from fast pyrolysis of wood and bark during bio-oil production". *Journal of Colloid and Interface Science,* **310**(1), pp. 57–73.

[50] Bhattacharya, P., Steele, P. H., Hassan, E. B. M., Mitchell, B., Ingram, L., and Pittman Jr, C. U., 2009. "Wood/plastic copyrolysis in an auger reactor: Chemical and physical analysis of the products". *Fuel,* **88**(7), pp. 1251–1260.

[51] Thangalazhy-Gopakumar, S., Adhikari, S., Ravindran, H., Gupta, R. B., Fasina, O., Tu, M., and Fernando, S. D., 2010. "Physiochemical properties of bio-oil produced at various temperatures from pine wood using an auger reactor". *Bioresource Technology,* **101**(21), pp. 8389–8395.

[52] Brewster, R., 2011. paint.net.

[53] Wu, C. F. J., and Hamada, S., 2009. *Experiments: Planning, Analysis, and Optimizations*, 2nd ed. John Wiley and Sons Inc., Hoboken, New Jersey USA.

[54] Dietenberger, M., Green, D., Kretschmann, D., Hernandez, R., Highley, T., Ibach, R., Liu, J., McDonald, K., Miller, R., Moody, R., Rowell, R., Simpson, W., Soltis, L., TenWolde, A., Wolfe, R., Vick, C., White, R., Williams, R. S., Winandy, J., and J., Y., 1999. Wood handbook: Wood as an engineering material.

[55] Incropera, F. P., and DeWitt, D. P., 2002. *Fundamentals of Heat and Mass Transfer*, fifth ed. John Wiley & Sons, Hoboken, NJ.

[56] Omega. Emissivity of common materials. www.omega.com/literature/transactions/ volume1/emissivityb.html.

[57] Huber, G. W., Iborra, S., and Corma, A., 2006. "Synthesis of transportation fuels from biomass: Chemistry, catalysts, and engineering". *Chemistry Review,* **106**, pp. 4044–4098.

[58] ASTM, 2011. Astm e11-01 standard specification for wire cloth and sieves for testing purposes. ASTM Standard E11-01, 2011, "Standard Specification for Wire Cloth and Sieves for Testing Purposes," ASTM International, West Conshohocken, PA, DOI: 10.1520/E0011-01, www.astm.org.

[59] Kline, S. J., and McClintock, F. A., 1953. "Describing uncertainties in single-sample experiments". *Mechanical Engineering,* **75**(1).

[60] Scientech, Inc., 2005. Scientech zeta series specifications.

[61] Bamford, C. H., Crank, J., and Malan, D. H., 1946. "The combustion of wood". *Proceedings Cambridge Philosophical Society,* **42**, pp. 166–182.

[62] Azeez, A. M., Meier, D., Odermatt, J., and Willner, T., 2010. "Fast pyrolysis of african and european lignocellulosic biomasses using py-gc/ms and fluidized bed reactor". *Energy & Fuels,* **24**(3), pp. 2078–2085.

[63] Branca, C., Giudicianni, P., and Di Blasi, C., 2003. "GC/MS characterization of liquids generated from low-temperature pyrolysis of wood". *Industrial and Engineering Chemistry Research,* **42**(14), pp. 3190–3202.

[64] Evans, R. J., and Milne, T. A., 1987. "Molecular characterization of the pyrolysis of biomass". *Energy & Fuels,* **1**(2), pp. 123–137.

[65] Shafizadeh, F., and Chin, P. P. S., 1977. *Thermal Deterioration of Wood*. American Chemical Society, Washington, pp. 57–81.

[66] Branca, C., Albano, A., and Di Blasi, C., 2005. "Critical evaluation of global mechanisms of wood devolatilization". *Thermochimica Acta,* **429**(2), pp. 133–141.

[67] Gronli, M. G., Varhegyi, G., and Blasi, C. D., 2002. "Thermogravimetric analysis and devolatilization kinetics of wood". *Industrial and Engineering Chemistry Research,* **41**, pp. 4201–4208.

[68] White, J. E., and Catallo, W. J., 2011. "Biomass pyrolysis kinetics: A comparative critical review with relevant agricultural residue case studies". *Journal of Analytical and Applied Pyrolysis*. doi:10.1016/j.jaap.2011.01.004.

[69] Bevington, P. R., and Robinson, D. K., 2003. *Data Reduction and Error Analysis for the Physical Sciences*, third ed. McGraw-Hill, New York, NY.

[70] Draper, N. R., and Smith, H., 1966. *Applied Regression Analysis*. John Wiley & Sons, Inc., New York, NY.

[71] Kennedy, J., and Eberhart, R. "Particle swarm optimization". Vol. 4, Piscataway, NJ: IEEE, pp. 1942–1948.

[72] Bratton, D., and Kennedy, J., 2007. "Defining a standard for particle swarm optimization". Proceedings of the 2007 IEEE Swarm Intelligence Symposium, pp. 120–127.

[73] del Valle, Y., Venayagamoorthy, G., Mohagheghi, S., Hernandez, J., and Harley, R., 2008. "Particle swarm optimization: Basic concepts, variants and applications in power systems". *IEEE Transactions on Evolutionary Computation,* **12**(2), p. 171.

[74] Fu, Q., Argyropoulos, D. S., Tilotta, D. C., and Lucia, L. A., 2008. "Understanding the pyrolysis of CCA-treated wood part i. effect of metal ions". *Journal of Applied Pyrolysis,* **81**, pp. 60–64.

[75] Reed, T. B., and Gaur, S., 1997. *The High Heat of Fast Pyrolysis for Large Particles*, Vol. 1 of *Developments in Thermochemical Biomass Conversion*. Chapman and Hall, Suffolk, Great Britain.

[76] Scott, D. S., Majerski, P., Piskorz, J., and Radlein, D., 1999. "A second look at fast pyrolysis of biomass - the RTI process". *Journal of Analytical and Applied Pyrolysis,* **51**, pp. 23–37.

[77] Shafizadeh, F., and McGinnis, G. D., 1971. "Chemical composition and thermal analysis of cottonwood". *Carbohydrate Research,* **16**(2), pp. 273–277.

[78] Bilbao, R., Millera, A., and Arauzo, J., 1989. "Kinetics of weight loss by thermal decomposition of xylan and lignin. influence of experimental conditions". *Thermochimica Acta,* **143**, pp. 137–148.

[79] Bilbao, R., Millera, A., and Arauzo, J., 1989. "Thermal decomposition of lignocellulosic materials: influence of the chemical composition". *Thermochimica Acta,* **143**, pp. 149–159.

[80] Varhegyi, G., Antal, M. J., Szekely, T., and Szabo, P., 1989. "Kinetics of the thermal decomposition of cellulose, hemicellulose, and sugarcane bagasse". *Energy & Fuels,* **3**(3), pp. 329–335.

[81] Antal Jr, M. J., and Varhegyi, G., 1995. "Cellulose pyrolysis kinetics: The current state of knowledge". *Industrial and Engineering Chemistry Research,* **34**(3), pp. 703–717.

[82] Varhegyi, G., Antal Jr, M. J., Jakab, E., and Szabo, P., 1997. "Kinetic modeling of biomass pyrolysis". *Journal of Analytical and Applied Pyrolysis,* **42**(1), pp. 73–87.

[83] Many, J. J., Velo, E., and Puigjaner, L., 2003. "Kinetics of biomass pyrolysis: a reformulated three-parallel-reactions model". *Industrial & Engineering Chemistry Research,* **42**(3), pp. 434–441.

[84] Ramiah, M. V., 1970. "Thermogravimetric and differential thermal analysis of cellulose, hemicellulose, and lignin". *Journal of Applied Polymer Science,* **14**(Compendex), pp. 1323–37.

[85] Yang, H., Yan, R., Chen, H., Zheng, C., Lee, D. H., and Liang, D. T., 2006. "In-depth investigation of biomass pyrolysis based on three major components: hemicellulose, cellulose and lignin". *Energy & Fuels,* **20**(1), pp. 388–393.

[86] Hosoya, T., Kawamoto, H., and Saka, S., 2007. "Cellulose-hemicellulose and cellulose-lignin interactions in wood pyrolysis at gasification temperature". *Journal of Analytical and Applied Pyrolysis,* **80**(1), pp. 118–125.

[87] Couhert, C., Commandre, J.-M., and Salvador, S., 2009. "Is it possible to predict gas yields of any biomass after rapid pyrolysis at high temperature from its composition in cellulose, hemicellulose and lignin?". *Fuel,* **88**(3), pp. 408–417.

[88] Navarro, M. V., Murillo, R., Mastral, A. M., Puy, N., and Bartroli, J., 2009. "Application of the distributed activation energy model to biomass and biomass constituents devolatilization". *AIChE Journal,* **55**(10), pp. 2700–2715.

[89] Di Blasi, C., 1998. "Comparison of semi-global mechanisms for primary pyrolysis of lignocellulosic fuels". *Journal of Analytical and Applied Pyrolysis,* **47**(1), pp. 43–64.

[90] Lanzetta, M., and Di Blasi, C., 1998. "Pyrolysis kinetics of wheat and corn straw". *Journal of Analytical and Applied Pyrolysis,* **44**(2), pp. 181–192.

[91] Durbak, I., Green, D. W., Highley, T. L., Howard, James, L., McKeever, D. B., Miller, R. B., Pettersen, R. C., Rowell, R. M., Simpson, W. T., Skog, K. E., White, R. H., Winandy, J. E., and Zerbe, J. I., 1998. *Wood*, fourth ed., Vol. 25. John Wiley and Sons, Inc., pp. 627–664.

[92] Koufopanos, C. A., Papayannakos, N., Maschio, G., and Lucchesi, A., 1991. "Modelling of the pyrolysis of biomass particles. studies on kinetics, thermal and heat transfer effects". *Canadian Journal of Chemical Engineering,* **69**(Compendex), pp. 907–915.

[93] Williams, P. T., and Besler, S., 1993. "The pyrolysis of rice husks in a thermogravimetric analyser and static batch reactor". *Fuel,* **72**(2), pp. 151–159.

[94] Pyle, D., and Zaror, C., 1984. "Heat transfer and kinetics in the low temperature pyrolysis of solids". *Chemical Engineering Science,* **39**(1), p. 147.

[95] Di Blasi, C., 1996. "Kinetic and heat transfer control in the slow and flash pyrolysis of solids". *Industrial and Engineering Chemsitry Research,* **35**, pp. 37–46.

[96] Bryden, K. M., Ragland, K. W., and Rutland, C. J., 2002. "Modeling thermally thick pyrolysis of wood". *Biomass and Bioenergy,* **22**(1), pp. 41–53.

[97] Chan, W.-C. R., Kelbon, M., and Krieger, B. B., 1985. "Modelling and experimental verification of physical and chemical processes during pyrolysis of a large biomass particle". *Fuel,* **64**(11), pp. 1505–1513.

[98] Jiang, X., and Ellis, N., 2010. "Upgrading bio-oil through emulsification with biodiesel: Thermal stability". *Energy & Fuels,* **24**(4), pp. 2699–2706.

[99] Raveendran, K., Ganesh, A., and Khilar, K. C., 1996. "Pyrolysis characteristics of biomass and biomass components". *Fuel,* **75**(8), pp. 987–998.

[100] Miller, R. S., and Bellan, J., 1997. "A generalized biomass pyrolysis model based on the superimposed celluose hemicellulose and lignin kinetics". *Combustion Science and Technology,* **126**, pp. 97–137.

[101] Di Blasi, C., 2000. "The state of the art of transport models for charring solid degradation". *Polymer International,* **49**(10), pp. 1133–1146.

[102] Basu, P., and Kaushal, P., 2009. "Modeling of pyrolysis and gasification of biomass in fluidized beds: A review". *Chemical Product and Process Modeling,* **4**(Compendex).

[103] Wagenaar, B. M., Prins, W., and van Swaaij, W. P. M., 1993. "Flash pyrolysis kinetics of pine wood". *Fuel Processing Technology,* **36**(1-3), pp. 291–298.

[104] Jiang, G., Nowakowski, D. J., and Bridgwater, A. V., 2010. "A systematic study of the kinetics of lignin pyrolysis". *Thermochimica Acta,* **498**(1-2), pp. 61–66.

[105] Nunn, T. R., Howard, J. B., Longwell, J. P., and Peters, W. A., 1985. "Product compositions and kinetics in the rapid pyrolysis of milled wood lignin". *Industrial & Engineering Chemistry Process Design and Development,* **24**(3), pp. 844–852.

[106] Reina, J., Velo, E., and Puigjaner, L., 1998. "Kinetic study of the pyrolysis of waste wood". *Industrial & Engineering Chemistry Research,* **37**(11), pp. 4290–4295.

[107] MathWorks, I., 2008. *Matlab R2008b*, 7.7.0.471 (r2008b) ed. The MathWorks, Inc.

[108] Brown, A. L., Dayton, D. C., and Daily, J. W., 2001. "A study of cellulose pyrolysis chemistry and global kinetics at high heating rates". *Energy & Fuels,* **15**(5), pp. 1286–1294.

[109] Roy, C., Yang, J., Blanchette, D., Korving, L., and Caumia, B. D., 1997. *Development of a novel vacuum pyrolysis reactor with improved heat transfer potential*, Vol. 1. Chapman and Hall, London.

[110] Roy, C., Blanchette, D., and de Caumia, B., 2000. Horizontal moving stirred bed reactor, January 30, 1998.

[111] Yang, J., Malendoma, C., and Roy, C., 2000. "Determination of the overall heat transfer coefficient in a vacuum pyrolysis moving and stirred bed reactor". *Transactions of the Institute of Chemical Engineers,* **78**(4), p. 10.

[112] Gupta, M., Yang, J., Metral, S., and Roy, C., 2004. "Flow characterization of moving and stirred bed vacuum pyrolysis reactor from rtd studies". *Chemical Engineering Research and Design,* **82**(1), pp. 34–42.

[113] Kansa, E. J., Perlee, H. E., and Chaiken, R. F., 1977. "Mathematical model of wood pyrolysis including internal forced convection". *Combustion and Flame,* **29**, pp. 311–324.

[114] Di Blasi, C., 1996. "Heat, momentum and mass transport through a shrinking biomass particle exposed to thermal radiation". *Chemical Engineering Science,* **51**(7), pp. 1121–1132.

[115] Gronli, M. G., and Melaaen, M. C., 2000. "Mathematical model for wood pyrolysis-comparison of experimental measurements with model predictions". *Energy and Fuels,* **14**, pp. 791–800.

[116] Bharadwaj, A., Baxter, L. L., and Robinson, A. L., 2004. "Effects of intraparticle heat and mass transfer on biomass devolatilization: Experimental results and model predictions". *Energy and Fuels,* **18**, pp. 1021–1031.

[117] Papadikis, K., Gu, S., and Bridgwater, A. V., 2009. "Cfd modelling of the fast pyrolysis of biomass in fluidised bed reactors: Modelling the impact of biomass shrinkage". *Chemical Engineering Journal,* **149**(1-3), pp. 417–427.

[118] Papadikis, K., Gu, S., and Bridgwater, A. V., 2009. "Cfd modelling of the fast pyrolysis of biomass in fluidised bed reactors. part b. heat, momentum and mass transport in bubbling fluidised beds". *Chemical Engineering Science,* **64**(5), pp. 1036–1045.

[119] Bird, R. B., Stewart, W. E., and Lightfoot, E. N., 2007. *Transport Phenomena*, second ed. John Wiley & Sons, New York, NY.

[120] Nield, D. A., and Bejan, A., 2006. *Convection in Porous Media*, 3rd ed. Springer Science+Business Media, Inc., New York, NY.

[121] Milosavljevic, I., Oja, V., and Suuberg, E. M., 1996. "Thermal effects in cellulose pyrolysis: Relationship to char formation processes". *Industrial & Engineering Chemistry Research,* **35**(3), pp. 653–662.

[122] Perry, R. H., and Green, D. W., 2007. *Perry's Chemical Engineers' Handbook*, eighth ed. McGraw-Hill, New York, NY.

[123] Miyanami, K., Fan, L.-S., Fan, L. T., and Walawender, W. P., 1977. "Mathematical model for pyrolysis of a solid particle - effects of the heat of reaction". *Canadian Journal of Chemical Engineering,* **55**(Compendex), pp. 317–325.

[124] Di Blasi, C., 2000. "Modelling the fast pyrolysis of cellulosic particles in fluid-bed reactors". *Chemical Engineering Science,* **55**(24), pp. 5999–6013.

[125] Lu, H., Ip, E., Scott, J., Foster, P., Vickers, M., and Baxter, L. L., 2010. "Effects of particle shape and size on devolatilization of biomass particle". *Fuel,* **89**(5), pp. 1156–1168.

[126] Janse, A. M. C., Westerhout, R. W. J., and Prins, W., 2000. "Modelling of flash pyrolysis of a single wood particle". *Chemical Engineering and Processing,* **39**(3), pp. 239–252.

[127] Babu, B. V., and Chaurasia, A. S., 2003. "Modeling for pyrolysis of solid particle: kinetics and heat transfer effects". *Energy Conversion and Management,* **44**(14), pp. 2251–2275.

[128] Jalan, R. K., and Srivastava, V. K., 1999. "Studies on pyrolysis of a single biomass cylindrical pellet–kinetic and heat transfer effects". *Energy Conversion and Management,* **40**(5), pp. 467–494.

[129] Di Blasi, C., 2002. "Modeling intra- and extra-particle processes of wood fast pyrolysis". *AIChE Journal,* **48**(10), pp. 2386–2397.

[130] Di Blasi, C., 1994. "Numerical simulation of cellulose pyrolysis". *Biomass and Bioenergy,* **7**, pp. 87–98.

[131] Horne, P. A., and Williams, P. T., 1996. "Influence of temperature on the products from the flash pyrolysis of biomass". *Fuel,* **75**(9), pp. 1051–1059.

[132] Shaddix, C. R., and Huey, S. P., 1997. *Combustion Characteristics of Fast Pyrolysis Oils*, Vol. 1 of *Developments in Thermochemical Biomass Conversion*. Chapman and Hall, Suffolk, Great Britain.